NOTE TO USERS

This reproduction is the best copy available.

UMI®

HEAT PIPE PERFORMANCE ENHANCEMENT THROUGH COMPOSITE WICK DESIGN

By

George S. Franchi

A thesis submitted to
the Faculty of Graduate Studies and Research
in partial fulfillment of
the requirements for the degree of

Master of Applied Science

Ottawa-Carleton Institute for
Mechanical and Aerospace Engineering

Department of
Mechanical and Aerospace Engineering
Carleton University
Ottawa, Ontario
July, 2006

Your file Votre référence
ISBN: 978-0-494-33631-1
Our file Notre référence
ISBN: 978-0-494-33631-1

Abstract

This study examines the enhancement of heat pipe thermal performance through the employment of composite wicks. These wicks were fabricated from a biporous structure comprised of fine metal powders, sintered onto layers of coarse pore copper mesh. Wick structures were conceived to exploit both the effects of enhanced evaporation heat transfer at the liquid/vapour interface and the extension of the capillary limit. A number of composite wick heat pipe configurations were fabricated and tested to assess performance improvements in comparison to conventional designs. Tests were conducted in horizontal, gravity assisted and against gravity conditions to determine whether these designs were orientation dependent. At various heat inputs, some configurations achieved thermal performance levels over three times higher than those of conventional heat pipes. During against gravity tests, virtually all composite designs outperformed the conventional heat pipe at all heat inputs. These results clearly demonstrated that heat pipe performance was substantially improved through composite wick design.

Acknowledgements

Who to thank and where to begin? I think I will start by offering a warm-hearted thanks to my supervisor, Professor Huang, for providing guidance and inspiration for this milestone in my career. I will never forget the kind words and wisdom you imparted to me, not only in matters of engineering, but more importantly towards all aspects of life involving integrity and honesty. Long after the classroom lectures and experiments have faded from memory, these most important of qualities will endure. Thank you, Professor.

Many thanks to the Department of Mechanical and Aerospace Engineering for the financial assistance awarded to me, without which I could not have completed this endeavour. I am also indebted to Materials and Manufacturing Ontario, Acrolab and INCO for their invaluable aid during this research program. For their technical support and expertise, I would like to extend my appreciation to Stephan Biljan, Steve Truttmann, Fred Barrett and Gary Clements. To my heat pipe research colleagues Feng Cai and Michel Garcia, thank you both for your advice and experience. I avoided countless difficulties and pitfalls from your hard-earned knowledge.

Most importantly, I want to thank my family. Try as I may, I could never hope to find words eloquent enough to express my gratitude. You mean the world to me, and I love you with all my heart.

Table of Contents

Abstract iii

Acknowledgements iv

Table of Contents v

List of Tables x

List of Figures xii

1 Introduction 1

1.1 History 1

1.2 Applications 3

1.2.1 Electronics cooling 3

1.2.2 Aerospace 5

1.2.3 Pipelines 6

1.3 Operation 7

1.4 Enhanced Heat Transfer with Composite Wicks 8

1.5 Objective and Approach 9

2 Theory 11

2.1 Capillary Limit 11

2.1.1 Surface tension and capillary pressure 12

2.1.2 Liquid pressure drop 17

2.1.3 Vapour pressure drop 21

2.1.4 Hydrostatic pressure 22

2.1.5 General expression for the capillary limit 23

2.2 Sonic Limit 23

2.3 Boiling Limit 24

2.4 Entrainment Limit 31

2.5 Graphical Representation of Heat Transfer Limitations 33

2.6 Prediction of Thermal Performance 34

2.6.1 Equivalent thermal resistance network 35

2.6.2 Heat pipe operating temperature 41

2.6.3 Effective thermal conductivity of wicks 42

3 Heat Pipe Design 46

3.1 Working Fluid Selection 46

3.2 Container 50

3.3 Wick Design 54

3.3.1 Metal screens 55

3.3.2 Axial grooves 58

3.3.3 Sintered metal wicks 62

3.3.4 Composite wicks 67

4 Experimental Procedure 74

4.1 Container and Wick Materials 74

4.2 Wick Configurations 78

4.2.1 Homogeneous wicks 80

4.2.2 Composite wicks 81

4.3 Heat Pipe Design and Manufacture 84

4.3.1 Design 85

4.3.2 Wick cutting 89

4.3.3 Degreasing and deoxidizing 90

4.3.4 Metal powder application 91

4.3.5 Rolling and insertion 95

4.3.6 Sintering 97

4.3.7 Fluid charging and sealing 100

4.4 Heat Pipe Test Rig 102

4.4.1 Heater and annulus 103

4.4.2 Cooling jacket and chiller 106

4.4.3 Insulation 108

4.4.4 Instrumentation 110

4.4.5 Data acquisition system 114

4.5 Test Procedure 117

4.5.1 Heat pipe preparation 117

4.5.2 Orientations 121

4.5.3 Testing and data collection 123

4.5.4 Data reduction program 126

5 Results and Discussion 128

5.1 Summary of Tests Performed 128

5.2 Scanning Electron Microscopy 129

5.2.1 Configuration A 130

5.2.2 Configuration H 131

5.2.3 Configuration K 133

5.2.4 Configuration B 134

5.2.5 Configuration E 137

5.2.6 Configuration I 139

5.2.7 Configuration J 140

5.2.8 Configuration L 142

5.3 Effective Thermal Conductivity and Maximum Heat Input Rate 143

5.3.1 Configuration A 144

5.3.2 Configuration H 147

5.3.3 Configuration K 150

5.3.4 Configuration B 155

5.3.5 Configuration E 164

5.3.6 Configuration J 170

5.3.7 Configuration L 177

5.3.8 Summary of composite wicks with highest thermal performance 185

5.3.9 Uncertainty analysis 187

6 Conclusions and Recommendations 194

6.1 Remarks on Results 194

6.2 Remarks on Manufacturing 196

6.3 Remarks on Testing 197

6.4 Concluding Words 197

Appendix A Heat Pipe Design Calculations 199

Appendix B Fluid Charging 211

Appendix C Cooling Jacket Drawings 214

Appendix D Data Acquisition Program 226

Appendix E "thermalPerformance" Program 230

Appendix F Additional Performance Results 237

7 References 260

List of Tables

Table 2-1: Effective Pore Radii of Simple Wicks [16] 17

Table 2-2: Wetted Perimeter for Various Wicks [1] 32

Table 2-3: Heat Pipe Thermal Resistances [10] 36

Table 2-4: Effective Thermal Conductivities of Various Wicks [1] 44

Table 3-1: Heat Pipe Working Fluids and Their Corresponding Temperature Ranges [10] 47

Table 3-2: Material/Working Fluid Compatibility Data [38] 50

Table 3-3: Values for n, m and B of the Initial Stage Sintering Equation [56] 66

Table 4-1: Copper Tubing Properties [68], [69], [70] 75

Table 4-2: 100-Mesh Copper Screen Properties [1], [68] 76

Table 4-3: Properties of Metco 55 Copper Powder [71] 76

Table 4-4: Properties of Nickel Powder [73] 78

Table 4-5: Summary of Wick Identification 79

Table 4-6: Conventional Heat Pipe Design Specifications 88

Table 4-7: Band Heater Properties 104

Table 4-8: Properties of Delrin® [68] 106

Table 4-9: Properties of Refrigerated Recirculation Chiller [74] 108

Table 4-10: Properties of Insulation [68] 109

Table 4-11: Thermocouple Properties [75] 111

Table 4-12: Multimeter Properties [76] 112

Table 4-13: Thermistor Properties [75] 113

Table 4-14: Flowmeter Properties [77] 113

Table 4-15: Properties of Thermocouple Modules [78] 114

Table 4-16: Properties of Analog Input Module [79] 115

Table 4-17: Properties of Network Module [80] 115

Table 4-18: Properties of OMEGATHERM® [81] 120

Table 5-1: List of Heat Pipe Tests 129

Table 5-2: Thermal Performance Summary for A7 147

Table 5-3: Thermal Performance Summary for H3 150

Table 5-4: Thermal Performance Summary for K1 and K2 155

Table 5-5: Thermal Performance Summary for Runs 1 and 2 of B8 164

Table 5-6: Thermal Performance Summary for E7 170

Table 5-7: Thermal Performance Summary for J3 176

Table 5-8: Summary of Findings from Cao et al. [67] 181

Table 5-9: Maximum Heat Input Rate Comparison, Against Gravity 183

Table 5-10: Thermal Performance Summary for L2 184

Table 5-11: Measurement Uncertainties Used in Equation (5-5) 189

Table 5-12: Uncertainty Summary for Heat Pipe B8 190

List of Figures

Figure 1-1: Heat Pipe Cooling System for a Mobile Pentium 4 Chip [4] 3

Figure 1-2: Module Heat Flux Rise versus Time [8] 4

Figure 1-3: Pipeline Support with Integrated Heat Pipes for Permafrost Preservation [14] 7

Figure 1-4: Schematic Diagram of a Heat Pipe [15] 8

Figure 2-1: Wetting Meniscus Geometry at Liquid/Vapour Interface [16] 13

Figure 2-2: Geometry of Meniscus in a Cylindrical Tube [16] 14

Figure 2-3: Capillary Limit versus Effective Pore Radius for Copper Mesh Wicks [17] 16

Figure 2-4: Permeability versus Effective Pore Radius for Copper Mesh Wicks [17] 19

Figure 2-5: Tortuosity of Coarse Pores (Left) Compared to Fine Pores (Right) 19

Figure 2-6: Heat Flux versus Excess Temperature [20] 21

Figure 2-7: Gravity Assisted Operation, ϕ Negative 22

Figure 2-8: Heat Transfer Modes 1 and 2 in the Evaporator [1] 25

Figure 2-9: Heat Transfer Modes 3 and 4 in the Evaporator [1] 26

Figure 2-10: Pool Boiling Curve for Plane Surface Submerged Under Water [1] 27

Figure 2-11: Heat Flux versus Excess Temperature [28] 30

Figure 2-12: Heat Flux versus Excess Temperature for Wicks with Vapour Channels [23] 31

Figure 2-13: Heat Transfer Limitations as a Function of Temperature [16] 34

Figure 2-14: Thermal Resistance Network of a Heat Pipe [30] 35

Figure 2-15: Simplified Thermal Resistance Network [10] 37

Figure 2-16: Estimation of Heat Pipe Operating Temperature [10] 42

Figure 2-17: Thermal Conductivity for Heat Transfer in (a) Parallel and (b) Series [1].. 43

Figure 3-1: Variation of Liquid Transport Factor with Temperature [5]..... 48

Figure 3-2: Heat Pipe Container and Wick Dimensions..... 51

Figure 3-3: Wick Pore Radius (μm) versus Permeability (μm^2) [39] 54

Figure 3-4: Plain Wire Screen Weave (Left), Twill Screen Weave (Right) [40] 56

Figure 3-5: Metal Screen Wick Dimensions..... 57

Figure 3-6: Cross-section of Heat Pipe with Rectangular Axial Grooves [45] 58

Figure 3-7: Friction Factor Reynolds Number Product for Rectangular Passages [16] ... 61

Figure 3-8: Phases during Sintering Process 63

Figure 3-9: Neck Formation in Sintered Bronze Powder [55]..... 64

Figure 3-10: Surface Diffusion versus Volume Diffusion [58] 65

Figure 3-11: Thin Film Evaporation in Porous Structures [61]..... 69

Figure 3-12: Composite Metal Powder Wick [60] 70

Figure 3-13: Triangular Grooves (a) without and (b) with Fine Pores [46] 71

Figure 3-14: Wang and Catton's Results [46] 73

Figure 4-1: Spherical Copper Powder Morphology..... 77

Figure 4-2: Filamentary Nickel Powder Morphology 78

Figure 4-3: Schematics of Configuration A (Left) and Configurations H and K (Right). 80

Figure 4-4: Liquid/Vapour Interface Covered with Metal Powder, Configurations B and I 82

Figure 4-5: Wall/Wick and Liquid/Vapour Interfaces Covered with Metal Powder, Configurations E and J..... 83

Figure 4-6: Metal Powder Applied throughout Wick Thickness, Configuration L 84

Figure 4-7: Schematic of Mesh Weave [28] 87

Figure 4-8: Model for Required Width of Mesh 89

Figure 4-9: Wick Cutting Tools 90

Figure 4-10: End Plugs 91

Figure 4-11: Homogeneous Copper Metal Powder Heat Pipe Manufacturing Assembly 92

Figure 4-12: Metal Powder Application Patterns for Configurations B, E, I and J 93

Figure 4-13: Spray Patterns for Configurations L and H 93

Figure 4-14: Nickel Powder Sprayed Wick, Configuration B 94

Figure 4-15: Composite Copper Wick Manufacturing 95

Figure 4-16: Configuration J with Rolling Tools 96

Figure 4-17: Placement of End Plugs for Wick Centering 97

Figure 4-18: Nickel Powder, Sintered at 800°C for 1.5 Hours 98

Figure 4-19: Copper Powder, Sintered at 850°C for 1 Hour 98

Figure 4-20: Nickel Powder, Sintered at 940°C for 1 Hour 99

Figure 4-21: Heat Pipe Test Rig Schematic 103

Figure 4-22: Dimensions of Copper Annulus Half 105

Figure 4-23: Heater and Annulus Assembly 105

Figure 4-24: Cooling Jacket 107

Figure 4-25: Insulation Covering Cooling Jacket and Heater 110

Figure 4-26: Thermocouple Locations on Heat Pipe 111

Figure 4-27: Thermocouple Attachment 118

Figure 4-28: Teflon Tape Seal 118

Figure 4-29: Clamped Cooling Jacket on Orientation Pedestal 119

Figure 4-30: Thermal Paste Application 120

Figure 4-31: Heater Assembly Secured to Evaporator Section 121

Figure 5-1: Configuration A 130

Figure 5-2: Configuration H 131

Figure 5-3: Configuration H, Higher Magnification 132

Figure 5-4: Sintering in Nickel Powder 132

Figure 5-5: Configuration K 133

Figure 5-6: Neck Formation in Configuration K 134

Figure 5-7: Liquid/Vapour Interface of Configuration B 135

Figure 5-8: Increased Surface Area in Configuration B 136

Figure 5-9: Sintering between Nickel Powder and Copper Mesh 137

Figure 5-10: Configuration E 138

Figure 5-11: Wall/Wick Interface of Configuration E 138

Figure 5-12: Configuration I 139

Figure 5-13: Liquid/Vapour Interface of Configuration I 140

Figure 5-14: Configuration J 141

Figure 5-15: Wall/Wick Interface of Configuration J 142

Figure 5-16: Horizontal and Gravity Assisted Effective Thermal Conductivities for A7 145

Figure 5-17: Axial Temperature Distribution of A7, Against Gravity Operation 146

Figure 5-18: Against Gravity Effective Thermal Conductivity Results for A7 146

Figure 5-19: Horizontal and Gravity Assisted Effective Thermal Conductivities for H3 149

Figure 5-20: Against Gravity Effective Thermal Conductivity Results for H3 149

Figure 5-21: Horizontal and Gravity Assisted Results for Configuration K 151

Figure 5-22: Against Gravity Effective Thermal Conductivity Results for K1 and K2. 152

Figure 5-23: Axial Temperature Distribution for K1, Against Gravity 153

Figure 5-24: Comparison of Horizontal Thermal Performance between B8 and A7 156

Figure 5-25: Comparison of Gravity Assisted Thermal Performance between B8 and A7 158

Figure 5-26: Against Gravity Thermal Performance Comparison between B8, A7 and H3 160

Figure 5-27: Testing Repeatability for B8, Horizontal Orientation 161

Figure 5-28: Testing Repeatability for B8, Gravity Assisted Orientation 162

Figure 5-29: Testing Repeatability for B8, Against Gravity Orientation 162

Figure 5-30: Comparison of Horizontal Thermal Performance between E7 and A7 165

Figure 5-31: Comparison of Gravity Assisted Performance between E7 and A7 167

Figure 5-32: Against Gravity Performance Comparison between E7, A7 and H3 168

Figure 5-33: Comparison of Horizontal Performance between J3 and A7 171

Figure 5-34: Comparison of Gravity Assisted Performance between J3 and A7 173

Figure 5-35: Against Gravity Performance Comparison between J3, A7 and K1 174

Figure 5-36: Axial Temperature Distribution for J3, Against Gravity 175

Figure 5-37: Comparison of Horizontal Performance between L2 and A7 178

Figure 5-38: Comparison of Gravity Assisted Performance between L2 and A7 181

Figure 5-39: Against Gravity Performance Comparison between L2, A7 and H3 182

Figure 5-40: Best Performing Configurations, Horizontal Operation 186

Figure 5-41: Best Performing Configurations, Gravity Assisted Operation..... 186

Figure 5-42: Best Performing Configurations, Against Gravity Operation..... 187

Figure 5-43 Uncertainty for B8, Horizontal Orientation 191

Figure 5-44: Uncertainty for B8, Gravity Assisted Orientation 191

Figure 5-45: Uncertainty for B8, Against Gravity Orientation..... 192

1 Introduction

The need for progressively efficient, high performance heat transfer equipment in electronics cooling, heat recovery systems and spacecraft thermal management has produced numerous successful innovations. Perhaps the most remarkable of these is the heat pipe, a heat transfer device with a thermal conductivity much higher than any solid material. Through vapourization and condensation heat transfer processes, very high heat transfer rates with minimal variations in end-to-end temperature are possible. Since heat pipes do not contain any moving parts, they have gained a reputation of exceptional reliability, with the additional benefit of completely passive operation.

Although the heat pipe has proven itself a practical tool for thermal control, certain heat transfer limitations hinder its capabilities. Coupled with industrial demands for greater heat removal capacity in increasingly compact designs, conventional heat pipes have often proven inadequate. Thus, to keep pace, the heat pipe must evolve. Since heat pipe performance is intimately associated with heat transfer and fluid behaviour in porous materials, advancement of the art may very well depend on the application of enhanced, porous engineering materials.

1.1 History

The historical development of the heat pipe began in 1836 with the United Kingdom patent of the Perkins Tube, comprised of a closed tube containing a small amount of water for the purpose of transferring heat [1]. Although the Perkins Tube was not

technically a heat pipe, the operating principles and mechanism of heat transfer were analogous. The first patent describing the modern day heat pipe was filed in 1944 by Gaugler, who was working for General Motors at the time [1]. This device, used in a refrigeration unit, was made of an outer tube, a working fluid and a capillary structure to pump the fluid against gravity.

The heat pipe was somewhat forgotten until its emergence as a viable system for spacecraft thermal management. In 1964, the heat pipe was reinvented by Grover et al. at Los Alamos National Laboratories during research for the United States Space Program [1], [2]. His experiments demonstrated the feasibility of heat pipes as high performance heat transmission devices for space applications. It was Grover who first coined the name "heat pipe". Although these experiments renewed much interest in heat pipes, worldwide research did not begin until after Cotter's work on theoretical heat pipe analysis was published in 1965 [3]. Heat pipe research centers were then established in the United Kingdom, Italy and the former USSR.

Today, every developed country has contributed in some way to the development of heat pipe technology, with Russia and the United States leading the state-of-the-art. Heat pipes are currently being used in a wide array of industries, ranging from electronics and space exploration to petroleum pipelines. Industrial manufacturers are capable of heat pipe production rates of 50 000 units per month [4]. Research programs worldwide continue to explore potential heat pipe applications, more advanced modeling techniques and new,

high performance materials. The heat pipe has become a universally accepted, reliable thermal management tool with ample opportunity for research.

1.2 Applications

Heat pipe applications reflect their remarkable versatility. Microelectronics cooling and spacecraft temperature control are two main areas where heat pipes are extensively used. Other notable industrial uses include the preservation of permafrost in pipeline applications.

1.2.1 Electronics cooling

Electronics cooling represents the most widespread industrial use of heat pipes [5]. The higher performance electronics of the early 1990's demanded more efficient heat removal devices. Laptop computer manufacturers first used heat pipes in 1994 to dissipate 6 W of heat [6]. By 1999, approximately 60% of all laptop computers employed heat pipes for their cooling needs. Figure 1-1 shows a typical heat pipe and heat sink for laptop computer thermal management.

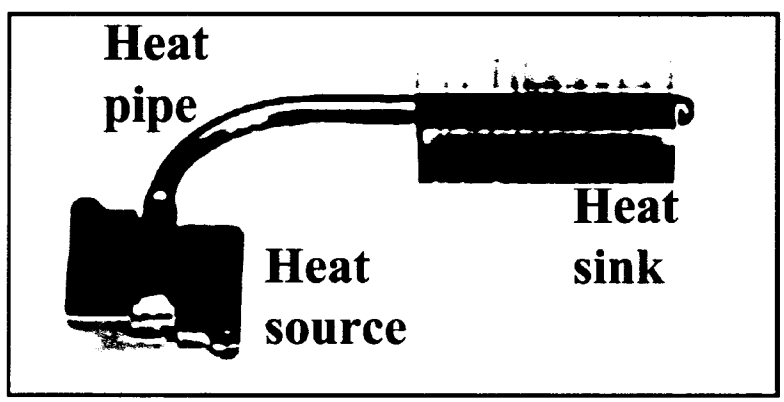

Figure 1-1: Heat Pipe Cooling System for a Mobile Pentium 4 Chip [4]

Presently, Intel's Mobile Pentium 4 processor requires 35 W of heat removal at a heat flux of 24 W/cm^2 [7], and all manufacturers make use of heat pipe technology in their laptops. Current designs capable of meeting this demand commonly use 3 to 6 mm outside diameter copper/water heat pipes. However, the increasing trend towards higher heat removal rates in more compact designs must be met with higher performance thermal management devices. According to Moore's Law, the performance of electronic modules doubles approximately every 18 months [8]. This in turn causes an exponential growth in heat flux from the component surface, shown in Figure 1-2.

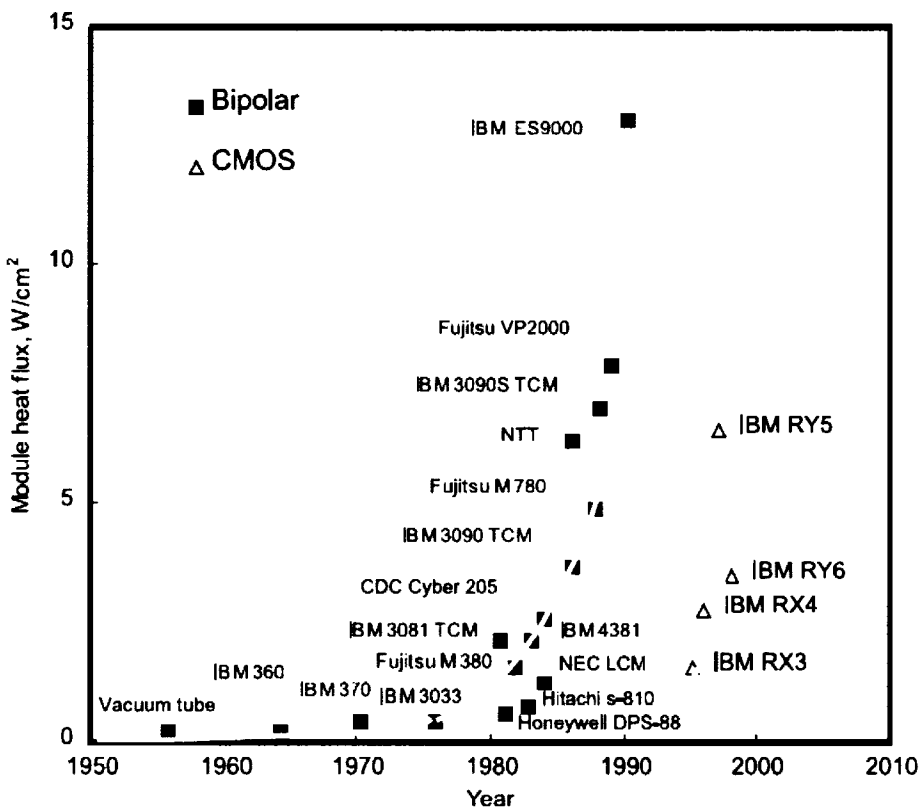

Figure 1-2: Module Heat Flux Rise versus Time [8]

Some electronic components produce heat fluxes greater than 100 W/cm^2 [9] while requiring operating temperatures lower than 120°C. Projected trends demand even higher performance from the electronics thermal control industry. It is therefore necessary to improve heat pipe performance to further enhance waste heat dissipation. Since heat pipe performance is strongly dependent on the properties of its porous wick [10], numerous research programs have taken aim at heat transfer augmentation through advancements in wick design.

1.2.2 Aerospace

Aluminium-ammonia heat pipes are extensively used for aerospace and spacecraft applications, due to their low weight penalty. Spacecraft thermal management also includes the field of microelectronics and component temperature control.

Satellite isothermalisation is one instance where heat pipes have been particularly indispensable. Thermal gradients resulting from external heating and cooling can be minimized by redistributing heat from the hot side to the cold side, thus reducing structural distortion. For example, if one side of a satellite faces the sun while the other side faces deep space, solar radiation will heat one side while the other side reaches very cold temperatures. This will impose significant thermal stresses on the satellite. To counter this, thermal engineers have exploited the heat pipe's nearly isothermal behaviour with great success [1].

The Russian satellites MAGION 4 and 5, launched in 1995 and 1996 respectively, used U-shaped heat pipes with sintered copper wicks and acetone as the working fluid [11]. These heat pipes, with a diameter of 10 mm and length of 0.6 m, were reported to dissipate 60 W of heat. Another current project being conducted by NASA employs a heat pipe for laser cooling. The Geoscience Laser Altimeter System (GLAS) uses remote laser sensing for land topography. The laser requires 100 W of heat dissipation to function. This is accomplished with a sintered nickel wick heat pipe, measuring 25 mm in diameter and 150 mm in length [12].

1.2.3 Pipelines

Heat pipe technology is used in numerous additional applications. One important instance deserving mention is perhaps the largest project to ever use heat pipes. Initiated by the Alyeska Pipeline Service Company in 1974, construction of the Trans-Alaska Pipeline required the use of 130 000 heat pipes for the purpose of permafrost preservation around vertical supports. This would ensure year-round structural stability of above-ground pipeline sections. The heat pipe manufacturer, McDonnell Douglas, used 5 to 7.5 cm diameter, steel-ammonia heat pipes with lengths varying from 9 to 23 m [13]. These heat pipes, shown in Figure 1-3, demonstrated heat removal rates of 300 W.

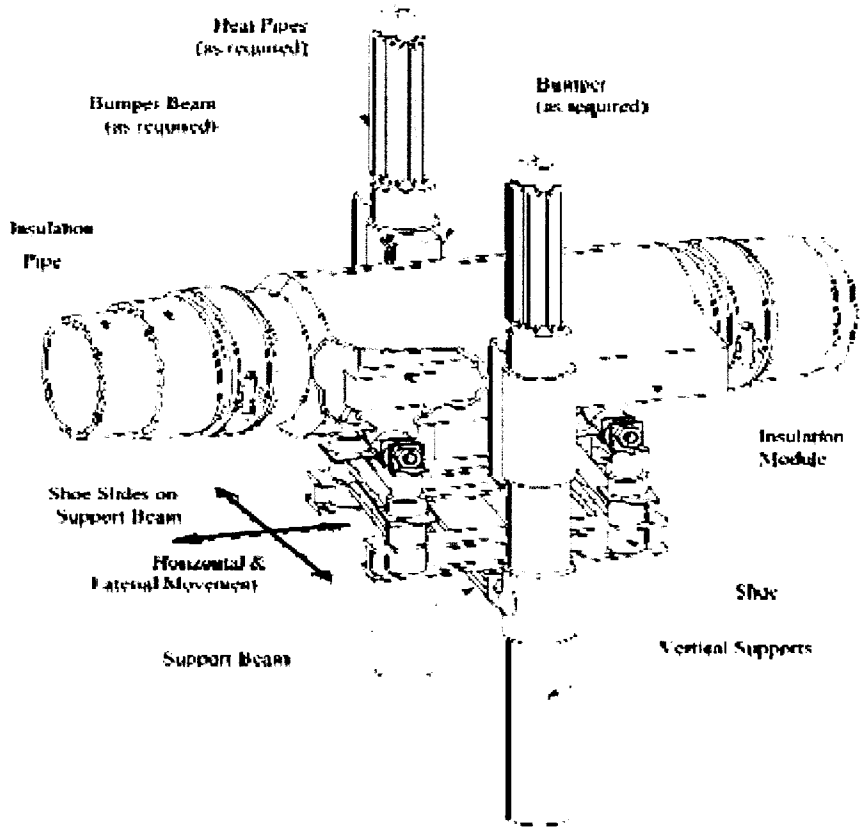

Figure 1-3: Pipeline Support with Integrated Heat Pipes for Permafrost Preservation [14]

1.3 Operation

A heat pipe essentially consists of a sealed container, a porous wicking material and a working fluid. Air is evacuated from the container and an adequate amount of working fluid is added to fully saturate the wick. The container is then sealed and the heat pipe is connected to a heat source and heat sink.

Heat pipes can be divided into three distinct sections: the evaporator, an adiabatic section and the condenser. Heat addition takes place in the evaporator by conduction through the container and wick. The working fluid then evaporates, absorbing its latent heat of

vapourization. A pressure difference causes the vapour to flow through the constant temperature adiabatic section to the condenser. Here, it gives off its latent heat, condensing into liquid. The porous wick then transports the fluid back to the evaporator by capillary action where the cycle repeats itself. A schematic of heat pipe components and operation is shown below in Figure 1-4.

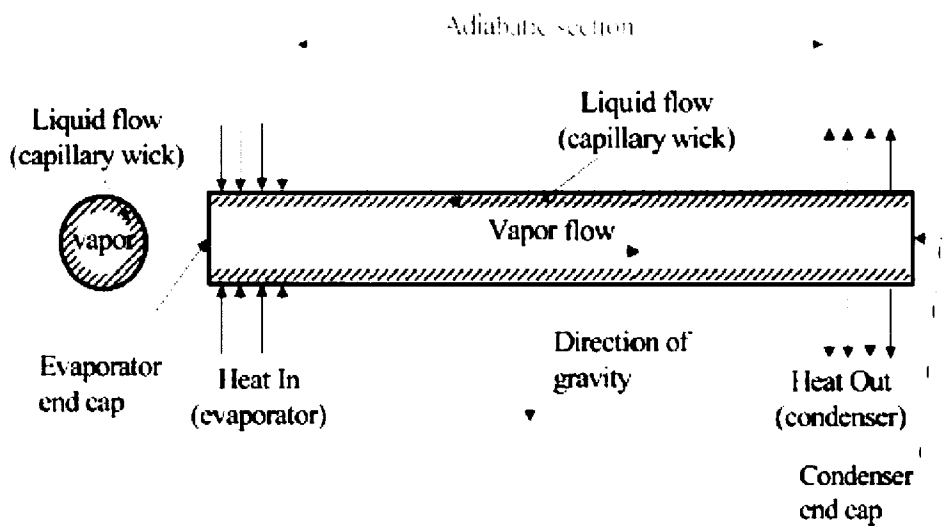

Figure 1-4: Schematic Diagram of a Heat Pipe [15]

1.4 Enhanced Heat Transfer with Composite Wicks

The wick is the essential element in heat pipe operation, since it provides the means for continuous heat transfer. Two important parameters to consider during the wick design stage are its pore size and liquid permeability. As will be presented in Section 2.1 , an ideal wick would have small pores for high capillary pressure, along with high liquid permeability to facilitate liquid flow. Most heat pipes have homogeneous wicks, that is, wicks with one characteristic microstructure. This poses a problem, since a fine pore

structure, favourable for capillary pressure, increases the liquid path length through the wick, resulting in a higher liquid pressure drop [1]. Conversely, a wick with high permeability suffers from poor capillary pressure, yet possesses the advantage of low liquid pressure drops.

Thus, homogeneous wicks must balance capillary pumping pressure and liquid permeability to achieve some compromise in performance. On the other hand, composite wicks offer a solution to this anomaly. If a porous structure with both small and large pores could be manufactured, both parameters may be satisfied simultaneously. The fine pore layer would provide the means for high capillary pressure, while the large pore layers would ensure high liquid permeability. Furthermore, the addition of fine pores should augment evaporation heat transfer due to a substantial increase in evaporative surface area. Through these mechanisms, heat pipe performance should increase significantly.

1.5 Objective and Approach

The objective of this research program is the enhancement of heat pipe performance through the development of composite wick structures. Moderate temperature heat pipes are commonly employed in electronics cooling, therefore this is the intended field of application. Heat transfer performance will be assessed based on the maximum heat transfer rate along with the effective thermal conductivity of the heat pipe.

Composite wick heat pipes will be manufactured from large pore metal substrate materials, combined with a secondary fine pore structure of metal powder. Manufacturing

techniques must be developed, including cleaning, application methods, heat pipe fabrication, furnace processing and fluid charging. Various wick configurations will be attempted to improve heat transfer performance. Following this, the design and manufacture of a heat pipe test rig will be carried out, including instrumentation, controls and data analysis software. Finally, composite wick heat pipe performance testing will be carried out to quantify improvements in heat transfer in comparison to conventional designs. Test variables will include heat input rates and gravitational orientation, since these factors affect heat pipe performance.

2 Theory

Steady state heat pipe theory consists of hydrodynamic and heat transfer analyses. The hydrodynamic analysis is concerned with the liquid pressure drop in the wick, as well as the vapour pressure drop in the vapour passage. Heat transfer analyses are used to model heat transport through the heat pipe [1]. Using a combination of these, theoretical heat pipe performance can be predicted. However, numerous heat transfer limitations constrain heat transport under certain circumstances. Of these, the limit with the lowest heat transport capability will determine a heat pipe's maximum performance. The major limitations on a heat pipe's heat transport capability are:

- the capillary limit
- the sonic limit
- the boiling limit
- the entrainment limit

Although other less common heat transport limits exist, the above will be the focus of discussion in this section.

2.1 Capillary Limit

A heat pipe's wick provides the necessary flow path for the liquid to return from the condenser to the evaporator. It also supplies the capillary pressure needed to pump the fluid from one end to the other. Along the heat pipe, there exists a pressure gradient

between the vapour and the liquid at the liquid/vapour interface. This pressure gradient forces the meniscus back into the wick, creating capillary pressure [16]. For proper heat pipe operation, the maximum capillary pumping pressure provided by the wick (ΔP_c) must be greater than or equal to the sum of the following pressure drops [5]:

- The liquid pressure drop needed to transport the liquid from the condenser to the evaporator through the wick (ΔP_l)
- The vapour pressure drop required to move the liquid from the evaporator to the condenser through the vapour passage (ΔP_v)
- The hydrostatic pressure due to gravity (ΔP_g)

This can be expressed mathematically as:

$$\Delta P_c \geq \Delta P_l + \Delta P_v + \Delta P_g \tag{2-1}$$

The above equation is referred to as the capillary limit and is the most significant limitation to heat transport for moderate temperature heat pipes [10]. If this condition is not satisfied, the wick will not be able to return the working fluid to the evaporator, and evaporator dryout will occur [10].

2.1.1 Surface tension and capillary pressure

The phenomenon of surface tension is responsible for creating the capillary pressure required to return the working fluid from the condenser to the evaporator. A molecule in

a liquid is attracted by other liquid molecules surrounding it. Since these forces are in equilibrium, no resultant force acts on this molecule. However, if this molecule is placed at the surface of the liquid, unbalanced attractive forces are imposed on it by the molecules inside the liquid. Therefore, a resultant inward force acts to pull the surface molecule in that direction. This has the effect of giving the liquid drop a shape of minimum area. This attractive force per unit length is called surface tension, and is a property of the fluid and the surrounding medium [5].

When a liquid is in contact with a solid medium, the liquid surface molecules experience forces from the solid surface molecules as well as from the internal liquid molecules. If attractive forces exist between the liquid and the solid, the liquid free surface will be concave and the liquid "wets" the solid, as shown in Figure 2-1. Conversely, if these forces are repulsive, the resultant liquid free surface will be convex and the liquid is termed "non-wetting".

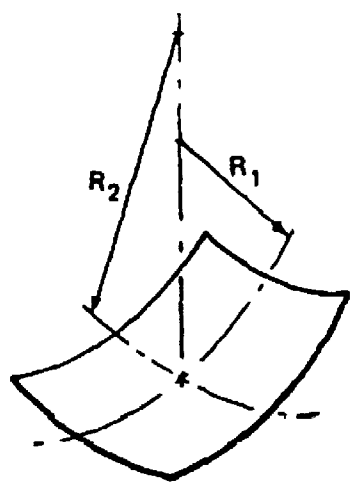

Figure 2-1: Wetting Meniscus Geometry at Liquid/Vapour Interface [16]

If a perfectly wetting liquid is used such that the contact angle is zero, we obtain:

$$\Delta P_{c,\max} = \frac{2\sigma}{r} \tag{2-5}$$

Equation (2-5) is the expression for the maximum capillary pressure developed in a cylindrical pore [1]. Other pore shapes yield similar results. For example, it can be shown that a rectangular capillary tube with $R_1 = \infty$ *and* $R_2 = W/2$ produces a maximum capillary pressure of:

$$\Delta P_{c,\max} = \frac{2\sigma}{W} \tag{2-6}$$

where W is the width of the tube. Generalizing the Laplace and Young Equation for any pore geometry, we therefore obtain:

$$\Delta P_{c,\max} = \frac{2\sigma}{r_{eff}} \tag{2-7}$$

where r_{eff} is the "effective" pore radius. From Equation (2-7), one can appreciate how a decrease in r_{eff} would influence the maximum capillary pressure. This effect is shown in Figure 2-3, where the maximum capillary pressure of various copper mesh screens are plotted versus their pore radii [17]. The capillary pressure increases dramatically for pore radii smaller than 300 μm.

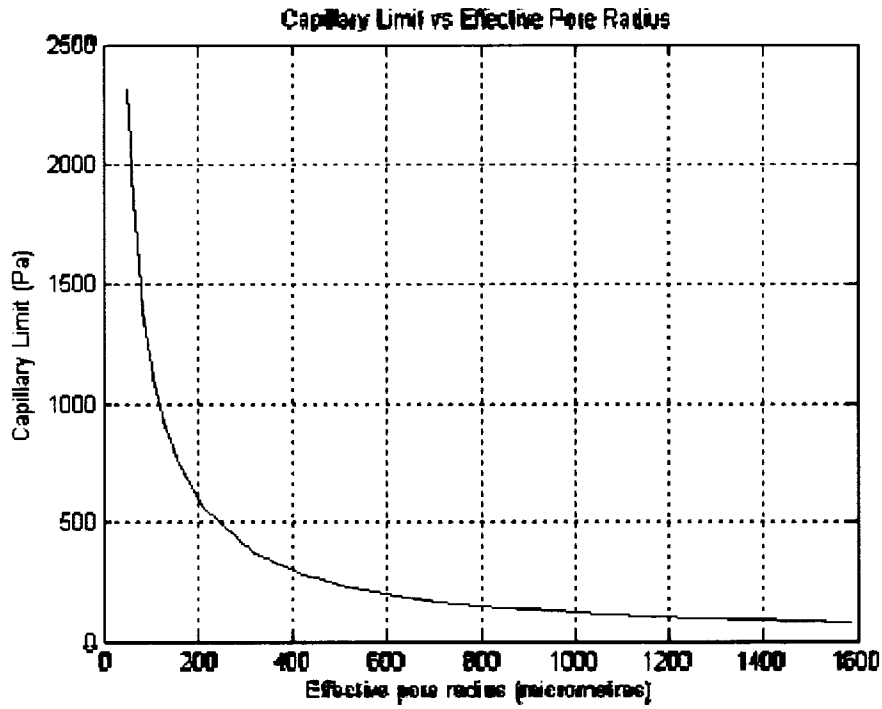

Figure 2-3: Capillary Limit versus Effective Pore Radius for Copper Mesh Wicks [17]

Values of r_{eff} for other simple pore geometries are listed in Table 2-1. For more complex geometries, the effective pore radius must be determined experimentally.

Wick Structures	Expressions for r_{eff}	
Cylindrical pores	$r_{eff} = r$	r = radius of pores
Rectangular groove	$r_{eff} = w$	w = groove width
Triangular groove	$r_{eff} = \frac{w}{\cos\beta}$	w = groove width β = half angle
Parallel wires	$r_{eff} = w$	w = wire spacing
Wire screens	$r_{eff} = \frac{w + d_w}{2}$	w = wire spacing d_w = wire diameter
Pack spheres	$r_{eff} = 0.41 r_s$	r_s = sphere radius

Table 2-1: Effective Pore Radii of Simple Wicks [16]

2.1.2 Liquid pressure drop

Concerning the liquid pressure drop term (ΔP_l) of Equation (2-1), liquid flow in the wick is almost always laminar [5]. Since mass flow in the evaporator and the condenser varies with axial position, an effective length (l_{eff}) for fluid flow is commonly used for pressure drop calculations [1], [5], [16]:

$$l_{eff} = l_a + \frac{l_e + l_c}{2} \qquad (2\text{-}8)$$

where l_a is the length of the adiabatic portion of the heat pipe, and l_e and l_c are the lengths of the evaporator and condenser sections respectively. Faghri simplifies the Continuity

and Momentum Equations to obtain an expression for the axial liquid pressure drop in the wick [1]:

$$\Delta P_l = \frac{\mu_l \dot{m}_l l_{eff}}{\rho_l A_w K} \tag{2-9}$$

where μ_l is the dynamic viscosity of the liquid, $\dot{m}_l$ is the liquid mass flow rate, ρ_l is the liquid density, A_w is the cross-sectional area of the wick and K is the wick's liquid permeability. Equation (2-9) can also be expressed in terms of the evaporator heat input, Q_{in}:

$$\Delta P_l = \frac{\mu_l Q_{in} l_{eff}}{\rho_l A_w h_{fg} K} \tag{2-10}$$

where h_{fg} is the latent heat of vapourization of the working fluid. Equation (2-10) demonstrates that in order to minimize the liquid pressure drop term, the liquid permeability of the wick should be as high as possible. However, liquid permeability decreases rapidly with decreasing pore size, the smaller pore sizes being favourable for high capillary pressure. Refer to Figure 2-4 for an illustration of this trend from manufacturer's data for copper mesh wicks [17].

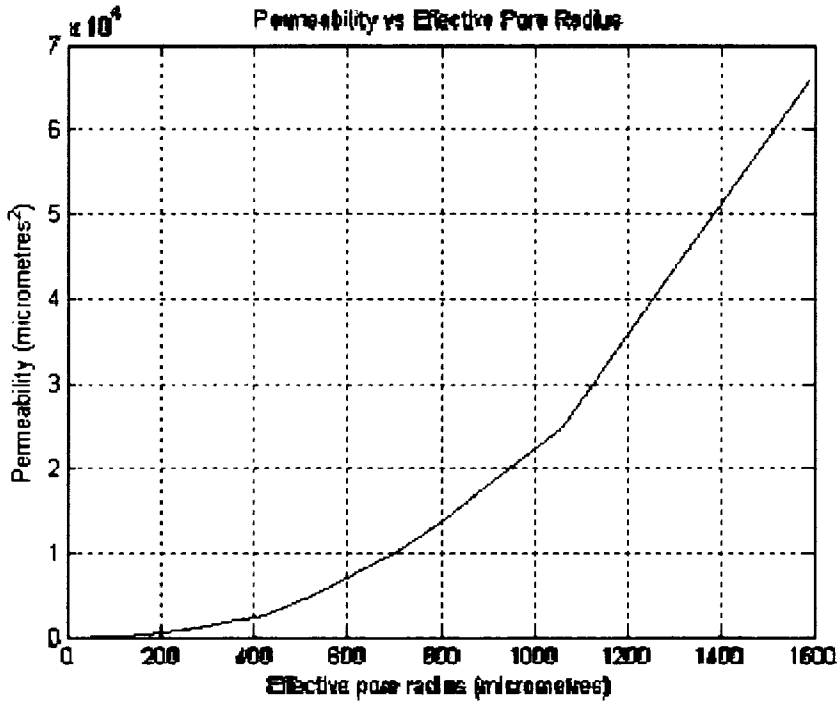

Figure 2-4: Permeability versus Effective Pore Radius for Copper Mesh Wicks [17]

This effect is primarily due to tortuosity, or an increase in the liquid flow path length associated with the finer pores, which causes a larger liquid pressure drop [18]. Figure 2-5 illustrates this phenomenon.

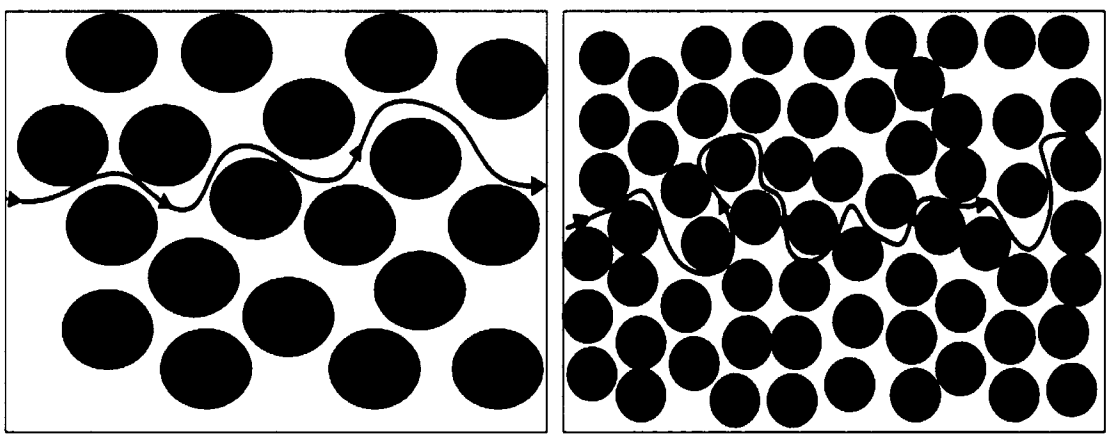

Figure 2-5: Tortuosity of Coarse Pores (Left) Compared to Fine Pores (Right)

Here, the anomaly of homogeneous wicks becomes evident: oftentimes a wick with one characteristic pore size cannot simultaneously satisfy both high liquid permeability and high capillary pressure [18]. However, some researchers have reported significant performance improvements employing composite wicks containing large and small pores. A study conducted by Canti et al. [20] characterized various stainless steel wicks based on liquid permeability, capillary head and heat transfer performance. Wick configurations in this study consisted of fused metal powder, metal screens or hybrid, layered compositions of these two structures.

It was discovered that the hybrid wick possessed the best combination of liquid permeability and capillary pressure. Additionally, this wick exhibited the highest heat transfer performance when tested in against gravity operation. It was postulated that this performance increase was attributable to the presence of the large pores from the metal screen layers and the fine pores from the fused metal powder. The large pores allowed high liquid permeability while the fine pores generated high capillary pressure. Results from the most unfavourable heat transfer condition are shown in Figure 2-6, where heat flux is plotted versus the temperature difference between the heater wall (T_w) and the saturation temperature of the liquid (T_s) at atmospheric pressure. For this test, the heater was positioned at its highest point above the water reservoir, such that the water was required to travel through the wick against gravity towards the heat source. Clearly, the hybrid wick demonstrated superior heat transfer performance in comparison to both homogeneous wicks.

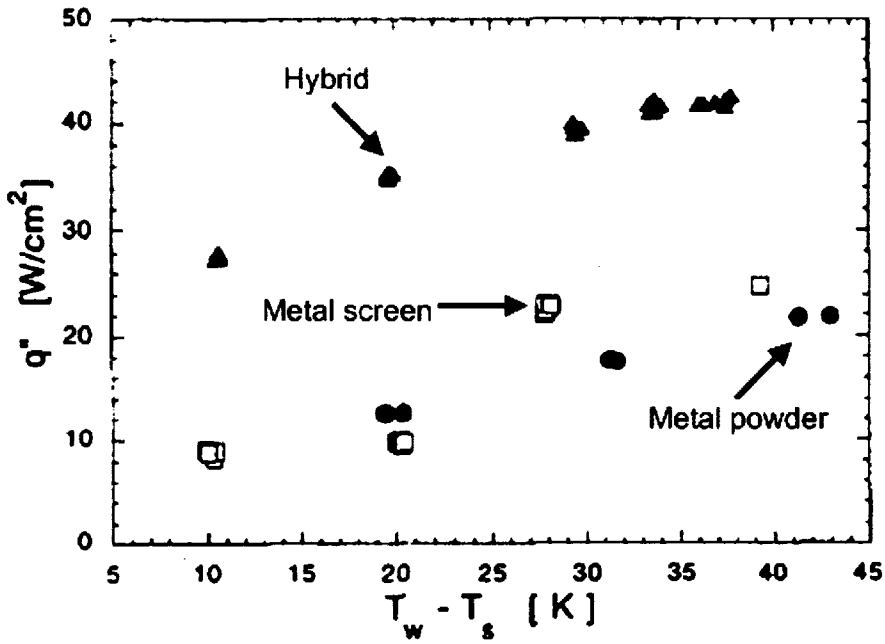

Figure 2-6: Heat Flux versus Excess Temperature [20]

2.1.3 Vapour pressure drop

The vapour pressure drop term of Equation (2-1), ΔP_v, can be approximated in conventional heat pipes by assuming incompressible, laminar flow [1], [16]. One widely used one-dimensional analysis proposed by Busse assumes laminar vapour flow and constant vapour density [21]. An expression relating the vapour pressure drop to the evaporator heat input is then obtained through:

$$\Delta P_v = \frac{8\mu_v Q_{in} l_{eff}}{\pi \rho_v R_v^4 h_{fg}} \tag{2-11}$$

where μ_v is the vapour dynamic viscosity, ρ_v is the vapour density and R_v is the vapour space radius.

2.1.4 Hydrostatic pressure

The expression for the hydrostatic pressure term of Equation (2-1), ΔP_g, can be positive, negative or zero depending on the orientation of the heat pipe. The hydrostatic pressure is given by:

$$\Delta P_g = \rho_l g L_t \sin\phi \tag{2-12}$$

where ρ_l is the density of the liquid, g is the acceleration due to gravity, L_t is the total length of the heat pipe and ϕ is the angle between the heat pipe and the horizontal plane. According to the sign convention of Equation (2-1), if the condenser is above the evaporator, ϕ is negative so that ΔP_g acts to decrease the right hand side of the inequality. See Figure 2-7 for a graphical representation. The liquid returning to the evaporator will be aided by gravity, thus increasing the capillary limit. The converse is true when the evaporator is above the condenser.

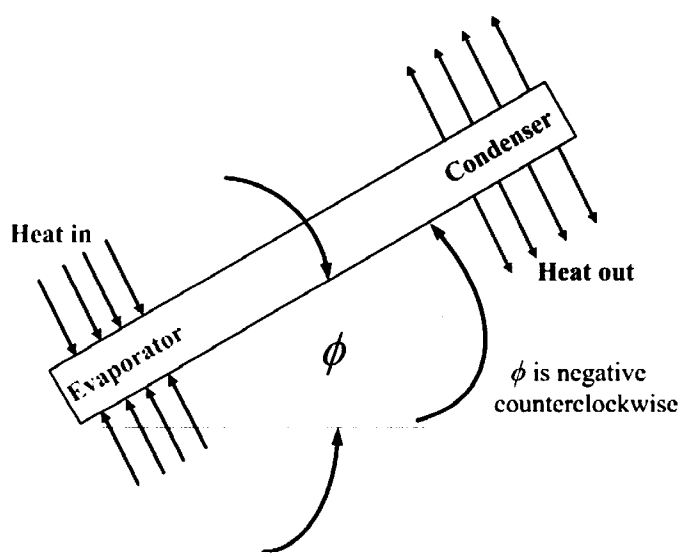

Figure 2-7: Gravity Assisted Operation, ϕ Negative

2.1.5 General expression for the capillary limit

Combining Equations (2-1), (2-7), (2-10), (2-11) and (2-12), an expression for the capillary limit of a conventional heat pipe is obtained:

$$\frac{2\sigma}{r_{eff}} \geq \frac{\mu_l Q_{in} l_{eff}}{\rho_l A_w h_{fg} K} + \frac{8\mu_v Q_{in} l_{eff}}{\pi \rho_v R_v^4 h_{fg}} + \rho_l g L_t \sin\phi \qquad (2\text{-}13)$$

For proper heat pipe operation, the above condition must be satisfied. If Equation (2-13) is violated, heat pipe dryout will occur. This is defined as the inability of the wick to continuously supply liquid to the evaporator for heat transport. The onset of the capillary limit can be detected by a sudden and continuous increase in evaporator wall temperature [1]. If the heat input is not decreased at this point, the wick will dry out completely, and heat pipe failure will ensue.

2.2 Sonic Limit

This heat transfer limitation occurs when the vapour velocity at the evaporator exit approaches the local speed of sound [1]. When this happens, choked flow limits the vapour mass flow rate. Accordingly, the heat transfer limit is also reached. Liquid metal heat pipes are susceptible to this, particularly during transient startup. However, the sonic limit is not as serious a failure as the capillary limit, since an increase in the evaporator temperature will in turn increase the sonic limit. Conversely, decreasing the condenser temperature will not increase the heat transfer rate under choked conditions. Thus, one distinct sign associated with this type of failure is a high axial temperature gradient.

The theoretical analysis is accomplished using the principles of conservation of mass, momentum and energy. The relation between the maximum axial heat transport (Q_s) at unity Mach Number was first suggested by Levy [22]:

$$Q_s = \frac{\rho_o c_o h_{fg} A_v}{\sqrt{2(K'+1)}} \tag{2-14}$$

where ρ_o is the density of the vapour at the evaporator and A_v is the area of the vapour passage. The speed of sound, c_o, is calculated with:

$$c_o = \sqrt{K' R_{vap} T_o} \tag{2-15}$$

where R_{vap} is the vapour gas constant and T_o is the evaporator end cap temperature. The ratio of specific heats, K', is given by:

$$K' = \frac{C_p}{C_V} \tag{2-16}$$

where C_p is the specific heat of the vapour during a constant pressure process, and C_v is the specific heat of the vapour during a constant volume process.

2.3 Boiling Limit

If the radial heat flux in the evaporator is too high, the heat pipe may exceed the boiling limit. This phenomenon causes vapour bubbles to form in the wick, and if severe enough, a vapour barrier will form between the heat pipe wall and the liquid. Very high

evaporator wall temperatures are observed when this limit is surpassed, since liquid transport to the pipe wall has been effectively blocked by vapour entrapment in the wick [1].

Figure 2-8 and Figure 2-9 show the four modes of heat transfer progressively leading to this type of failure. During the first mode, conduction and natural convection transfer heat through the liquid saturated wick. In Mode 2, liquid starts receding into the pores of the wick as the heat flux increases. If the capillary force is not high enough to deliver liquid to the evaporator, dryout will occur at this stage. Here, conduction still controls heat transfer.

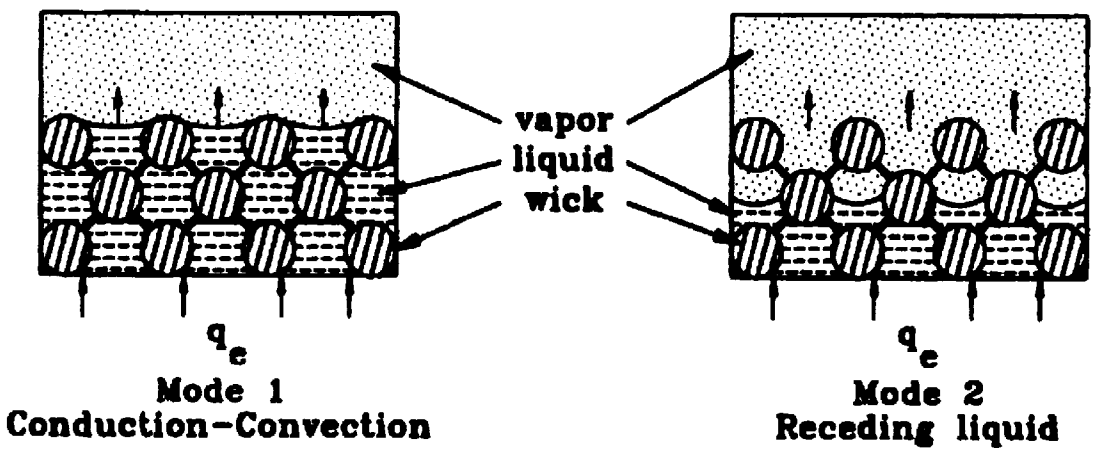

Figure 2-8: Heat Transfer Modes 1 and 2 in the Evaporator [1]

In Mode 3, nucleate boiling begins with the formation of vapour bubbles at the heat pipe wall. These bubbles work through the wick and burst at the liquid/vapour interface. Nucleate boiling does not necessarily pose a problem, so long as the vapour bubbles can escape from the wick [23]. Indeed, many researchers have concluded that nucleate

boiling permits very high forced convective heat transfer rates [1], [24]. However, this heat transfer regime does not exist for very long. With higher temperature differences between the wall and the vapour, heat transfer rates decrease. This is the onset of Mode 4, where film boiling arises. Here, larger quantities of vapour are generated and may form an insulating layer against the heat pipe wall if it cannot escape. As a result, liquid flow to the wall is impeded, causing a rapid increase in wall temperature.

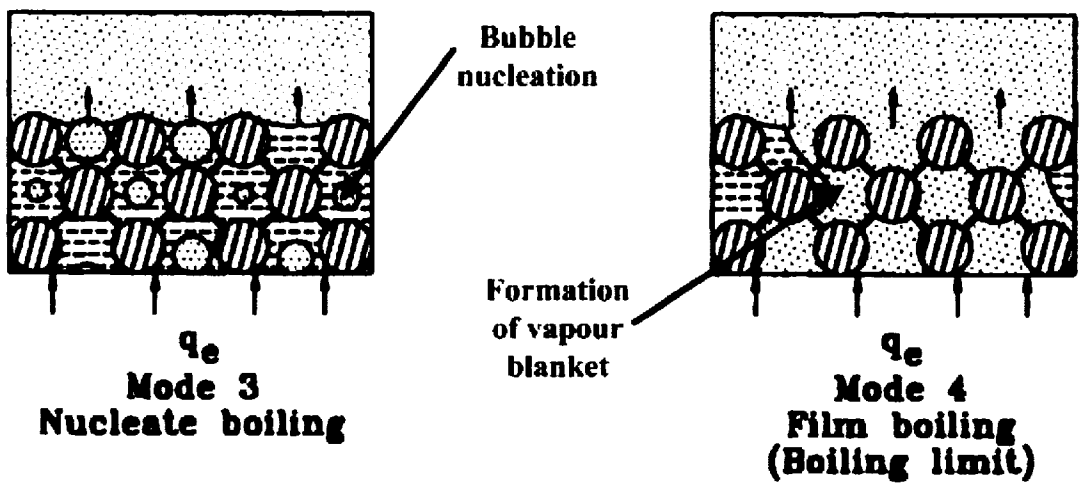

Figure 2-9: Heat Transfer Modes 3 and 4 in the Evaporator [1]

The above heat transfer modes are analogous to the phenomenon of boiling heat transfer. In Figure 2-10, the different regimes that occur during boiling heat transfer are shown through variations of heat flux (q) versus excess temperature, or superheat (T_w - T_{sat}). The excess temperature is defined as the difference between the surface or wall temperature (T_w) and the saturation temperature of the fluid (T_{sat}) at a given pressure. From A to B, free convection currents are responsible for heat transfer, moving liquid to the liquid/vapour interface where evaporation can occur. This is comparable to Modes 1 and 2 of Figure 2-8.

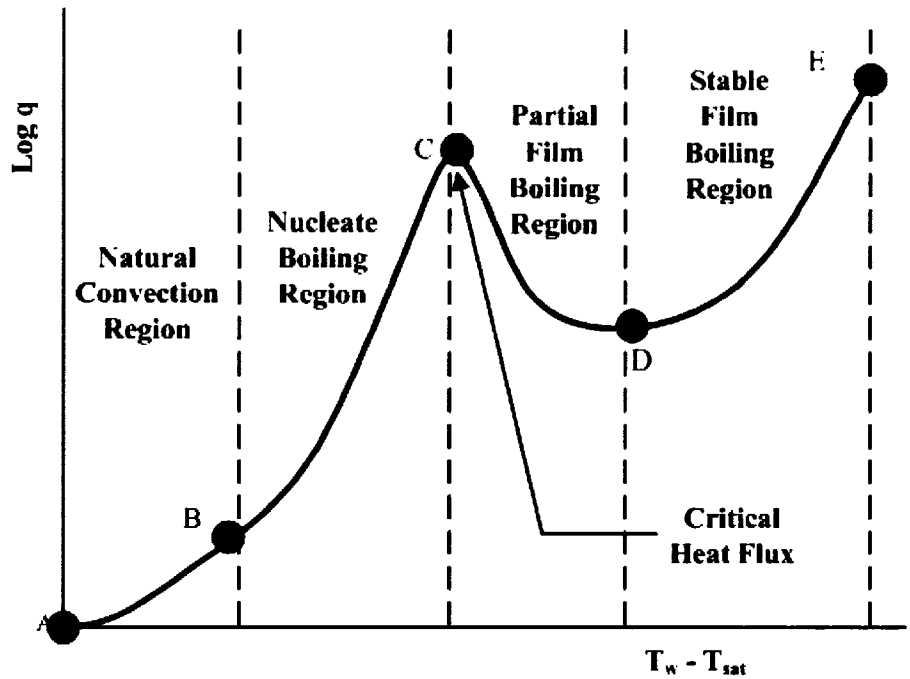

Figure 2-10: Pool Boiling Curve for Plane Surface Submerged Under Water [1]

As the superheat is increased from *B* to *C*, nucleate boiling is initiated and the Critical Heat Flux (*CHF*) is rapidly reached at *C*. This is similar to Mode 3 of Figure 2-9. Most notable here is the substantial increase in heat flux associated with relatively small increments in superheat. This rapid increase may be attributable to intense agitation of the fluid at the heat transfer surface [25], [26]. Thus, if a heat pipe can be induced to function in the nucleate boiling regime, very high performance should result. However, if the generated vapour cannot escape, film boiling, shown in Mode 4 of Figure 2-9, will greatly reduce the heat pipe's effectiveness. This corresponds to the even higher superheat regions from *C* to *D* and *D* to *E* of Figure 2-10. The formed vapour blanket acts as an insulating layer, greatly increasing the radial temperature drop across the wick.

According to convention, nucleate boiling in heat pipe wicks must be avoided, since precise control of this mode of heat transfer is unreliable [1], [16]. This process is composed of two events: bubble initiation followed by bubble growth and motion. Small bubbles are always present in the wick. However, for bubble growth and subsequent failure to occur, vapour superheat is required. This occurs at a critical wall-to-vapour temperature difference calculated by [1]:

$$\Delta T_{crit} = T_w - T_v = \frac{2\sigma T_v}{h_{fg}\rho_v}\left(\frac{1}{R_b} - \frac{1}{R_{men}}\right) \tag{2-17}$$

where T_w is the heat pipe wall temperature, T_v is the vapour temperature, σ is the surface tension of the liquid, h_{fg} is the latent heat of vapourization of the working fluid, ρ_v is the vapour density, R_b is the radius of the vapour bubble and R_{men} is the radius of the meniscus at the liquid/vapour interface. The meniscus radius is usually estimated to be equal to the effective pore radius of the wick (r_{eff}), while R_b is commonly calculated by [27]:

$$R_b = \sqrt{\frac{2\sigma T_{sat} k_l (v_v' - v_l')}{h_{fg} q_r}} \tag{2-18}$$

where T_{sat} is the saturation temperature of the working fluid, k_l is the liquid thermal conductivity and q_r is the radial heat flux. The specific volumes of the saturated vapour and liquid are given by v_v' and v_l' respectively. In the absence of sufficient experimental data, Faghri [1] and Chi [16] suggest using a value on the order of $R_b = 10^{-7}$ for a

conventional heat pipe. To prevent bubble growth, a critical heat input rate (Q_b) is related to the boiling heat transfer limit. For cylindrical heat pipes, this limit is given by [1]:

$$Q_b = \frac{2\pi L_e k_{wick} \Delta T_{crit}}{\ln\left(\frac{R_i}{R_v}\right)} \tag{2-19}$$

where L_e is the length of the evaporator, R_i is the inner radius of the pipe wall and R_v is the vapour space radius. The effective thermal conductivity of the saturated wick is denoted k_{wick} and depends on the thermal conductivities of both the solid wick and the working fluid. More specific cases have been solved for various wick configurations. These will be covered in Section 2.6.3.

Although nucleate boiling has traditionally been avoided, numerous researchers have acknowledged its potential for heat pipe performance enhancement, [24], [28]. Brautsch and Kew performed experiments on metal screen wicks to study heat transfer processes associated with the boiling and capillary limits. Tests were conducted in both submerged pool boiling and against gravity modes. They found that at low heat fluxes, porous structures increased heat transfer performance over bare surfaces. As pore size decreased, heat transfer performance increased, particularly during against gravity operation. Moreover, during against gravity operation, the maximum attainable heat flux increased with the number of layers, however the heat transfer coefficient decreased due to an increase in the thermal resistance across the wick [28]. Results are shown in Figure 2-11. Also notable here is the superior performance of the bare surface at higher heat fluxes.

Thus, it was concluded that porous surfaces improved heat transfer performance over bare surfaces at low heat fluxes due to an increased number of nucleation sites. Higher heat fluxes enabled the bare surface to outperform the porous structures, attributable to vapour entrapment in the wicks.

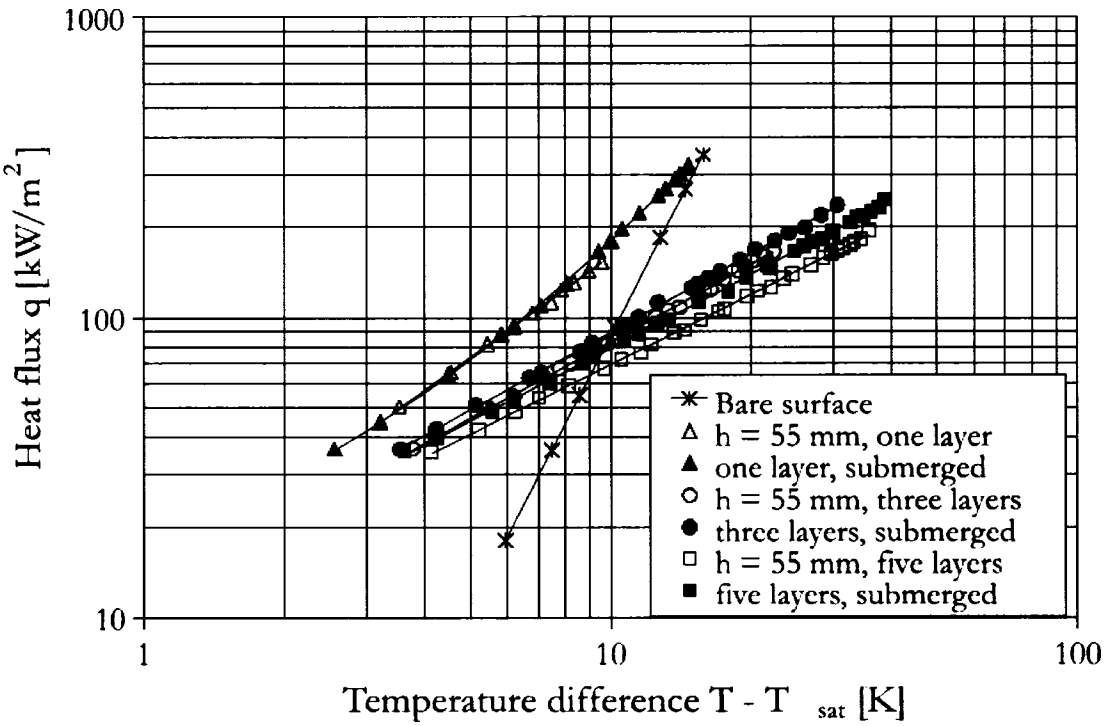

Figure 2-11: Heat Flux versus Excess Temperature [28]

Mughal and Plumb conducted experiments on heat pipe wicks with various thicknesses and configurations. Channels were cut into the wick to facilitate vapour evacuation during nucleate boiling. Copper foam wicks with 7 and 15 vapour channels were compared to a plain wick. They discovered that heat transfer was enhanced when vapour channels were present, the highest performance being achieved by the 15-channel wick [23]. Figure 2-12 displays Mughal and Plumb's findings. There was a distinct increase in. heat flux with an increase in the number of vapour channels. This was credited to

nucleate boiling and the augmented egress of vapour through vapour evacuation channels. Therefore, they concluded that nucleate boiling increased heat transfer performance and extended the boiling limit, provided the generated vapour was permitted to escape from the wick.

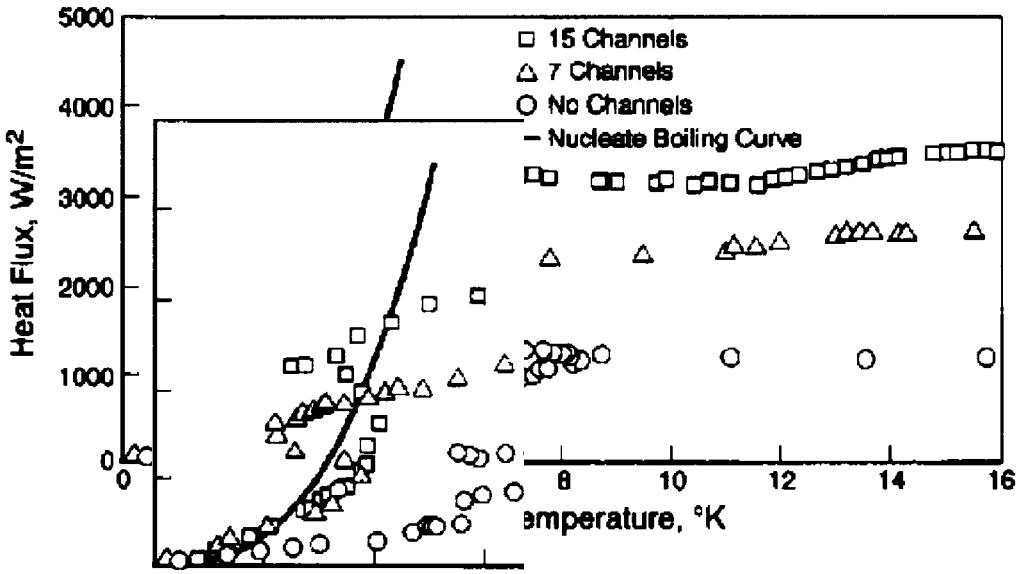

Figure 2-12: Heat Flux versus Excess Temperature for Wicks with Vapour Channels [23]

The mechanism responsible for this increase in performance is the decrease in the wick temperature drop during nucleate boiling. Since conduction controls heat transfer at low heat fluxes, there is a comparatively large temperature drop through the liquid saturated wick. When nucleate boiling is encountered, this temperature drop is progressively minimized due to intense liquid agitation from the movement of vapour bubbles.

2.4 Entrainment Limit

When the vapour velocity in the heat pipe is very high, shear forces at the liquid/vapour interface can pull the liquid from the wick and into the vapour stream. This reduces the

liquid flow to the evaporator resulting in diminished heat transport capacity. Cotter first discovered this phenomenon in 1967 and proposed an operational limit based on a ratio of inertial vapour forces to surface tension forces, known as the Weber Number [29]. He postulated that entrainment occurred when the Weber Number (W_e) equalled unity:

$$W_e = \frac{2R_{h,w}\rho_v \overline{w}^2}{\sigma} = 1 \tag{2-20}$$

where $R_{h,w}$ is the hydraulic radius of the wick surface pore, ρ_v is the vapour density and $\overline{w}$ is the mean axial vapour velocity. The hydraulic radius of the wick surface pore is given by:

$$R_{h,w} = \frac{2A_{lv}}{P} \tag{2-21}$$

where A_{lv} is the surface pore area and P is the wetted perimeter of the pore. Wetted perimeter values for various simple wicks are listed in Table 2-2.

Wick Type	**Wetted Perimeter, P**	**Notes**
Screen	$R_{h,w} = 0.5W$	W_{wire} = wire spacing
Axial grooves	$R_{h,w} = W$	W = groove width
Packed spheres	$R_{h,w} = 0.205D$	D = sphere diameter

Table 2-2: Wetted Perimeter for Various Wicks [1]

In terms of heat transport capacity, the entrainment limit (Q_{ent}) is expressed as:

$$Q_{ent} = A_v h_{fg} \left(\frac{\sigma \rho_v}{2R_{h,w}} \right)^{\frac{1}{2}} \tag{2-22}$$

where A_v is the vapour space area.

2.5 Graphical Representation of Heat Transfer Limitations

The above heat transfer limitations are represented schematically in Figure 2-13 . The dotted lines represent extensions of the limitation lines beyond their effective segments. For example, even though the capillary limit can be plotted from the onset of heat input up to Point 3, it does not govern the heat transfer performance in this regime. Instead, the sonic and entrainment limits control performance since they possess lower values here.

The maximum heat transport rate will be governed by the heat transfer limit with the lowest numerical value. Generally, the low vapour pressures and high vapour velocities encountered at startup trigger either the sonic or entrainment limits, while the capillary and boiling limits restrain performance at higher temperatures.

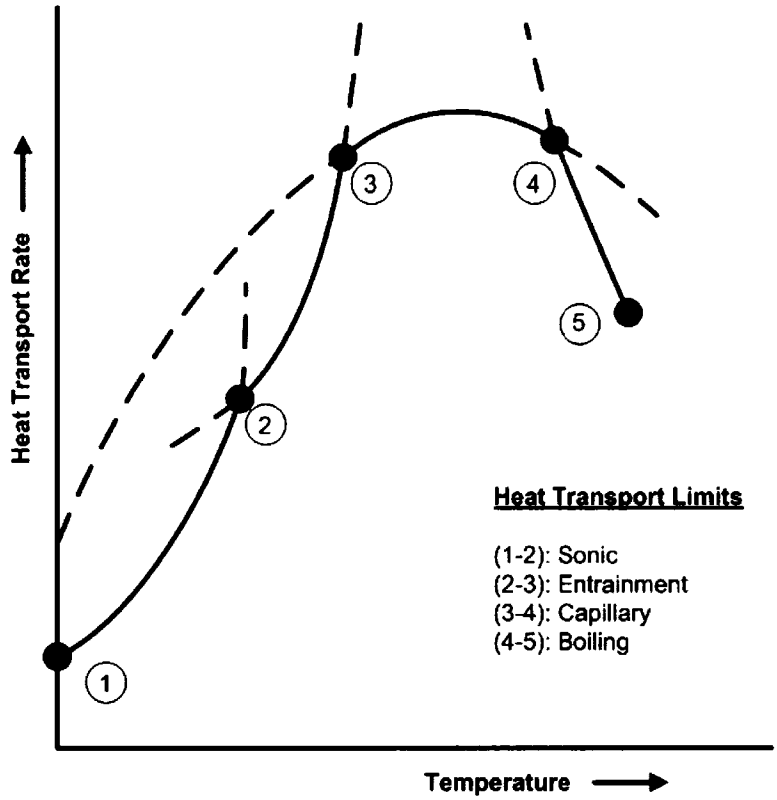

Figure 2-13: Heat Transfer Limitations as a Function of Temperature [16]

2.6 Prediction of Thermal Performance

Ultimately, a heat pipe designer's goal is to achieve optimum thermal performance. This could include a low axial temperature drop, high "effective" thermal conductivity or high heat transfer rates. Invariably, realizing high thermal performance requires minimizing the heat pipe's overall thermal resistance. Like the capillary limit, this is also closely related to wick design parameters. Even though a heat pipe may theoretically perform well, its real-world performance can suffer greatly from high heat source and sink resistances. Accordingly, source and sink resistances should also be minimized.

2.6.1 Equivalent thermal resistance network

By specifying wick conditions as well as heat source and sink parameters, the thermal performance of a heat pipe can be predicted. Temperatures, effective thermal conductivities and overall heat transfer coefficients can be estimated using an equivalent thermal resistance network [30], [31]. A typical thermal resistance network is presented in Figure 2-14.

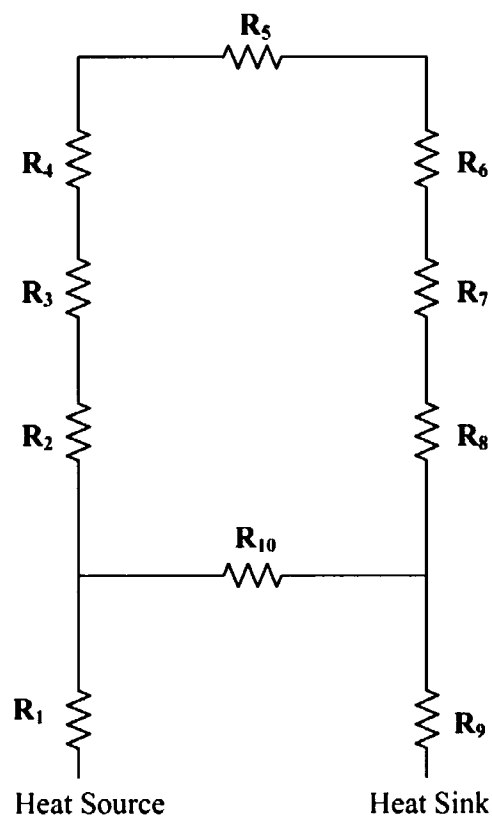

Figure 2-14: Thermal Resistance Network of a Heat Pipe [30]

The equivalent resistances are as follows:

- R_1, R_9: External source and sink resistances
- R_2, R_8: Radial evaporator and condenser wall resistances
- R_3, R_7: Radial evaporator and condenser wick resistances

- R_4, R_6: Radial evaporator and condenser liquid/vapour interface resistances
- R_5: Axial vapour core thermal resistance
- R_{10}: Axial wall/wick resistance

Typical values for these resistances are listed in Table 2-3 for comparison.

Resistance	**Value (°C/W)**
R_1, R_9	On the same order of magnitude as the overall heat pipe resistance
R_2, R_8	10^{-1}
R_3, R_7	10^{1}
R_4, R_6	10^{-5}
R_5	10^{-8}
R_{10}	10^{2} - 10^{4}

Table 2-3: Heat Pipe Thermal Resistances [10]

The vapour core resistance (R_5) and the gas-liquid interface resistances (R_4 and R_6) are small and are usually neglected [10], [31]. Moreover, the wall/wick axial resistance is essentially infinite compared to all other resistances. Since this is in parallel with the vapour core resistance, it can be eliminated from the network. The simplified network is shown superimposed on a heat pipe in Figure 2-15.

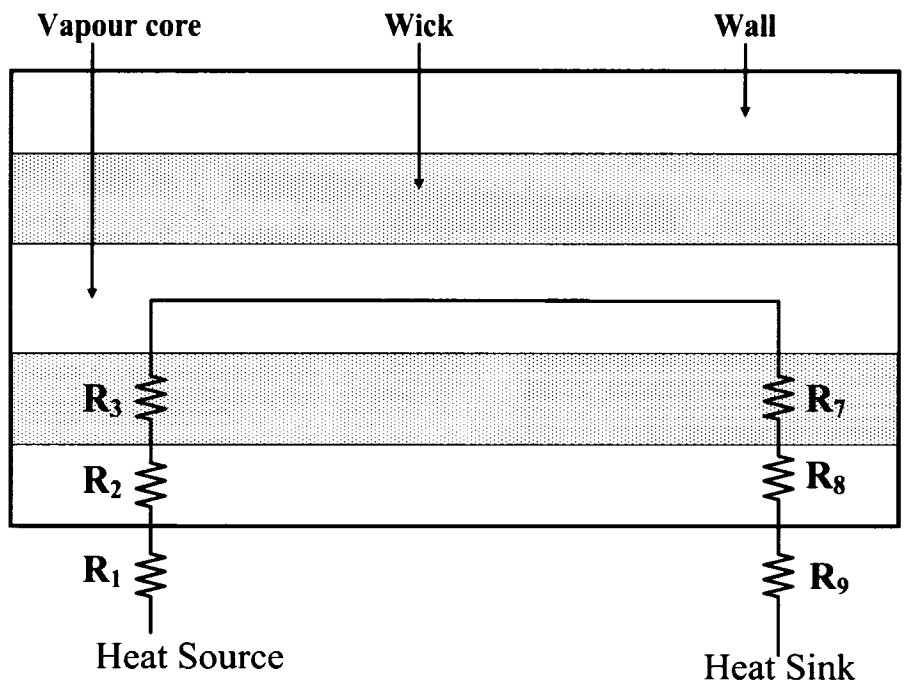

Figure 2-15: Simplified Thermal Resistance Network [10]

The defining heat transfer relationship is:

$$Q = \frac{1}{R_{HP}} \Delta T \tag{2-23}$$

where Q is the heat transfer rate, ΔT is the overall temperature difference between the heat source and the heat sink, and R_{HP} is the equivalent thermal resistance of the heat pipe, heat source and heat sink.

From the above discussion and Figure 2-15, it has been shown that the simplified circuit consists of six equivalent resistances in series. With respect to a conventional cylindrical heat pipe, the values of these equivalent resistances are given below. By adding these together, R_{HP} can be calculated:

$$R_1 = \frac{1}{h_e A_e} \tag{2-24}$$

$$R_2 = \frac{\ln\left(\frac{r_o}{r_i}\right)}{2\pi L_e k_{wall}} \tag{2-25}$$

$$R_3 = \frac{\ln\left(\frac{r_i}{r_v}\right)}{2\pi L_e k_{wick}} \tag{2-26}$$

$$R_7 = \frac{\ln\left(\frac{r_i}{r_v}\right)}{2\pi L_c k_{wick}} \tag{2-27}$$

$$R_8 = \frac{\ln\left(\frac{r_o}{r_i}\right)}{2\pi L_c k_{wall}} \tag{2-28}$$

$$R_9 = \frac{1}{h_c A_c} \tag{2-29}$$

The convective heat transfer coefficients of the evaporator and condenser are denoted h_e and h_c. The external evaporator and condenser heat transfer surface areas are A_e and A_c. Outer and inner pipe wall radii are represented by r_o and r_i, while the vapour core radius is r_v. The lengths of the evaporator and condenser are L_e and L_c, and the thermal conductivities of the wall and wick are k_{wall} and k_{wick}.

The overall heat transfer coefficient of the heat pipe without source and sink resistances is given by [16]:

$$U_{HP}' = \frac{1}{R_{HP}' \cdot A_{HP}} = \frac{1}{(R_2 + R_3 + R_7 + R_8) \cdot A_{HP}} \tag{2-30}$$

where A_{HP} is the heat pipe cross-sectional area based on the tube outside diameter. Equation (2-23) now becomes:

$$Q = U_{HP}' \cdot A_{HP} \cdot \Delta T_{HP}' \tag{2-31}$$

where $\Delta T_{HP}'$ is the temperature difference between the heat pipe's evaporator and condenser. Equation (2-31) is useful in determining the thermal performance of a heat pipe independent of its heat source and heat sink. If source and sink resistances are included, the thermal performance of the heat pipe in its true operational state is found using:

$$U = \frac{1}{R \cdot A_{HP}} = \frac{1}{(R_1 + R_2 + R_3 + R_7 + R_8 + R_9) \cdot A_{HP}} \tag{2-32}$$

and Equation (2-23) can be expressed as:

$$Q = U \cdot A_{HP} \cdot \Delta T \tag{2-33}$$

Equation (2-33) can be used to calculate a heat pipe's axial temperature gradient or its heat transfer capacity in its true operational condition, provided it remains within the limits outlined in Sections 2.1 to 2.4 . Equations (2-24) to (2-29) are useful for calculating the temperature at any point in the heat pipe [30].

Finally, with the known axial temperature drop, an overall effective thermal conductivity for the heat pipe may be expressed. Fourier's Law of Heat Conduction states that the rate of heat transferred in a body is proportional to the temperature gradient in the direction of heat flow, multiplied by some proportionality constant [26]:

$$Q = -kA\frac{\partial T}{\partial x} \tag{2-34}$$

where Q is the heat transfer rate, k is the thermal conductivity of the material, A is the cross-sectional area normal to heat flow, ∂T is the temperature difference between the cooler and hotter sides of the material and ∂x is the distance parallel to the heat flow. The negative sign is inserted to indicate that heat must flow in the direction of decreasing temperature [32]. Thus, Fourier's Law can be used to express the "effective" thermal conductivity of the heat pipe. In the context of the heat pipe, Q, the heat transferred by the heat pipe and ∂T, the difference between the evaporator and condenser temperatures, are taken to be positive. The effective thermal conductivity is also a positive quantity.

Therefore, the negative sign of Equation (2-34) is dropped. Rearranging Equation (2-34) for k_{eff}, and substituting l_{eff} for ∂x and A_{HP} for A:

$$k_{eff} = \frac{Q \cdot l_{eff}}{A_{HP} \Delta T} \tag{2-35}$$

where k_{eff} is the overall effective thermal conductivity of the heat pipe, Q is the heat input to the evaporator, l_{eff} is the heat pipe's effective length, A_{HP} is the cross-sectional area of the heat pipe and ΔT is the temperature drop from the heat pipe's evaporator to its condenser.

2.6.2 Heat pipe operating temperature

It should also be mentioned that the so-called heat pipe operating temperature is frequently taken as being equal to the vapour temperature of the adiabatic section. Since the vapour core thermal resistance is negligible, this temperature is effectively that of the vapour temperature at the evaporator exit, shown in Figure 2-16. This implies that only resistances R_1, R_2 and R_3 must be calculated in order to estimate the operating temperature of a heat pipe under a known heat input.

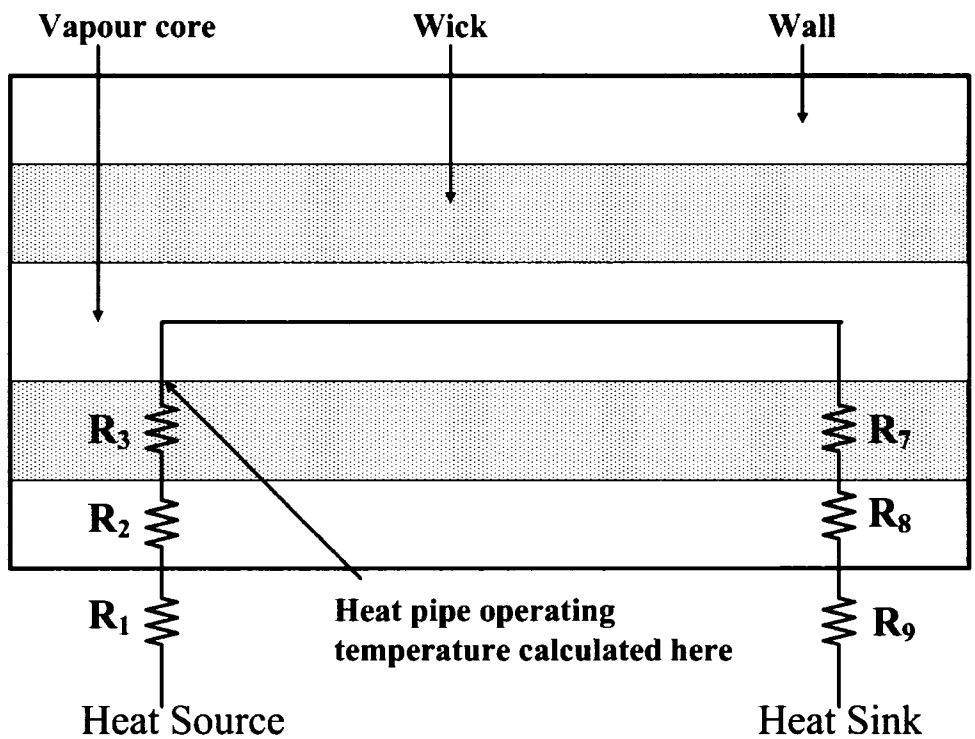

Figure 2-16: Estimation of Heat Pipe Operating Temperature [10]

Assuming no heat is lost along the heat pipe, the heat input is equal to the heat removed at the heat sink. Moreover, this heat must travel through the various sections of the heat pipe, such that Equation (2-23) can be used in conjunction with the appropriate thermal resistances to calculate the temperature of the vapour at the evaporator exit. In such a manner, the operating temperature of the heat pipe may be estimated.

2.6.3 Effective thermal conductivity of wicks

The effective thermal conductivity of the saturated wick, k_{wick}, depends on the thermal conductivities of both the solid wick and the working fluid. If heat conduction occurs in parallel, k_{wick} can be approximated by the weighted arithmetic mean of the solid wick and

the working fluid. On the other hand, if conduction is in series, k_{wick} is estimated by taking a weighted average of the two thermal conductivities. These scenarios are illustrated in Figure 2-17.

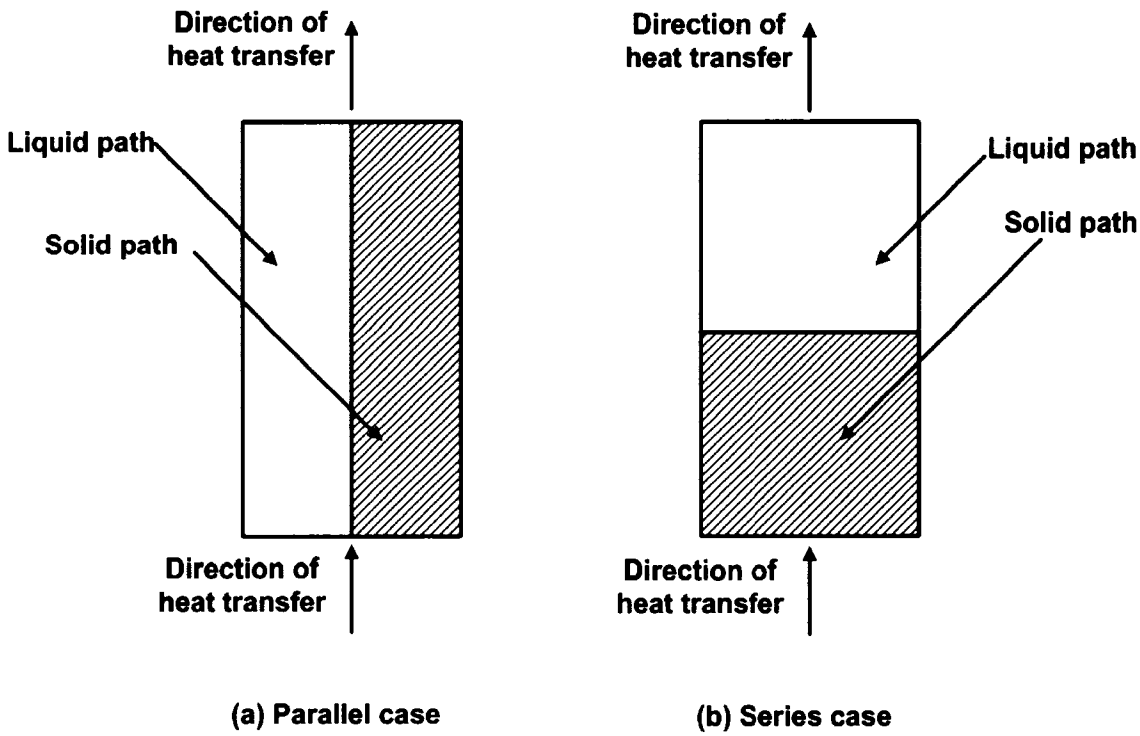

Figure 2-17: Thermal Conductivity for Heat Transfer in (a) Parallel and (b) Series [1]

These simplest of models represent two boundary values between which the effective thermal conductivity must lie [1]:

$$k_{wick}^{Series} \leq k_{wick} \leq k_{wick}^{Parallel} \tag{2-36}$$

Expressed mathematically:

$$\left[\frac{k_l k_s}{\varepsilon k_s + k_l(1-\varepsilon)}\right] \le k_{wick} \le \left[(1-\varepsilon)k_s + \varepsilon k_l\right] \tag{2-37}$$

Here, k_l and k_s are the liquid and solid thermal conductivities and ε is the wick porosity. For unsintered wrapped screen wicks, the effective thermal conductivity is commonly calculated using [10], [16]:

$$\left[k_{wick} = \frac{k_l\left[k_l + k_s - (1-\varepsilon)(k_l - k_s)\right]}{(k_l + k_s) + (1-\varepsilon)(k_l - k_s)}\right] \tag{2-38}$$

In the above expression, k_s is the thermal conductivity of the solid portion of the wick. Effective thermal conductivities for other common wicks are listed in Table 2-4.

Wick Structure	**Effective Thermal Conductivity (k_{eff})**	**Porosity (ε)**
Wrapped metal screens, plain	$\frac{k_l\left[k_l + k_s - (1-\varepsilon)(k_l - k_s)\right]}{(k_l + k_s) + (1-\varepsilon)(k_l - k_s)}$	$1 - \frac{1.05\pi N d}{4}$
Wrapped metal screens, sintered	$k_l\left(\frac{k_s}{k_l}\right)(1-\varepsilon)^{0.59}$	$1 - \frac{1.05\pi N d}{4}$
Packed spherical metal powder, plain	$\frac{k_l\left[2k_l + k_s - 2(1-\varepsilon)(k_l - k_s)\right]}{2k_l + k_s + (1-\varepsilon)(k_l - k_s)}$	Measure experimentally
Packed spherical metal powder, sintered	$\frac{k_s\left[2k_s + k_l - 2\varepsilon(k_s - k_l)\right]}{2k_s + k_l + \varepsilon(k_s - k_l)}$	Measure experimentally

Table 2-4: Effective Thermal Conductivities of Various Wicks [1]

For wrapped screen wicks, N is the Wire Number and d is the wire diameter. These quantities, along with wick porosity, are covered in greater detail in Section 3.3.1. One important observation can be drawn from the equations comparing sintered wicks to non-sintered wicks: the effective thermal conductivity increases by approximately one order of magnitude. The positive effect this would have on the thermal performance is significant. Through the sintering process, the effective thermal conductivity of the liquid-saturated wick would increase, and two of the largest thermal resistances in the equivalent thermal resistance network of Figure 2-15 (R_3 and R_7) would be minimized. Referring to Equations (2-32) to (2-35), this would reduce the axial temperature drop, and thus the effective thermal conductivity would increase. The sintering process is discussed further in Section 3.3.3.

3 Heat Pipe Design

Oftentimes, engineering design is an iterative procedure. Heat pipe design is no exception to this, since many preliminary decisions must be made without precise knowledge of their outcome. This section provides a brief overview of the more important aspects of heat pipe design, focusing on the selection of working fluids, wicking structures and containers.

3.1 Working Fluid Selection

Upon completion of the operating temperature estimate, the working fluid selection process can begin. Several factors must be considered here. Firstly, the heat pipe operating temperature range must be between the fluid's melting point and critical temperatures [10], [16]. The critical temperature of a fluid is defined as the temperature above which a gas cannot be liquefied, or the temperature above which a substance cannot exhibit distinct gas and liquid phases [33]. Under these criteria, Table 3-1 shows various working fluids and their corresponding useful temperature ranges. Water, ammonia and methanol are suitable for moderate temperature heat pipes. High temperature heat pipes make use of mercury, caesium, potassium and sodium at the lower end of the range, while lithium and silver are desirable for very high temperature applications.

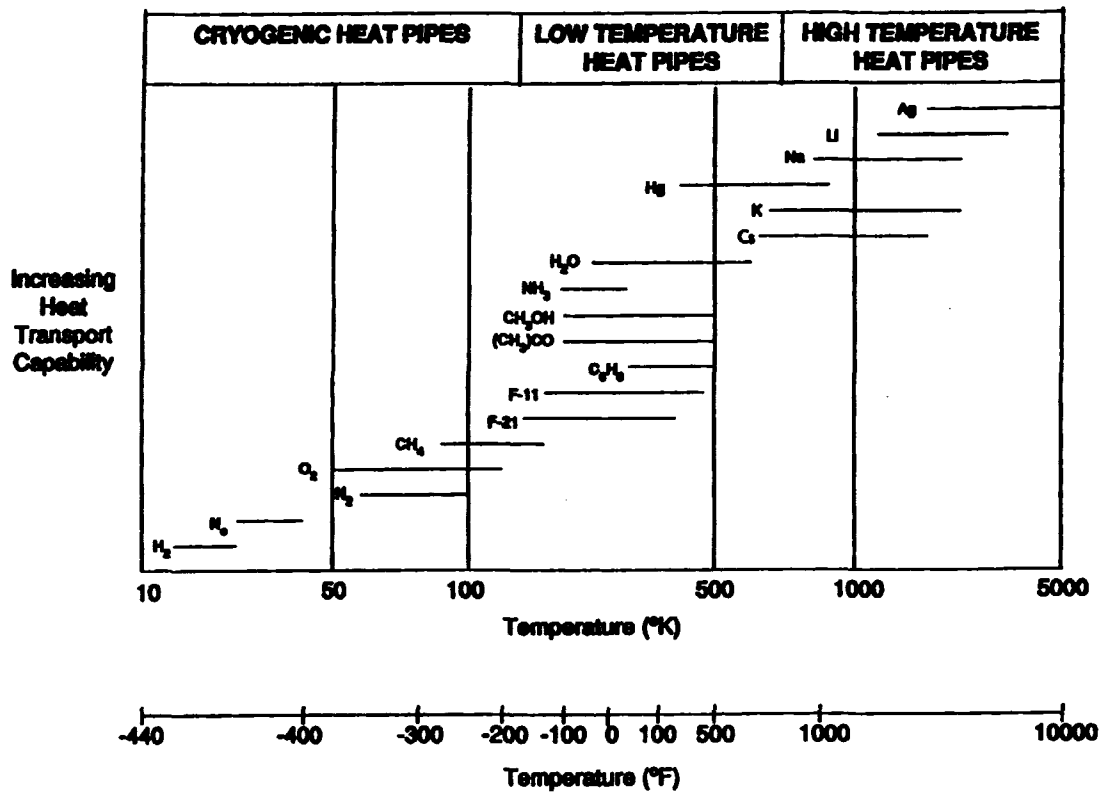

Table 3-1: Heat Pipe Working Fluids and Their Corresponding Temperature Ranges [10]

Since the above-mentioned rule-of-thumb usually yields a number of candidate working fluids, optimization is commonly accomplished by considering the Liquid Transport Factor (N_l), also called the Liquid Figure of Merit [16]:

$$N_l = \frac{\sigma \rho_l h_{fg}}{\mu_l} \tag{3-1}$$

where σ is the surface tension of the fluid, ρ_l is the liquid density, h_{fg} is the latent heat of vapourization of the fluid and μ_l is the liquid dynamic viscosity. Since these properties change with temperature, the optimum working fluid will possess the highest Liquid

Transport Factor in the heat pipe operating temperature range. Figure 3-1 illustrates the variation of the Liquid Transport Factor with temperature for a few common working fluids. Water is a desirable working fluid for lower temperature applications, while sodium has better performance at temperatures greater than 500 K.

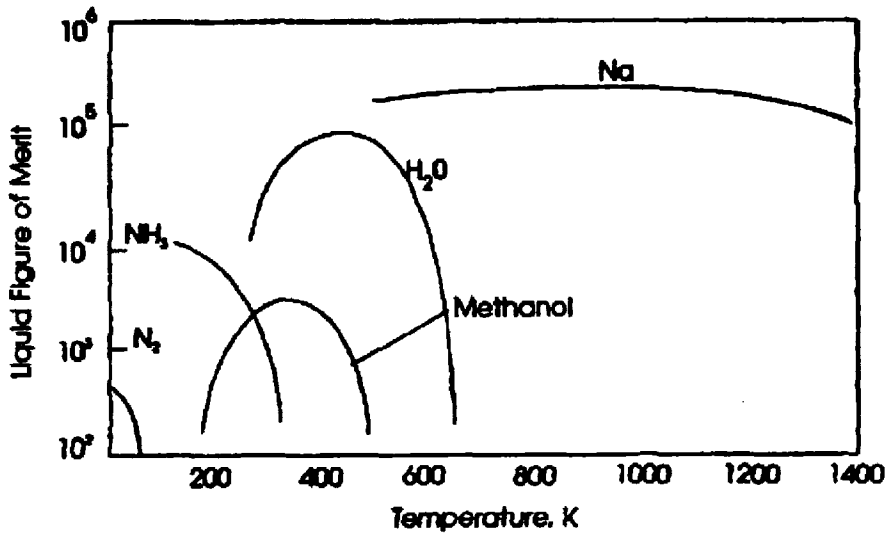

Figure 3-1: Variation of Liquid Transport Factor with Temperature [5]

Other important factors to consider during fluid selection are vapour pressure levels, liquid-solid wettability, liquid thermal conductivity and material compatibility. Excessively high vapour pressures must be avoided, otherwise an excessively thick-walled container will be required to prevent rupture [5]. Conversely, if the vapour pressure is too low, very high vapour velocities can trigger the sonic limit. The working fluid should also have an affinity for the wick and container material [3], [10]. This is referred to as the wettability of the fluid. If the liquid readily wets the wick and container, the contact angle will be equal to zero and the generated capillary pressure will reach a

maximum value, as discussed in Section 2.1.1. Clearly, this is a favourable quality, since the capillary limit will increase for perfectly wetting fluids.

High thermal conductivity is another favourable property, since the working fluid is relied on to conduct heat through the saturated wick [1], [10]. Lastly, the working fluid must be compatible with the container and wick materials. If an incompatible working fluid is used, chemical reactions could generate non-condensable gases (NCGs) [10], [34], which accumulate at the condenser end of the heat pipe, impeding heat flow to the heat sink. This leads to long-term performance degradation. However, life tests with copper-water heat pipes have yielded excellent results, with no degradation in performance after 20000 hours [35]. A long-term test on a sodium-filled stainless steel heat pipe also demonstrated compatibility after 9000 hours [36]. Life tests on stainless steel/water heat pipes revealed an incompatibility between these, with hydrogen gas generation detected within 2 hours of start-up [37]. Table 3-2 summarizes the compatibility data of various low temperature material/working fluid combinations.

Material	Water	Acetone	Ammonia	Methanol
Copper	R	R	NU	R
Aluminum	GNC	R	R	NR
Stainless	GNT	PC	R	GNT
Nickel	PC	PC	R	R
Refrasil	R	R	R	R

R	Recommended by literature
PC	Probably compatible
NR	Not recommended
NU	Not used
UK	Unknown
GNC	Generation of gas at all temperatures
GNT	Generation of gas at elevated temperatures when oxide is present

Table 3-2: Material/Working Fluid Compatibility Data [38]

3.2 Container

The heat pipe container must provide structural support for the wick and containment of internal pressure from vapourization of the working fluid. Additionally, it must be compatible with the wick and working fluid to prevent the formation of non-condensable gases. Refer to Table 3-2 for material compatibility data. High thermal conductivity is important to minimize the radial thermal resistance at the evaporator and condenser.

Typically, container design involves estimating the vapour core diameter (d_v), the wick thickness (t_{wick}), the wall thickness (t_{wall}) and the resulting outer diameter (d_o) of the container [16]. Figure 3-2 illustrates these dimensions.

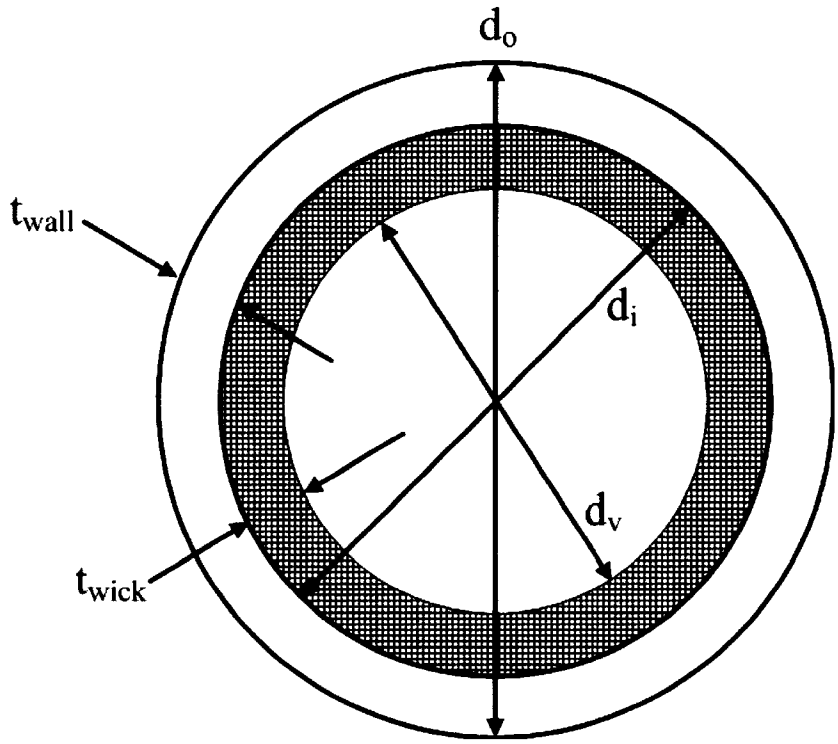

Figure 3-2: Heat Pipe Container and Wick Dimensions

The vapour core diameter is usually designed to avoid compressible flow, and Chi suggests specifying a Mach Number of 0.2 for this purpose [16]:

$$M_v = \frac{Q}{\frac{\pi d_v^2}{4} \rho_v h_{fg} \sqrt{K' R_{vap} T_v}} = 0.2 \qquad (3\text{-}2)$$

where Q is the heat transfer rate, d_v is the vapour core diameter, ρ_v is the vapour density, h_{fg} is the latent heat of vapourization, K' of Equation (2-16) is the ratio of specific heats, R_{vap} is the vapour gas constant and T_v is the vapour temperature. Rearranging Equation (3-2) for d_v:

$$d_v = \left(\frac{20Q}{\pi \rho_v h_{fg} \sqrt{K' R_{vap} T_v}} \right)^{\frac{1}{2}} \tag{3-3}$$

Preliminary estimates of the capillary limit must be determined next to obtain the internal diameter (d_i) of the container. Referring to Equation (2-13), this step is necessary because both the liquid and vapour pressure drop terms of the capillary limit depend on the wick cross-sectional area. The internal diameter of the heat pipe can then be estimated by adding twice the wick thickness (t_{wick}) to the vapour core diameter:

$$d_i = d_v + 2t_{wick} \tag{3-4}$$

The outside container diameter (d_o) can therefore be expressed as:

$$d_o = d_i + 2t_{wall} \tag{3-5}$$

where t_{wall} is the wall thickness. Next, using data from candidate container materials, the equation for hoop stress in a pressurized thin-walled cylinder can be used to estimate the container wall thickness:

$$\sigma_{\max} = \frac{P d_o}{2t_{wall}} \tag{3-6}$$

where P is the pressure differential across the tube wall. For heat pipe design, P is taken to be the vapour pressure of the working fluid at the maximum intended operating temperature. Rearranging Equation (3-6) for t_{wall} and substituting Equation (3-5) for d_o:

$$t_{wall} = \frac{d_i}{\frac{2\sigma_{\max}}{P} - 2} \tag{3-7}$$

The maximum allowable hoop stress, σ_{max}, is specified as being no more than ¼ of the material's ultimate tensile strength at the heat pipe operating temperature under the ASME code for unfired pressure vessels [16].

Minimum end cap thicknesses must also be specified. End caps may be hemispherical, flat or conical. For a flat, circular end cap, the maximum allowable stress is given by [16]:

$$\sigma_{\max} = \frac{Pd_{cap}^2}{8t_{cap}^2} \tag{3-8}$$

where d_{cap} is the end cap diameter and t_{cap} is the end cap thickness. Again, σ_{max} is equivalent to ¼ of the material's ultimate tensile strength. Rearranging Equation (3-8) for t_{cap}:

$$t_{cap} = \left(\frac{Pd_{cap}^2}{8\sigma_{\max}} \right)^{\frac{1}{2}} \tag{3-9}$$

3.3 Wick Design

The main purpose of the wick is to provide the necessary capillary pumping pressure required to axially displace the working fluid. Circumferential fluid distribution around the evaporator and condenser sections also relies on the wick. In Section 2.1 , the capillary limit was shown to depend on the effective pore size as well as the liquid permeability. An optimum wick would possess the smallest effective pore size (for high capillary pressure) with the highest liquid permeability. Referring to Equation (2-13), this would have the effect of increasing the capillary pressure term on the left hand side of the equation, while decreasing the liquid pressure drop term on the right. The capillary limit would therefore increase if such a structure could be achieved.

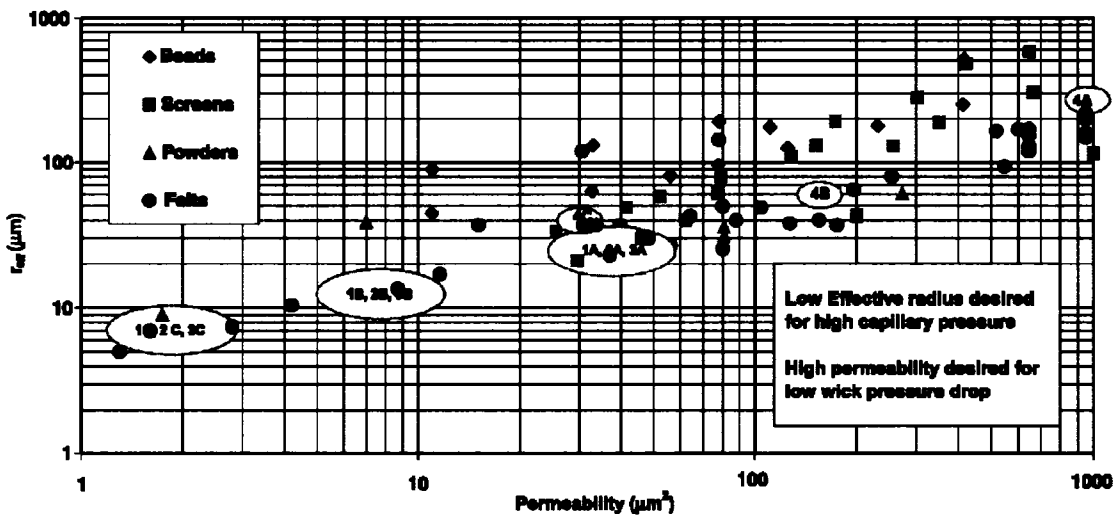

Figure 3-3: Wick Pore Radius (μm) versus Permeability (μm^2) [39]

However, for wicks with one characteristic pore size, decreasing the pore diameter also decreases liquid permeability, such that a compromise must be reached between these two factors. Figure 3-3 clearly demonstrates this phenomenon, with the lowest

permeability coinciding with the smallest pore radius [39]. If either the liquid permeability or the effective pore radius is inadequate, the heat pipe's performance will suffer. Therefore, the need for composite wicks that strike a balance between both of these requirements is evident. Interestingly, sintered metal powders and felts cover the largest scope, implying that they may be tailor-made for numerous applications.

Another critical aspect in high performance wick design involves evaporation heat transfer. A number of research programs have confirmed that optimization of porous material properties has significantly enhanced evaporation heat transfer performance. Moreover, some researchers have conclusively shown that porous media with two characteristic pore radii offer substantial improvements in evaporation performance over single pore sized structures. Thus, considerations on wick selection and design involve a discussion of conventional heat pipe wicking structures, followed by a review of relevant studies in evaporation heat transfer in biporous media.

3.3.1 Metal screens

Metal screens are commonly used as wicks due to their widespread availability, low cost and simplification of the heat pipe manufacturing process [16]. In their most economical form, they consist of drawn metal wires, woven together and crimped in place using a ram. Typically, plain carbon steels, copper, nickel and stainless steels are popular materials for metals screens [40]. Some common weave configurations for fine screens are shown in Figure 3-4.

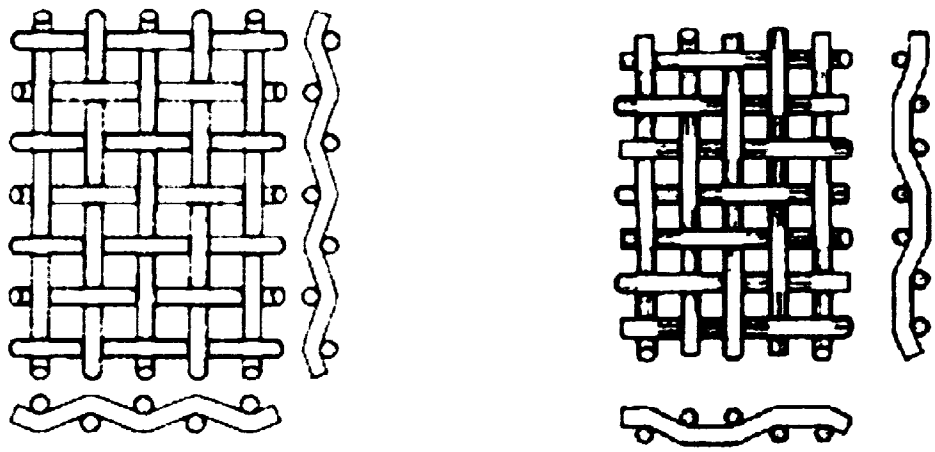

Figure 3-4: Plain Wire Screen Weave (Left), Twill Screen Weave (Right) [40]

One commonly used expression for the fineness of the weave is the Mesh Number (N). This describes the number of apertures per linear inch of screen [41]. A higher Mesh Number indicates a finer weave. For example, a 100-mesh wire screen has 100 apertures per linear inch while a 250-mesh screen has 250 apertures per linear inch. Typically, heat pipe applications use 100 to 400-mesh screens. The effective pore size of metal screens can be theoretically calculated using [16]:

$$r_{eff} = \frac{W_{wire} + d_{wire}}{2} \tag{3-10}$$

where W_{wire} is the wire spacing and d_{wire} is the wire diameter, shown in Figure 3-5.

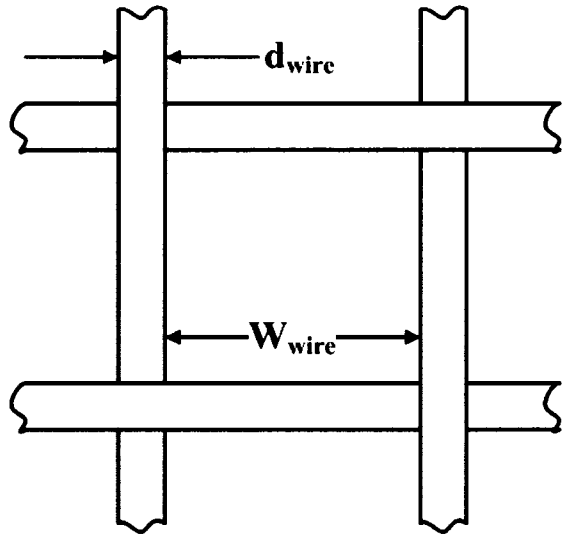

Figure 3-5: Metal Screen Wick Dimensions

More commonly, the effective pore radius is expressed in terms of the Mesh Number (N) [16], [42]:

$$r_{eff} = \frac{1}{2N} \tag{3-11}$$

Some researchers have discovered that Equation (3-11) overestimates the effective pore radius of screen wicks [43]. Therefore, this gives a conservative estimate of the maximum capillary pressure the wick can develop, and so it can safely be used in design calculations. Liquid permeability (K) is calculated with [42], [44]:

$$K = \frac{d_{wire}^2 \varepsilon^3}{122(1-\varepsilon)^2} \tag{3-12}$$

The porosity (ε) is given by [10], [16]:

$$\varepsilon = 1 - \frac{\pi S N d_{wire}}{4} \tag{3-13}$$

where S (≈1.05) is the crimping factor, accounting for the fact that screens are not crossed rods [16]. Metal screens are commonly used due to their balance between ease of wick manufacture, fair liquid permeability and average capillary pumping performance [1], [16]. However, because of their limited capillary pumping ability, metal screens may exhibit poor performance in unfavourable orientations. Furthermore, because of their low effective thermal conductivity [1], heat pipes with metal screens suffer from relatively high axial temperature drops.

3.3.2 Axial grooves

Another simple type of wicking structure consists of axial grooves embedded into the container wall. This type of heat pipe is most common in aerospace applications. Cross-sections can be trapezoidal, rectangular or triangular [11], [45], [46]. An axially grooved heat pipe cross section is shown in Figure 3-6.

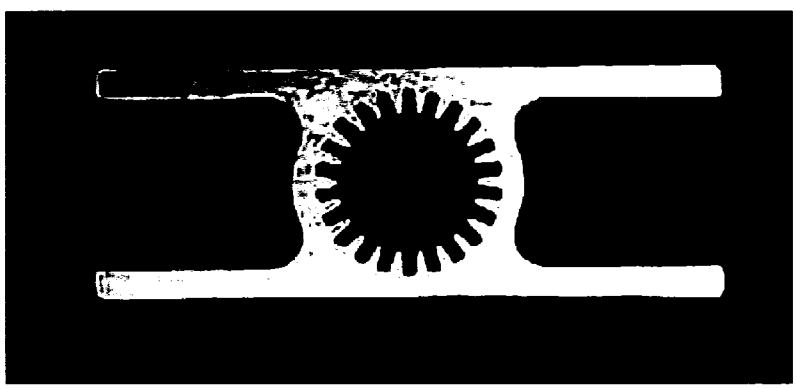

Figure 3-6: Cross-section of Heat Pipe with Rectangular Axial Grooves [45]

Extrusion is the most common form of manufacture [45]. In this bulk deformation process, the work metal is forced to flow through a die opening by means of a ram, and therefore the final part assumes the cross-sectional shape of the die [48]. Aluminium is the material of choice because of its low weight penalty and formability [5]. Other manufacturing processes have also been employed, especially for very fine capillary grooves. For example, miniature heat pipes with triangular axial grooves have been manufactured with etching processes [49]. Target material removal occurs through selective chemical attack of unprotected surfaces using an aqueous solution, while a protective layer covers the bulk of the material [50]. Characteristic dimensions as small as 80 μm have been achieved using this technique [10].

As previously listed in Table 2-1, the effective pore radii for rectangular and triangular grooves can be calculated using [16]:

$$r_{eff,rect} = w \tag{3-14}$$

$$r_{eff,tri} = \frac{w}{\cos\beta} \tag{3-15}$$

where w is the groove width and β is the half-included angle of the triangular groove. The liquid permeability for axial grooves is given by [16]:

$$K = \frac{2\varepsilon r_{h,l}^2}{f_l \mathrm{Re}_l} \tag{3-16}$$

where $r_{h,l}$ is the hydraulic radius of the groove and $f_l Re_l$ is the friction factor Reynolds Number product. For a rectangular cross-section,

$$\varepsilon = \frac{w}{s} \tag{3-17}$$

$$r_{h,l} = \frac{2w\delta}{w + 2\delta} \tag{3-18}$$

where s is the groove pitch and δ is the groove depth. The groove pitch is defined as the width of one groove plus the width of the wall separating one groove from the next. For rectangular grooves, the friction factor Reynolds Number product can be obtained from Figure 3-7.

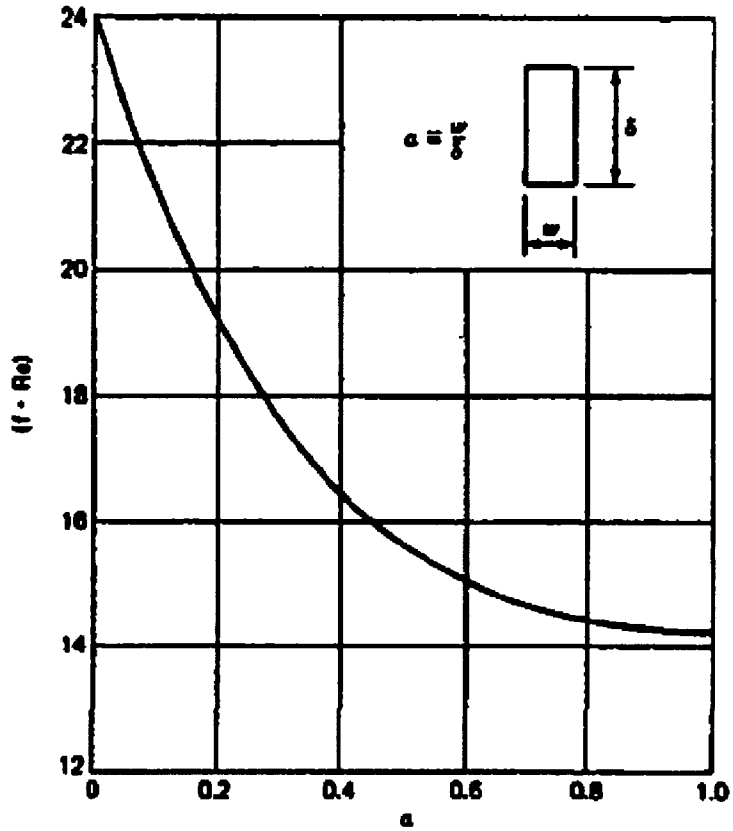

Figure 3-7: Friction Factor Reynolds Number Product for Rectangular Passages [16]

Typically, axially grooved wicks have the highest liquid permeability of all wick designs, however they are limited due to poor capillary pumping ability [1]. Moreover, because the vapour flow shear stress acts on the open-channelled liquid flow, these types of wicks are more susceptible to the entrainment limit than others. For these reasons, axially grooved wicks are most commonly used in zero gravity applications where vapour velocities are not excessively high.

3.3.3 Sintered metal wicks

Perhaps the most versatile wicking structure, sintered metal powders and felts can be tailored to a wide variety of requirements [51]. Highly porous structures can be achieved, with effective pore sizes a few microns in diameter [52].

In this category, heat pipe wicks are normally fabricated using the loose powder solid-state sintering technique. It is termed "solid-state" because powder particle bonding takes place at temperatures significantly lower than the melting temperature of the material. In the case of powder metallurgy, metal powder is mixed with a cement-like binder and is either applied onto the substrate metal (ie: the container) or formed into the desired shape and inserted into the heat pipe container. It is then placed in a furnace with a protective atmosphere to prevent metal oxidation, which occurs at an accelerated rate during high temperatures [53]. Oxide formation would inhibit diffusion bonding, the driving transport mechanism behind the sintering process [53]. Typical sintering environments include methane, hydrogen and vacuum atmospheres.

Since the purpose of this operation is to produce a highly porous structure, sample preparation, process time and temperature must be designed to achieve this result. Therefore, there is little or no sample compaction prior to sintering. Sintering temperature and time are instead selected with the objective of neck formation between adjacent particles, while maintaining an open pore structure of interconnected voids. Sintering usually takes place in three distinct phases [53]: debinding, sintering and cooling, shown schematically in Figure 3-8. The debinding phase is necessary to expel the binder before

proceeding to the sintering temperature. The binder should burn off without decomposition, since this would leave carbon residue on the wick. Then, the sintering temperature is reached, typically 70-90% of the metal's absolute melting temperature [50]. After sintering for the prescribed time, the cooling step begins, where the wick is cooled to a temperature low enough to avoid oxidation. The wick is then safely removed from the furnace.

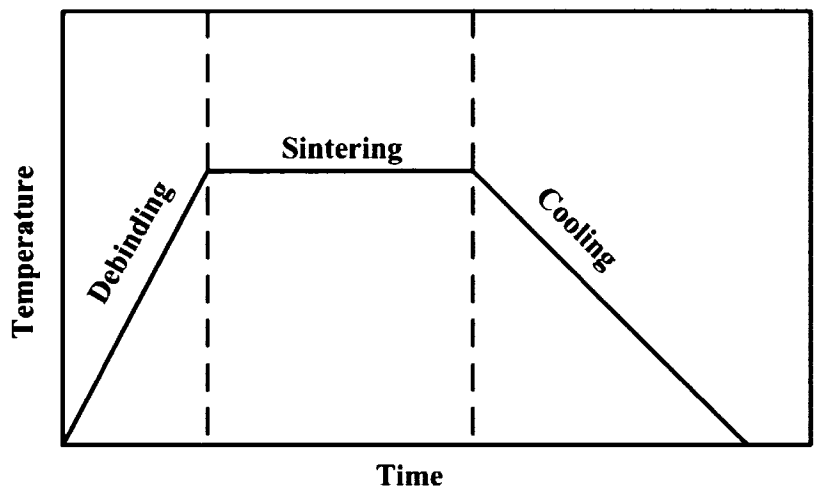

Figure 3-8: Phases during Sintering Process

It is generally agreed that the driving force behind the sintering process is a reduction in surface energy [50], therefore neck growth and pore annihilation proceed with increasing time and temperature. Accordingly, process design is essential for adequate particle bonding, while avoiding excessive pore closure.

Solid-state sintering is a diffusion controlled process. Diffusion is defined as the transport of material by atomic motion [54]. Heated solid metal particles in contact with each other will experience diffusion, and necks will form between them, as illustrated in Figure 3-9.

This phenomenon increases with temperature, so that higher diffusion rates are achieved at higher temperatures.

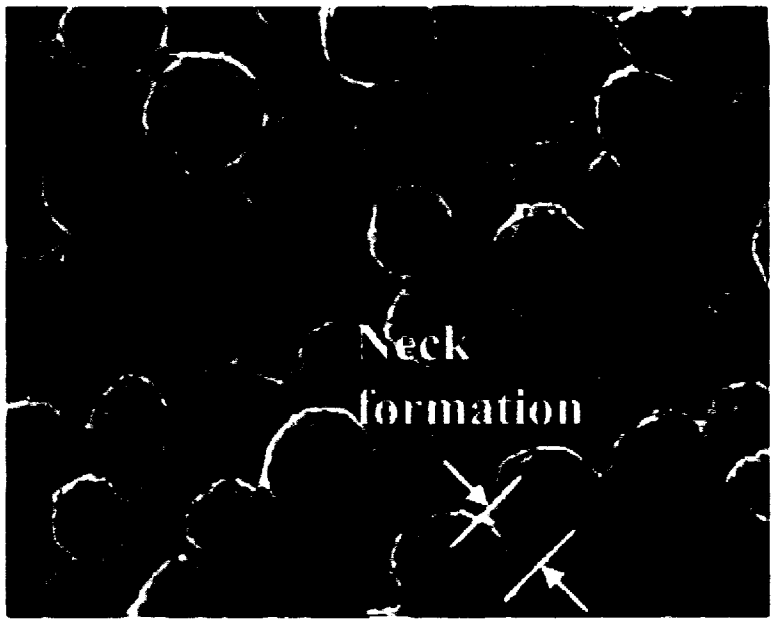

Figure 3-9: Neck Formation in Sintered Bronze Powder [55]

The diffusion coefficient (D) is the constant of proportionality between the diffusion mass flux and the concentration gradient of Fick's First Law, and describes the rapidity of atomic diffusion [54]. Thus, a higher diffusion coefficient is indicative of faster diffusion and sintering rates. Since diffusion is a thermally-activated process, it follows an Arrhenius temperature dependence [56]. For the self-diffusion of a pure metal, the diffusion coefficient at a given temperature is given by [57]:

$$D_{SD} = D_o \exp\left(\frac{-Q_{SD}}{RT}\right) \tag{3-19}$$

where D_{SD} is the self-diffusion coefficient, D_o is the diffusion constant for the diffusing species, Q_{SD} is the activation energy for self-diffusion, R is the Universal Gas Constant, and T is the absolute temperature. During the initial stages of sintering, it is possible to estimate neck formation size using [56]:

$$\left(\frac{X}{D}\right)^n = \frac{Bt}{D^m} \tag{3-20}$$

where X is the neck diameter, D is the particle diameter, t is the sintering time and n and m are constants dependant on the mechanism of mass transport. The coefficient B contains material properties and the diffusion coefficient [56].

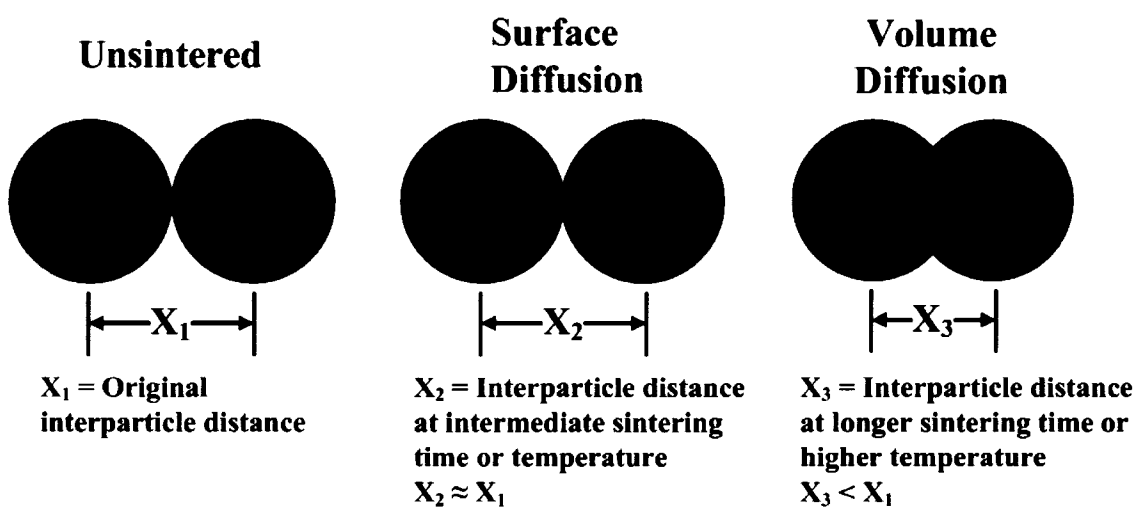

Figure 3-10: Surface Diffusion versus Volume Diffusion [58]

For example, nickel powder has been shown to experience surface diffusion at temperatures around 450°C, while at 900°C, volume diffusion is dominant [58]. During low temperature surface diffusion, mass transport occurs along the surface of the

material, and the interparticle distance does not change. However, when the sintering temperature is high enough, the interparticle distance shrinks and mass transport is favourable through the bulk of the material during volume diffusion. These mechanisms are shown in Figure 3-10. Under these mass transport mechanisms, *n*, *m* and *B* are given in Table 3-3.

Mechanism	**n**	**m**	**B**
Volume Diffusion	5	3	$\frac{80 D_v \gamma \Omega}{kT}$ D_v= volume diffusion coefficient γ = surface energy Ω = atomic volume k = Boltzmann's constant T = absolute temperature
Surface Diffusion	7	4	$\frac{56 D_s \gamma \Omega^{\frac{4}{3}}}{kT}$ D_s = surface diffusion constant

Table 3-3: Values for n, m and B of the Initial Stage Sintering Equation [56]

For sintered wicks, accurate predictions of the theoretical effective pore radius and liquid permeability are usually not reliable. However, estimates based on a spherical model are sometimes used if particle geometry is similar. For unconsolidated packed spheres, the effective pore radius can be theoretically calculated using [10]:

$$r_{eff} = 0.21 d_{av} \tag{3-21}$$

where d_{av} is the average particle diameter. The theoretical permeability (K) is given by:

$$K = \frac{d^2 \varepsilon^3}{150(1-\varepsilon)^2} \tag{3-22}$$

where d is the particle diameter and the porosity (ε), is assumed to be 0.48 [10]. Equations (3-21) and (3-22) are not accurate for the complex morphologies associated with most sintered metal wicks. Therefore, wick properties are usually directly determined with experimental methods.

3.3.4 Composite wicks

The above sections discussed conventional wick design, widely accepted due to their relative ease of manufacture and predictable performance. However, these homogeneous structures possess some shortcomings, namely their compromise between liquid permeability and capillary pumping performance, as well as a relatively small evaporative surface area. The anomaly between liquid permeability and capillary pressure in homogeneous wicks was previously discussed in Section 2.1.2, with examples of higher performing composite layered structures presented from the study conducted by Canti et al. [20]. To review, they concluded that the presence of both fine and coarse pores permitted a better compromise between liquid permeability and capillary pressure

generation. Therefore, for a higher performance heat pipe, a layered composite wick consisting of both coarse and fine pores should be considered during the design process.

Evaporation heat transfer can also benefit from the employment of composite wicks. Heat pipes function because of phase changes. In other words, the latent heat of vapourization is the mechanism responsible for the very high heat transport rates characteristic of heat pipes. Composite porous materials have been shown to increase this effect, and a few relevant studies on evaporation heat transfer are discussed below.

When compared to planar surfaces, porous media have been shown to improve heat transfer [59]. As the working fluid evaporates, it absorbs its latent heat of vapourization. This process is increased due to the enhanced heat transfer that occurs in the so-called thin film regions that exist near the contact line between liquids and solids, shown in Figure 3-11 [60], [61].

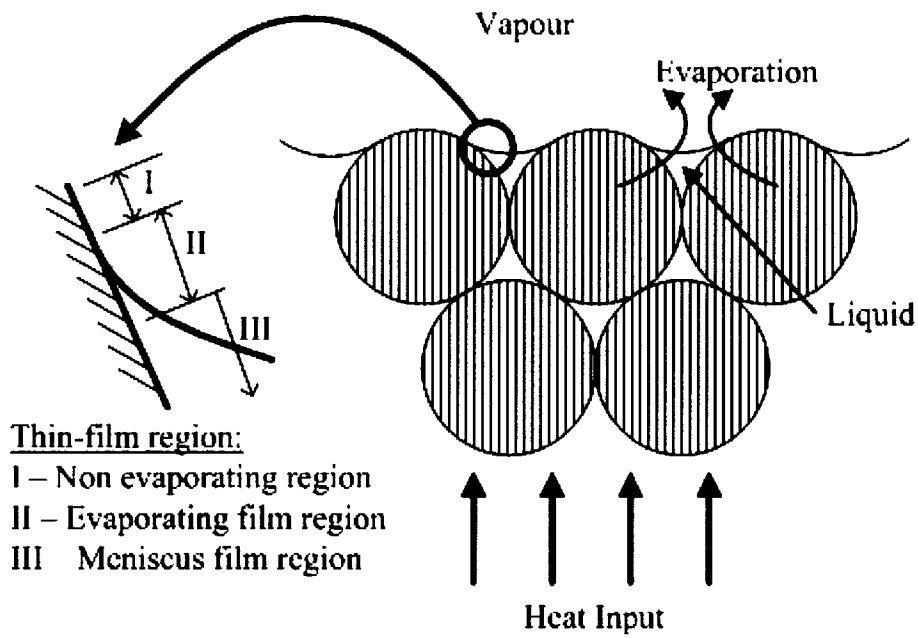

Figure 3-11: Thin Film Evaporation in Porous Structures [61]

In the non-evaporating region *(Region I)*, attractive forces at the liquid-solid interface prevent evaporation. As the film thickness increases, these forces decrease rapidly and evaporation is permitted in the evaporating film region (*Region II*). Evaporation also takes place in the meniscus region (*Region III*), however the thicker liquid film produces a higher thermal resistance to heat flow. Therefore, the most favourable heat transfer occurs in the evaporating thin film region due to low thermal resistance coupled with negligible attractive forces at the liquid-solid interface.

Consequently, by increasing the thin film area in an evaporator's wick, one would expect an improvement in heat transfer. This can be done by employing a highly porous structure with a fine pore size [61], [62]. The use of homogeneous wicks can satisfy this

requirement. However, heat transfer experiments with composite wicks have been shown to further improve this effect.

Konev et al. investigated the use of composite porous sintered wicks for evaporation heat transfer [63]. They concluded that when compared to homogeneous wicks, composite porous media enhanced heat transfer, owing to higher effective thermal conductivities. However, they failed to recognize the important contribution from the increased thin film area.

North et al. conducted a similar study, where a biporous sintered nickel wick consisting of two characteristic pore sizes was designed to increase the density of evaporating menisci in capillary structures [60]. Clusters of sintered nickel powder contained the small pores, while spaces between the clusters formed the large pores, shown in Figure 3-12. A monoporous nickel wick was also tested for comparison.

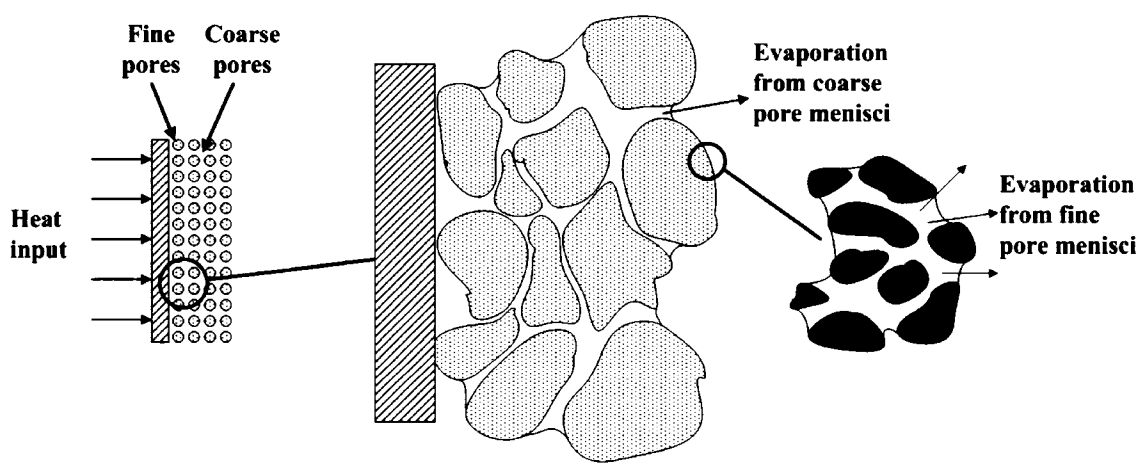

Figure 3-12: Composite Metal Powder Wick [60]

At low heat fluxes, heat transfer was suspected to be controlled by conduction through the liquid saturated wick because of a linear relationship between heat flux and temperature. As the heat flux increased, it was postulated that vapour preferentially filled the large pores, forming menisci around the small pores. This significantly increased the thin film evaporation area, and the heat flux increased dramatically while the temperature difference between the heated wall and the vapour remained approximately constant. In contrast, the homogeneous wick had a much higher temperature difference for the same heat flux and experienced dryout much sooner. Thus, it was concluded that composite wicks with small and large pores were desirable for heat pipes.

Wang and Catton arrived at similar conclusions based on numerical simulations. In one of their studies, evaporation heat transfer from triangular axial grooves was modeled with and without a fine porous coating [46]. These configurations are shown in Figure 3-13.

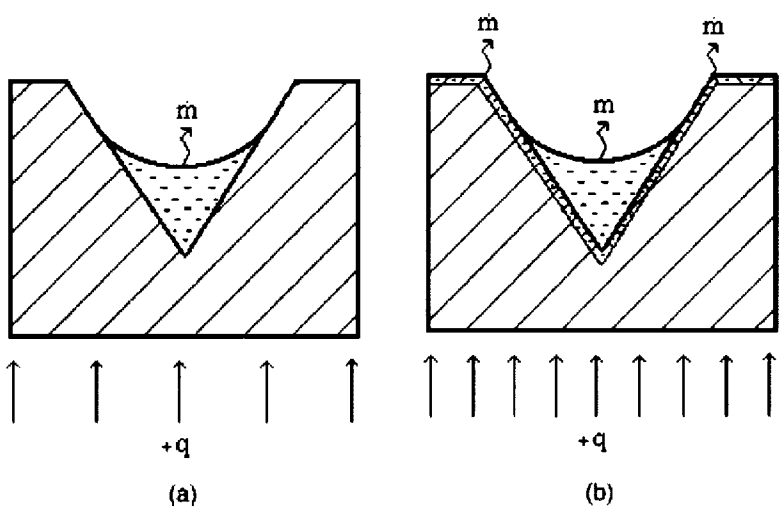

Figure 3-13: Triangular Grooves (a) without and (b) with Fine Pores [46]

While the composite wick on the right could experience mass transfer (and consequently heat transfer) from both the menisci of the groove and the fine pores, the plain triangular groove would only be permitted mass transfer from the large meniscus.

They concluded that evaporation heat transfer was augmented three to six times over conventional triangular grooves by the inclusion of a fine porous layer. This was attributable to the extension of thin film evaporative surface area associated with the fine pores. Figure 3-14 summarizes these findings as a plot of heat transfer coefficient (h_{total}) versus increasing groove meniscus (R_m). In all instances, the composite wick outperformed the triangular groove, with the highest performance reached at the smallest meniscus radius. This was explained by the increased exposure of fine pore evaporative surface area with decreasing meniscus radius. In comparison, the standard triangular groove only experienced modest performance gains, since there was little extension of thin film evaporative surface area with decreasing meniscus radius.

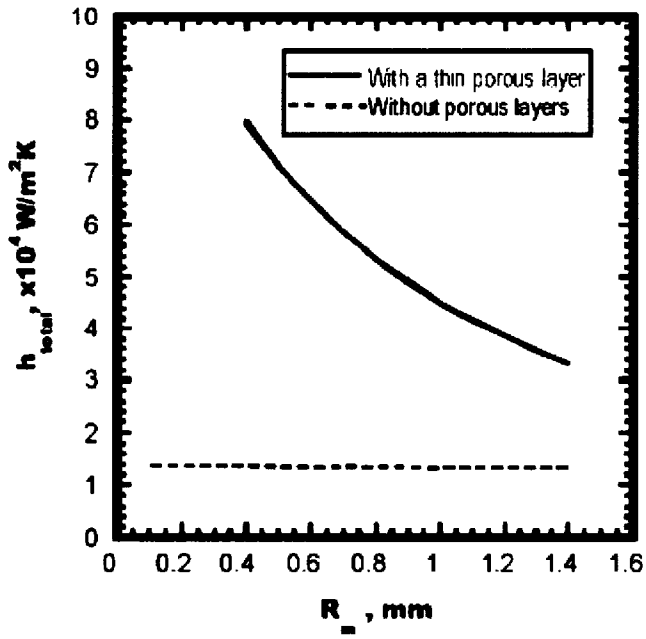

Figure 3-14: Wang and Catton's Results [46]

Numerous other studies support enhanced evaporation heat transfer through composite wick design, the large pore sizes being in the 200-800 μm range with the fine pores approximately an order of magnitude smaller [65], [66], [67]. Consequently, composite wicks are most likely favourable over homogeneous configurations, and should be given consideration during the heat pipe design process.

4 Experimental Procedure

This section covers all aspects of the experimental investigation regarding heat pipe performance enhancement through the employment of composite wicks. Wick and container materials are selected, along with various composite wick configurations believed to be of merit. Heat pipe design and manufacturing is discussed, followed by particulars on the construction of a heat pipe test rig used for performance validation. In addition, test procedures are presented, including heat pipe preparation, data collection and data manipulation.

4.1 Container and Wick Materials

Materials were chosen based on thermophysical and mechanical properties, powder morphology, manufacturing and processing considerations and supplier availability. Since water was chosen as the working fluid for this study due to its high Liquid Transport Factor, compatibility considerations were also of importance.

Copper tubing was selected for the container material due to its high thermal conductivity, its availability in a wide range of standard sizes and its common use in moderate temperature heat pipes. A 3/8" outside diameter (*O.D.*) was chosen for ease of manufacture, the smaller sizes being less accommodating towards wick insertion. Medium pressure tubing, known as Type L Refrigeration Grade Tubing, was chosen for its thin wall. This would ensure low thermal resistance while still providing adequate strength. Refer to Section 4.3.1 for container design calculations. Tubing was selected in

5 ft. straight lengths to eliminate bending and straightening operations. This would also provide excellent thermal contact between the wall and the wick, guaranteeing a kink-free container. Copper tubing data is listed in Table 4-1

Type L Copper Tubing: Properties	**Value**
Supplier	McMaster-Carr
UNS designation	UNS C12200
Composition	99.9% Cu (min.) 0.02% P (nom.)
O.D.	0.375" 9.525 mm
I.D.	0.315" 8 mm
Wall thickness	0.03" 0.762 mm
0.2% Yield Strength (assume fully annealed condition)	Approximately 48 MPa
Thermal conductivity (at 20°C)	340 W/m°C

Table 4-1: Copper Tubing Properties [68], [69], [70]

Copper mesh was chosen as the standard wick material. Again, this was primarily due to its high thermal conductivity as well as its widespread use in heat pipe applications. The springback effect of rolled copper mesh was also considered to be very beneficial, since this promoted reliable thermal contact between the wick and the container wall. Since preliminary heat pipe tests demonstrated suitable performance from 100-mesh copper screen wicks [72], it was decided to employ this standard configuration, with composite wicks derived from this baseline. Table 4-2 lists properties for 100-mesh copper screen.

Copper Mesh: Properties	**Value**
Supplier	McMaster-Carr
Mesh number (N)	100
Wire diameter (d_{wire})	0.0045" 114.3 μm
Effective pore radius (r_{eff}) *Equation (3-11)*	0.005" 127 μm
Pore diameter	0.01" 254 μm
Porosity (ε) *Equation (3-13)*	62.9%
Permeability (K) *Equation (3-12)*	193 μm^2
Thermal conductivity (k) *(assume pure copper at 20°C)*	Approximately 400 W/m°C

Table 4-2: 100-Mesh Copper Screen Properties [1], [68]

Composite wicks would employ 100-mesh copper screen as the large pore substrate. Fine pores were provided by metal powders applied to the screen at various locations assumed to be favourable for enhanced heat transfer performance. Metco 55 copper powder, shown in Figure 4-1, was chosen as one candidate, since this would not pose a compatibility issue with the working fluid, the container and the wick. Copper powder specifications are listed in Table 4-3.

Metco 55 Copper Powder: Properties	**Value**
Manufacturer	Sulzer-Metco
Morphology	Spherical
Composition	Cu 99%
Particle size	45 μm (min) 90 μm (max)

Table 4-3: Properties of Metco 55 Copper Powder [71]

Figure 4-1: Spherical Copper Powder Morphology

INCO Type 255 nickel powder was another candidate metal powder primarily chosen for its unique morphology, with properties listed in Table 4-4. As a result of its filamentary nature, characteristics of this metal powder include a very fine pore size, a high surface area to mass ratio and high porosity upon sintering. Also, because of their high corrosion resistance in aqueous environments, copper-nickel alloys would be desirable in heat pipes to avoid non-condensable gas formation. Therefore, sintering nickel powder onto copper mesh was not believed to be detrimental to heat pipe integrity, although further research would be necessary for confirmation of this theory. Type 255 nickel powder morphology is illustrated in Figure 4-2.

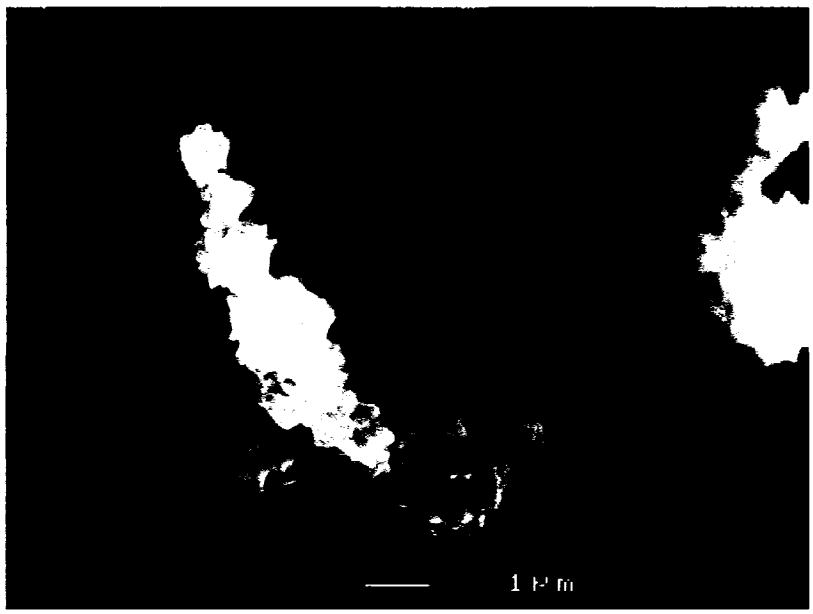

Figure 4-2: Filamentary Nickel Powder Morphology

Type 255 Nickel Powder: Properties	Value
Manufacturer	INCO Special Products
Morphology	Filamentary
Composition	Ni 97.9%
Particle size	2.2 μm (min) 2.8 μm (max)

Table 4-4: Properties of Nickel Powder [73]

4.2 Wick Configurations

Wick configurations ranged from homogeneous copper mesh or sintered metal powders to composite arrangements of layered copper mesh and metal powders, sintered together. Composite designs were selected to enhance evaporation heat transfer and increase the capillary limit based on the previous findings from researchers presented in Sections 2.1 and 3.3 . Wick designs were assigned identification codes based on an arbitrary

alphanumeric naming system. The first alphabetic character identifies the specific configuration, while the next numeric character represents sequential attempts of the same configuration. Since some designs were unsuccessful and not all configurations were reported, there are omissions in the identification list. However, the list is representative of successfully manufactured wick designs, and candidates for heat transfer performance testing were selected from these. These codes are summarized in Table 4-5.

Identification	**Configuration**
A	100-mesh copper screen, unsintered
B	100-mesh copper screen, liquid/vapour interface covered with nickel powder, sintered
E	100-mesh copper screen, wall/wick and liquid/vapour interfaces covered with nickel powder, sintered
H	100-mesh copper screen as carrier, heavily covered with nickel powder, sintered
I	100-mesh copper screen, liquid/vapour interface covered with copper powder, sintered
J	100-mesh copper screen, wall/wick and liquid/vapour interfaces covered with copper powder, sintered
K	Copper powder, sintered
L	100-mesh copper screen, lightly covered with nickel powder throughout structure, sintered

Table 4-5: Summary of Wick Identification

4.2.1 Homogeneous wicks

Wicks included plain unsintered copper screens and sintered metal powders. These baseline designs represent the relatively high permeability and low capillary pressure of mesh wicks to the high capillary pressure and low permeability of sintered metal powders. By comparing composite wicks to these standard configurations, differences in performance could be quantified.

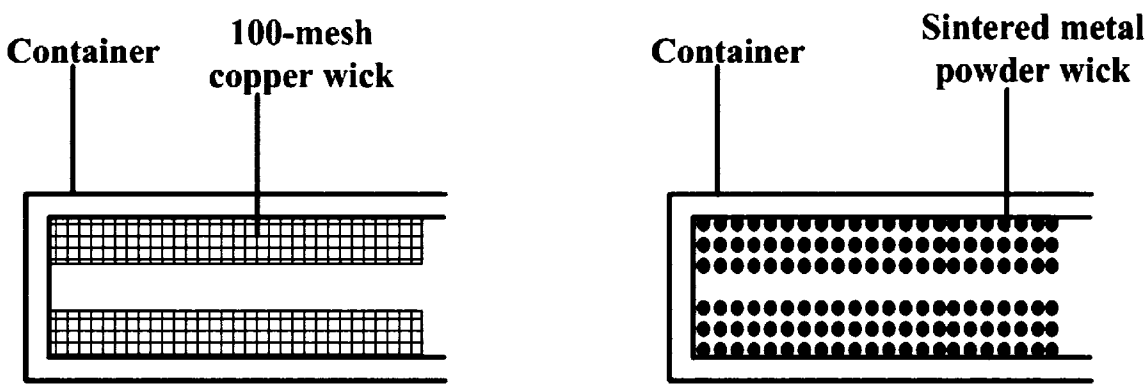

Figure 4-3: Schematics of Configuration A (Left) and Configurations H and K (Right)

The unsintered copper screen wick shown in Figure 4-3 was named Configuration "A", and was formed from layers of mesh, rolled tightly around a mandrel of appropriate size. The wick, still wrapped around the mandrel, was then carefully inserted into the container. Upon insertion, the mandrel was removed, leaving the unobstructed vapour core. The heat pipe was then ready for charging and sealing.

Sintered metal powder wicks were constructed by mixing metal powder with a binder. The mixture was poured around a centred mandrel and air dried. Alternatively, this slurry was applied to a 100-mesh copper carrier, rolled and inserted. Upon drying, the mandrel

was removed, exposing the vapour core. The container and wick were then vacuum furnace sintered, charged with working fluid and sealed. Copper powder wicks were named Configuration "K", while nickel powders were termed Configuration "H". Schematics of these configurations are shown in Figure 4-3.

4.2.2 Composite wicks

Composite wicks were designed to exploit enhanced evaporation heat transfer and to achieve a superior compromise between liquid permeability and capillary pressure over conventional wicks.

The first composite configuration, shown in Figure 4-4, was comprised of layers of 100-copper mesh, with an integral layer of metal powder at the liquid/vapour interface. This fine pore layer would serve a twofold purpose:

- To significantly increase the number evaporating surface menisci, thereby enhancing evaporation heat transfer.
- To increase the wick's capillary pumping ability. This would increase the capillary limit, greatly enhancing against gravity heat transfer performance.

The layers of copper mesh would provide a higher permeability liquid flow path, thus ensuring a lower liquid pressure drop. This property would also increase the capillary limit.

Composite nickel powder wicks following this design were assigned the name Configuration "B", while copper powder composite wicks with this construction were identified as Configuration "I". Metal powders were mixed with a binder to a liquid consistency and applied onto the mesh.

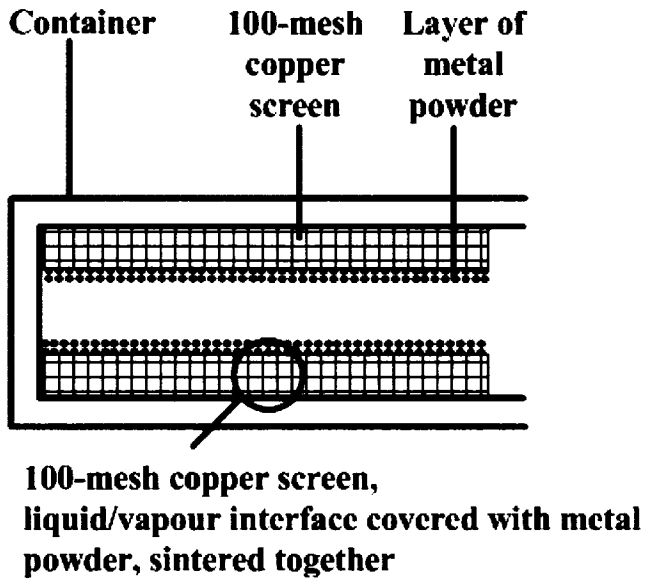

Figure 4-4: Liquid/Vapour Interface Covered with Metal Powder, Configurations B and I

Another composite configuration similar to the above included an additional layer of metal powder at the wall/wick interface, shown in Figure 4-5 . The fine pore layer at the wall/wick interface was included because it could augment performance through an increase in the wall/wick contact area, thus decreasing the contact resistance. This would lower the heat pipe end-to-end temperature drop. Powder application techniques were identical to the above. Composite nickel powder wicks with this construction were called Configuration "E". Similarly, copper powder composite wicks possessing this design were named Configuration "J".

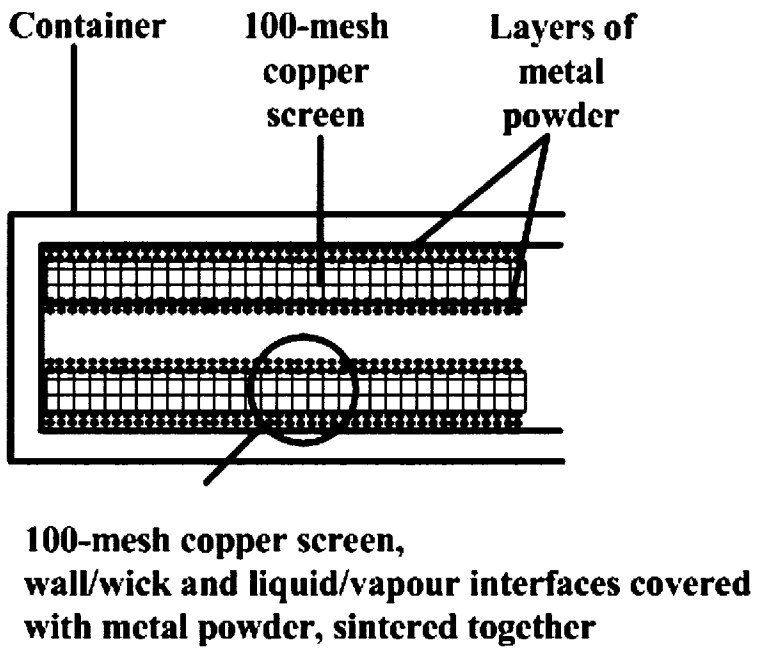

Figure 4-5: Wall/Wick and Liquid/Vapour Interfaces Covered with Metal Powder, Configurations E and J

The last composite configuration employed a 100-mesh copper screen, uniformly covered with a thin layer of nickel powder. This was labelled as Configuration "L", shown in Figure 4-6 . A copper powder variation was not attempted due to difficulties in coverage control, explained further in Section 4.3.4. This configuration was designed to not only increase the number of evaporating menisci at the liquid/vapour interface, but throughout the whole wick thickness as well. Of course, another possible benefit associated with this fine pore microstructure was believed to be an increase in the wick's capillary pumping ability.

Another postulation leading to the selection of Configuration "L" was associated with liquid recession into the wick. If a fine pore arrangement existed exclusively at the

liquid/vapour interface as in Configuration B, liquid could potentially recede beyond this layer at higher heat fluxes. The evaporating menisci would then dry out, resulting in performance degradation. The extension of evaporating menisci throughout the wick thickness could mitigate this potential problem.

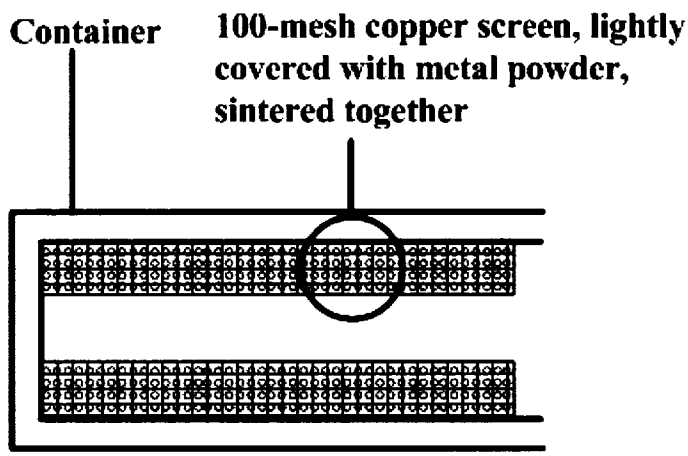

Figure 4-6: Metal Powder Applied throughout Wick Thickness, Configuration L

4.3 Heat Pipe Design and Manufacture

Because of their widespread use in electronics cooling, the focus of this study was the performance enhancement of moderate temperature heat pipes. As previously mentioned, water was chosen as the working fluid, with copper tubing selected as a container. Copper and nickel powders, in combination with copper mesh, were chosen for wick materials. This section details the design and manufacture of the moderate temperature copper/water and copper/nickel/water heat pipes that were tested in this research program.

4.3.1 Design

Design calculations were based on a conventional 25 cm long (9.84"), 9.525 mm (3/8") O.D. copper/water heat pipe with a 100-mesh copper screen wick, operating in the horizontal position. Referring to the naming convention in Section 4.2 , this wick is known as Configuration A. Because circular, flat end caps and solder filling would be used for sealing, some clearance was required at each tube end. This amounted to an additional 1.57 cm, for a total tube length of 26.57 cm. Copper tube details are listed in Table 4-1. Complete calculations are presented in Appendix A.

Since tube dimensions were already determined, design calculations began with the estimation of the maximum allowable vapour temperature based on the hoop stress. Assuming a fully annealed material state with a safety factor of 3 on the yield strength of 48 MPa, the maximum allowable vapour temperature was estimated to be approximately 235°C based on the tube wall. This temperature corresponded to a vapour pressure of approximately 3 MPa. Although it was recommended to use ¼ of the material's ultimate tensile strength in Section 3.2 , the alternative use of one third the yield strength added an even greater measure of safety for this particular copper alloy. Moreover, because the end caps were soldered into place and their strength was not supplied by the manufacturer, an additional safety factor was considered here. Using Equation (3-8) with a safety factor of 4 on the previously determined maximum allowable hoop stress, a maximum vapour temperature of approximately 185°C was estimated based on the end cap strength. This corresponded to a vapour pressure of 1.2 MPa. Since the heat pipe's thermal resistances were not yet calculated, the maximum allowable wall temperature associated with the

estimated vapour temperature was unknown. Therefore, for added safety, it was decided to keep the maximum temperature of the evaporator wall in the 150-160°C range during testing and back-calculate the resultant vapour temperature based on this assumption.

Next, the minimum vapour core diameter was determined using Equation (3-3). The maximum heat input and the assumed vapour temperature were estimated to assess their effect on the vapour core diameter. Assuming a conservatively high estimate of 300 W for the maximum heat input and a vapour temperature of 160°C, the minimum vapour core diameter necessary to avoid compressibility effects was calculated to be 0.75 mm, a very small dimension. Therefore, any vapour core diameter greater than this would ensure incompressible vapour flow. It should be mentioned that the above assumptions led to a very conservative estimate of the minimum vapour core diameter, meaning there was essentially no danger of encountering compressible flow with the proposed design. The final vapour core diameter required an estimate of the wick thickness, described below.

The required wick thickness was calculated based on a 4-layer, 100-mesh copper design. This configuration was chosen to accommodate one or two layers of metal powder-coated screen on the outermost and innermost layers, sandwiching a two or three-layer metal screen core. Referring to Table 4-2, the wire diameter was approximately 114 μm.

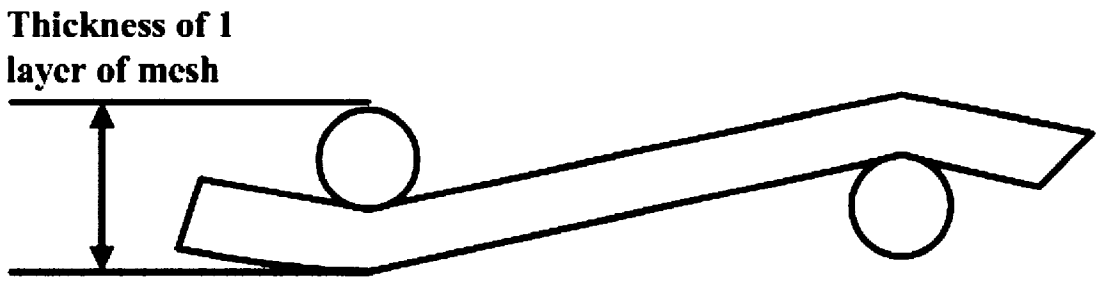

Figure 4-7: Schematic of Mesh Weave [28]

Figure 4-7 illustrates the layout of a plain mesh weave, used to estimate the wick thickness. The thickness of 1 layer of 100-mesh copper screen was therefore approximated as 228 μm. Therefore, four layers would measure 0.91 mm thick. As a result, the final vapour core diameter was roughly 6.2 mm, much larger than the minimum value of 0.75 mm.

Using Equations (2-30) and (2-31), the heat pipe operating temperature was calculated based on evaporator and condenser wall temperatures of 160°C and 24°C respectively. Neglecting source and sink thermal resistances, the operating temperature, defined as the vapour temperature at the evaporator exit, was calculated to be approximately 90°C. Then, employing this operating temperature, capillary and boiling limits were computed. Equation (2-13) was rearranged to solve for the maximum evaporator heat input at the capillary limit, estimated to be approximately 139 W in the horizontal orientation. The boiling limit was calculated to be much higher at approximately 895 W. Therefore, it appeared that the capillary limit would be encountered before the boiling limit. The entrainment limit was not calculated since this is not usually problematic in moderate temperature mesh-wick heat pipes. The sonic limit was indirectly considered in the

calculation of the minimum vapour core diameter, and it was shown that compressibility effects were negligible.

To summarize, all heat pipes manufactured for this study would closely follow the design specifications of the standard heat pipe described above, with some minor geometric variations to the wick structure. For example, some composite wicks would employ layers of sintered metal powder. This would slightly decrease the vapour core diameter. Specifications for the conventional, benchmarking heat pipe (ie: Configuration A) are listed below in Table 4-6.

Conventional Heat Pipe: Specifications	**Value**
Length	10.46" 26.57 cm
O.D.	3/8" 9.525 mm
I.D.	0.315" 8 mm
Vapour core diameter	0.244" 6.2 mm
Wick	100-mesh Cu wick, 4 layers
Working fluid	Water
Operating temperature	≈90°C
Source temperature	≈160°C
Sink temperature	≈24°C
Capillary limit	≈139 W
Boiling limit	≈894 W

Table 4-6: Conventional Heat Pipe Design Specifications

4.3.2 Wick cutting

Since the wick was rolled around a mandrel from a single flat sheet of mesh, length and width dimensions were required. The wick length was selected to be 25 cm. To estimate the width of the cut, the wick was modeled as concentric circles, shown in Figure 4-8.

The four circumferences were added, yielding a required mesh width of approximately 92 mm. A metal template 250 mm long by 92 mm wide was fabricated for wick cutting purposes. Using the wick cutting template and a sharp utility blade on a clean, rubber cutting mat, all wicks were cut to the same dimensions. Tools are shown in Figure 4-9.

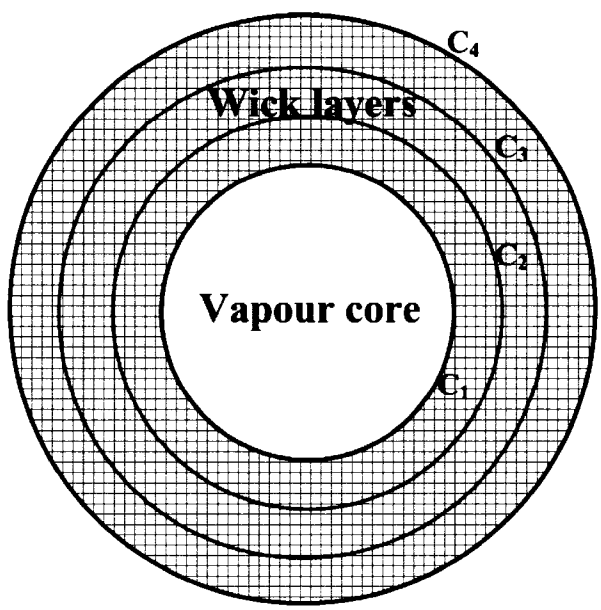

Width of flat mesh sheet = $C_{tot} = C_1 + C_2 + C_3 + C_4$

Figure 4-8: Model for Required Width of Mesh

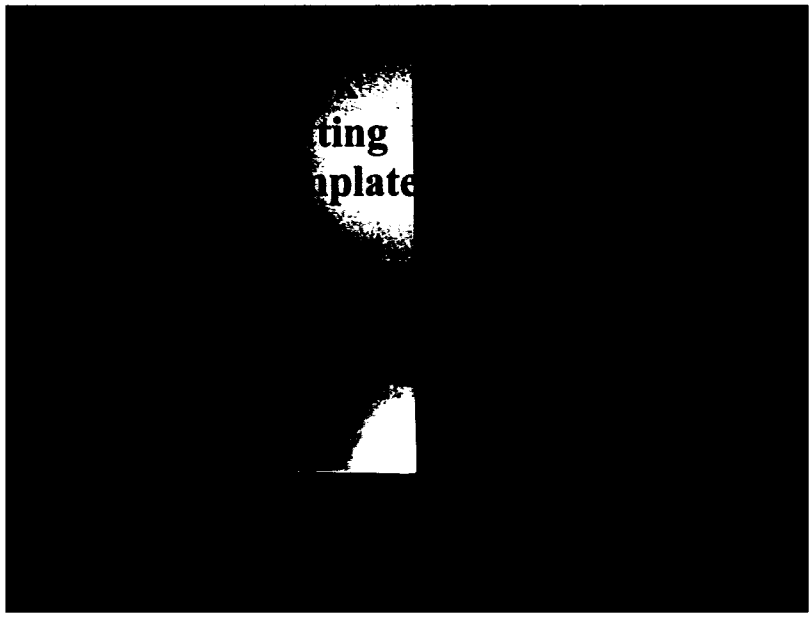

Figure 4-9: Wick Cutting Tools

4.3.3 Degreasing and deoxidizing

Because of the importance of material cleanliness in heat pipe manufacturing, a methodical procedure was developed for material preparation. These steps were followed for all heat pipes prior to processing:

1. Immerse parts for 30 min. in ultrasonic bath consisting of a 1:1 volumetric ratio solution of Simple Green® all-purpose cleaner and water.
2. Rinse parts with running water for 5 min.
3. Immerse parts in ultrasonic acetone bath for 20 min. Air dry.
4. Deoxidize parts in an ultrasonic acid bath consisting of 100 ml of phosphoric acid (H_3PO_4) + 100 ml of nitric acid (HNO_3) + 1800 ml of water. Copper tubes should be etched for 30 min. Copper mesh should be etched for 20 min. Rinse parts with running water for 5 min.

5. Rinse in acetone and air dry.

Following deoxidation and cleaning, the standard wick configuration was prepared for rolling and insertion into the container. For composite wicks, additional processing steps are described in Section 4.3.4.

4.3.4 Metal powder application

Homogeneous copper metal powder wicks (Configuration K) were formed using a slurry mixture of metal powder and binder. A mud-like slurry consistency was selected to ensure metal particles would remain suspended during the drying process. A 4.76 mm (0.1875") mandrel was centred in the container using a mandrel centering end plug. The end plugs, shown in Figure 4-10, were designed to both centre the mandrel and provide clearance for end caps.

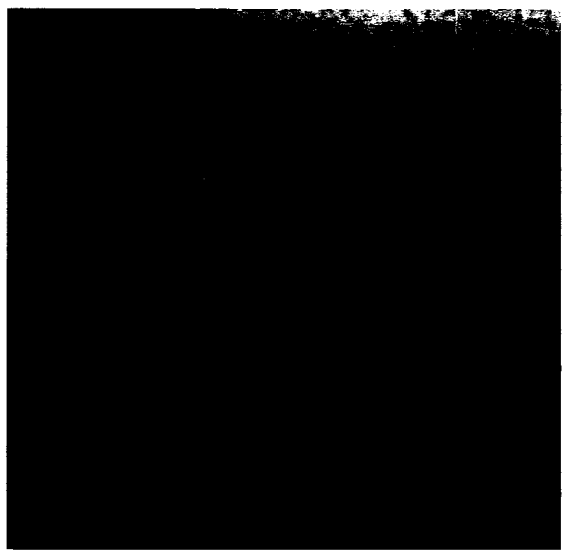

Figure 4-10: End Plugs

By means of syringe injection, the slurry was forced into the annular spacing between the mandrel and the container wall. An additional end plug was fitted on the opposite end of the assembly to form the slurry into the wick shape. Details are shown in Figure 4-11. Slurry drying was accelerated using a hot air dryer for approximately 8 hours, after which the heat pipes were prepared for vacuum furnace processing.

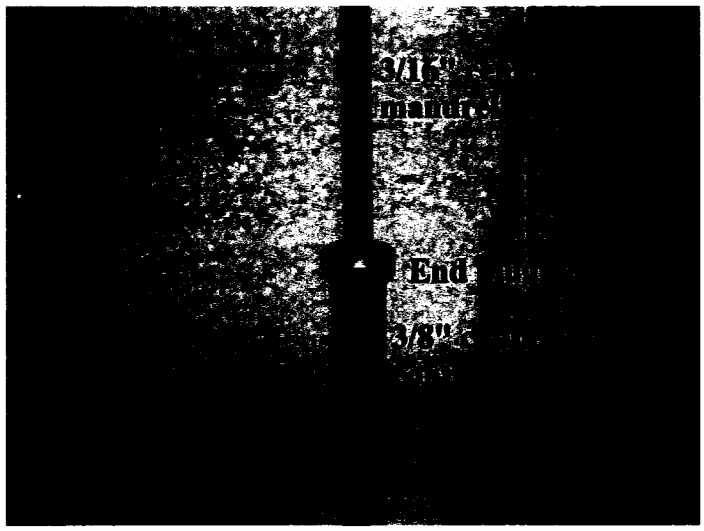

Figure 4-11: Homogeneous Copper Metal Powder Heat Pipe Manufacturing Assembly

Composite wicks were formed by applying a metal powder and binder slurry to a 100-mesh copper screen. A spray application technique was employed for all nickel powder wicks, including the homogeneous nickel powder configuration described above.

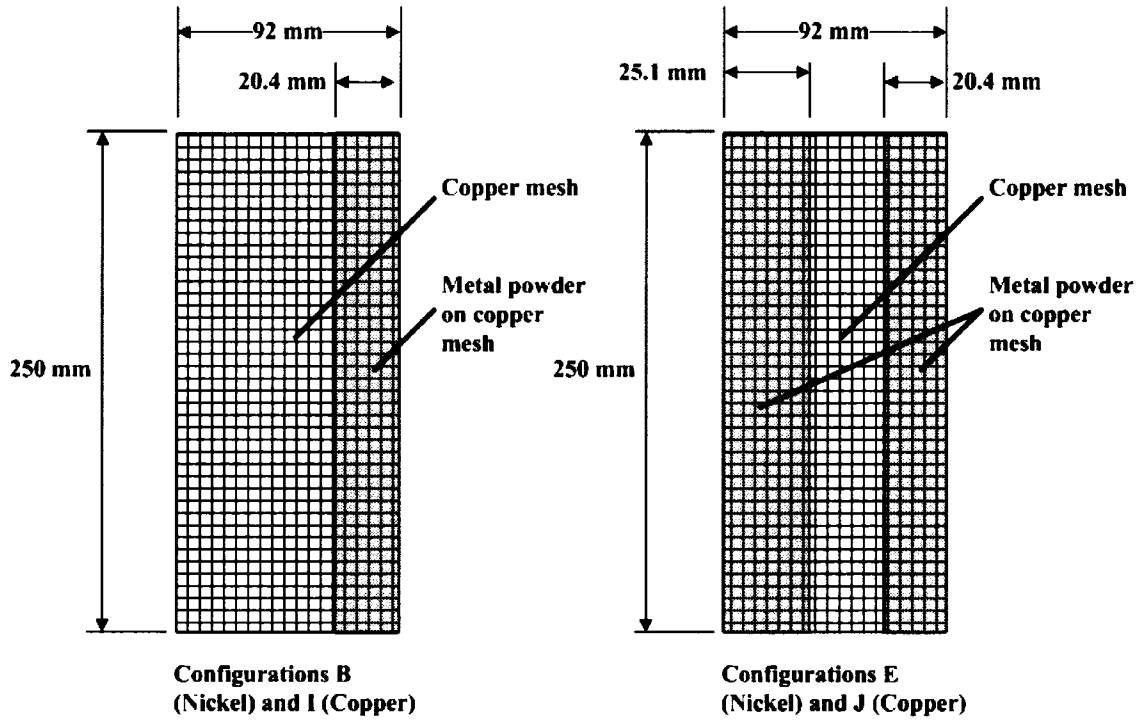

Figure 4-12: Metal Powder Application Patterns for Configurations B, E, I and J

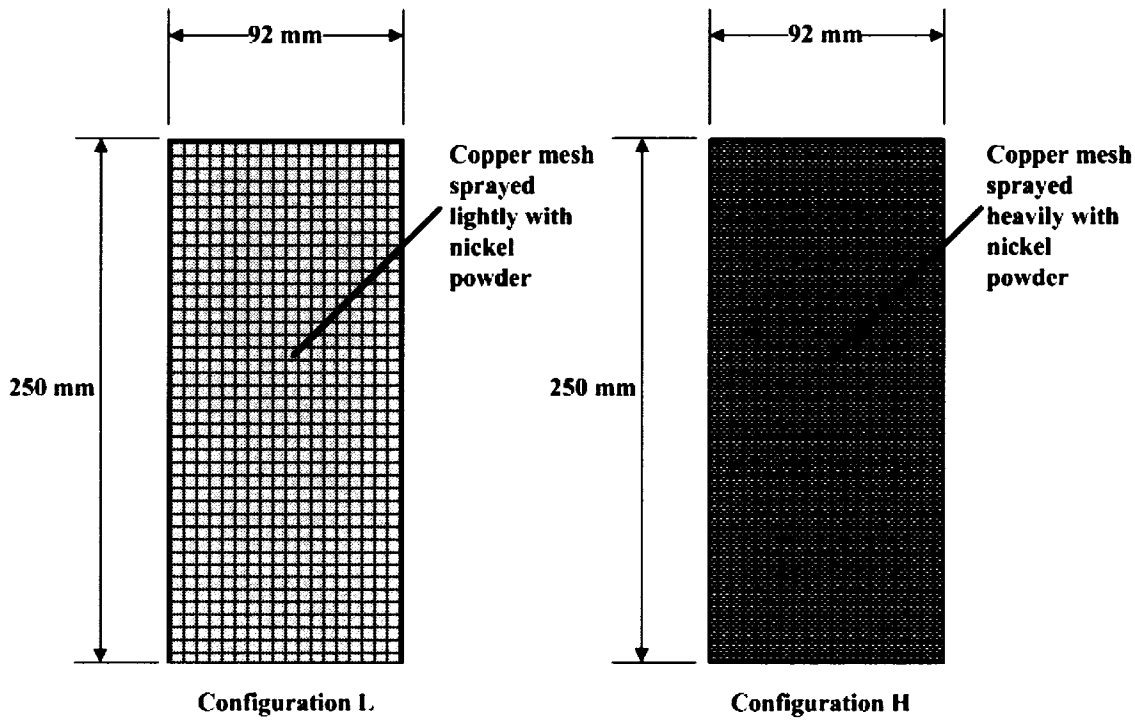

Figure 4-13: Spray Patterns for Configurations L and H

Figure 4-12 and Figure 4-13 illustrate spray patterns associated with the various wick configurations. For configurations B and I, the metal powder treated portion of the wick was sized by estimating the inner circumference of the wick. Similarly, configurations E and J were estimated using inner and outer wick circumferences. Prior to spraying, wicks were masked with paper to prevent unintentional overspray onto copper mesh layers. Masking paper was not necessary for configurations L and H since the copper mesh would be completely coated to some extent with nickel powder. Following the spraying process, the masking paper was removed and the wicks were allowed to dry for approximately 1 hour. At this point, the wicks were fully prepared for rolling and insertion. Figure 4-14 shows configuration B after spraying and prior to masking paper removal.

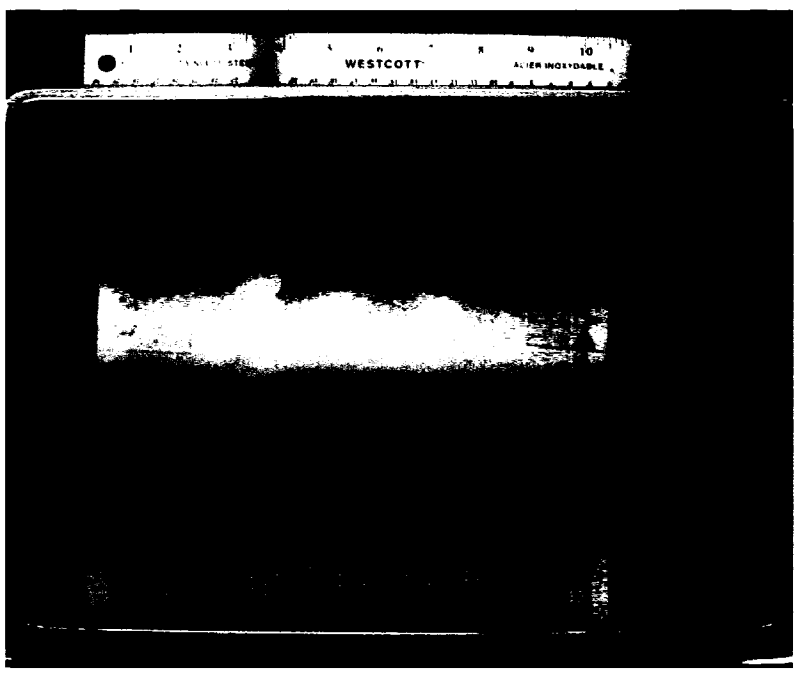

Figure 4-14: Nickel Powder Sprayed Wick, Configuration B

Attempts were made to spray apply copper powder onto copper mesh to form configurations I and J. However, these were unsuccessful due to clogging of the spray gun nozzle. A powder sifting technique was therefore developed to produce configurations I and J. For masking, the mesh was sandwiched between two cleaned steel beam sections. Metal was used in favour of paper masking since the binder could saturate the paper, resulting in paper disintegration and contamination of the wick. Firstly, binder was applied onto unmasked portions of the copper mesh. Next, copper powder was carefully sifted onto the binder-saturated wick using a sieve. Then, the wicks were allowed to dry for approximately 1 hour prior to rolling and insertion.

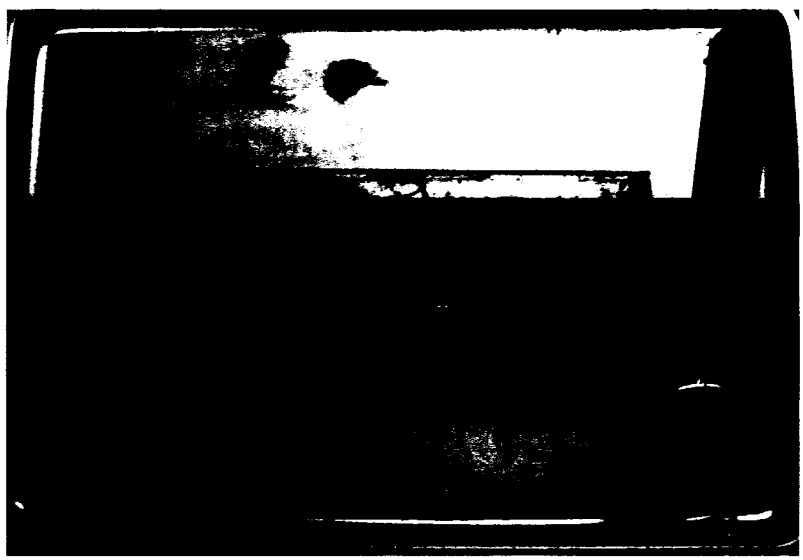

Figure 4-15: Composite Copper Wick Manufacturing

4.3.5 Rolling and insertion

Prior to rolling and insertion of wicks into their containers, all work area surfaces coming into contact with heat pipe components were thoroughly cleaned with soap and water, followed by a rinse in isopropyl alcohol or acetone. Isopropyl alcohol was used to

decontaminate the rubber rolling mat, while acetone was used to clean end plugs and mandrels. Rolling and insertion tools are shown in Figure 4-16.

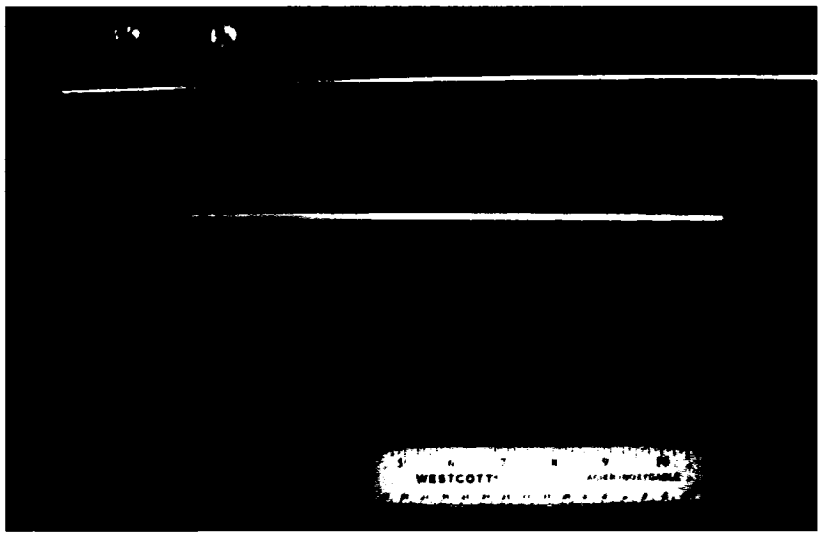

Figure 4-16: Configuration J with Rolling Tools

A 3/16" (4.76 mm) mandrel was used to roll all wicks. The mandrel was placed on top of the wick, and rolling was initiated by folding the leading edge of the wick over and around the mandrel. By commencing the roll at the appropriate edge, composite layers would be positioned correctly in the wick. Even hand pressure was applied across the wick throughout the rolling procedure. Rolling was repeated until the wick was wrapped tightly enough around the mandrel to initiate insertion into the container. Initial insertion resistance was kept as high as possible to ensure good wall/wick contact.

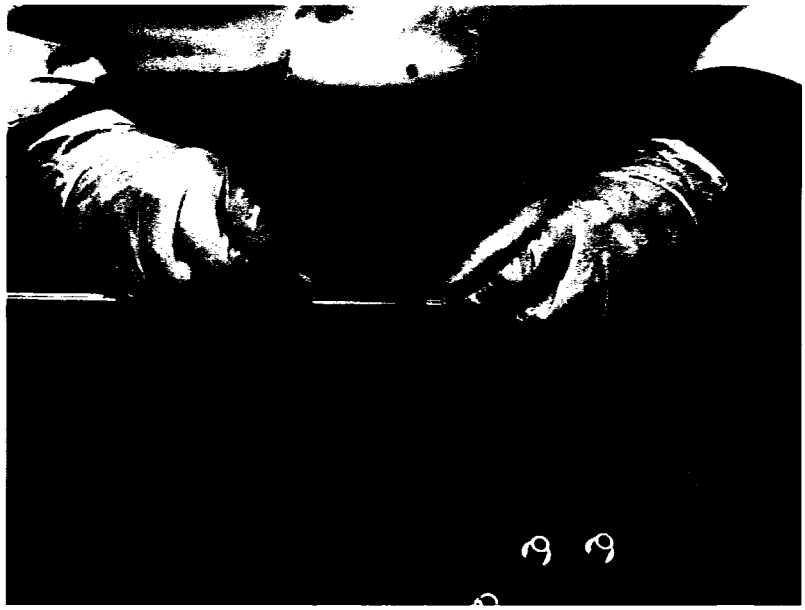

Figure 4-17: Placement of End Plugs for Wick Centering

Rolling and insertion then carefully proceeded in alternate steps until the wick was completely inserted into the container. End plugs were then slipped over the mandrel and pushed into opposite ends of the container to properly locate and center the wick, demonstrated in Figure 4-17. The end plugs and mandrel were then removed from the container. At this point, container/wick assemblies were completely prepared for sintering.

4.3.6 Sintering

Sintering trial exercises were performed to estimate the best combination of time and temperature prior to actual manufacturing operations. Trial runs were performed on nickel powder samples at sintering temperatures ranging from 700°C to 980°C. Time at the sintering temperature was varied from 0.5 to 1.5 hours. One copper powder sintering trial was also performed at 850°C for one hour. Inadequate nickel powder bonding,

illustrated in Figure 4-18, was observed for trials with sintering temperatures up to 800°C for any length of time attempted. Some copper powder bonding was observed in Figure 4-19, however to ensure sufficient strength, increased neck formation was desired.

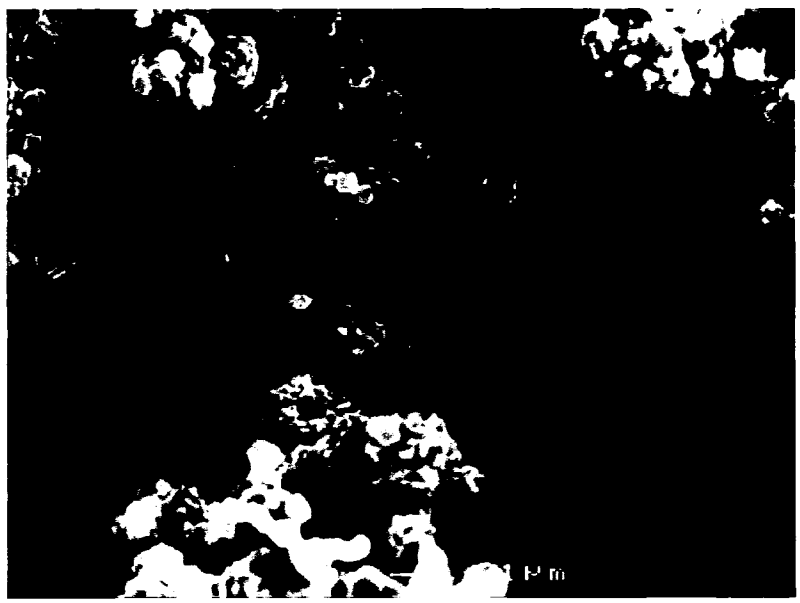

Figure 4-18: Nickel Powder, Sintered at 800°C for 1.5 Hours

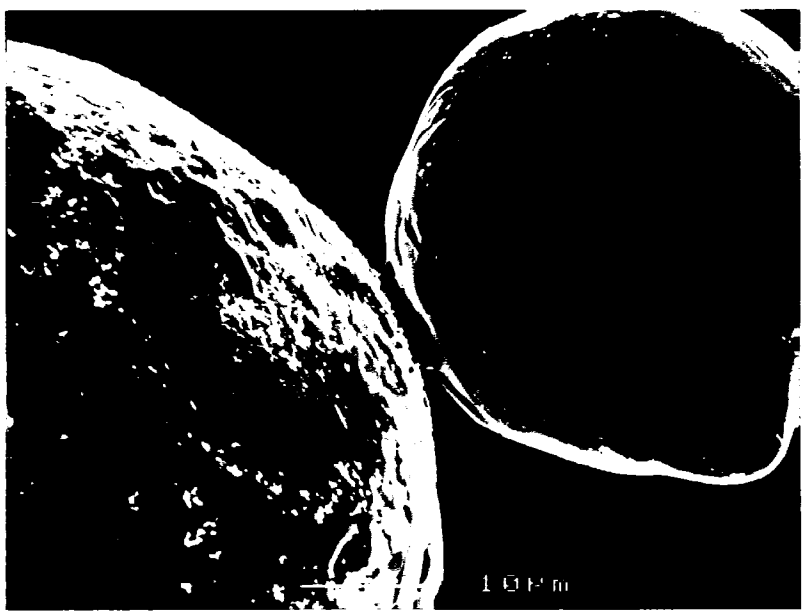

Figure 4-19: Copper Powder, Sintered at 850°C for 1 Hour

When the sintering temperature was increased to values over 900°C, significant nickel particle bonding was observed. See Figure 4-20 for an example of an adequately sintered porous nickel wick. Sufficient particle bonding was achieved, while still maintaining high porosity. It was therefore decided to process all samples at the same sintering temperature of 940°C for 1 hour, since desirable results were obtained during these trial experiments.

Figure 4-20: Nickel Powder, Sintered at 940°C for 1 Hour

During sintering, container/wick assemblies were placed on a commercially-pure titanium tray coated a surface protection agent. This would prevent unwanted diffusion bonding between the components and the tray. Additionally, a layer of fire brick wafers covered the tray for added safety against unwanted bonding. To prevent surface oxidation, sintering took place in a vacuum environment using the following procedure:

1. Ambient temperature: Achieve a vacuum level of at least $1x10^{-2}$ torr in furnace chamber. Backfill chamber with argon. Evacuate and repeat. Achieve a vacuum level of at least $1x10^{-4}$ torr before activating heating elements.
2. Ambient-550°C: Ramp up temperature as quickly as possible while maintaining a vacuum level of at least $1x10^{-2}$ torr. Hold at 550°C for 45 min. to ensure complete volatilization of binder.
3. 550°C-900°C: Ramp up temperature in increments of 50°C every 10 min. while maintaining a vacuum level of at least $1x10^{-4}$ torr.
4. 900°C-940°C: Ramp up temperature in two increments of 20°C every 4 min. to prevent temperature overshoot.
5. 940°C: Hold for 1 hour at sintering temperature.
6. 940°C-20°C: Furnace cool to room temperature.

After furnace processing, the container/wick assemblies were removed and measured to estimate fluid charging amounts, described in Section 4.3.7.

4.3.7 Fluid charging and sealing

For homogeneous metal powder wicks, working fluid charging amounts were estimated by performing measurements on container/wick assemblies. From these measurements of mass and geometric dimensions, wick porosities were calculated. Wherever 100-mesh copper screen was employed, including for composite wicks, wick porosity was estimated using Equation (3-13). In turn, porosity was used to estimate fluid charging amounts using the following expression from Chi [16]:

$$m = A_v L_t \rho_v + A_w L_t \varepsilon \rho_l \qquad (4\text{-}1)$$

where m is the mass of the fluid charge, A_v is the cross-sectional area of the vapour core, L_t is the heat pipe length, ρ_v is the vapour density, A_w is the wick cross-sectional area, ε is the wick porosity and ρ_l is the liquid density. A slight overcharge was included as a precautionary measure against premature dryout. See Appendix B for complete calculations. A summary of the procedure followed for fluid charge estimation is described below:

1. Measure outside and inside tube diameters and condenser and evaporator end cap clearances using Vernier calipers. Measure tube lengths. From tube lengths and end cap clearances, verify wick lengths. These should be approximately 250 mm.
2. Measure vapour core diameters using hole gauge and Vernier calipers. Weigh post-sintered container/wick assemblies. By subtracting the cross-sectional area of the vapour core from the cross-sectional area of the tube I.D., the area of the wick is calculated.
3. For homogeneous metal powder wicks, use mass and geometry measurements to estimate the volume of solid wick material and the total volume of the wick. The porosity is calculated by subtracting the volume of solid material from the total volume of the wick, then dividing by the total wick volume. For all other wicks, approximate the porosity using Equation (3-13).
4. Calculate the fluid charge using Equation (4-1). Add a 10% fluid overcharge.

Fluid charging and sealing was completed using proprietary procedures at Acrolab of Windsor, Ontario, a heat transfer engineering company specializing in heat pipe manufacture. With the fluid charging and sealing steps completed, heat pipe manufacturing was accomplished. Thermal performance testing, described in the following sections, would be carried out next to evaluate improvements in heat transfer associated with composite wick designs.

4.4 Heat Pipe Test Rig

The heat pipe test rig in this study was designed to both apply and remove heat from heat pipes while recording all important analytical data. A band heater and copper annulus clamped over the evaporator portion of the heat pipe, while a plastic cooling jacket enabled liquid to flow across the condenser end. Insulation was wrapped around all exposed areas to minimize heat losses to the ambient. Thermocouples were fastened axially along the container to capture temperature profiles, subsequently used in effective thermal conductivity calculations. A LabView data acquisition program recorded, monitored and displayed information during testing. Upon test completion, data files were generated for further analysis of thermal performance. A test rig schematic is illustrated in Figure 4-21.

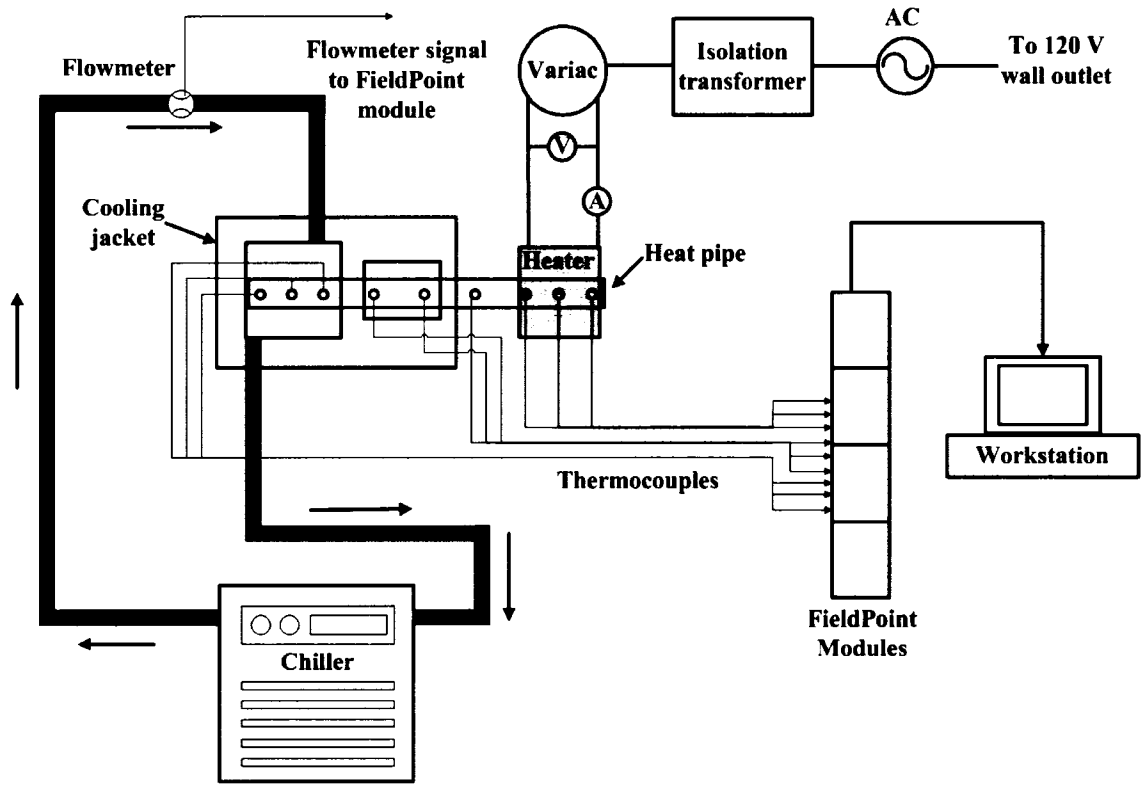

Figure 4-21: Heat Pipe Test Rig Schematic

4.4.1 Heater and annulus

A one-piece band heater from Omega Engineering was selected for heating purposes. This design was selected for its ability to deliver a uniform heat flux to the evaporator. Additionally, its high clamping force would minimize the thermal contact resistance between the band heater, the copper annulus and the heat pipe. Power was controlled through a variable voltage power supply, connected to an isolation transformer to prevent power fluctuations. Band heater details are listed in Table 4-7.

Clamp- Style Band Heater: Properties	**Value**
Supplier	Omega Engineering
Model number	HBZ-12224
Diameter	2.125" 5.4 cm
Heated length	2.25" 5.7 cm
Maximum power	400 W
Voltage	120 V

Table 4-7: Band Heater Properties

Since the diameter of the available heater was greater than the heat pipe outside diameter, a metallic annulus was designed to eliminate this gap. Copper was selected for its high thermal conductivity, ensuring lower heat losses to the ambient. A split design was selected to enable good thermal contact and space for thermocouple instrumentation, with dimensions illustrated in Figure 4-22. Some additional clearance was designed between annulus halves to accommodate thermocouple wiring on the evaporator section of the heat pipe. This was manufactured by slotting the annulus from the outside diameter to the concentric hole using a 1/8" saw. The heater and annulus assembly is shown in Figure 4-23.

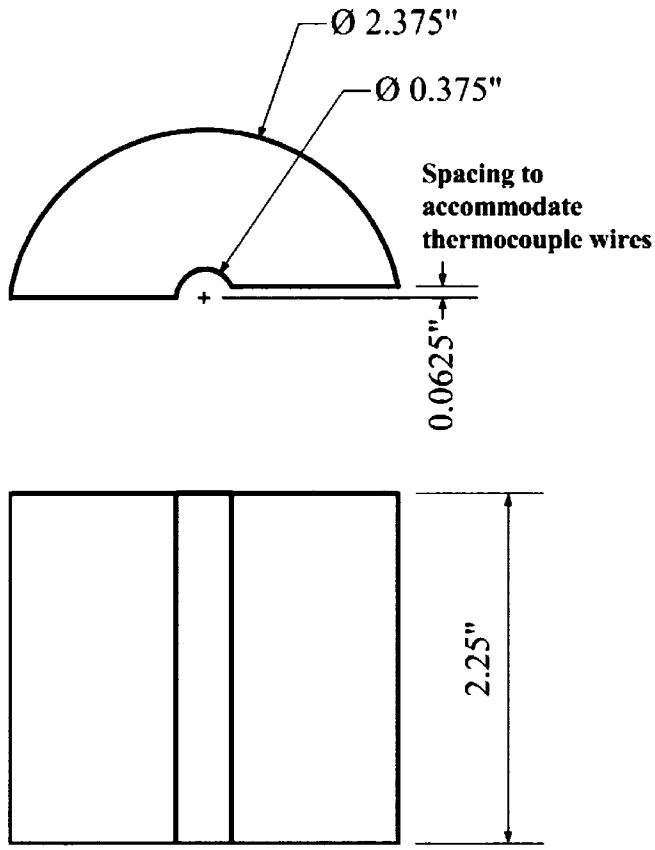

Figure 4-22: Dimensions of Copper Annulus Half

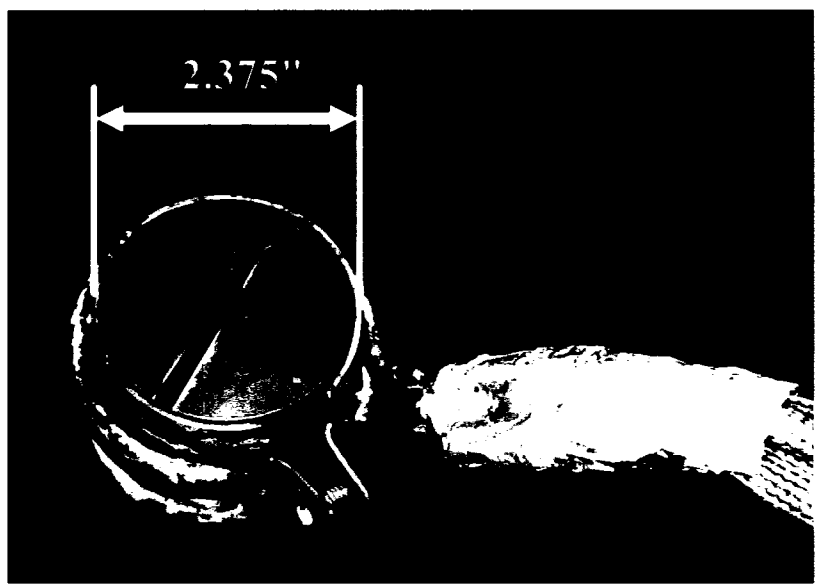

Figure 4-23: Heater and Annulus Assembly

4.4.2 Cooling jacket and chiller

The cooling jacket, comprised of top and bottom halves, was machined from two solid blocks of Delrin®, selected for its manufacturability and low thermal conductivity. Properties of Delrin® are listed in Table 4-8. Two internal pockets were designed, one to allow coolant flow around the condenser end of the heat pipe and the other to provide air insulation for part of the adiabatic section. Some space was left between the heater and the cooling jacket to prevent overheating at higher heat input rates.

Delrin®: Properties	**Value**
Supplier	McMaster-Carr
Maximum operating temperature	82°C
Minimum operating temperature	7°C
Machinability	Excellent Use standard tooling
Thermal conductivity	0.36 W/m°C
Coefficient of thermal expansion	122.4 μm/m°C

Table 4-8: Properties of Delrin® [68]

Semicircular grooves were machined into each half of the cooling jacket to both provide support to the heat pipe and to ensure a leak-proof seal. An o-ring groove followed the perimeter of the coolant pocket to seal against leaks. Right angle, cast iron pipe fittings were secured into National Pipe Thread (*NPT*) threaded holes for coolant inlet and outlet flows. A staggered design was employed for increased coolant circulation across the heat pipe, one fitting being positioned on a lower plane than the other. Inlet and outlet holes were also positioned at opposite ends of the cooling pocket for the same reason. To

provide access for the condenser-end thermocouples, wires were passed through a bolt with a concentrically drilled hole. The hole was then filled with hot-melt glue to seal against leaks. The sealed bolt assembly was then tightened into a tapped hole through the top half of the cooling jacket. After inserting an instrumented heat pipe, the top and bottom halves of the cooling jacket assembly were clamped together using twelve through bolts. The cooling jacket is shown in Figure 4-24, while design drawings are presented in Appendix C.

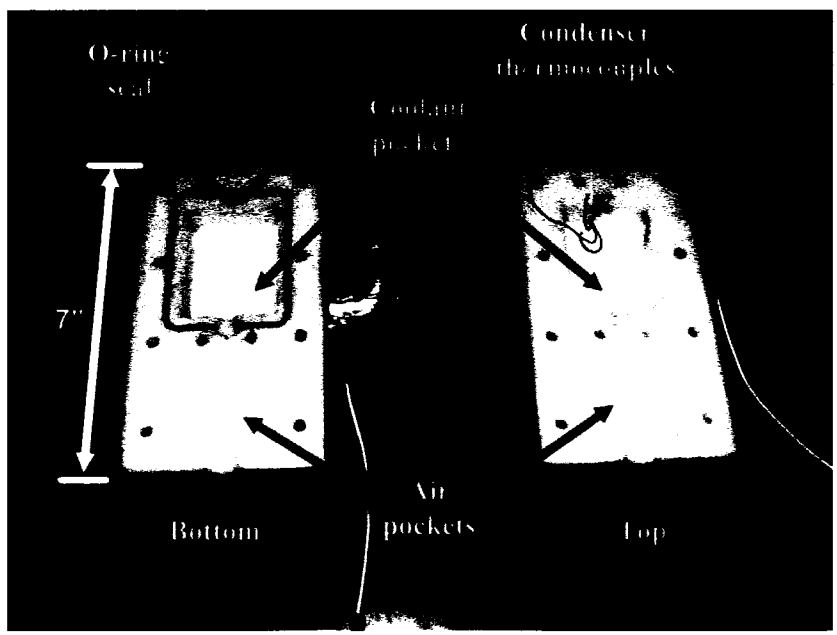

Figure 4-24: Cooling Jacket

A Cole-Parmer refrigerated recirculation chiller was selected to supply temperature-controlled coolant to the cooling jacket. Details are listed in Table 4-9. The chiller outlet hose connected to the cooling jacket inlet, while the chiller inlet hose connected to the

cooling jacket outlet. Reinforced, braided polyvinylchloride tubing with a ½" I.D. and a ¾" O.D. was selected for this purpose.

Cole-Parmer Chiller: Properties	Value
Manufacturer	Cole-Parmer Instrument Co.
Model number	12920-10
Temperature range	-5 to 40°C
Cooling capacity	0°C 350 W 10°C 780 W 20°C 1100 W
Pump pressure	5.5 psi
Pump flow	10 gal(US)/min 38 l/min

Table 4-9: Properties of Refrigerated Recirculation Chiller [74]

A 50/50 volumetric mixture of automotive coolant and distilled water was chosen as the cooling fluid. Since a high coolant flow rate was not necessary, a system of flow control bypass valves was installed to limit this to more manageable levels. One valve controlled bypass flow from the chiller outlet to the chiller inlet, while another valve controlled the inlet flow to the cooling jacket. In this fashion, cooling flow was lowered from approximately 38 l/min to 1.5 l/min.

4.4.3 Insulation

To minimize ambient heat losses, all exposed surfaces were covered with a flexible alumina-silica based high-temperature pipe and tube wrap, as illustrated in Figure 4-25. Most importantly, this insulation was selected because of its resistance to extreme heat, a

situation it could encounter in the vicinity of the band heater during high heat inputs. Other desirable attributes were its flexibility and low thermal conductivity. See Table 4-10 for insulation properties.

Insulation: Properties	**Value**
Supplier	McMaster-Carr
Material	Alumina and silica based ceramic fibres
Dimensions	12 ft long x 3" wide x ½ " thick
Temperature range	-10°C to 1260°C
Thermal conductivity	0.036 W/m°C

Table 4-10: Properties of Insulation [68]

Insulated surfaces included the band heater periphery, the ends of the copper annulus, the exposed portion of the heat pipe's adiabatic section and all cooling jacket surfaces, except for the base during horizontal heat pipe testing. Insulation was not added underneath the base because it would upset the mechanical stability of the cooling jacket, and heat losses from this surface were negligible in this orientation. However during vertical tests, the cooling jacket base was covered with insulation to minimize the expected free convection heat losses.

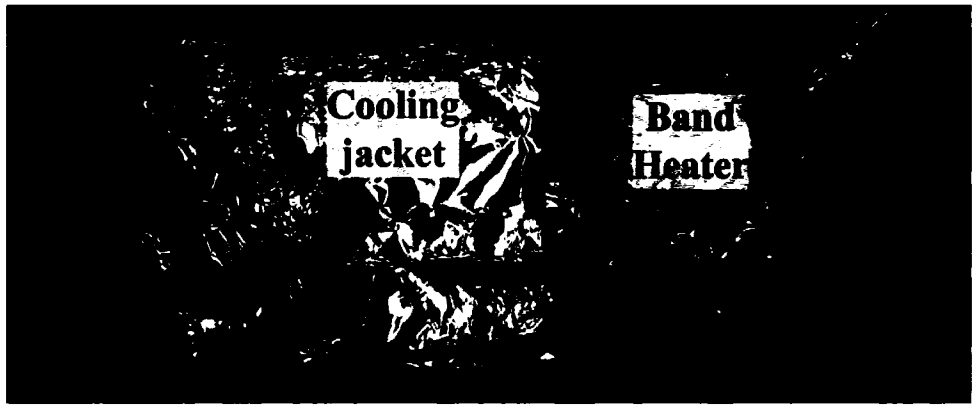

Figure 4-25: Insulation Covering Cooling Jacket and Heater

4.4.4 Instrumentation

Test rig instrumentation included thermocouples for heat pipe temperature measurements along with a voltmeter and an ammeter to record the power input to the heater. Additionally, two thermistors, a flowmeter and numerous other thermocouples were employed in an attempt to perform a heat balance on the test rig. However, since to date this has not yet been accomplished, a brief description is included in this section for future research purposes.

For temperature measurements in the evaporator and adiabatic sections, 30 gauge glass-braid insulated K-type thermocouples were selected. These were ideal because of their small size and high temperature capabilities. The condenser section employed the same type of thermocouple, however waterproof Teflon insulation was chosen since it was immersed in the coolant pocket. Thermocouple specifications are presented in Table 4-11. Nine thermocouples, spaced apart as shown in Figure 4-26, were fastened to each heat pipe to record temperature profiles.

Thermocouples: Properties	Glass Insulated	Teflon Insulated
Manufacturer	Omega Engineering	Omega Engineering
Product number	GG-K-30	TT-K-30
Type	K-type	K-type
Wire diameter (30 gauge)	0.01" 0.2546 mm	0.01" 0.2546 mm
Measurement temperature range	-200°C to 1250°C	-200°C to 1250°C
Maximum insulation operating temperature	482°C	200°C
Limits of error (special)	1.1°C or 0.4% of reading, whichever is greater	1.1°C or 0.4% of reading, whichever is greater

Table 4-11: Thermocouple Properties [75]

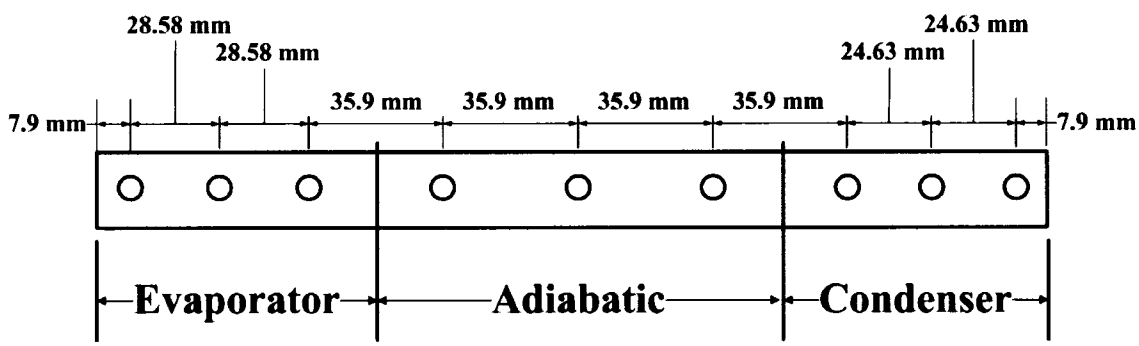

Figure 4-26: Thermocouple Locations on Heat Pipe

Heater input power was recorded using two Fluke 45 Dual Display Multimeters, one to measure voltage and the other to measure current. By multiplying these two values, the power input to the heater could be calculated [10]. This was also estimated as the evaporator heat input (Q_{in}):

$$P_{in} \approx Q_{in} = V \times I \tag{4-2}$$

where P_{in} is the input power to the heater, V is the measured voltage and I is the measured current. Multimeter specifications are listed in Table 4-12.

Fluke 45 Multimeters: Properties	**Value**
Manufacturer	Fluke Corporation
Type	Multifunction bench multimeter
Volts (AC)	Range: 0 V to 750 V Resolution:1 μV to 0.01 V Accuracy: ±0.2%+100 mV (from 0-100 V)
Current (AC)	Range: 15μA to 10A Resolution: 0.1μA to 10mA Accuracy: ±2%+10 mA (from 1-10 A)

Table 4-12: Multimeter Properties [76]

Although a heat balance was attempted to account for all heat flow into and out of the test rig, results were not included the results of Section 5.3 since further investigation is still required. The associated heat balance instrumentation is as follows. To measure the heat removal rate, two high precision thermistors were inserted into drilled and tapped holes on the inlet and outlet elbows of the cooling jacket. These elements exhibited large changes in resistance with temperature, making them favourable for the measurement of minute temperature changes. However, since the data acquisition system could only record voltage or current signals, voltage divider circuits were added to each thermistor to convert these resistances to voltages. Thermistor details are listed in Table 4-13. A flowmeter monitored the coolant flow rate through the cooling jacket by means of a current signal. See Table 4-14 for flowmeter specifics.

Thermistors: Properties	**Value**
Manufacturer	Omega Engineering
Product number	ON-401-PP
Type	Laboratory grade, waterproof, immersion type thermistor. Encased in vinyl sheath.
Resistance at 25°C	2252 Ω
Measurement range	-80°C to 100°C
Accuracy	±0.1°C

Table 4-13: Thermistor Properties [75]

Flowmeter: Properties	**Value**
Manufacturer	Kobold Instruments, Inc.
Product number	DPM-1120-N2-L443
Type	Pelton wheel flow sensor
Measurement range	0.05 to 2 l/min
Current output range	4 to 20 mA
Power	24 V (DC)
Accuracy	±2.5% of full scale reading

Table 4-14: Flowmeter Properties [77]

Additional thermocouples were used as part of the heat balance instrumentation. These were identical to the thermocouples detailed in Table 4-11 and are described next. Three thermocouples, spaced radially 120° apart, were fastened to the outside of the heater insulation. Additionally, two thermocouples were placed in the vicinity of the cooling jacket to monitor ambient temperature. These were all employed in the heat balance to approximate the heat lost to the ambient through natural convection. Two additional thermocouples were taped to the outside of the cast iron elbows for an alternative measurement of the heat removal rate.

4.4.5 Data acquisition system

The data acquisition system includes FieldPoint modules designed by National Instruments, a desktop computer and a LabView data acquisition program.

Two FieldPoint thermocouple modules were used to record all temperature signals. These modules could record up to eight thermocouple readings each, while providing built-in 60 Hz noise filtering and voltage-to-temperature conversion for all common thermocouples. One FieldPoint analog input module recorded the analog input signals from the flowmeter and thermistors. The entire module assembly was powered by one FieldPoint network module, which also communicated data to the desktop computer. FieldPoint module properties are listed in Table 4-15, Table 4-16, and Table 4-17.

Thermocouple Modules: Properties	Value
Manufacturer	National Instruments Corporation
Product number	FP-TC-120
Type	Thermocouple module
Channels	8
Resolution	16-bit
Noise filtering	50 and 60 Hz
Supported thermocouples	J,K,R,S,T,N,E,B
Cold-junction accuracy	0.15°C typ., 0.3°C max.

Table 4-15: Properties of Thermocouple Modules [78]

Analog Input Module: Properties	Value
Manufacturer	National Instruments Corporation
Product number	FP-AI-100
Type	Analog input module
Channels	8
Resolution	12-bit
Current input ranges	0 to 20 mA, 4 to 20 mA, ±20 mA
Voltage input ranges	0 to 1 V, 0 to 5 V, 0 to 15 V, 0 to 30 V ±1 V, ±5 V, ±15 V, ±30 V

Table 4-16: Properties of Analog Input Module [79]

Network Module: Properties	Value
Manufacturer	National Instruments Corporation
Product number	FP-1000
Type	Network and power source module
Power supply range	11-30 V (DC)
Communication ports	1 RS-232 port 1 RS-485 port

Table 4-17: Properties of Network Module [80]

The data acquisition program "*HeatPipeDatAcq*" was written with LabView, a graphical programming language for data flow visualization. Main features of the graphical user interface are a real-time thermocouple temperature graph, warning indicators for excessive flow rate and overheating conditions, and data logging controls. A "*Setup*" page enables the user to select temperature and flow rate limits, sampling rates, filenames and data logging frequency. A "*Monitor*" page allows observation of all measured parameters and data capture control settings. During a test, two files are created: one file captures all data points (*full data file*) and the other only records data points during steady-state operation (*steady-state file*).

Once the "*Start*" button on the "*Monitor*" page is depressed, the test commences and data is logged to the full data file. Depending on data logging frequency and sampling rate, data points are an average of all data collected between the last logged data point and the next. For example, if a sampling rate of 10 Hz was selected with a data logging frequency of 1 Hz, one data point would be appended to the full data file every second. This data point would be calculated using the average of the 10 data samples taken during the last second.

Whenever the power level is changed, the new voltage and current must be manually recorded in the "*Voltage*" and "*Current*" fields. Following an increase in power, the heat pipe is allowed time to reach thermal equilibrium. Transient periods can be monitored by means of the real-time temperature graph on the "Monitor" page, shown as decaying exponential curves. All thermocouple temperatures are displayed, and upon flattening of temperature curves, steady-state operation can be distinguished from transient operation. Here, it should be mentioned that steady-state temperature meters also indicated steady-state operation, however these were not as reliable as the real-time graph and were not usually employed.

When steady state is achieved, the "*Take Data*" button is depressed. This records data at the prescribed sampling rate and data logging frequency, but then calculates an arithmetically-averaged data point from all data samples taken in a one minute interval. This steady-state data point is then added to the steady-state file. Upon test completion, the "*Stop*" button is depressed, terminating data capture to the full data file. At this point,

the data acquisition program has created two complete Comma Separated Value (*.csv*) files, easily manipulated by spreadsheet programs such as Excel. Depressing the "*Exit Program*" button closes the program. A flowchart and screenshots of "*HeatPipeDatAcq*" are found in Appendix D.

4.5 Test Procedure

A discussion of heat pipe preparation, testing orientations, data collection and data reduction comprise important aspects of the test procedure followed for all heat pipe experiments.

4.5.1 Heat pipe preparation

Prior to testing, all heat pipe thermocouple locations were marked using Vernier calipers and a scribe. See Figure 4-26 for thermocouple locations. They were then cleaned with acetone to remove any contamination to ensure good thermocouple/container surface adherence. Evaporator and adiabatic thermocouples were then attached to the heat pipe outer surface with aluminium tape, shown in Figure 4-27. A small amount of Teflon tape, shown in Figure 4-28, was wrapped around the circumferential sealing contact area of the heat pipe. This prevented internal cooling jacket leaks between the cooling pocket and the air pocket.

Figure 4-27: Thermocouple Attachment

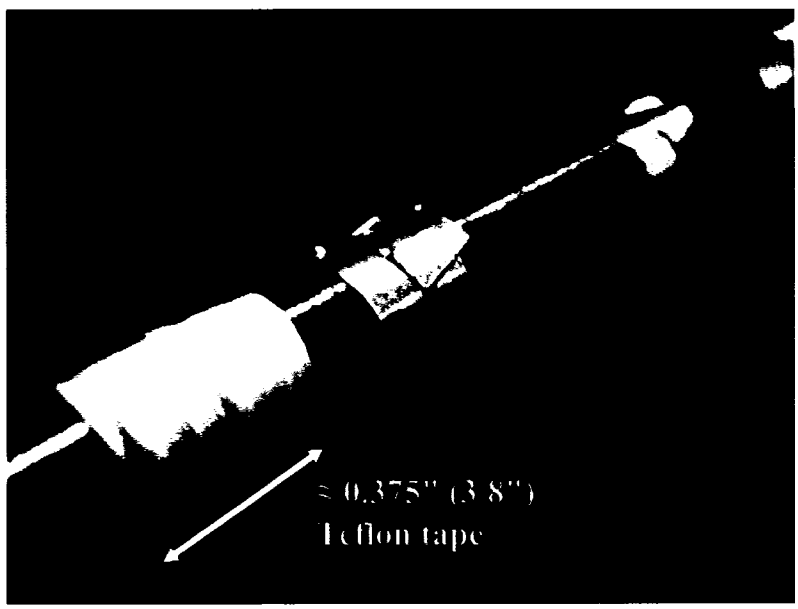

Figure 4-28: Teflon Tape Seal

Next, the heat pipe was placed in position over the top half of the cooling jacket for fastening of the condenser thermocouples. For ease of assembly, the top half of the cooling jacket was placed vertically on the orientation pedestal, a wooden assembly used

for against-gravity and gravity-assisted heat pipe tests. Then, both cooling jacket halves were clamped together tightly in a crosswise pattern with twelve through bolts, as demonstrated in Figure 4-29.

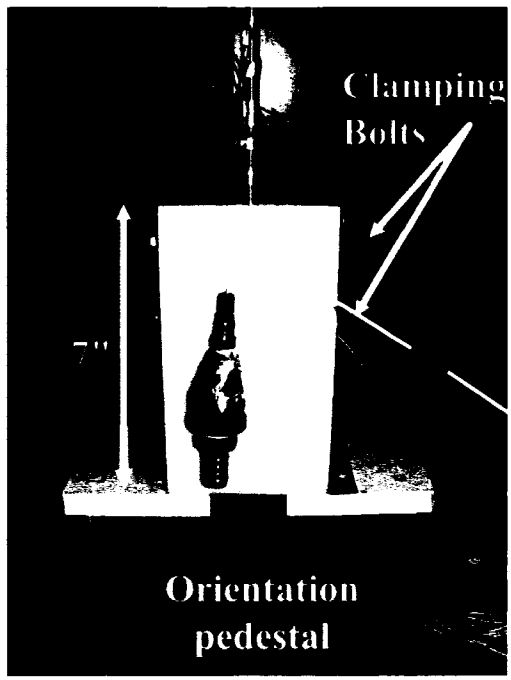

Figure 4-29: Clamped Cooling Jacket on Orientation Pedestal

To minimize thermal contact resistance between the band heater, the copper annulus and the heat pipe, OMEGATHERM® thermally conductive silicone paste was applied to the outer and inner surfaces of the copper annulus. Thermal paste application is shown in Figure 4-30. Properties of OMEGATHERM® are listed in Table 4-18.

OMEGATHERM®: Properties	Value
Manufacturer	Omega Engineering
Product number	OT-201
Type	Thermally conductive paste
Components	Aluminum oxide Zinc oxide Silicone resin
Thermal conductivity	2.308 W/m°C
Application temperature range	40°C to 200°C

Table 4-18: Properties of OMEGATHERM® [81]

Figure 4-30: Thermal Paste Application

The annulus was then fitted around the heat pipe evaporator, aligning the first and last evaporator thermocouples with the two ends of the annulus. The band heater was spread open slightly and slipped over the copper annulus halves. A nut and bolt clamped the band heater tabs together, tightly securing the assembly to the heat pipe, shown in Figure

4-31. Heat pipe test preparations were completed by connecting the coolant hoses to the cooling jacket and wrapping the assembly with insulation.

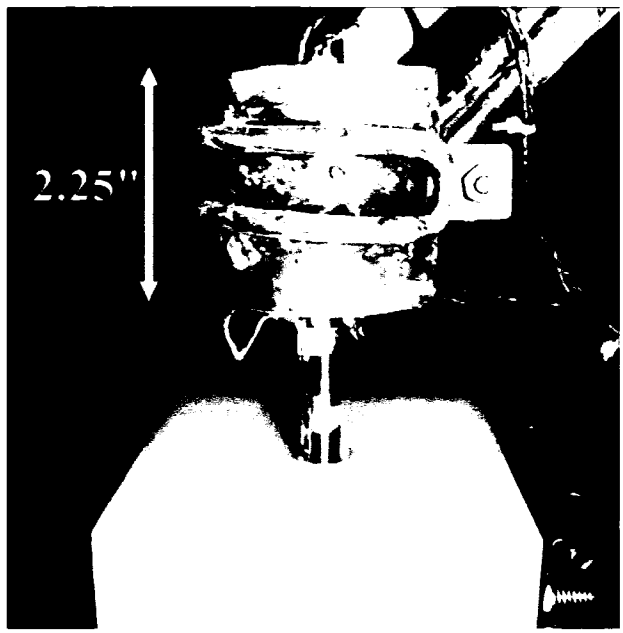

Figure 4-31: Heater Assembly Secured to Evaporator Section

4.5.2 Orientations

Each heat pipe was tested in three orientations: horizontal, gravity-assisted and against-gravity operation. This would allow for the evaluation of different heat pipe operational conditions and the underlying mechanisms of increased performance.

The horizontal test represented a standard operating situation, where both permeability and capillary pressure were expected to be important. Gravity-assisted operation corresponded to favourable conditions, where high permeability was believed to be the dominant factor for increased performance. Finally, the most severe test was evaluated

during against-gravity operation, where the development of high capillary pressure was most likely essential. In all tests, enhanced evaporation heat transfer was also hypothesized to manifest itself through lower axial temperature drops.

Coolant hoses were always connected to permit maximum coolant dwell time in the cooling pocket. This positioning also coincided with the most efficient orientation for coolant pocket air expulsion. For horizontal operation, the test assembly was positioned in a horizontal orientation such that the evaporator and condenser sections were on the same plane. The inlet coolant hose was connected to the lowest elbow fitting, while the outlet hose was connected to the higher fitting. Since the band heater and copper annulus were quite heavy and could cause heat pipe deformation, some additional insulation was wedged under the heater assembly for support.

During gravity-assisted test preparations, the test assembly was vertically oriented such that the heater assembly was positioned underneath the cooling jacket. This required the use of the orientation pedestal, shown previously in Figure 4-29. Again, coolant hoses were connected to facilitate air egress and enhanced cooling.

Against-gravity testing was similar to gravity-assisted tests, only the assembly was oriented with the heater assembly above the cooling jacket. Coolant hoses were reconnected in the opposite manner to gravity-assisted tests. That is, the gravity-assisted outlet connection was reconnected as the inlet during against-gravity tests and vice-versa.

4.5.3 Testing and data collection

Heat pipe test runs consisted of temperature measurements at stepwise increasing heater power settings. Heat inputs were approximately set in the following fashion, up to a maximum evaporator wall temperature ranging from 150°C to 160°C:

1. From 0 W to 40 W: increments of 10 W
2. From 40 W to 100 W: increments of 20 W
3. From 100 W to maximum: increments of 40 W

Some variations in the prescribed heat input settings were required to achieve the desired maximum evaporator temperatures. Therefore, some of the higher heat input increments did not exactly follow the pattern listed above. Also, if a minimum final increment of 5 W was not estimated to be attainable without exceeding the maximum allowable evaporator temperature, the test was ended prematurely. For example, heat pipe H3 attained a maximum heat input of 31 W with an evaporator temperature of 143°C. Since the previous 10 W increment (from 20 to 30 W) raised the evaporator temperature by 37°C, it was estimated that an additional increment in heat input would grossly exceed safe operating temperatures. Therefore, the test was halted at 31 W.

Filenames were selected using the following standard:

1. The first block of characters represented the heat pipe I.D. and consisted of "HP" plus the two character heat pipe name.

2. The next block of characters signified the test orientation: "horizontal" for horizontal tests, "assistG" for gravity-assisted tests and "againstG" for against gravity tests.
3. The final group of characters identified successive repeats of the same test. For example, "HPB7_horizontal_run1" signified that heat pipe B7 was being tested in the horizontal orientation for the first time.

A typical heat pipe test was performed in the following way. Typical settings are listed in brackets, while screenshots of "*HeatPipeDatAcq*" are available in Appendix D:

1. Launch data acquisition program "*HeatPipeDatAcq*". Click the "*Setup*" tab and enter desired data logging frequency (1Hz), sampling rate (10 Hz), temperature warning (150°C) and flow rate limit (1.6 l/min). Assign filename using previously explained file naming convention. Choose an appropriate file path.
2. Click the "*Monitor*" tab. Depress "*Start*" button on graphical user interface to begin taking data. Ensuring test assembly is at room temperature, take one "flow off" data point to record zero flowmeter reading (Note: this step was used in the heat balance and is not strictly necessary for the data reduction process presented in Section 4.5.4).
3. Start chiller and set coolant delivery temperature to 24°C to emulate room temperature sink conditions. Manipulate coolant hoses to work air bubbles out of cooling circuit.

4. When steady state is reached, take a "flow on" data point (See Note of Step 2).
5. Turn on power to the isolation transformer and the variac.
6. Set heater power level by rotating variac control knob until desired voltage and corresponding current to the heater is achieved (e.g.: for 10 W, typical settings were 18.8 V X 0.54 A ≈ 10 W). Record voltage and current in "*Voltage*" and "*Current*" fields on the "*Monitor*" page.
7. Monitor heat pipe thermal response using real-time temperature graph on "*Monitor*" page. When temperature curves exhibit a clear flattening trend, steady-state operation has been achieved. A steady-state data point may now be recorded. Prior to data capture, input any changes to the power settings in the "*Voltage*" and "*Current*" fields. Depress the "*Take Data*" button. Do not adjust any settings during steady-state data recording, indicated by the illuminated green light next to the "*Take Data*" button.
8. When the "*Take Data*" indicator turns off, increase the power level in steps corresponding to those previously outlined above. Repeat Steps 6 and 7 until the maximum recorded heat pipe temperature is between 150°C to 160°C. Once this is achieved, rotate the variac knob to the "zero" position. Switch variac and isolation transformer off. For faster heat pipe cooling, reduce coolant delivery temperature to 0°C.
9. When heat pipe temperature is sufficiently low (e.g.: ≈40°C), turn off chiller. Depress "*Stop*" button on "*Monitor*" page to end recording of test data. Depress "*Exit Program*" button to terminate program.

10. Retrieve data files from file path. Two files have been produced, each with the specified filename plus a file identity extension. The full data file has a "*.csv*" extension while the steady state file has a "*_ss_values.csv*" extension.

The steady state file was used for the data reduction of Section 4.5.4. Although the full data file was not needed, it could be used for test event troubleshooting or for heat pipe thermal transient response studies.

4.5.4 Data reduction program

Test data was manipulated with the MATLAB software program "thermalPerformance", available in Appendix E. Essentially, this program was written to calculate and plot heat pipe effective thermal conductivities for all recorded heater power input levels. Originally, the heat removed by the cooling circuit was to be used for effective thermal conductivity calculations. Because of unreliable heat balance measurements, results were based on heater input power levels instead. A general explanation of the data reduction procedure is described as follows.

Before data was manipulated, files were converted into a MATLAB-compatible binary format. This was accomplished by importing the comma separated value files into the MATLAB workspace and saving them as binary "MAT-files" with the same filenames as the originals.

The program "thermalPerformance" was executed by passing the desired filename as a character string to the data reduction program. The program began its routine by

initializing line markers, legend labels and loading file data. Evaporator, adiabatic, condenser and total heat pipe lengths were assigned next. To avoid measurement uncertainty in effective thermal conductivity calculations, the distance between the central evaporator and central condenser thermocouples was approximated using the effective length of Equation (2-8). Due to thermocouple spacing requirements, the calculated effective length was slightly shorter than the actual effective length measurements, however this would produce a conservative estimate of the effective thermal conductivity. Next, a large portion of code was dedicated to heat balance assessments, however in the context of the current study these calculations will not be elaborated upon.

Since the three evaporator and three condenser thermocouples were evenly spaced, the axial heat pipe temperature drop was based on the centrally-located thermocouple of each section. Thus, the temperature drop was calculated next by subtracting the second condenser temperature from the second evaporator temperature. Then, knowing the cross-sectional area of the heat pipe and employing Equation (2-35), the effective thermal conductivity was calculated for each heater power setting. The program then concluded with plotting routines for immediate graphical representation of test results.

5 Results and Discussion

In this section, experimental results are presented and discussed. A complete list of thermal performance tests is given. Wick morphology is examined through scanning electron microscopy and correlated with the obtained results. In support of effective thermal conductivity behaviour, some axial temperature gradients are also presented. Finally, the effects of biporous wicks on heat pipe thermal conductivity are graphically illustrated.

5.1 Summary of Tests Performed

A summary of heat pipes tested is listed in Table 5-1. Most notable is the absence of any "I" configuration heat pipes (i.e.: copper mesh with copper powder on the liquid vapour interface). Because of poor performance from previous copper mesh/copper powder heat pipes, it was decided this configuration would not produce any substantial performance advantage over conventional designs. As such, these configurations were eliminated from testing. Also of note, repeatability experiments were performed to assess both manufacturing reproducibility and test methodology. Manufacturing reproducibility tests were performed for configurations B, K and L. Test repeatability was accomplished by retesting heat pipe B8 in every orientation.

Heat Pipe I.D. and Configuration	Tests Performed
A7: 100-mesh copper screen, unsintered	1 horizontal, 1 gravity assisted, 1 against gravity
B7: 100-mesh copper screen, liquid/vapour interface covered with nickel powder, sintered	1 horizontal, 1 gravity assisted, 1 against gravity
B8: identical to B7	2 horizontal, 2 gravity assisted, 2 against gravity
E7: 100-mesh copper screen, wall/wick and liquid/vapour interfaces covered with nickel powder, sintered	1 horizontal, 1 gravity assisted, 1 against gravity
H3: 100-mesh copper screen as carrier, heavily covered with nickel powder, sintered	1 horizontal, 1 gravity assisted, 1 against gravity
J3: 100-mesh copper screen, wall/wick and liquid/vapour interfaces covered with copper powder, sintered	1 horizontal, 1 gravity assisted, 1 against gravity
K1: Copper powder, sintered	1 horizontal, 1 gravity assisted, 1 against gravity
K2: identical to K1	1 horizontal, 1 gravity assisted, 1 against gravity
L1: 100-mesh copper screen, lightly covered with nickel powder throughout structure, sintered	1 horizontal, 1 gravity assisted, 1 against gravity
L2: identical to L1	1 horizontal, 1 gravity assisted, 1 against gravity

Table 5-1: List of Heat Pipe Tests

5.2 Scanning Electron Microscopy

Scanning electron microscopy was employed to analyze wick morphology, including the degree of sintering and the interfacial microstructure. Samples were prepared from both flat, unrolled wicks and sectioned heat pipes. These assessments determined the effects of the sintering process on porous wick properties, such as adequate neck formation and satisfactory wall/wick contact. Manufacturing techniques were also assessed through biporous microstructure detection and evidence of increased evaporative surface area.

Homogeneous wick microstructures are presented first. These include Configurations A (copper mesh), H (nickel powder) and K (copper powder). Next, composite configurations are examined. These findings provided valuable insight into heat pipe performance predictions.

5.2.1 Configuration A

For comparison and reference, a few micrographs were taken of this copper mesh structure, one of which is shown in Figure 5-1. This mesh uses a plain weave construction, employed for wick thickness calculations in Section 3.3.1. Referring to the scale in Figure 5-1, the pore diameter seems slightly smaller than the theoretically calculated value of 254 μm. This may have produced better than expected performance during against gravity tests.

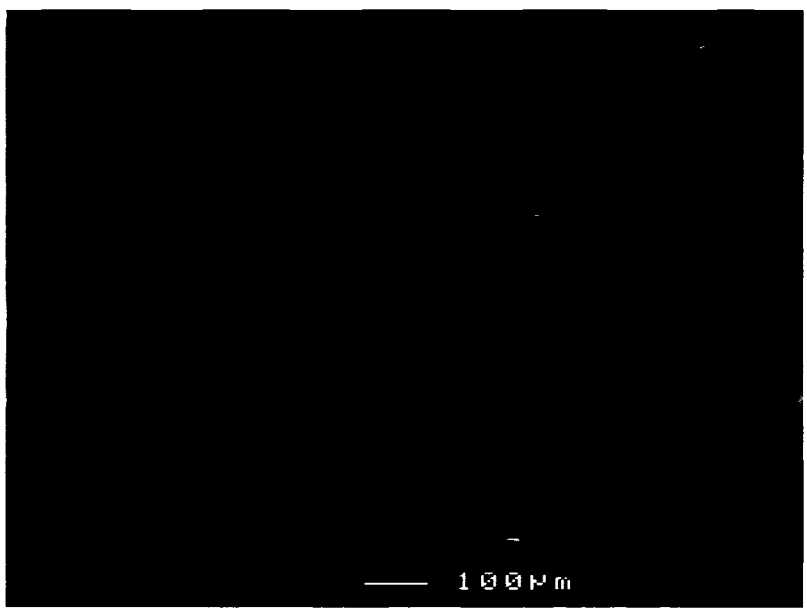

Figure 5-1: Configuration A

5.2.2 Configuration H

Sintered nickel powder formed this homogeneous wick structure. It was believed the filamentary morphology of these particles would produce a very porous microstructure with fine pores, both important contributing factors to thermal performance enhancement. Examining Figure 5-2 and Figure 5-3, it appears these predictions were correct. With reference to Figure 5-4, bonding between nickel particles is clearly distinguished. Also, with pore diameters on the order of 10 μm, it was predicted this structure would produce excellent against gravity thermal performance. Thus, because of this unique microstructure, high expectations were associated with Configuration H.

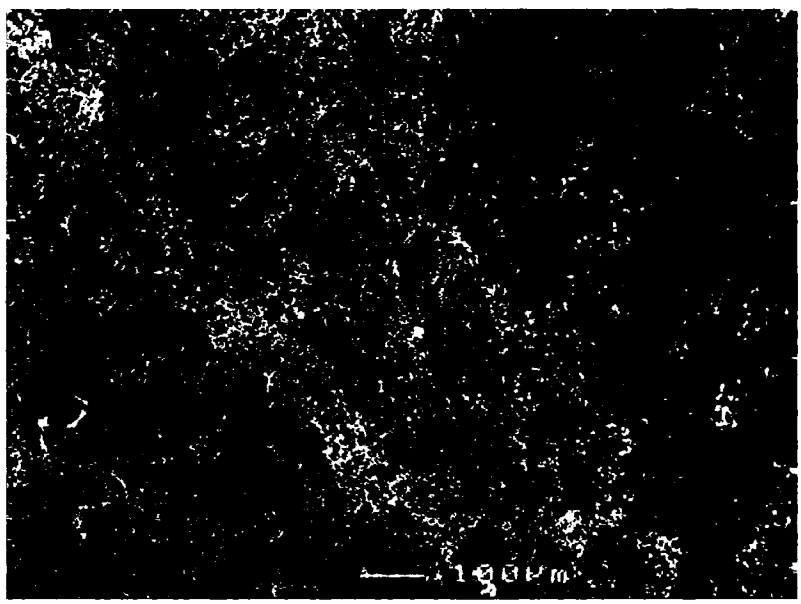

Figure 5-2: Configuration H

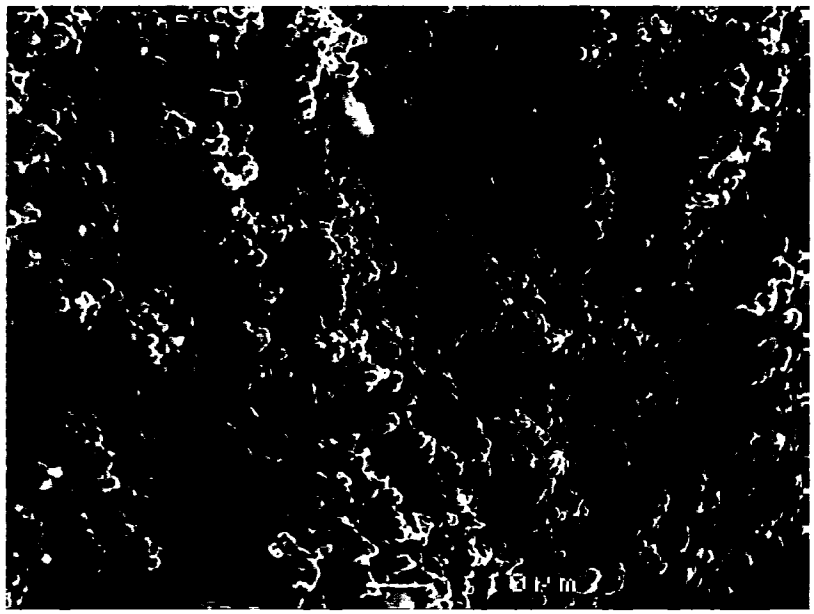

Figure 5-3: Configuration H, Higher Magnification

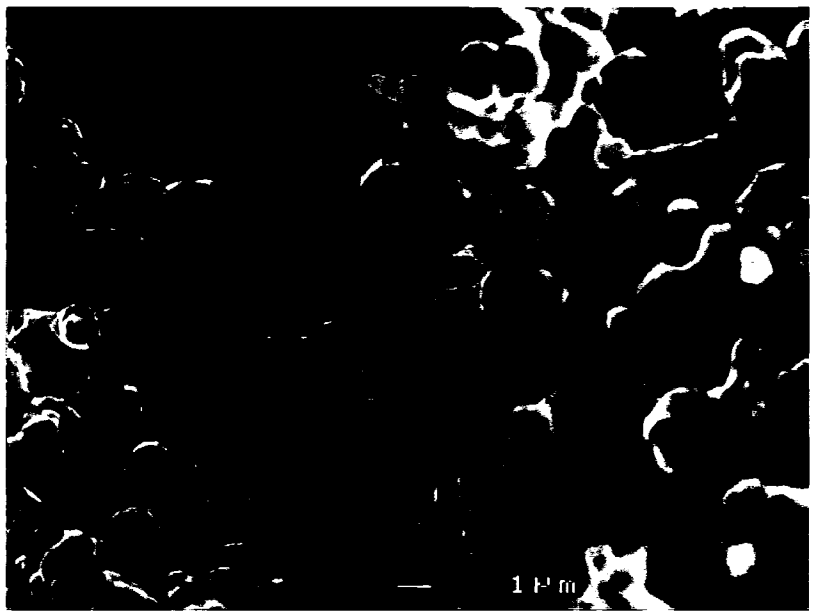

Figure 5-4: Sintering in Nickel Powder

5.2.3 Configuration K

For this homogeneous sintered copper powder configuration, samples were primarily examined for adequate sintering. Figure 5-5 illustrates this microstructure. The spherical copper particles did not seem to produce a highly porous structure in comparison to the filamentary nickel powder. This could lead to relatively poor thermal performance due to low liquid permeability. However, some performance advantage was still expected from this configuration during against gravity tests due to a much finer pore size than the copper mesh.

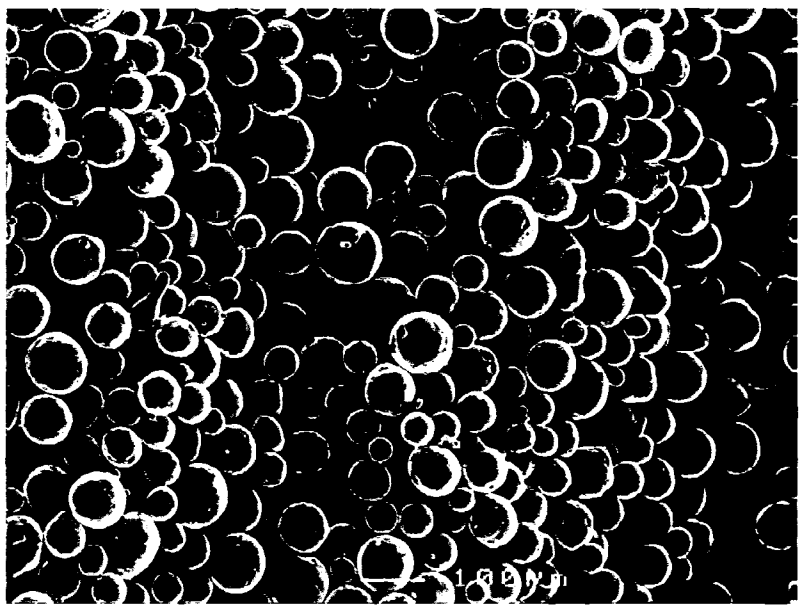

Figure 5-5: Configuration K

Only limited sintering was detected through modest neck formation, depicted in Figure 5-6. Comparing the preliminary observations from Figure 4-19 of Section 4.3.6 with the present results, neck formation was not noticeably improved. Therefore, it was likely that copper powder sintering parameters were not suitably chosen. However, increasing the

sintering temperature would not be an option since the melting point of copper (1085°C) was only marginally higher than the sintering temperature. Increasing the sintering time could have aided particle bonding somewhat, yet it seemed the poor sintering behaviour was largely associated with the relatively low surface area of the spherical copper powder. This in turn probably led to a lower particle surface energy and the observed sintering difficulties. Primarily due to the relatively low porosity, this configuration was not expected to perform well during horizontal and gravity assisted testing. Some sufficient performance was expected during against gravity testing due to its finer pore size relative to Configuration A.

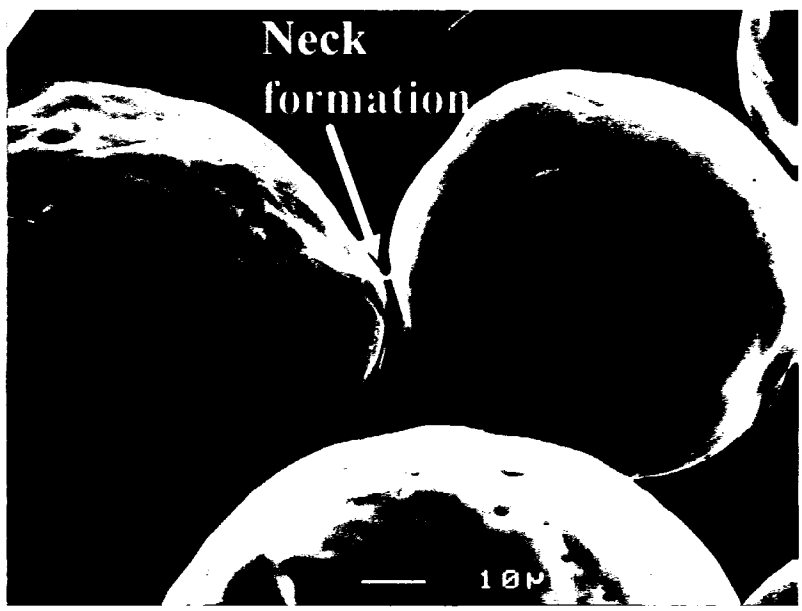

Figure 5-6: Neck Formation in Configuration K

5.2.4 Configuration B

This configuration featured nickel powder covering the liquid/vapour interface, illustrated in Figure 5-7. The presence of the unobstructed large pore structure is evident. Finer

pores can also be identified in Figure 5-8. Therefore, it was concluded that the powder application technique successfully produced a composite, biporous morphology. Closer examination of the fine pore nickel powder structure in Figure 5-8 revealed a significant increase in surface area over Configuration A, an important factor in enhanced evaporation heat transfer.

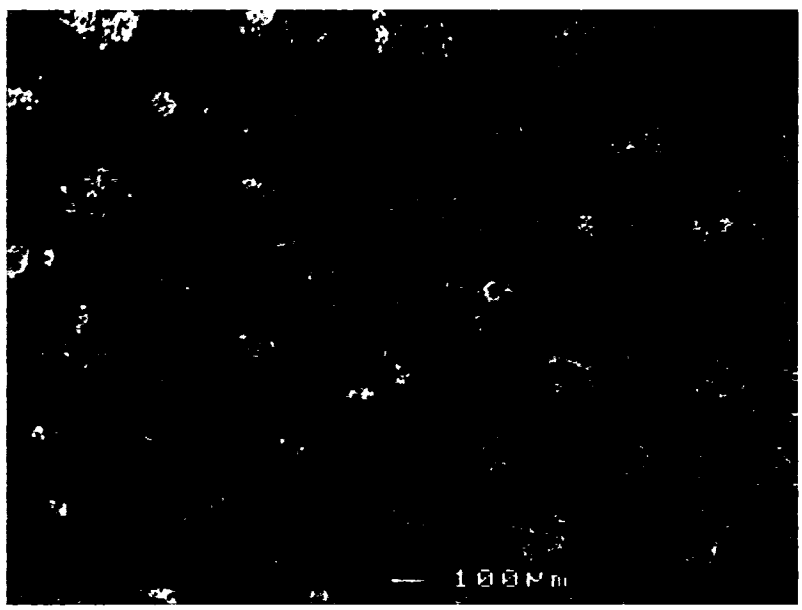

Figure 5-7: Liquid/Vapour Interface of Configuration B

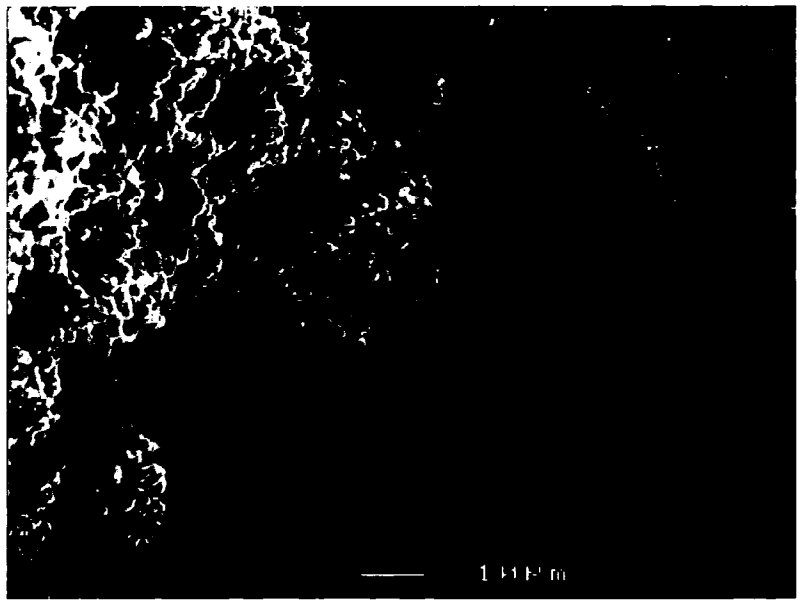

Figure 5-8: Increased Surface Area in Configuration B

Like Configuration H in Figure 5-4, sintering was observed between nickel powder particles. Moreover, bonding was also detected between the nickel powder and the copper mesh, shown in Figure 5-9. This indicated that sintering temperature and time were appropriately selected. Because of the above properties, Configuration B appeared to be a promising candidate for heat pipe performance enhancement.

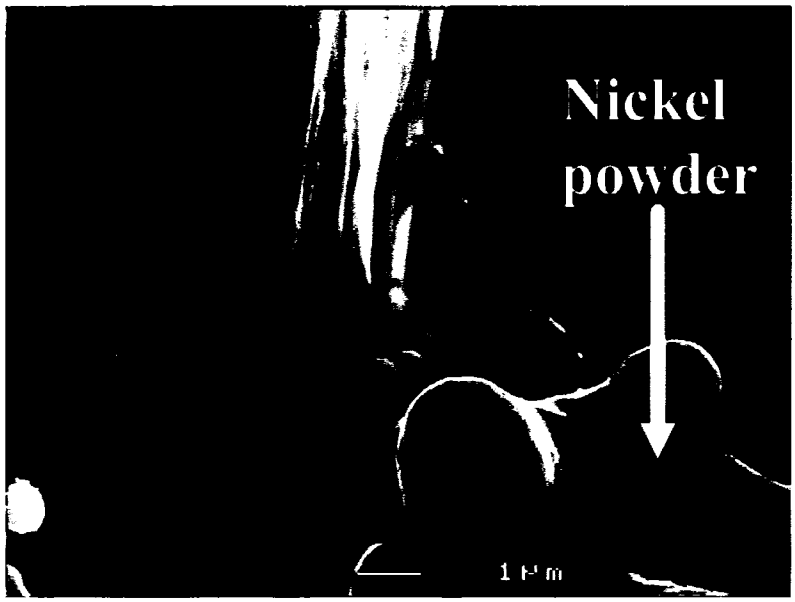

Figure 5-9: Sintering between Nickel Powder and Copper Mesh

5.2.5 Configuration E

Much like Configuration B, this structure included a fine pore nickel powder arrangement at the liquid/vapour interface in addition to a layer of nickel powder applied at the wall/wick interface. These two interfaces are displayed in Figure 5-10. Concerning the wall/wick interface, generally poor contact was observed, with noticeable gaps between the container and the wick, illustrated in Figure 5-11. These could potentially increase the contact resistance and trap vapour, increasing the radial temperature drop and reducing the effective thermal conductivity. However, like Configuration B, an increase in surface area and an acceptable level of sintering was observed. Refer to Figure 5-7 and Figure 5-8 for these similarities. Therefore, this configuration also displayed promising characteristics as a composite wick for heat pipes. Conversely, at higher heat fluxes, decreased performance was expected due to vapour entrapment at the wall/wick interface.

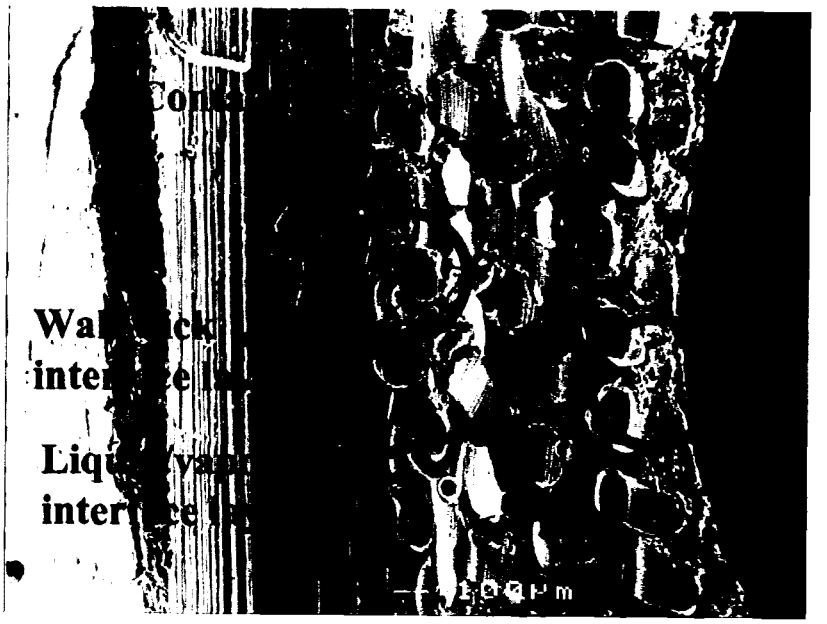

Figure 5-10: Configuration E

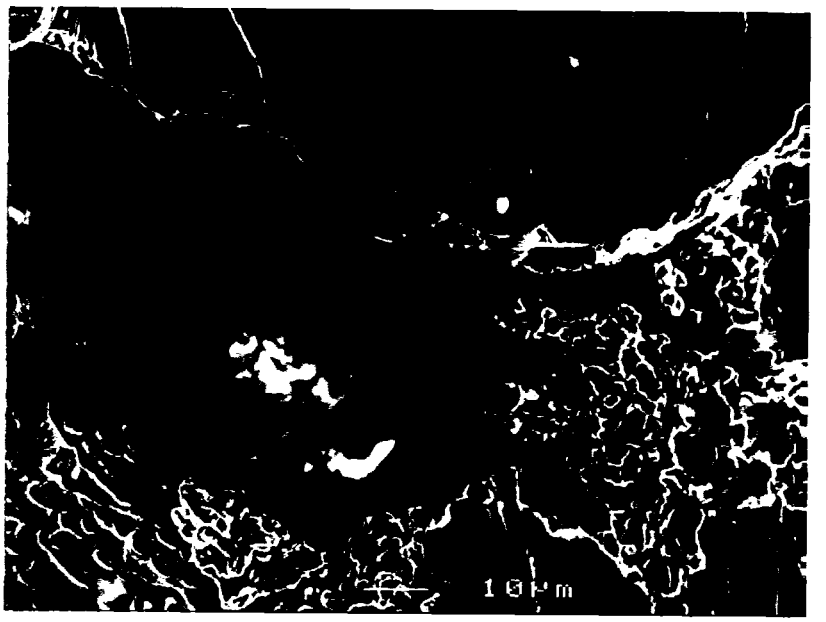

Figure 5-11: Wall/Wick Interface of Configuration E

5.2.6 Configuration I

A fine layer of copper powder was applied at the liquid/vapour interface in this configuration, shown in Figure 5-12. Referring to Figure 5-13, there was little evidence of a biporous structure, since the copper powder completely covered the larger pores of the copper mesh. This was expected to cause poor heat transfer performance, since any generated vapour would not be permitted an easy exit path to the vapour core. It was therefore concluded that the sifting application technique of Section 4.3.4 was not a completely successful composite wick fabrication method. Similar to Configuration K shown in Figure 5-6, very little evidence of sintering was detected. For these reasons, Configuration I was predicted to exhibit poor thermal performance.

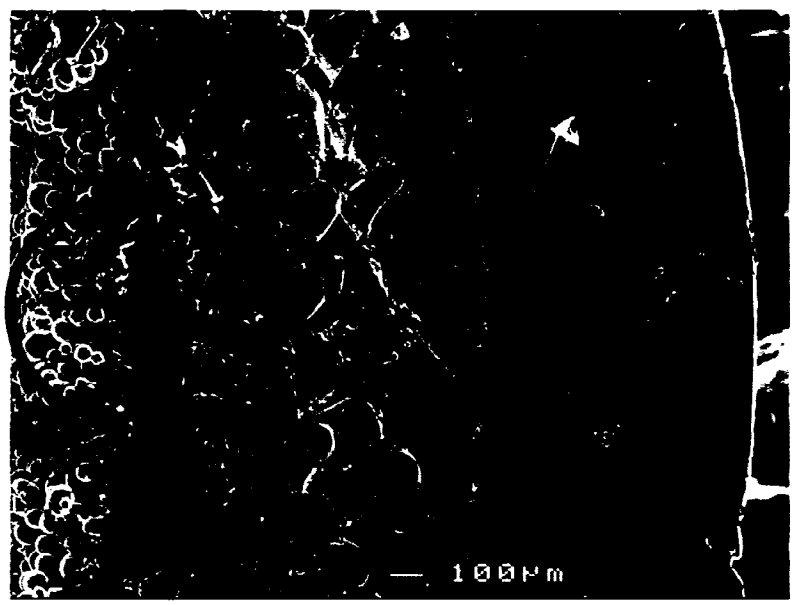

Figure 5-12: Configuration I

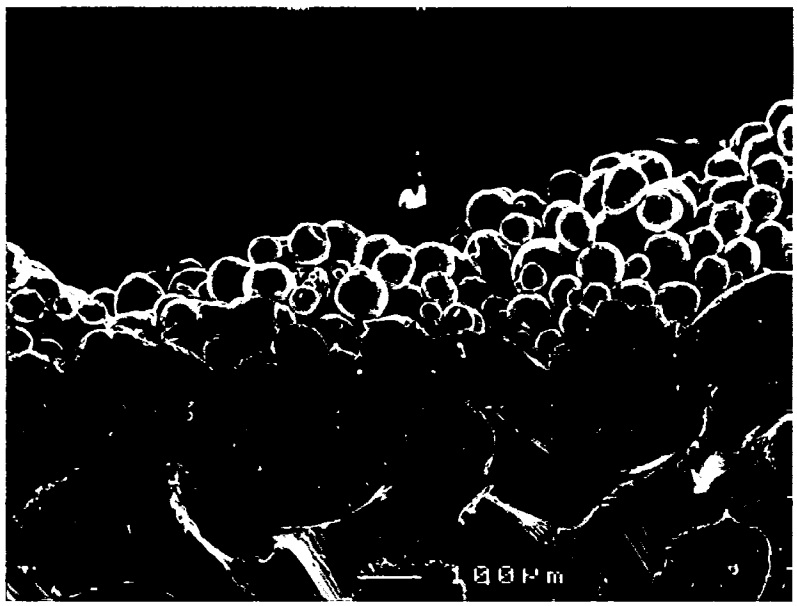

Figure 5-13: Liquid/Vapour Interface of Configuration I

5.2.7 Configuration J

Configuration J was similar to Configuration I in that the liquid/vapour interface was covered with copper powder to increase the evaporative surface area. The difference arose from the addition of another fine pore layer at the wall/wick interface to decrease contact resistance. See Figure 5-14 for a cross-sectional view of this wick structure.

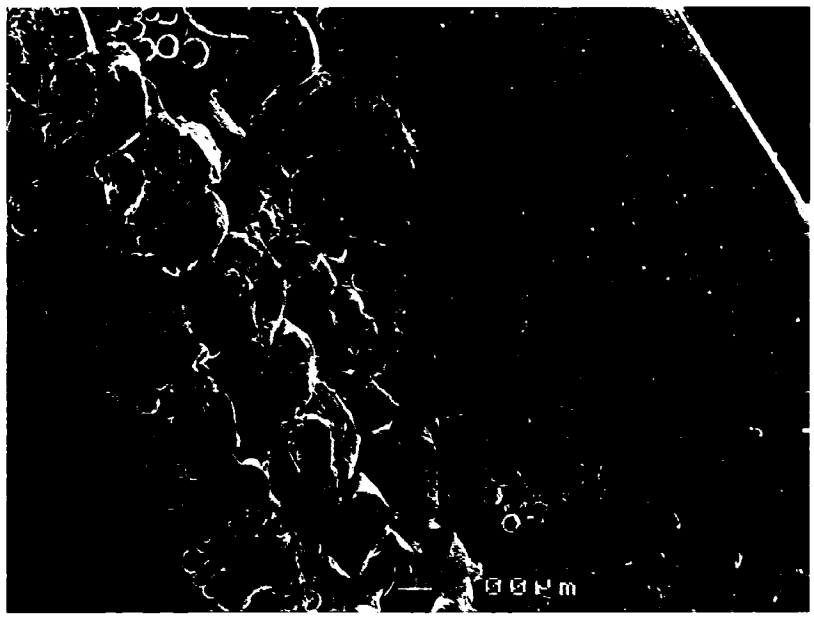

Figure 5-14: Configuration J

Like Configuration I, this structure experienced the same difficulties in powder coverage control and adequate sintering. Referring to Figure 5-15, the large pores at the wall/wick interface are completely covered by copper powder. Again, this indicated the sifting application technique could not produce the desired biporous microstructure. Another factor contributing to large pore blockage was associated with the selected powder size and mesh combination. The powder size was clearly too large for the 100-mesh copper screen, and a finer powder could have produced better results. Moreover, voids and disbondments were observed between the wall and the wick. Similar to Configuration E, shortcomings in performance could potentially be attributed to vapour entrapment in these voids. For these reasons, it was predicted that heat pipes with Configuration J would exhibit reduced heat transfer performance, particularly at higher heat fluxes.

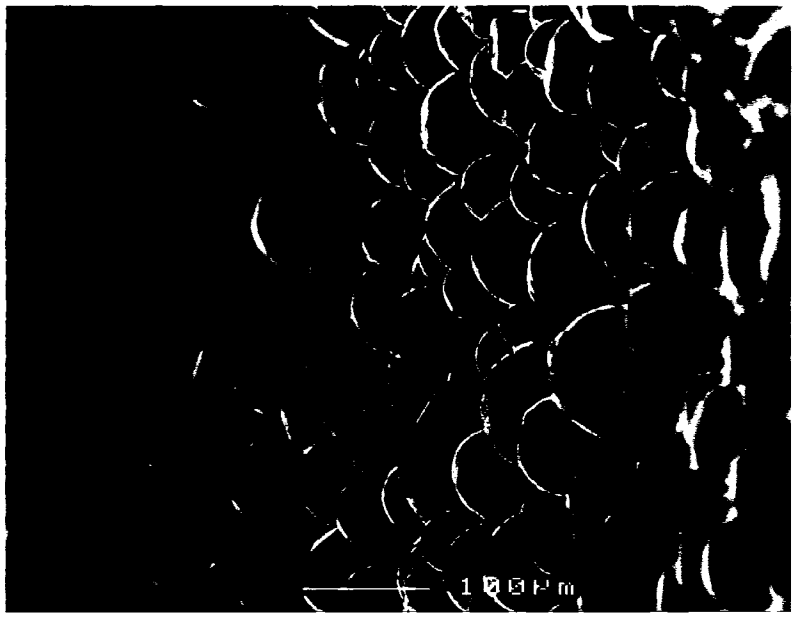

Figure 5-15: Wall/Wick Interface of Configuration J

5.2.8 Configuration L

A biporous structure throughout the wick thickness was the aim of this configuration, achieved through the spray application of nickel powder. Regrettably, since this configuration was selected in the later stages of this research, no additional samples were prepared in time for SEM analysis. Consequently, no preliminary results could be drawn prior to testing. However, sample morphology was expected to closely resemble Configuration B of Figure 5-7, only this structure would exist throughout the entire radial thickness of the wick. It was postulated that this would enable enhanced evaporation heat transfer throughout the full heat flux range, as well as offering superior performance during against gravity operation from increased capillary pressure.

5.3 Effective Thermal Conductivity and Maximum Heat Input Rate

The best indicator of thermal performance enhancement is expressed in terms of an effective thermal conductivity, as discussed in Section 2.6.1. Also of great importance is the maximum achievable heat input rate for a given orientation. A presentation of the heat transfer performance attained by each heat pipe configuration is discussed here. Firstly, heat pipes containing homogeneous wick configurations are presented. These include Configurations A (copper mesh), H (nickel powder) and K (copper powder). Then, composite configurations are graphically compared with homogeneous wick results to gauge whether performance increases have been achieved. For quick reference, heat transfer performance summaries are tabulated at the end of each subsection.

The measured heat pipe temperatures were plotted versus axial position for preliminary analysis of thermal performance. Nine thermocouples were fastened on each heat pipe at the axial locations shown in Figure 4-26 of Section 4.4.4. The zero axial reference position was taken to be the evaporator end cap. Maximum evaporator temperatures and axial temperature drops were also compared using these graphs to determine improvements in heat transfer at various power settings. However, because of the extensive amount of experimental data, only key results are presented here. Complete results for axial temperature profiles are available in Appendix F, as well as any additional effective thermal conductivity results not presented in the following sections.

One note about the line plots of Appendix F: the heater power input labels listed in plot legends were not exactly equal to those experienced during testing. However, since

variations between these were negligible, it was decided to standardize line plot labels for clarity. On the other hand, the effective thermal conductivity calculations of the following sections relied on the actual heater power input levels experienced during testing.

5.3.1 Configuration A

Generally, the conventional monoporous copper mesh-wick heat pipe seemed to perform reasonably well in comparison to the composite wick heat pipes, including during against gravity tests. In horizontal operation, no signs of the capillary limit could be distinguished up to approximately 140 W, detected by a sudden and continuous rise in the evaporator wall temperature.

Moreover, this configuration achieved some of the best gravity assisted results, most likely due to its relatively high liquid permeability. At heat inputs up to 220 W during gravity assisted testing, A7 did not seem to reach the capillary limit. For safety, both tests were terminated prior to dryout due to high evaporator temperatures. Figure 5-16 displays horizontal and gravity assisted effective thermal conductivities for A7. The highest effective thermal conductivities were achieved at the highest heat inputs, another indicator that dryout was not encountered.

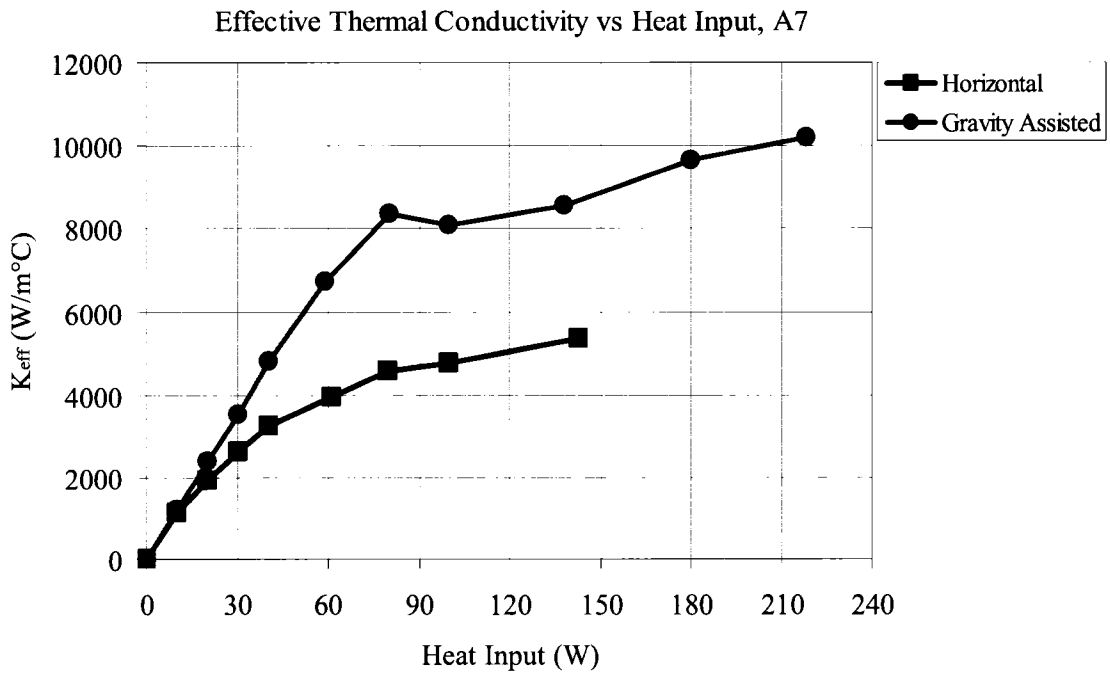

Figure 5-16: Horizontal and Gravity Assisted Effective Thermal Conductivities for A7

However, as the heat input was increased during against gravity operation, some evidence of impending dryout was observed, particularly at levels greater than 30 W. See Figure 5-17 for axial temperature distributions demonstrating this phenomenon. Progressively higher temperature differences between evaporator and adiabatic thermocouples were observed here, a universally recognized sign of wick dryout. As a result, this configuration could only function against gravity up to heat inputs of 50 W before evaporator temperatures became excessively high. This result was most probably due to the relatively low capillary pumping ability of the 100-mesh copper screen. The addition of a secondary fine pore structure was expected to improve this outcome significantly. See Figure 5-18 for against gravity effective thermal conductivity values of A7. Most noticeable is the decrease in effective thermal conductivity after peaking at

approximately 30 W, attributable to the increasing axial temperature drop with heat input, shown in Figure 5-17. All axial temperature profiles for A7 are available in Appendix F.

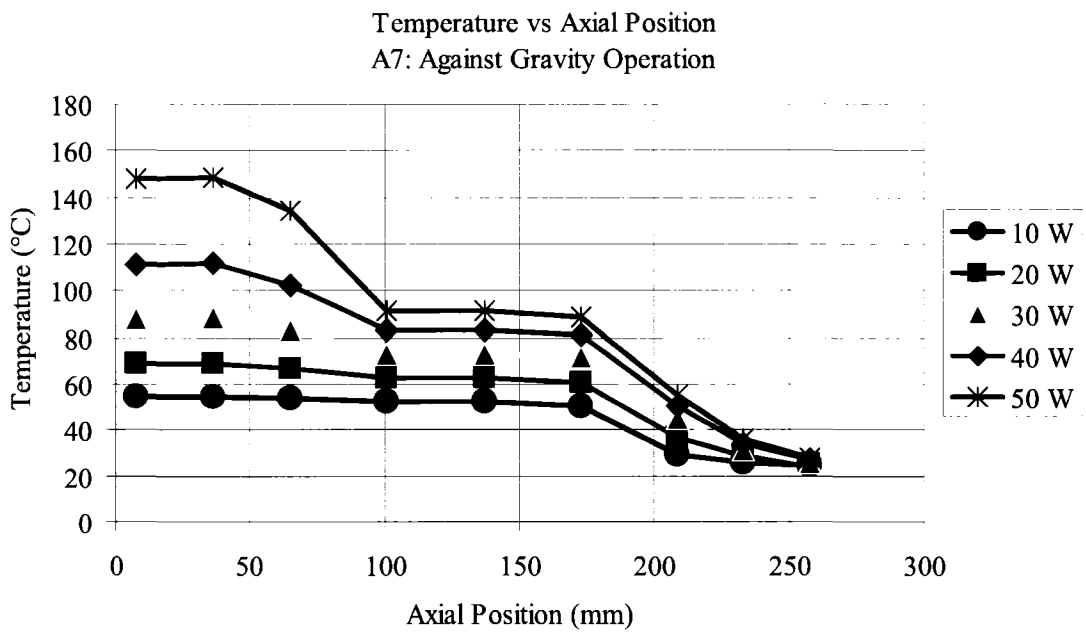

Figure 5-17: Axial Temperature Distribution of A7, Against Gravity Operation

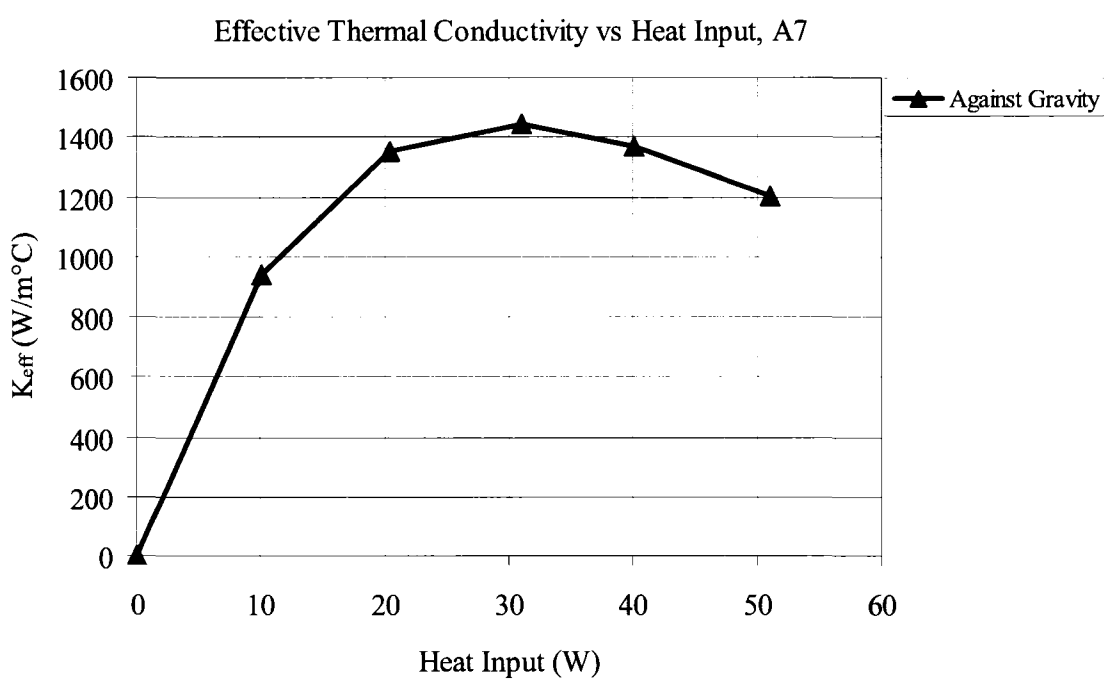

Figure 5-18: Against Gravity Effective Thermal Conductivity Results for A7

Heat pipe	A7
Maximum heat inputs tested and corresponding maximum evaporator temperatures	Horizontal: 142.9 W at 152.5°C Gravity assisted: 218.4 W at 147.7°C Against gravity: 51 W at 148.3°C
Maximum effective thermal conductivities	Horizontal: 5351 W/m°C at 142.9 W Gravity assisted: 10219 W/m°C at 218.4 W Against gravity: 1443 W/m°C at 31 W

Table 5-2: Thermal Performance Summary for A7

5.3.2 Configuration H

Configuration H was comprised of a homogeneous, sintered nickel powder wick with pore diameters on the order of 10 μm. It was predicted that this wick structure would produce enhanced against gravity thermal performance.

In all instances, this configuration did not perform well when compared to the results of Configuration A in Figure 5-16. Figure 5-19 confirms this, displaying unsatisfactory effective thermal conductivities during horizontal and gravity assisted testing. In particular, against gravity performance was surprisingly poor when compared to the results of heat pipe A7 in Figure 5-18. Configuration H only reached an effective thermal conductivity of 572 W/m°C at 30 W, shown in Figure 5-20. In contrast, the much coarser pore wick of Configuration A achieved an effective thermal conductivity of 1443 W/m°C at 30 W, over twice the level of Configuration H. It was expected that the fine pore nickel powder structure would outperform all other configurations in against gravity operation,

yet it exhibited the worst performance of all the tested heat pipes. Referring to Figure 5-4 on page 132, sintering trials produced a highly porous microstructure with high surface area density and pore diameters at least an order of magnitude smaller than the copper mesh. This should have greatly increased the capillary pumping ability of the heat pipe.

However, Figure 5-20 displays poor against gravity results, with heat pipe A7 easily outperforming this configuration. This should not have occurred, since Configuration H possessed a higher capillary pumping ability due to a much finer pore structure. The most likely cause of this inadequacy could have been related to an overestimation of the wick porosity and fluid charge. For heat pipe H3, a porosity of 80% was estimated using the procedure outlined in Section 4.3.7. This led to a fluid charge of roughly 7.5 g, or about 1.8 times higher than the average liquid fill amount for all other configurations.

A fluid overcharge this excessive could have caused blockage at the condenser end, filling the vapour passage with liquid. Axial heat transfer may have been hampered by the presence of a high thermal resistance liquid slug at the condenser end, instead of a negligibly low vapour thermal resistance. As a result, the effective thermal conductivity would suffer a significant degradation in performance. Kempers et al. also concluded that a substantial fluid overcharge would increase the heat pipe thermal resistance significantly [82]. In their study, the heat pipe with the highest fluid charging amount also possessed the highest thermal resistance. Table 5-3 summarizes the thermal performance results for H3.

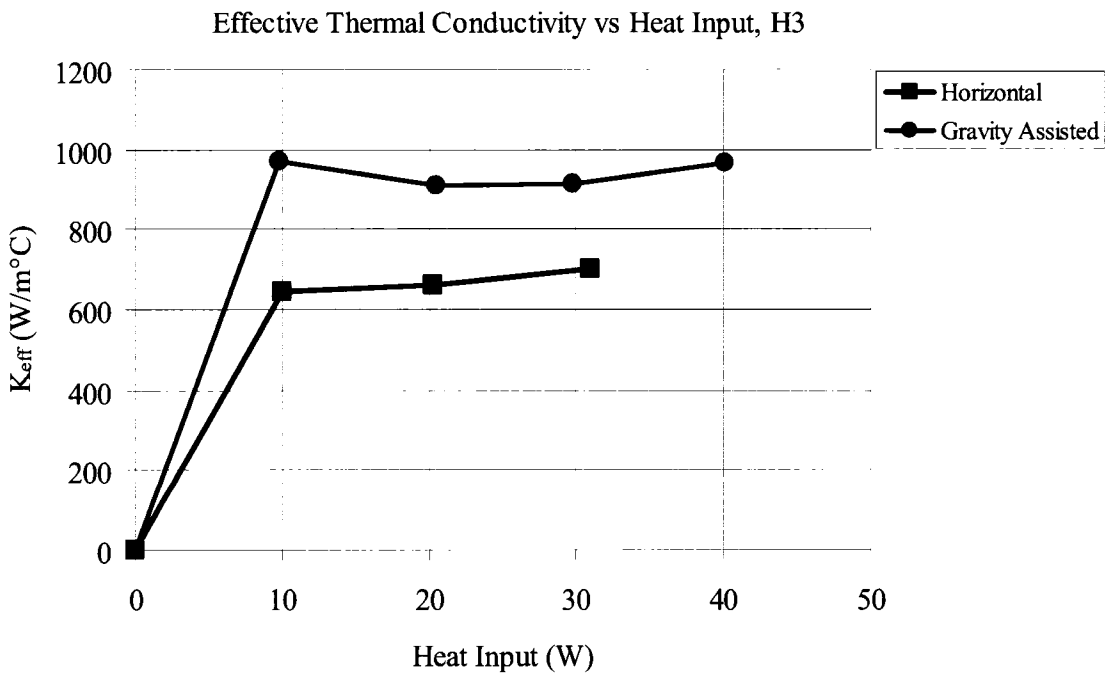

Figure 5-19: Horizontal and Gravity Assisted Effective Thermal Conductivities for H3

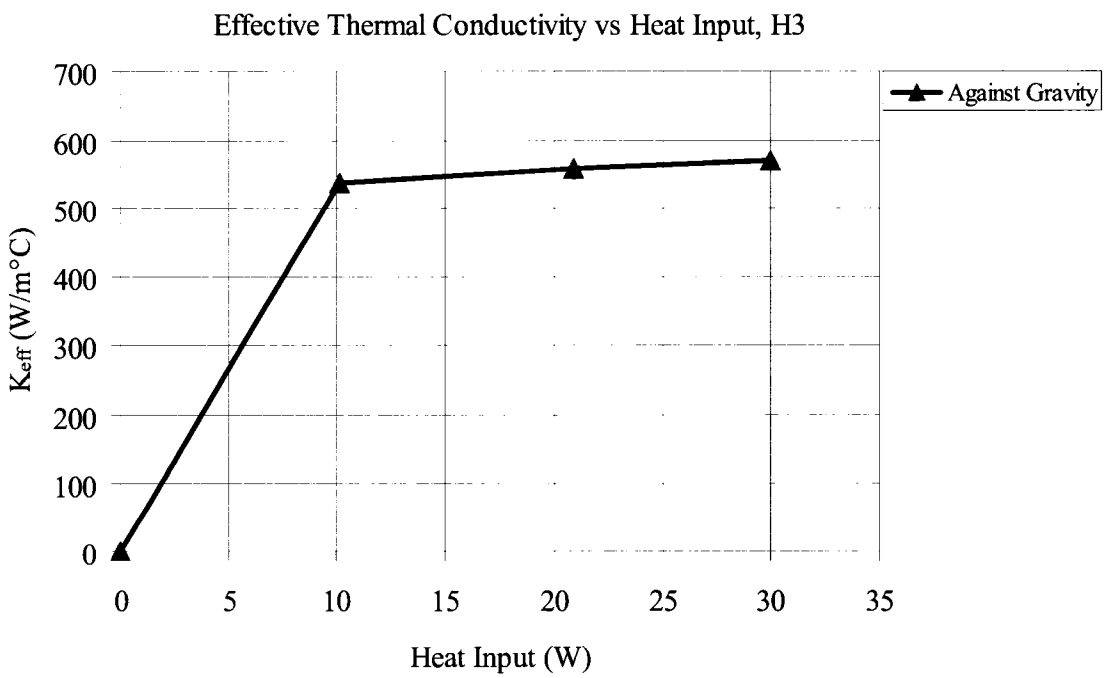

Figure 5-20: Against Gravity Effective Thermal Conductivity Results for H3

Heat pipe	H3
Maximum heat inputs tested and corresponding maximum evaporator temperatures	Horizontal: 30.9 W at 143°C Gravity assisted: 40.1 W at 139.4°C Against gravity: 30 W at 164.1°C
Maximum effective thermal conductivities	Horizontal: 700 W/m°C at 30.9 W Gravity assisted: 971 W/m°C at 9.8 W Against gravity: 572 W/m°C at 30 W

Table 5-3: Thermal Performance Summary for H3

5.3.3 Configuration K

Sintered copper powder formed the homogeneous wick of this configuration. Two similar heat pipes, K1 and K2, were fabricated and tested to assess manufacturing repeatability.

In horizontal operation, Configuration K did not perform as well as Configuration A, the best effective thermal conductivity being achieved by K1 at approximately 2100 W/m°C. The maximum horizontal heat input rate recorded was only 55 W. Refer to Figure 5-21 for horizontal and gravity assisted testing results. From the SEM analysis of Section 5.2.2, low porosity could have caused this decreased performance. The spherical copper powder seemed to form an undesirably dense microstructure, packing itself too closely together. Estimations from Section 4.3.1 confirmed these predictions of poor performance, with porosity calculated at approximately 44%. In comparison, copper mesh porosity was estimated to be over 62%, and the resulting horizontal performance for A7 was much higher than that exhibited by Configuration K.

Lower porosity would lead to a lower liquid permeability, a higher liquid pressure drop [10], and a decrease in thermal performance. Again, the problems associated with homogeneous wicks become evident here: although Configuration K possessed fine pores for high capillary pressure, fluid transport was most likely reduced due to low liquid permeability.

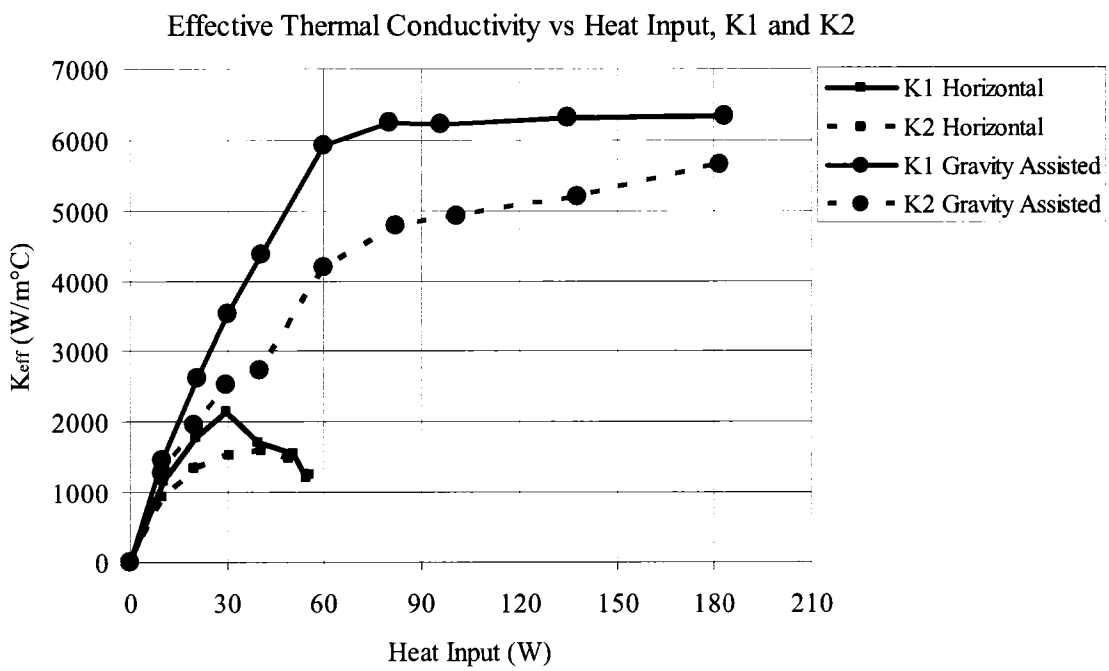

Figure 5-21: Horizontal and Gravity Assisted Results for Configuration K

Gravity assisted performance for Configuration K was also quite low, with K1 attaining a best effective thermal conductivity of 6343 W/m°C at 183 W, shown above in Figure 5-21. With the comparatively high permeability wick of A7 reaching over 10000 W/m°C, the difference can again most likely be attributed to the low porosity of Configuration K. In fact, the complete absence of a wick would most probably produce the best gravity

assisted results, since this represents the scenario with the least resistance to liquid flow [1], [10], [16].

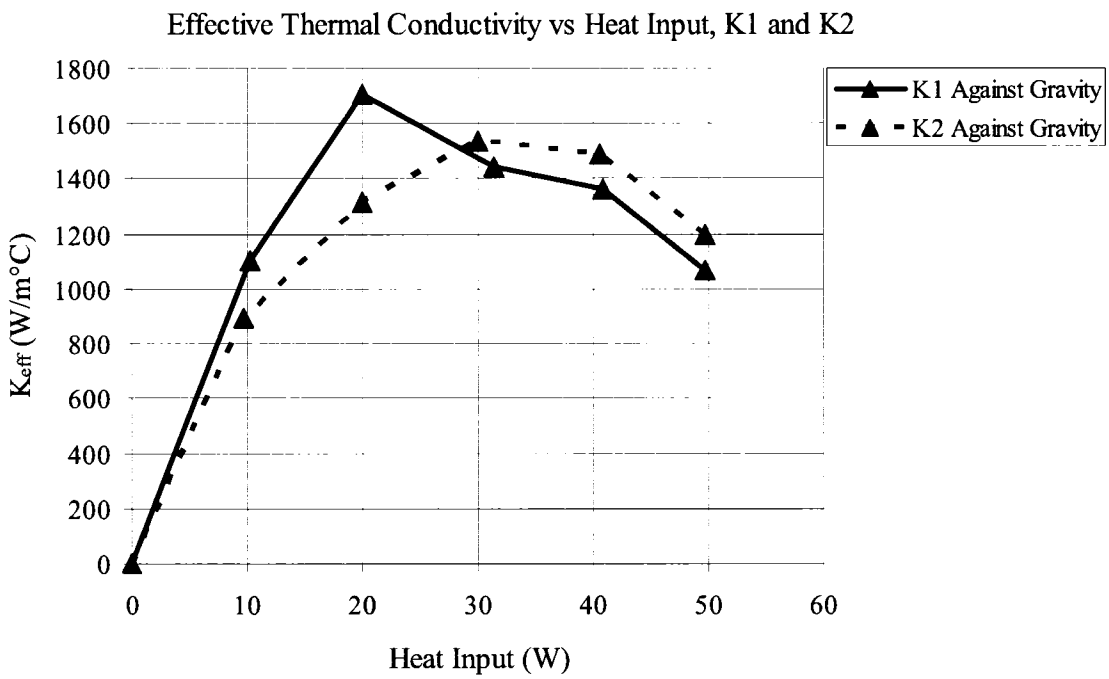

Figure 5-22: Against Gravity Effective Thermal Conductivity Results for K1 and K2

Against gravity performance was fair, however much higher effective thermal conductivities were expected from this configuration. The best against gravity effective thermal conductivity was 1700 W/m°C, recorded by K1 at 30 W. The maximum heat input rate achieved by both of these heat pipes was approximately equivalent at 50 W, perhaps because of the unsatisfactory compromise between high capillary pressure generation and low liquid permeability. Referring to the capillary limit expression of Equation (2-13), the net capillary pressure available for liquid transport would be reduced significantly by a low permeability wick. As a result, the capillary limit may

have been approached much sooner than expected. Another possible cause of the inadequate against gravity performance could be due to the greater wick thickness of this configuration. Because of the manufacturing process outlined in Section 4.3.4, wick thicknesses for K1 and K2 were approximately twice that of A7. This could have greatly increased the heat pipe's axial temperature drop. Since the liquid-saturated wick represents the largest resistance to heat transfer in the equivalent thermal resistance network shown in Figure 2-15, a much lower effective thermal conductivity would therefore be expected. In comparison to A7, only modest improvements in effective thermal conductivity were realized, and no significant gains were achieved in the maximum heat input rate.

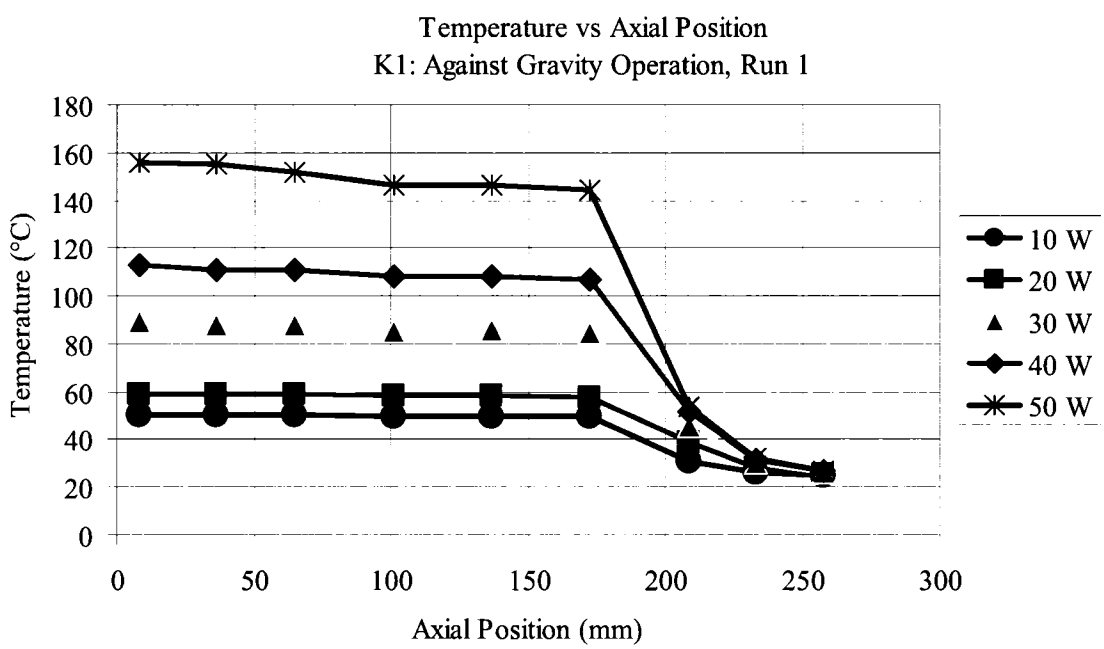

Figure 5-23: Axial Temperature Distribution for K1, Against Gravity

One unique characteristic of this configuration was the nearly isothermal behaviour along the first two thirds of the heat pipe length, displayed in Figure 5-23. The evaporator and adiabatic sections recorded very similar temperatures, with a maximum temperature variation of 11.5°C at 50 W. Here, Configuration K performed very well. Unfortunately, temperatures dropped dramatically along the condenser section, leading to the relatively low effective thermal conductivity values. One possible reason for this peculiar behaviour could be another instance of fluid overcharging, similar to the mechanism of performance degradation suggested for Configuration H. A liquid slug could have essentially inactivated a portion of the condenser end, greatly decreasing thermal performance [10]. Peterson also attributes these axial temperature characteristics to the presence of non-condensable gases [10]. This problem would also have a similar effect on performance to that of a liquid slug. That is, during operation, these gases would be swept towards the condenser end where they would impede heat flow and cause a distinct decrease in the axial temperature distribution.

Examining the effective thermal conductivity plots on pages 151 to 152, some conclusions can be made regarding manufacturing repeatability. Overall, K1 performed slightly better than K2, except in the against gravity orientation during higher heat inputs. Nevertheless, they still exhibit similar trends in performance. During fabrication, geometric wick measurements, porosity estimates and the required fluid charging amounts agreed well with each other. However, during final charging and sealing, K2 was slightly overfilled by approximately 8% in comparison to K1. This could have led to the discrepancy in effective thermal conductivity seen in the graphs. One observation in

particular should be discussed: Figure 5-22 suggests that K2's slight overfill actually aided heat transfer performance at higher heat inputs in the against gravity orientation, since it exhibited a higher effective thermal conductivity after approximately 30 W. Perhaps this was a result of delayed dryout due to a higher fluid charge. In other words, while dryout was initiated first in K1, K2 experienced dryout initiation at slightly higher heat inputs, and thus marginally better performance was produced in this region of the graph. Thermal performance results are listed in Table 5-4.

Heat pipe	K1	K2
Maximum heat inputs tested and corresponding maximum evaporator temperatures	Horizontal: 54.4 W at 159.3°C Gravity assisted: 183.2 W at 153.3°C Against gravity: 49.7 W at 155.9°C	Horizontal: 55.2 W at 147.9°C Gravity assisted: 181.6 W at 156.3°C Against gravity: 49.7 W at 138°C
Maximum effective thermal conductivities	Horizontal: 2144 W/m°C at 29.6 W Gravity assisted: 6343 W/m°C at 183.2 W Against gravity: 1704 W/m°C at 20 W	Horizontal: 1607 W/m°C at 40.3 W Gravity assisted: 5663 W/m°C at 181.6 W Against gravity: 1540 W/m°C at 30.1 W

Table 5-4: Thermal Performance Summary for K1 and K2

5.3.4 Configuration B

The addition of a sintered layer of nickel powder at the liquid/vapour interface was shown to enhance horizontal heat transfer performance at all heat inputs. Compared to the conventional copper mesh configuration of A7, heat pipe B8 displayed a clear

performance advantage, demonstrated in Figure 5-24. Heat pipe B8 reached a maximum effective thermal conductivity of 6374 W/m°C at 40 W. Although a slight decrease in performance was observed after 40 W, stable operation continued at levels around 5850 W/m°C until excessive evaporator temperatures required test cessation.

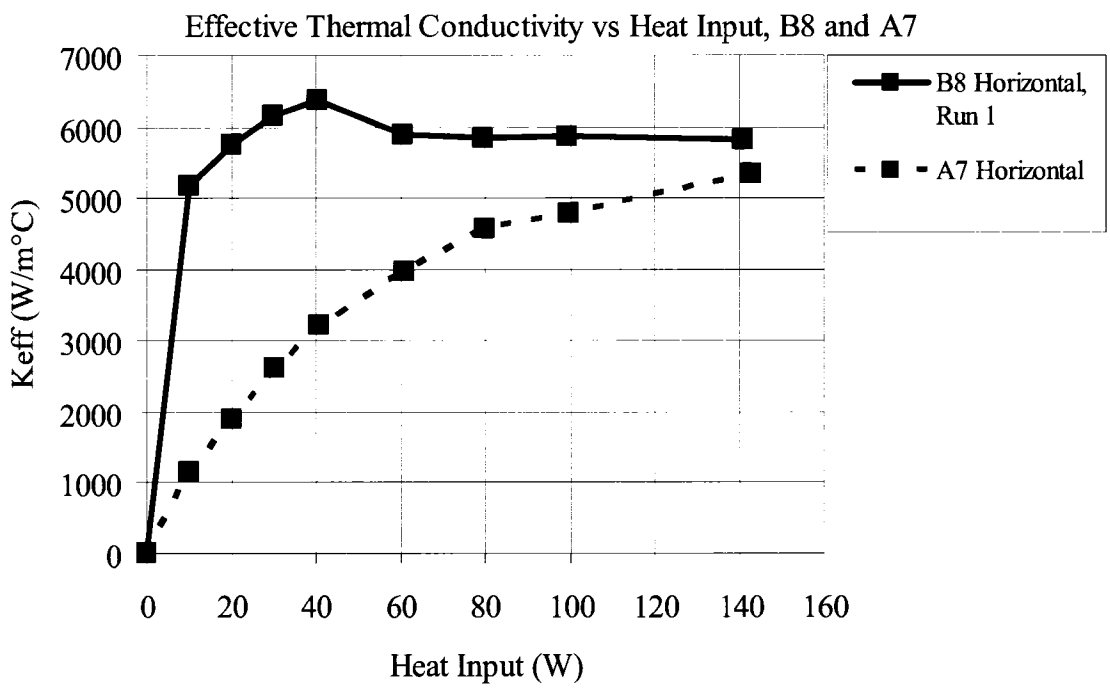

Figure 5-24: Comparison of Horizontal Thermal Performance between B8 and A7

This increased performance could have occurred due to enhanced evaporation heat transfer from a higher density of evaporating menisci at the liquid/vapour interface, as discussed previously in Section 3.3.4. Much like the findings of Hanlon and Ma [61], these results seemed to provide evidence of increased thin film evaporation due to a decrease in pore size and a higher density of evaporating menisci at the liquid/vapour

interface. Recalling Figure 5-8 on page 136, an increase in surface area, and hence a much higher number of evaporating menisci, was confirmed to exist in Configuration B.

When comparing gravity assisted results, Configuration B noticeably outperformed Configuration A at heat inputs below 180 W. Above this, the performance advantage was essentially lost, confirmed in Figure 5-25. A maximum effective thermal conductivity of approximately 13300 W/m°C was reached at 60 W, virtually doubling the performance of Configuration A at the same heat input. Again, the most likely cause of this substantial performance gain was likely attributed towards enhanced evaporation heat transfer from the higher density of fine pores at the liquid/vapour interface. Additionally, the presence of the large pores in the adjacent wick layers may have provided a low resistance liquid flow path, approaching the permeability of Configuration A. It seemed possible that the slight decrease in liquid permeability due to the presence of the biporous layer could have caused a somewhat lower maximum heat input rate (202 W) when compared to the results for A7 (218 W).

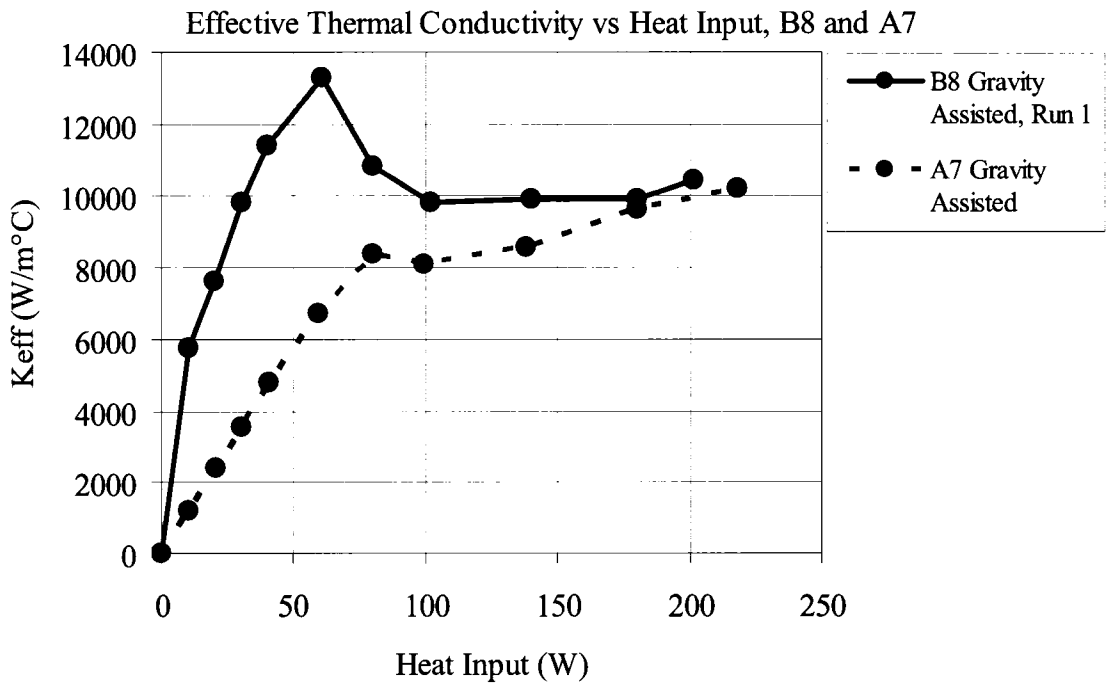

Figure 5-25: Comparison of Gravity Assisted Thermal Performance between B8 and A7

Another important observation can be made here regarding both the gravity assisted and horizontal operation of B8: at higher heat inputs, the performance increase over A7 diminished. It is believed this effect arose from liquid recession into the wick and subsequent dryout of the biporous layer, with the formation of evaporating menisci on the monoporous copper mesh structure underneath. With solely large pores comprising the inner wick layers, one would expect a decrease in the number of evaporating menisci, and hence, a decrease in the evaporative heat transfer rate. This is the effect observed in both Figure 5-24 and Figure 5-25.

Wih the diminishing trend in effective thermal conductivity at higher heat inputs, it is believed the large pores of the inner wick layers allowed continued performance at levels equivalent to those of A7. Additionally, the biporous layer seemed to allow vapour egress from the wick, such that a catastrophic decrease in performance was avoided. From these results, the conceptualization of a continuous biporous wick was postulated to offer better performance throughout the entire spectrum of heat inputs. Thus, the design and manufacture of Configuration L was initiated and realized, with results presented in Section 5.3.7.

In addition to promising horizontal and gravity assisted test results, impressive gains in performance over homogeneous configurations were revealed during against gravity testing. As illustrated in Figure 5-26, B8 clearly possessed an advantage in effective thermal conductivity over the poorly performing H3. With its fine pore sintered structure, H3 was expected to produce the best against gravity results, yet due to potential fluid overcharging issues discussed in Section 5.3.2, it did not exhibit the anticipated performance. In contrast, B8 reached a maximum effective thermal conductivity value of 3124 W/m°C at 10 W, over three times the performance of A7 and approximately six times that of H3. Like the previous observations regarding horizontal and gravity assisted tests, against gravity performance improvements tended to diminish with increasing heat input. The most likely cause was the previously mentioned liquid recession into the monoporous portion of the wick.

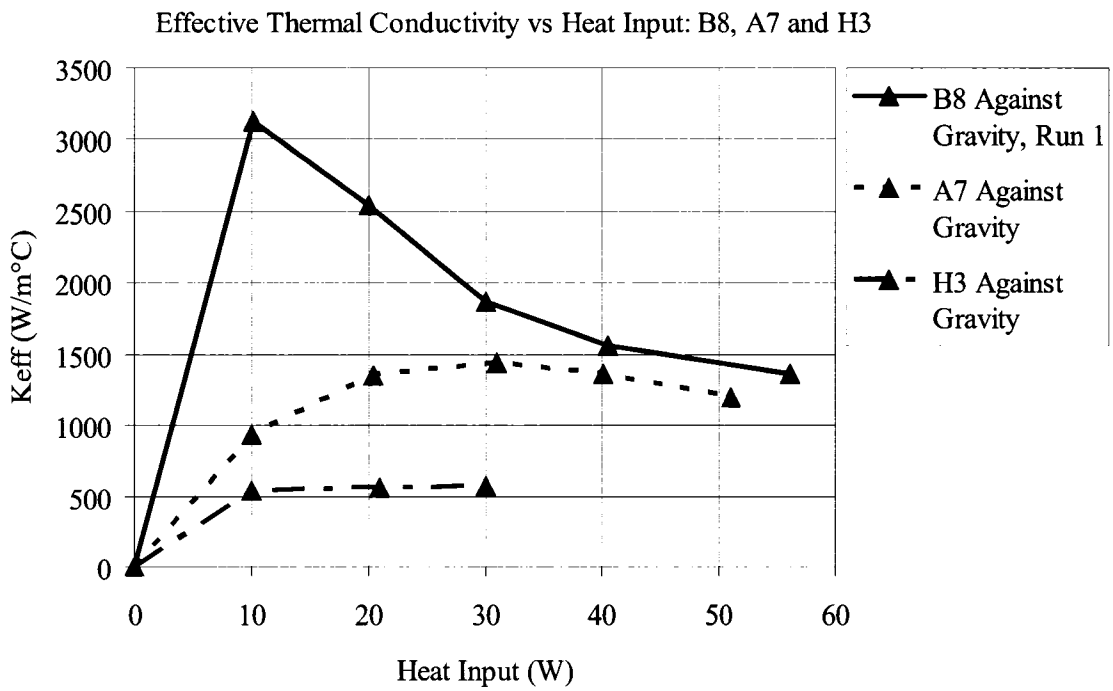

Figure 5-26: Against Gravity Thermal Performance Comparison between B8, A7 and H3

A maximum heat input of 56 W was achieved before evaporator temperatures became excessive. This was 5 W higher than A7 and 26 W higher than H3. Perhaps the fine pore layer at the liquid/vapour interface aided in the extension of the capillary limit, evidenced by the marginal improvement in the maximum heat input rate over A7. These results also encouraged an investigation into the effects of an increase in the number of composite wick layers on the maximum heat input rate. In particular, it was postulated that Configuration E would achieve even higher heat input rates due to the inclusion of two composite pore layers, one at the liquid/vapour interface and the other at the wall/wick interface. Moreover, because all wick layers of Configuration L possessed fine pores, it was assumed it would attain the best overall performance in the against gravity

orientation. The hypothesis of capillary limit enhancement from fine pore layer additions is further explored in Sections 5.3.5 and 5.3.7.

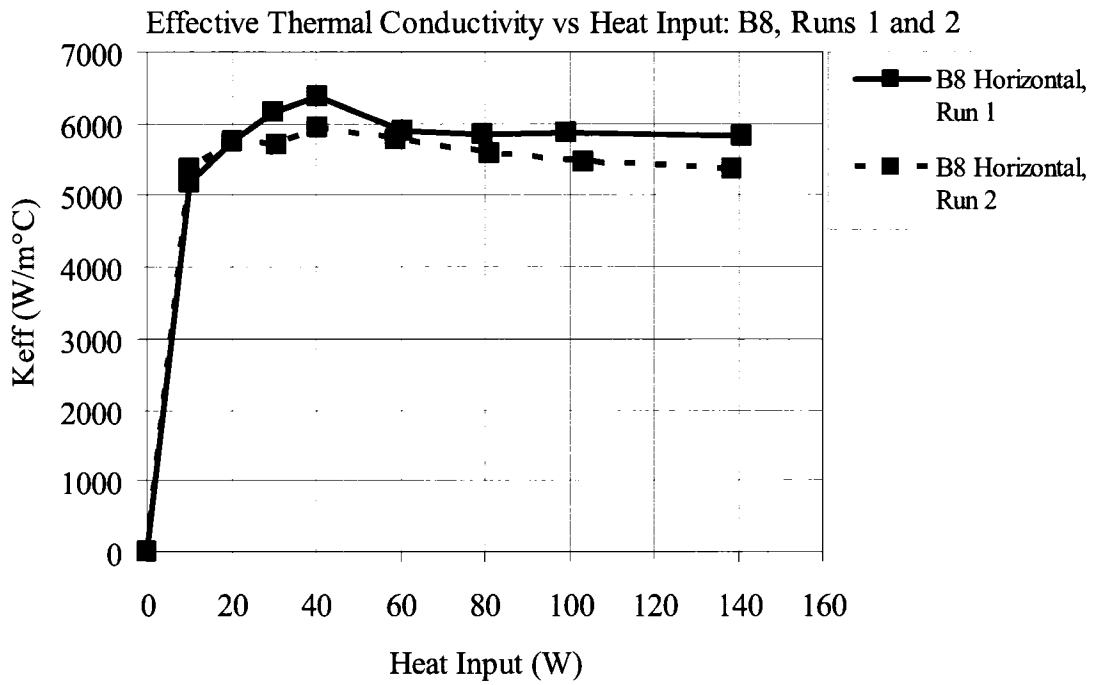

Figure 5-27: Testing Repeatability for B8, Horizontal Orientation

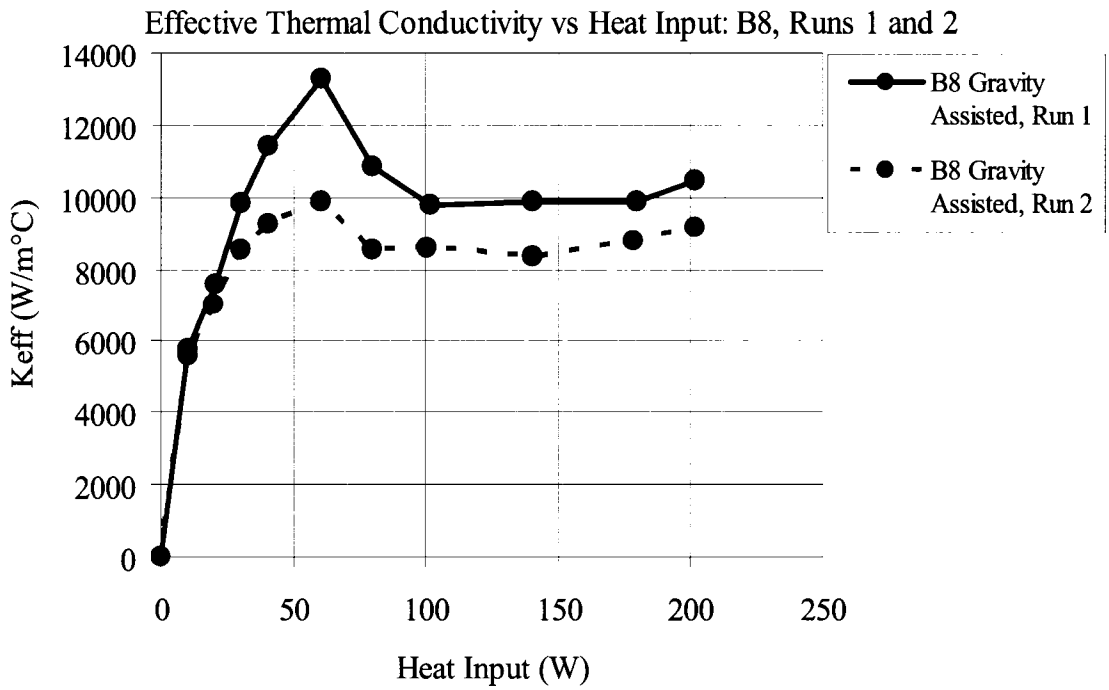

Figure 5-28: Testing Repeatability for B8, Gravity Assisted Orientation

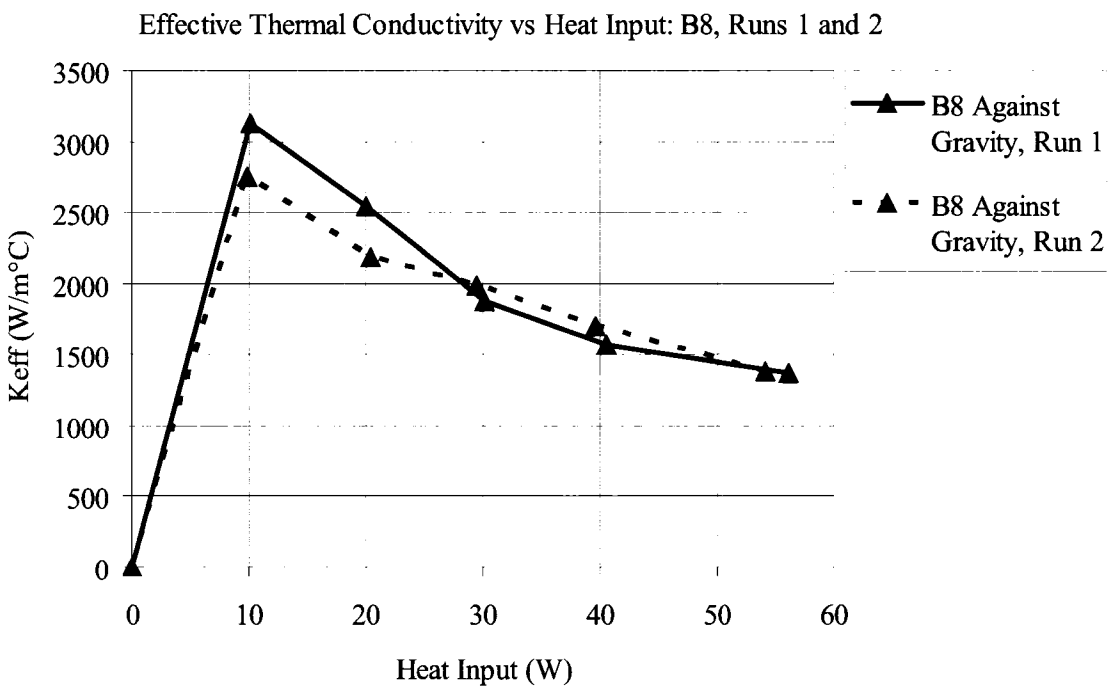

Figure 5-29: Testing Repeatability for B8, Against Gravity Orientation

Testing repeatability was also explored with B8. For this purpose, heat pipe B8 was completely removed, reinserted and tested using the procedures outlined in Sections 4.5.1 to 4.5.3. Horizontal testing repeatability is presented in Figure 5-27, while gravity assisted results are found in Figure 5-28. Against gravity results are given in Figure 5-29. Overall, retesting seemed to yield sufficient repeatability in heat pipe behaviour, allowing some measure of confidence in the results obtained.

From the above graphs of Runs 1 and 2, a maximum difference in effective thermal conductivity of approximately 8% was observed at 140 W during horizontal tests. During gravity assisted testing, variation in results reached a maximum of approximately 30% at 60 W. For against gravity operation, values differed by a maximum of 15% at 20 W. Interestingly, the two curves of Figure 5-28 display the same behaviour, with some amount of offset. This suggests the possibility of inadequacies in thermocouple mounting. Perhaps the taping procedure presented in 4.5.1 led to poor thermocouple/heat pipe contact. Another possibility is that the thermocouples measuring the axial temperature drop used in the effective thermal conductivity calculations were not properly positioned. One other peculiarity was noticed in reference to test repeatability: the first runs performed for B8 all exhibited higher performance than the second runs. The second round of tests took place from 8 to 20 days after the first. It seemed most likely that some performance degradation was detected, possibly due to the formation of non-condensable gases during the time period between testing. Perhaps the nickel-copper wick combination created a galvanic cell, with hydrogen gas generation as a product of this reaction. However, without further analysis, this speculation cannot be confirmed.

Additional rounds of testing could offer more insight into this potential problem. Summarized results for B8 are given in Table 5-5.

Heat pipe	B8 Run 1	B8 Run 2
Maximum heat inputs tested and corresponding maximum evaporator temperatures	Horizontal: 141 W at 146.3°C Gravity assisted: 201.6 W at 150.6°C Against gravity: 56.1 W at 145.3°C	Horizontal: 138.5 W at 146.1°C Gravity assisted: 201.5 W at 149.6°C Against gravity: 54.1 W at 144.2°C
Maximum effective thermal conductivities	Horizontal: 6375 W/m°C at 40.4 W Gravity assisted: 13272 W/m°C at 60.7 W Against gravity: 3124 W/m°C at 10.1 W	Horizontal: 5955 W/m°C at 40.5 W Gravity assisted: 9902 W/m°C at 60.6 W Against gravity: 2758 W/m°C at 9.9 W

Table 5-5: Thermal Performance Summary for Runs 1 and 2 of B8

5.3.5 Configuration E

A biporous, composite wick layer at the liquid/vapour interface was added to this configuration for the primary purpose of evaporation heat transfer enhancement. An additional layer at the wall/wick interface was also coated with nickel powder with the goal of decreasing the contact resistance. However, upon observation of results from B8, it was also believed this layer could potentially boost the capillary limit by providing increased liquid transport, especially against gravity.

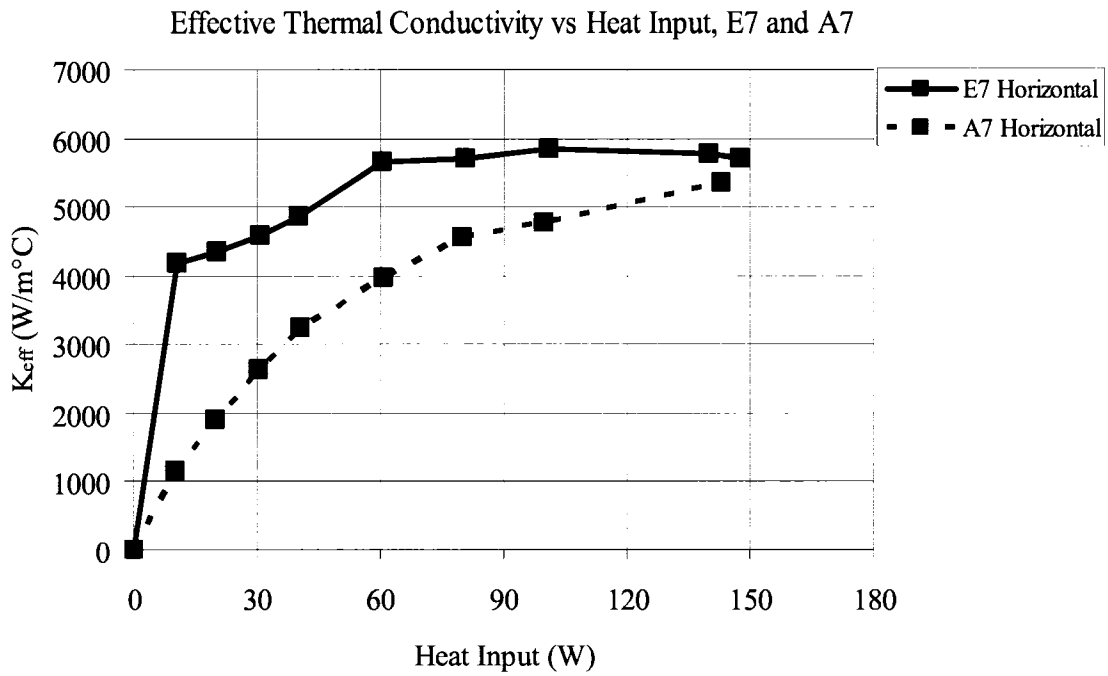

Figure 5-30: Comparison of Horizontal Thermal Performance between E7 and A7

Referring to Figure 5-30, the horizontal effective thermal conductivity of Configuration E showed considerable improvements over the conventional mesh wick design of A7 up to approximately 60 W. After this, the performance advantage tended to diminish, much like the effect observed in Configuration B. At 101 W, a maximum effective thermal conductivity of 5839 W/m°C was reached. The highest horizontal heat input rate achieved was approximately 148 W, 5 W higher than Configuration A and 7 W more than Configuration B.

The highest increase in performance occurred at a heat input of 10 W, where E7 produced an effective thermal conductivity over 3.5 times higher than that of A7. This could be evidence of increased evaporation heat transfer from the fine pore layer at the

liquid/vapour interface. The flattening of this curve could have resulted from liquid recession into the homogeneous wick layers underneath the composite layer. However, considering again the results from Configuration B in Figure 5-24, it is noted that E7 did not perform as well as B8 at lower heat inputs, suggesting that perhaps the inclusion of the fine porous layer at the wall/wick interface could have actually hindered horizontal performance somewhat. Another explanation for this comparatively lower performance is offered by the scanning electron microscopy results of Section 5.2.5. In Figure 5-11, gaps are shown to exist between the wall and the wick. These would certainly decrease performance by promoting vapour entrapment, thus increasing the contact resistance.

In Section 2.3 , the mechanisms of the boiling limit were presented. By decreasing the pore size in Equation (2-17), the critical superheat for boiling would also be reduced, and hence, the boiling limit calculated by Equation (2-19) would decrease. Yet there is no evidence of severe performance degradation, suggesting that even if Configuration E promoted bubble generation, at least some vapour was allowed to escape through the larger pores of the biporous structure.

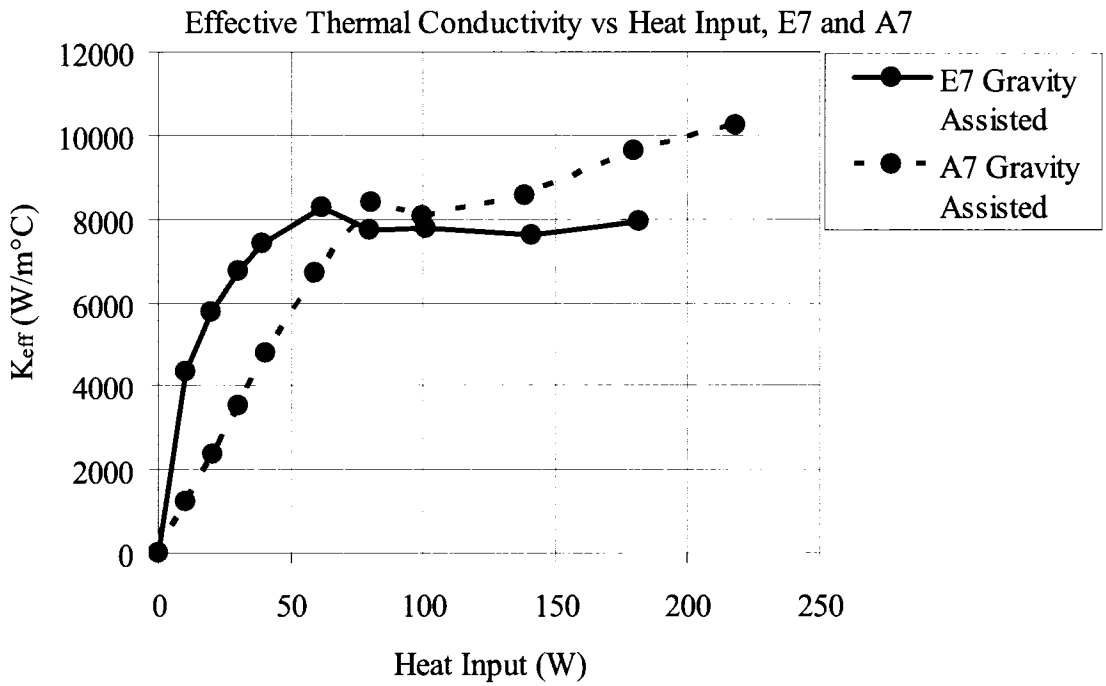

Figure 5-31: Comparison of Gravity Assisted Performance between E7 and A7

Comparing the gravity assisted performance in Figure 5-31, E7 only outperformed A7 at heat inputs below 80 W. Above 80 W, Configuration A reached higher effective thermal conductivities and a greater maximum heat input rate. The higher performance at lower heat inputs was again believed to be attributable to enhanced evaporation heat transfer from the fine pore composite wick layer. In comparison to B8, E7 did not perform as well in this orientation, with a best effective thermal conductivity of 8292 W/m°C at 62 W. This result was almost 5000 W/m°C lower than that achieved by B8 at 60 W. Perhaps the lower permeability wick of Configuration E or the aforementioned suggestions regarding the boiling limit and vapour entrapment contributed to the comparatively lower effective thermal conductivities. However with only the present data, the exact mechanism remains

unclear, and more experimentation is necessary to clarify the cause of this difference in performance.

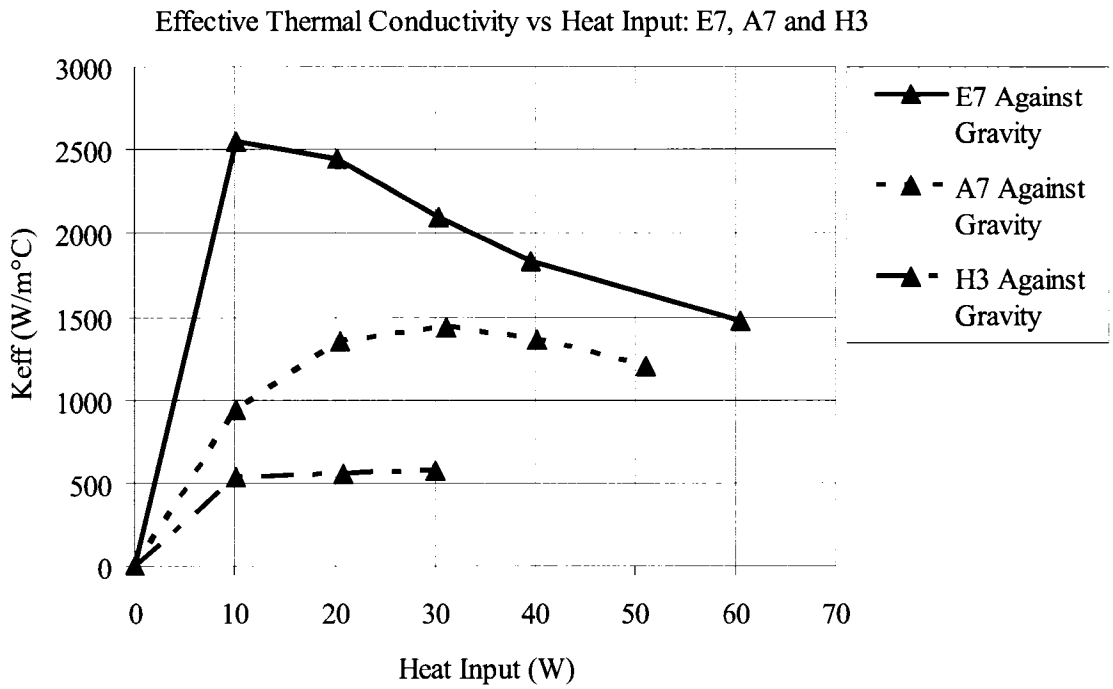

Figure 5-32: Against Gravity Performance Comparison between E7, A7 and H3

Configuration E performed very well in against gravity tests, clearly offering an advantage over the homogeneous wick heat pipes at all heat inputs. The best effective thermal conductivity was 2550 W/m°C, reached at 10 W. Additionally, it seemed that increasing the number of composite wick layers boosted the capillary limit, manifesting itself as an increase in the maximum heat input rate. Heat pipe E7 achieved an against gravity heat input rate of approximately 61 W, 5 W higher than B8 and 10 W higher than A7. This configuration had 2 composite wick layers, and it was believed that their inclusion was the cause of this enhanced performance. Therefore, the hypothesis of capillary limit augmentation through composite wick layer additions seemed to hold true.

The study conducted by Canti et al. [20] discussed in 2.1.2 also examined heat transfer enhancement using composite wicks. Findings suggested that a layered, composite wick structure of both fine and coarse pores augmented heat transfer performance over homogeneous designs [20]. They attributed this to an increase in capillary pumping ability through the fine pores, while still maintaining adequate liquid permeability with the presence of large pores. Furthermore, when the fine pore layer was positioned against the heat source, it performed better than if it was located at the liquid/vapour interface [20]. They explained this additional mechanism of enhanced heat transfer through an increase in the number of nucleation sites against the heat source.

Thus, the findings of Canti et al. appeared to be verified. That is, composite layered wicks could increase heat transfer performance through the simultaneous presence of both fine and coarse pore layers, offering a compromise between high capillary pressure and increased liquid permeability [20]. Conversely, no evidence was found to support the claim of augmented heat transfer from increased nucleation sites at the wall/wick interface, since B8 still exhibited a higher effective thermal conductivity. Also, it was never conclusively proven that the inclusion of the fine pore layer at the wall/wick interface decreased the thermal contact resistance, since the performance of Configuration B was superior to that of Configuration E.

Heat pipe	E7
Maximum heat inputs tested and corresponding maximum evaporator temperatures	Horizontal: 147.7 W at 146.8°C Gravity assisted: 181.5 W at 146.7°C Against gravity: 60.5 W at 146°C
Maximum effective thermal conductivities	Horizontal: 5839 W/m°C at 100.8 W Gravity assisted: 8292 W/m°C at 62 W Against gravity: 2549 W/m°C at 10.2 W

Table 5-6: Thermal Performance Summary for E7

5.3.6 Configuration J

Similar to Configuration E above, Configuration J employed fine pores at the liquid/vapour and wall/wick interfaces. However, instead of filamentary nickel powder, spherical copper powder was selected to form this composite wick. Enhanced evaporation heat transfer and increased capillary pumping ability were the objectives of this design. Also, in comparison to the nickel powder, it was believed the higher thermal conductivity of the copper powder would reduce the wick's thermal resistance, resulting in a higher effective thermal conductivity.

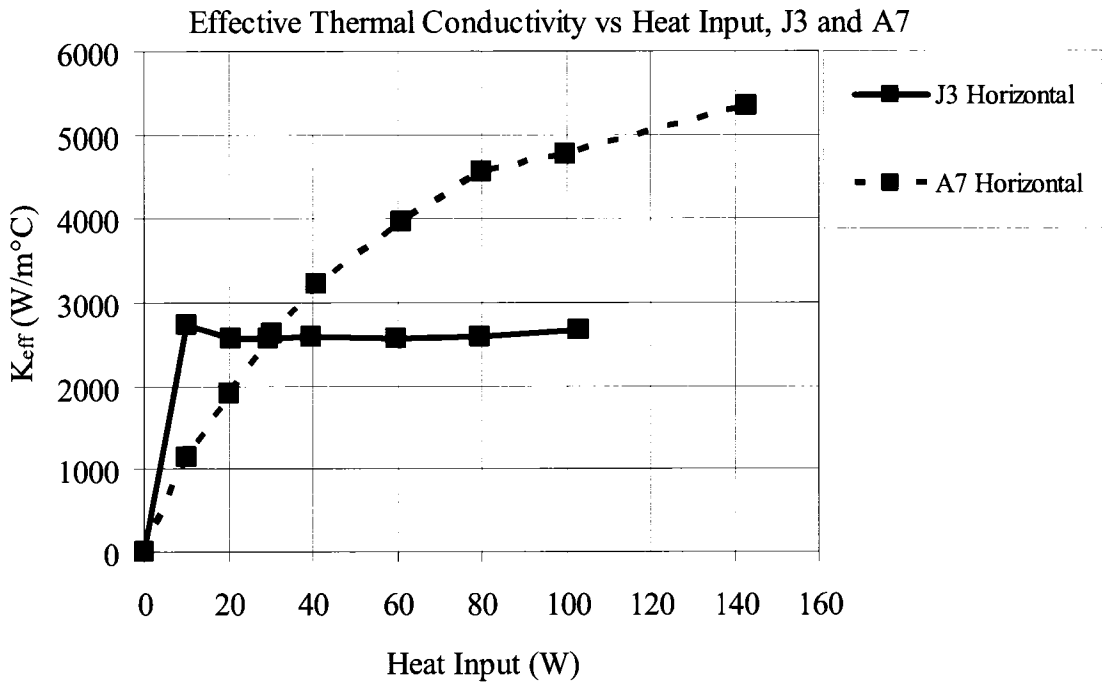

Figure 5-33: Comparison of Horizontal Performance between J3 and A7

In Figure 5-33, Configuration J displays some performance advantage over Configuration A at heat inputs below 30 W. At any heat input higher than 30 W, A7 noticeably outperforms heat pipe J3. Also, the maximum horizontal heat input achieved by J3 was 100 W, 40 W lower than that of A7. At this point, elevated evaporator temperatures required test termination. The best performance of J3 was reached at 10 W, with an effective thermal conductivity of 2724 W/m°C. Performance was nearly twice that of heat pipe A7, again supporting the argument of superior heat transfer through composite wick design. The mechanism for this could very well be related to enhanced evaporation heat transfer, although the effect was much less pronounced here than for Configurations B or E.

Comparing scanning electron microscopy images of the sintered nickel and copper structures, some rationale behind this performance difference is offered. The sintered nickel powder in Figure 5-8 of page 136 clearly shows both finer pores and a much higher density of evaporating menisci than the copper powder in Figure 5-6 of page 134. Recalling the thin film evaporation schematic of Figure 3-11 and the conclusions of Hanlon and Ma [61], a finer pore size offers a greater number of evaporating menisci and higher heat transfer performance. It logically follows that evaporation heat transfer performance should be greater for the nickel powder composite wicks than for the copper powder composite wicks.

Another possible cause of this modest performance could be due to the absence of a composite structure of fine and coarse pores in the interfacial layers of the wick. North et al. [60] found that composite structures offered substantial improvements in heat transfer performance due to the formation of a high density of evaporating menisci. Referring again to the SEM results of Section 5.2.7, Figure 5-15 shows that Configuration J possesses an essentially monoporous and homogeneous structure at the liquid/vapour interface. The copper particles seemed to completely block the larger openings of the copper mesh. This could have affected the performance in two ways: the tight packing of the copper particles could have impeded vapour egress at higher heat fluxes, and less surface area was available for evaporation heat transfer due to the homogeneous nature of this structure. These findings suggested that the application technique required refinement. Additionally, a finer powder or a larger mesh should be used in future attempts to achieve the desired composite microstructure.

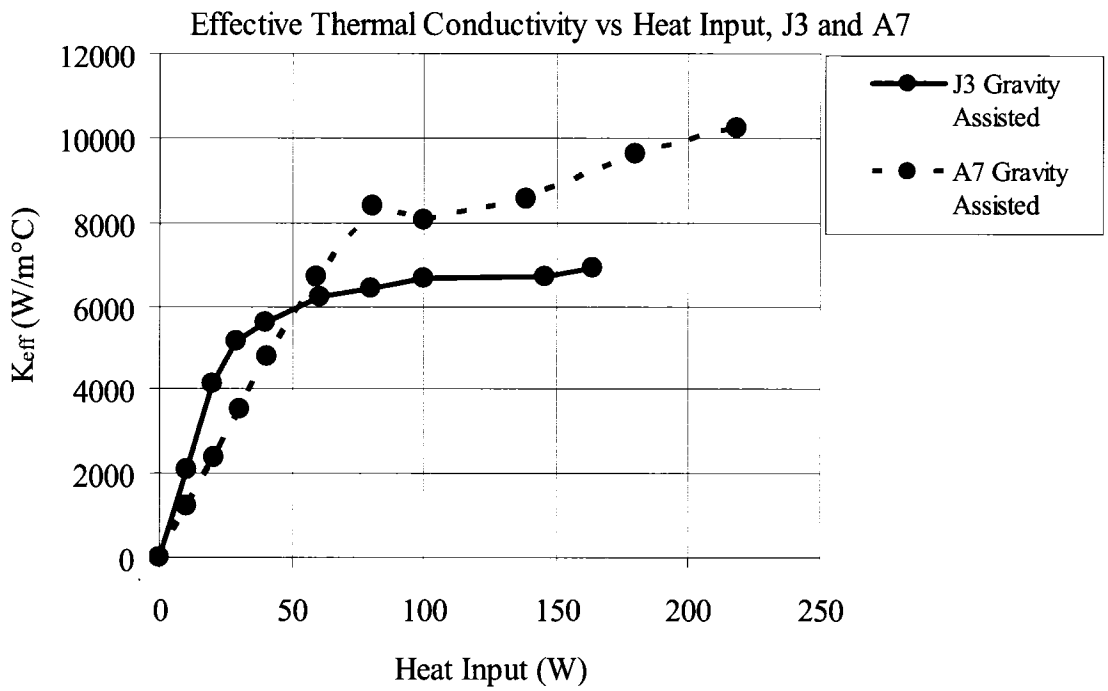

Figure 5-34: Comparison of Gravity Assisted Performance between J3 and A7

Gravity assisted performance for J3 was improved over A7 for heat inputs less than 60 W, illustrated in Figure 5-34. The greatest performance advantage was measured at 20 W, where J3 achieved an effective thermal conductivity of 4118 W/m°C, 1.7 times higher than A7. Beyond 60 W, A7 exhibited superior performance, reaching a maximum heat input rate of 218 W, much higher than that of J3 at 163 W.

Again, perhaps the monoporous nature of the interfacial layers caused this poor performance. It seems possible that the vapour generated at higher heat fluxes could have become trapped in the central wick layers as the liquid receded beneath the liquid/vapour interface. Fine pores and poor contact at the wall/wick interface, shown in Figure 5-15 on

page 142, could have also promoted bubble nucleation, leading to the formation of a vapour blanket and a high thermal resistance.

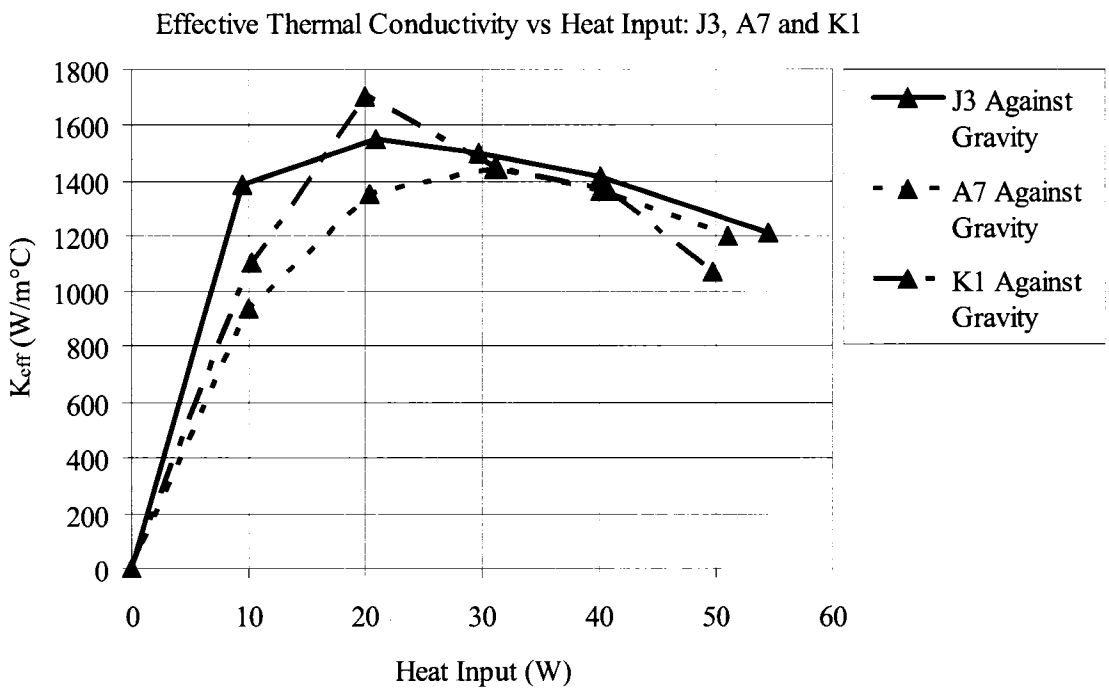

Figure 5-35: Against Gravity Performance Comparison between J3, A7 and K1

Against gravity operation of J3 revealed a slight increase in performance over homogeneous designs, as illustrated in Figure 5-35. Modest gains were achieved at 10 W, where J3 attained an effective thermal conductivity of 1391 W/m°C, 1.5 times higher than A7 and 1.25 times better than K1. However, results were much lower than those achieved by the nickel composite wick configurations B and E. At 21 W, J3 reached its highest effective thermal conductivity of 1553 W/m°C, yet K1 performed slightly better, most likely due to its overall finer pore structure. The additional composite layers of Configuration J could have aided in extending the capillary limit, suggested by an

increase in the maximum heat input rate. The maximum heat input rate of J3 was approximately 55 W, 4 W higher than A7 and 5 W more than K1. Perhaps the simultaneous inclusion of both fine and coarse pore layers promoted a better compromise between high capillary pumping ability and an acceptable level of liquid permeability.

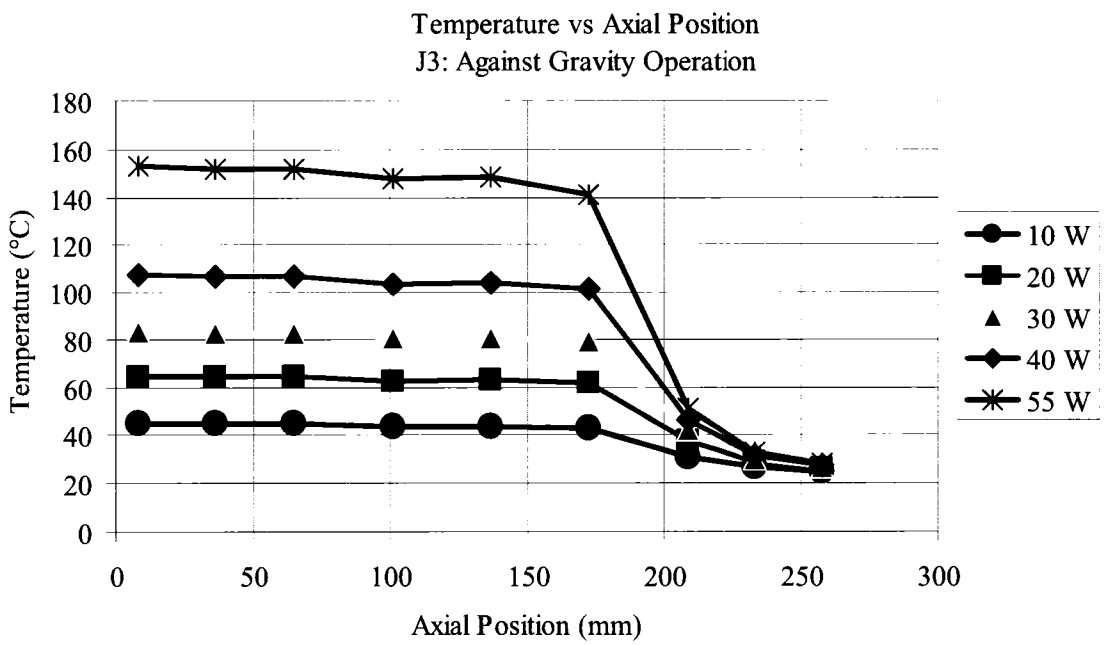

Figure 5-36: Axial Temperature Distribution for J3, Against Gravity

One peculiarity common to the sintered copper powder wicks is presented in Figure 5-36. It seems that Configuration J possessed the same low axial temperature drop along the first two thirds of the heat pipe, much like Configuration K in Figure 5-23. Very good performance was confirmed along this portion of the heat pipe, with an axial temperature drop of only 10°C occurring at 55 W. After this point, temperatures along the condenser section declined rapidly. The reason for the abrupt drop in temperature along the condenser is not known at this time. This was the origin of the low effective thermal

conductivities of this configuration. Like Configuration K, the presence of non-condensable gases or fluid overcharging could have potentially caused this behaviour. In addition to these factors, vapour entrapment could have also contributed to this inferior performance, however further experimentation is required to confirm these theories.

Test results for J3 are summarized in Table 5-7. Overall, the results of this configuration demonstrated the potential shortcomings of copper powder composite configurations in comparison to the superiority of the nickel powder composite wicks. Since Configuration J was tested before Configuration I and results were not promising, all "I" type heat pipes were eliminated from further trials. It was therefore concluded that further development and testing efforts would focus on sintered nickel powder composite wicks, or biporous wicks comprised of finer sintered copper powder.

Heat pipe	J3
Maximum heat inputs tested and corresponding maximum evaporator temperatures	Horizontal: 103 W at 152.6°C Gravity assisted: 163.4 W at 149.5°C Against gravity: 54.6 W at 152.9°C
Maximum effective thermal conductivities	Horizontal: 2724 W/m°C at 10 W Gravity assisted: 6934 W/m°C at 163.4 W Against gravity: 1553 W/m°C at 20.9 W

Table 5-7: Thermal Performance Summary for J3

5.3.7 Configuration L

Several key factors led to the design of this configuration. The studies conducted by North et al. [60] and Cao et al. [67] both concluded that composite wicks comprised of two characteristic pore sizes provided clear heat transfer performance advantages over monoporous wick designs. A significant increase in evaporative surface area was credited with these gains. The wicks in these studies consisted of a continuous, bimodal distribution of fine and coarse pores, formed with sintered metal powder. Additionally, the performance results from Configuration B and E suggested that an increase in the number of composite wick layers would lead to an extension of the capillary limit, most noticeable against gravity. Therefore, Configuration L was designed to exploit these effects, with a structure comprised throughout of fine nickel powder lightly applied to a large pore substrate of copper mesh.

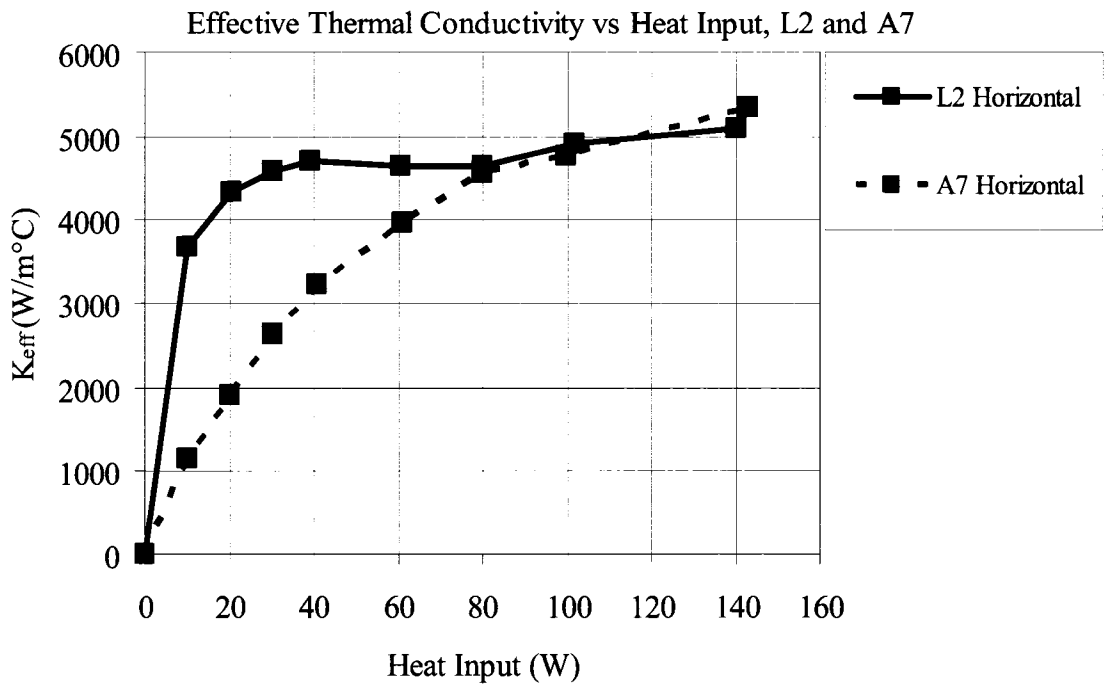

Figure 5-37: Comparison of Horizontal Performance between L2 and A7

Figure 5-37 illustrates the horizontal performance of L2 in comparison with A7. At heat inputs lower than 80 W, L2 outperformed A7. The highest increase in performance was achieved at a heat input of 10 W, where the effective thermal conductivity of L2 was over 3 times that of A7. The best effective thermal conductivity was 5103 W/m°C, attained at its maximum heat input rate of 140 W.

It appeared that the performance of L2 and A7 were equivalent above 80 W, suggesting that at higher heat fluxes, liquid recession into the wick did not expose any additional evaporating menisci. It was previously postulated that at higher heat fluxes, liquid recession into the wick would activate a higher number of evaporating menisci, and therefore heat transfer performance would increase dramatically. This theory was based

on the research conducted by North et al. [60] discussed in Section 3.3.4. Biporous wicks were employed to enhance evaporation heat transfer performance. The wicks were comprised of clusters of powder, sintered together. The fine pores were formed in the clusters, with the large pores residing in the spaces between the clusters. They discovered a previously undetected heat transfer regime, where at higher heat fluxes the wall/wick-to-vapour temperature difference remained virtually equivalent for a large range of heat fluxes. It was reasoned that higher heat fluxes exposed more evaporating menisci, thus encouraging better thermal performance through a significant increase in thin-film surface area. It seemed that the clusters acted as fluid reservoirs as the liquid receded further into the wick. With heat addition, vapour migrated into the spaces between the clusters, so that more evaporating menisci were activated. Consequently, very high heat transfer performance was achieved. It did not seem likely that this effect was present here, because the augmented effective thermal conductivity trend decayed and flattened instead of exponentially increasing, as would be the expected behaviour if this mechanism was active. Perhaps Configuration L did not perform as expected because it did not possess fluid reservoir clusters, since the biporous wick was formed with copper mesh and sintered nickel powder, and not clusters of sintered metal powder.

When results for Configuration B were reviewed in Figure 5-24, it was thought the characteristic bump and flattening of the effective thermal conductivity curve was caused by two phenomena. First, high evaporation heat transfer performance was encouraged by the biporous layer. Then, as the heat flux increased, liquid recession into the monoporous layers beneath the liquid/vapour interface produced a flattening of the effective thermal

conductivity curve. It was postulated that fewer evaporating menisci were present once the biporous layer dried out. Naturally, these results suggested that increasing the number biporous wick layers should extend the enhanced performance effect into higher heat flux regions. Unfortunately, no evidence of this was discovered in Configuration L, yet it still did offer substantial heat transfer advantages over the monoporous wick of A7 at low heat inputs.

Examining the particle sizes used in the studies from Cao et al. [67] could offer some insight into this unexpected behaviour. A qualitative summary of their results is presented in Table 5-8. The two monoporous samples produced the lowest heat transfer performance, and all biporous structures outperformed them at all heat fluxes. Two interesting observations can be deduced from this study: an optimum large pore size produced the best performance for the selected small pore size, and both the small and large pores from the study of Cao et al. [67] were greater than those used for the present study.

Overall, the pore sizes chosen in Configuration L were smaller than those of Cao et al. [67], the large pores measuring approximately 250 μm with the fine pores estimated at 2 to 25 μm. It therefore seems possible that the pore sizes of Configuration L could have caused this reduced performance at higher heat inputs, most likely due to vapour entrapment difficulties. Perhaps a greater small and large pore size would have extended the enhanced performance shown in the earlier portions of Figure 5-37 to the higher heat input regime.

Sample	Pore Size	Performance Rating
1 Monoporous	80 μm	Last
2 Monoporous	800 μm	Fourth
3 Biporous	Small pores: 80 μm Large pores: 200 μm	Third best
4 Biporous	Small pores: 80 μm Large pores: 400 μm	Best
5 Biporous	Small pores: 80 μm Large pores: 800 μm	Second best

Table 5-8: Summary of Findings from Cao et al. [67]

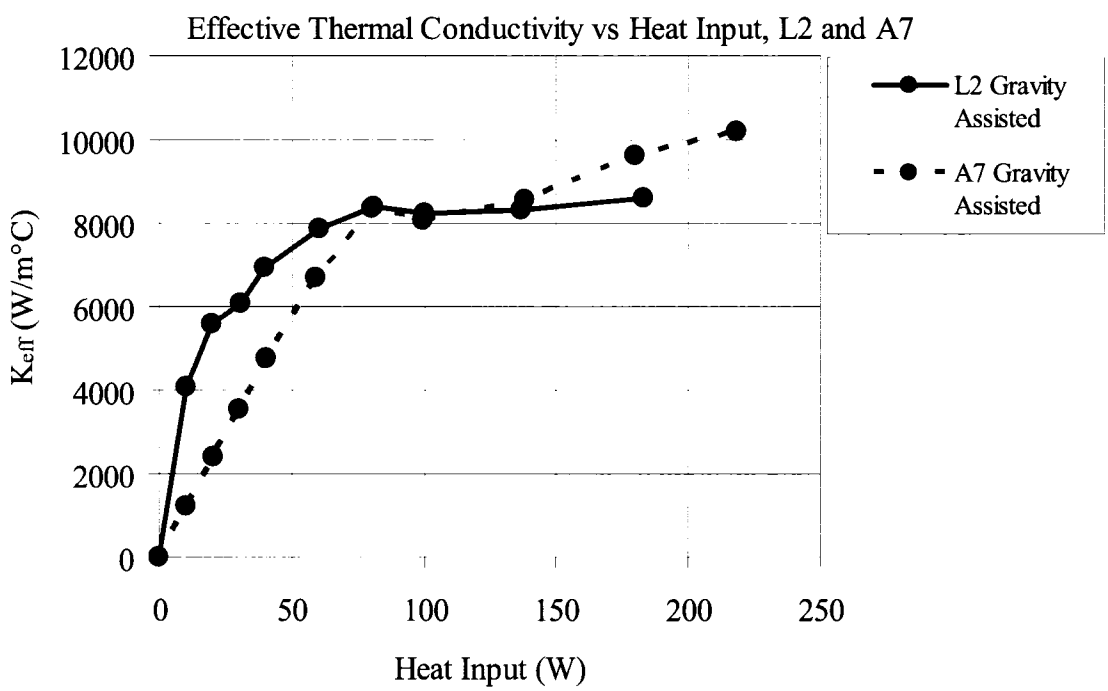

Figure 5-38: Comparison of Gravity Assisted Performance between L2 and A7

Investigating the gravity assisted performance of Configuration L in Figure 5-38, it can be appreciated that a performance advantage again existed in the low heat input regime below 80 W. Compared to A7, L2 performed over three times as well at 10 W. The

highest effective thermal conductivity measured was 8597 W/m°C at 183 W, significantly lower than the best performance of A7. The lower liquid permeability of L2 seemed to neutralize any evaporation heat transfer improvements offered by the fine pore structure during higher heat inputs. Overall, it appeared that the high permeability wick structure of Configuration A was favourable to all other configurations in the gravity assisted orientation, with the exception of Configuration B.

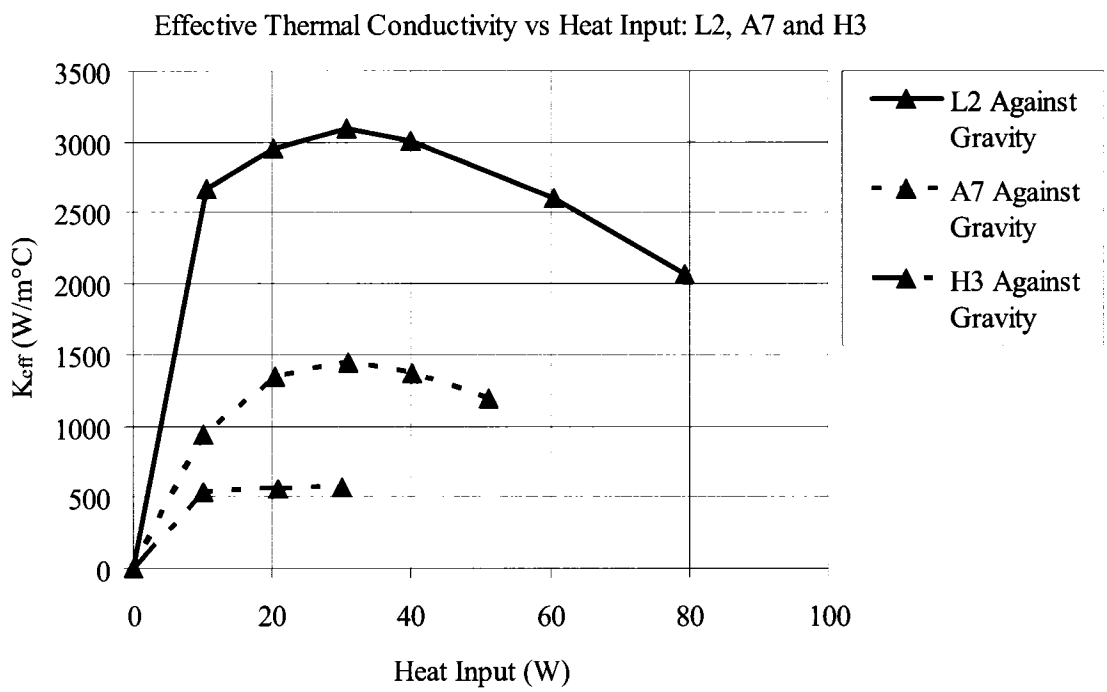

Figure 5-39: Against Gravity Performance Comparison between L2, A7 and H3

Against gravity testing, shown in Figure 5-39, revealed a significant finding: overall, Configuration L outperformed all other wick structures by a comfortable margin. The highest effective thermal conductivity achieved was 3096 W/m°C at 31 W, over twice

that of A7. Moreover, the maximum heat input rate was 80 W. This was 50 W higher than H3 and 29 W higher than A7.

Regarding the hypothesis suggested by the results of Configurations B and E, it did seem likely that increasing the number of composite wick layers encouraged the extension of the capillary limit. Table 5-9 summarizes the maximum heat input rates achieved by Configurations A, B, E and L. The trend of increasing heat input rate with the number of composite wick layers is evident. One can appreciate this observation by understanding the importance of the fine pores of the composite structure: they provide the capillary pressure necessary to transport the fluid against the forces of gravity. If there are a greater number of these pores, it can be reasonably assumed the capillary limit would be extended. The presence of the large pores should have also minimized the liquid pressure drop, as suggested in the findings of Cao et al. [67], so that a higher net capillary pressure would be available for liquid delivery. As for the poor performance of Configuration H, it is possible that although it possessed the greatest number of fine pores, its against gravity performance was hindered by very low liquid permeability. However, as mentioned before, this heat pipe was probably overcharged.

Configuration	Composite Layers	Max. Heat Input Rate
A	0	51 W
B	1	56 W
E	2	61 W
L	4	80 W

Table 5-9: Maximum Heat Input Rate Comparison, Against Gravity

It is thought that the above effects resulted in L2 achieving the highest against gravity performance. This belief is supported by the behaviour shown in Figure 5-39: the effective thermal conductivity curves display the same trend, yet the composite wick heat pipe (L2) offers much higher performance. A finer pore size would both extend the capillary limit and increase the effective thermal conductivity, provided liquid permeability is not greatly compromised. Conversely, there was no strong evidence supporting the mechanism of enhanced evaporation heat transfer, which is believed to exhibit itself as a characteristic hump in the effective thermal conductivity curves, shown in the results for Configuration B and E. Thermal performance results for Configuration L are summarized in Table 5-10.

Heat pipe	L2
Maximum heat inputs tested and corresponding maximum evaporator temperatures	Horizontal: 140.4 W at 146.5°C Gravity assisted: 183.2 W at 141.1°C Against gravity: 79.5 W at 146.7°C
Maximum effective thermal conductivities	Horizontal: 5103 W/m°C at 140.4 W Gravity assisted: 8597 W/m°C at 183.2 W Against gravity: 3096 W/m°C at 30.6 W

Table 5-10: Thermal Performance Summary for L2

5.3.8 Summary of composite wicks with highest thermal performance

The graphs displayed below illustrate the best performing composite wicks in comparison to the conventional, homogeneous configurations. All of the highest performing wicks contained nickel powder, while the wick containing copper powder did not exhibit favourable heat transfer characteristics and as such, it was not included in this summary.

Overall, B8 displayed the most desirable performance in horizontal and gravity assisted orientations, while L2 was favoured during against gravity operation. These results confirm that wick design must be tailored depending on the orientation of the heat pipe and the heat input, so that no solitary wick can satisfy all requirements and still offer the very best thermal performance. However, it can be appreciated that a better compromise in performance can be reached if a composite wick is employed over a homogeneous design.

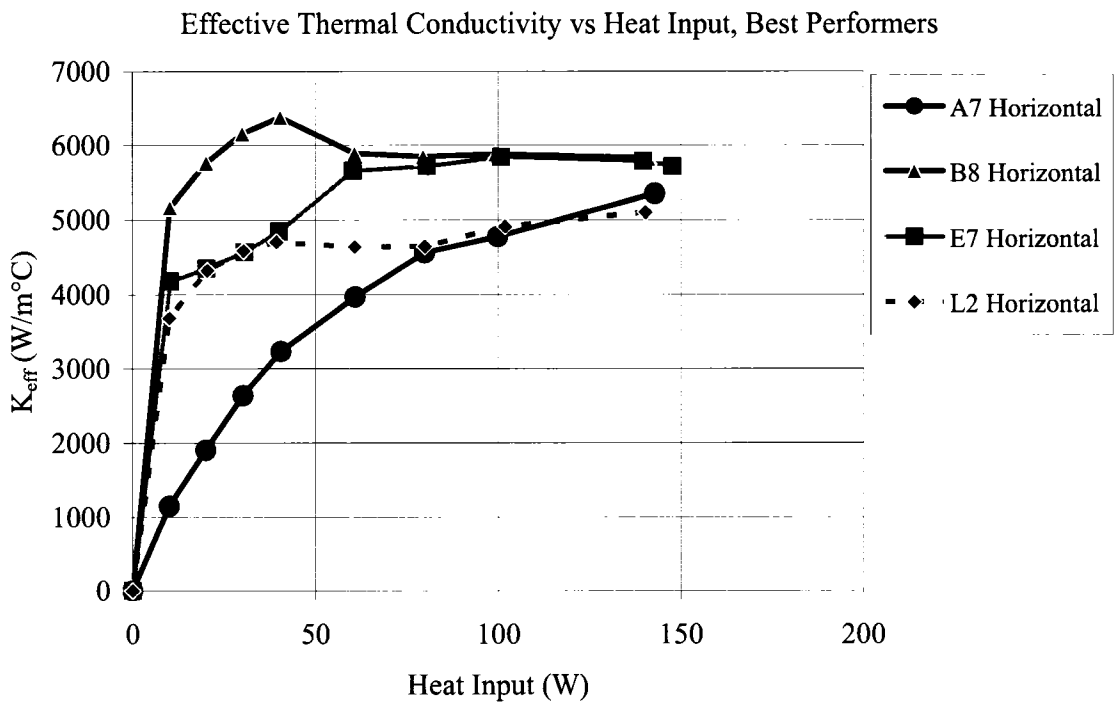

Figure 5-40: Best Performing Configurations, Horizontal Operation

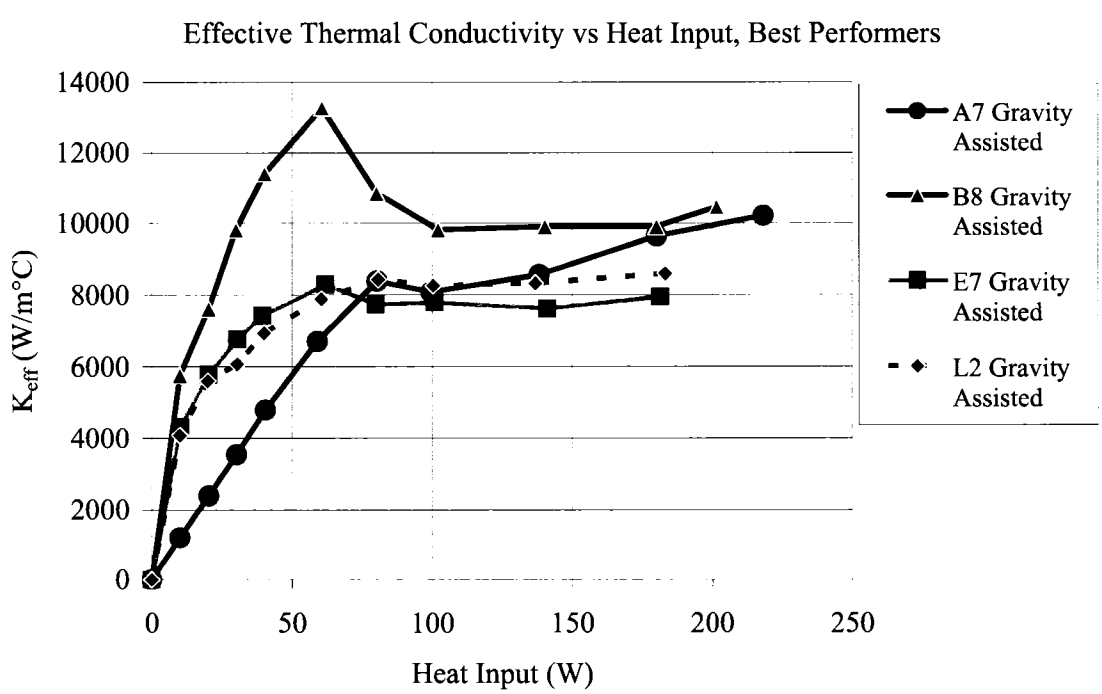

Figure 5-41: Best Performing Configurations, Gravity Assisted Operation

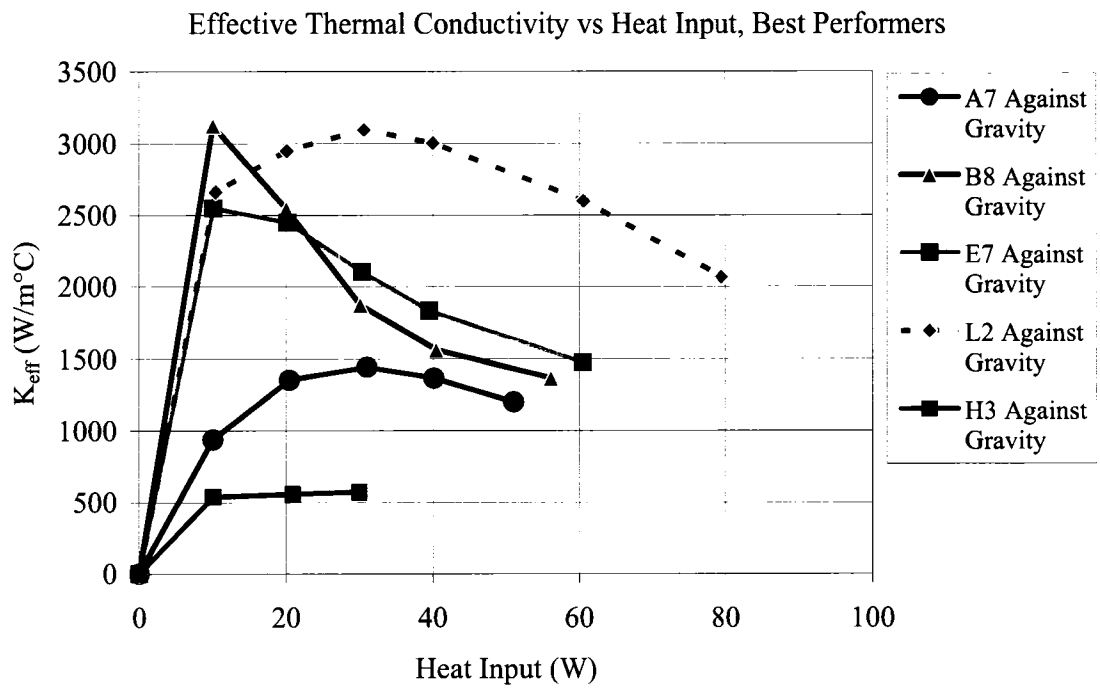

Figure 5-42: Best Performing Configurations, Against Gravity Operation

5.3.9 Uncertainty analysis

Uncertainties in the estimated effective thermal conductivities of the previous sections arose from measurements of the axial temperature drop, the voltage and current readings and the heat pipe effective length. Additionally, the tolerance on the outside diameter of the copper tubing presented some measure of uncertainty. An uncertainty analysis was conducted to assess the effects of these factors on the effective thermal conductivity calculated with Equation (2-35).

A universally accepted approach was employed for propagation of error calculations, the governing equation given by [83], [84]:

$$\sigma_z = \sqrt{\left(\frac{\partial z}{\partial x}\sigma_x\right)^2 + \left(\frac{\partial z}{\partial y}\sigma_y\right)^2 + \ldots} \tag{5-1}$$

where σ_z is the error on the quantity z, $\frac{\partial z}{\partial x}$ is the partial derivative of z with respect to the variable x, σ_x is the error on the variable x, and so on for any number of variables that z is dependant upon. Suppose z is expressed as:

$$z = Ax^n y^m u^{-p} \tag{5-2}$$

where x, y and u are variables that z is dependant upon. Then, Equation (5-1) can be simplified to deal with error propagation in expressions involving multiplication and division using [83]:

$$\sigma_z = z\sqrt{\left(\frac{n\sigma_x}{x}\right)^2 + \left(\frac{m\sigma_y}{y}\right)^2 + \left(\frac{p\sigma_u}{u}\right)^2 + \ldots} \tag{5-3}$$

Expressing the effective thermal conductivity of Equation (2-35) in terms of all of the measured quantities, we obtain:

$$k_{eff} = V \times I \times l_{eff} \times \frac{4}{\pi} \times d^{-2} \times \Delta T^{-1} \tag{5-4}$$

For the effective thermal conductivity estimations of Section 5.3 , the uncertainty on Equation (5-4) was calculated with Equation (5-3), yielding:

$$\sigma_{k_{eff}} = k_{eff}\sqrt{\left(\frac{\sigma_V}{V}\right)^2 + \left(\frac{\sigma_I}{I}\right)^2 + \left(\frac{\sigma_{l_{eff}}}{l_{eff}}\right)^2 + \left(\frac{2\sigma_d}{d}\right)^2 + \left(\frac{\sigma_{\Delta T}}{\Delta T}\right)^2} \qquad (5\text{-}5)$$

where σ_v is the error on the voltage measurement, σ_I is the error on the current measurement, σ_{leff} is the error on the measurement of the effective length, σ_d is the variation on the outside diameter of the heat pipe container, and $\sigma_{\Delta T}$ is the variation on the axial temperature drop. This last quantity was calculated with:

$$\sigma_{\Delta T} = \sqrt{\left(\sigma_{T,evap}\right)^2 + \left(\sigma_{T,cond}\right)^2} \qquad (5\text{-}6)$$

where $\sigma_{T,evap}$ is the error on the central evaporator temperature, and $\sigma_{T,cond}$ is the variation on the central condenser temperature. The errors employed in Equation (5-5) are summarized in Table 5-11.

Quantity	**Error (σ)**
Voltage (V)	±0.2% of voltage + 100 mV
Current (I)	±2% of current + 10 mA
Effective length (l_{eff})	±1 mm, the smallest division on scale
Tube outside diameter (d)	±0.0254 mm (tolerance from tube manufacturer)
Central evaporator temperature (T_{evap})	±1.1°C or 0.4% of temperature reading, whichever is greater
Central condenser temperature (T_{cond})	±1.1°C or 0.4% of temperature reading, whichever is greater

Table 5-11: Measurement Uncertainties Used in Equation (5-5)

As an example, effective thermal conductivity uncertainties for heat pipe B8 are summarized in Table 5-12, while uncertainties are graphically represented in Figure 5-43 to Figure 5-45.

Test	Heat Input (W)	K_{eff} ± Uncertainty (W/m°C)
B8 Horizontal Run1		
	10.2	**5169 ± 1558**
	20.1	**5759 ± 990**
	30.1	**6156 ± 768**
	40.4	**6375 ± 624**
	60.7	**5889 ± 377**
	79.4	**5844 ± 301**
	99.3	**5878 ± 260**
	141	**5825 ± 209**
B8 Gravity Assisted Run1		
	10	**5764 ± 1964**
	20.3	**7617 ± 1702**
	30.1	**9823 ± 1911**
	40.3	**11409 ± 1933**
	60.7	**13272 ± 1750**
	80.2	**10850 ± 916**
	102.1	**9816 ± 616**
	140.2	**9908 ± 488**
	180	**9904 ± 410**
	201.6	**10464 ± 417**
B8 Against Gravity Run1		
	10.1	**2758 ± 467**
	20.1	**2188 ± 157**
	30.1	**1990 ± 102**
	40.5	**1704 ± 68**
	56.1	**1381 ± 46**

Table 5-12: Uncertainty Summary for Heat Pipe B8

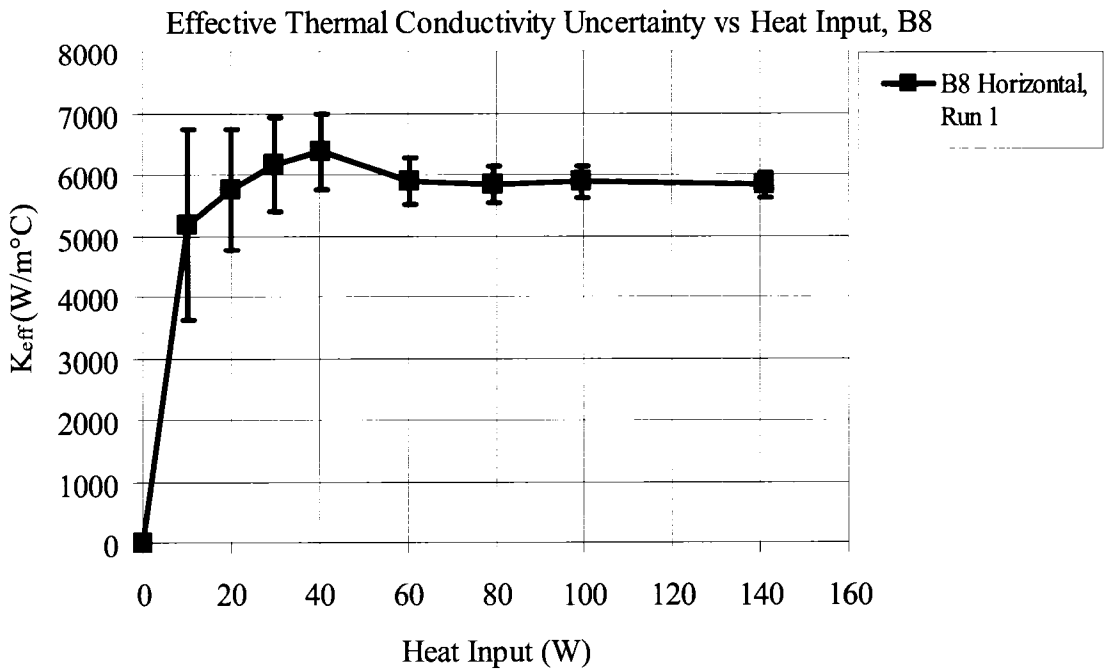

Figure 5-43 Uncertainty for B8, Horizontal Orientation

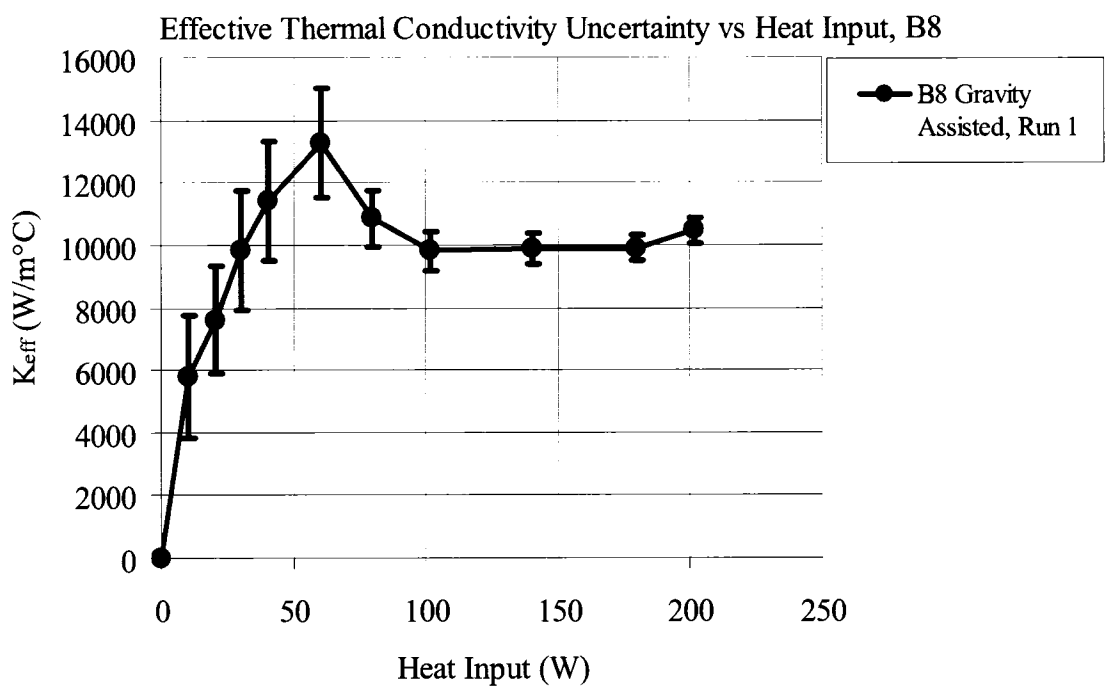

Figure 5-44: Uncertainty for B8, Gravity Assisted Orientation

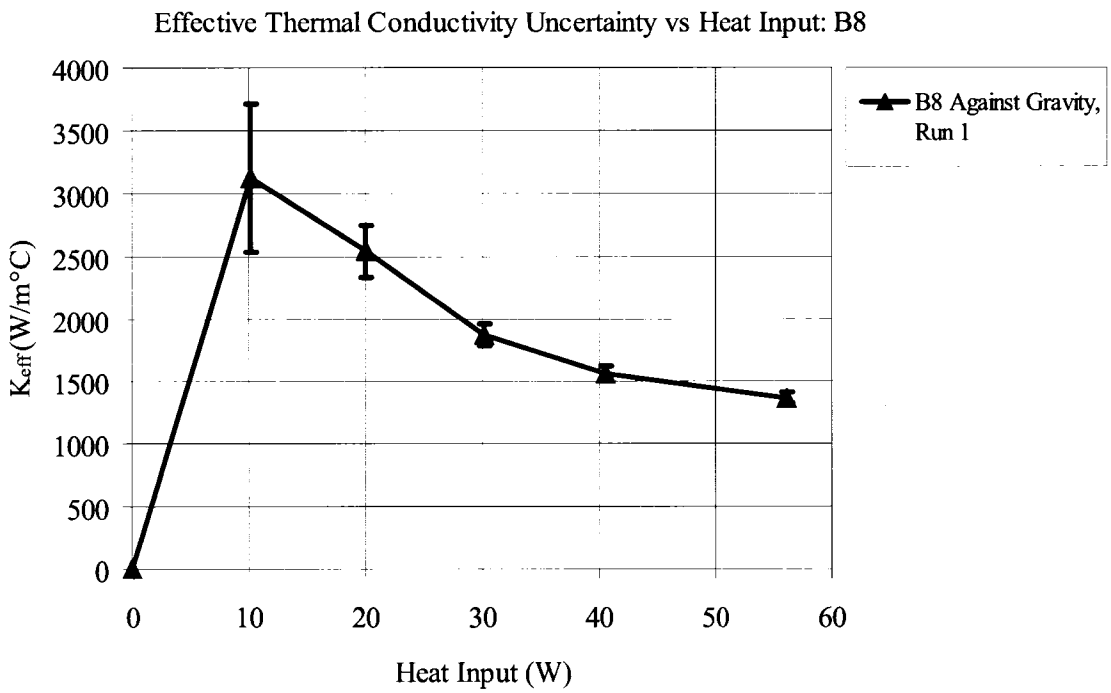

Figure 5-45: Uncertainty for B8, Against Gravity Orientation

Overall, it can be seen that the uncertainty tends to decrease as the heat input increases. Also, for all heat pipes, the uncertainty on the effective thermal conductivity was discovered to be the highest for the gravity assisted orientation, followed by the horizontal tests and the against gravity orientations. Reviewing Equation (5-5), it is understood why this is so: the last term in the equation is associated with the axial temperature difference. As the temperature difference decreases, this term becomes larger such that the overall uncertainty grows. Conversely, as the heat input is increased, the temperature difference increases, and hence, the error contribution from the temperature measurement decreases. Against gravity tests also tended to increase the axial temperature difference, since there was less net capillary pressure available for liquid delivery to the evaporator. Therefore, since gravity assisted operation tended to decrease

this axial temperature difference, these tests possessed the highest uncertainties at the lowest heat inputs.

The highest measured uncertainty for all experiments occurred during gravity assisted testing of B8. At 10 W, the estimated uncertainty was ± 34% of the calculated effective thermal conductivity. Incidentally, this particular data point was associated with the lowest axial temperature drop of all tests at 4.6°C. The lowest uncertainty (± 3%) occurred during against gravity testing of Configuration L at a heat input of 75 W. Because of the measurement uncertainties associated with the axial temperature drop, it was concluded that a more accurate thermocouple with a lower temperature range should have been used. In hindsight, T-type thermocouples would have been a more suitable choice for temperature measurement.

6 Conclusions and Recommendations

From the results presented in Section 5, several important conclusions can be drawn. Recommendations are suggested with respect to further investigations in evaporative heat transfer performance, porous material testing and heat pipe test rig refinement. These are given in the following sections.

6.1 Remarks on Results

The results obtained in the previous section led to the following conclusions. Firstly, composite wicks have been shown to offer significant heat pipe performance improvements over conventional, homogeneous structures. These thermal performance enhancements could be primarily attributed to:

1. Enhanced evaporation heat transfer due to an increase in the evaporating meniscus density at the liquid/vapour interface, and/or
2. An increase in the capillary pumping ability of the wick from the presence of a fine pore structure, while maintaining adequate liquid permeability through a large open pore network.

It is quite possible that both of the above mechanisms played an important role in the observed performance increases detailed in Section 5.3 . However without further testing, it is uncertain which factor made the greater contribution. Regarding the enhancement in capillary pumping capability, it seems reasonable to conclude that a greater number of

composite wick layers led to the increase in against gravity performance, particularly in the maximum heat input rate achieved. This was probably accomplished through an extension of the capillary limit and an augmentation of the net capillary pressure available for liquid transport. Hence, due to the presence of both fine and coarse pores, these biporous structures seemed to simultaneously increase the wick's capillary pumping capability while maintaining a high liquid permeability.

Some peculiarities in heat pipe behaviour have also been found. In particular, the decay of effective thermal conductivity at higher heat inputs, ubiquitous to all composite wicks, is not completely understood. This behaviour could have been caused by vapour entrapment in the wick, possibly caused by the fineness of the 100-mesh copper screen. Perhaps a coarser mesh would have provided larger pores for vapour escape. However, without direct visual observation of this phenomenon, this theory cannot be fully supported at present. Therefore, a research program should be initiated to visually investigate evaporation heat transfer processes in homogeneous and composite porous materials. These studies could assess:

1. The formation of evaporating menisci at increasing heat inputs,
2. The relative vapour entrapment resistances of the wicks, and
3. The associated gains in heat transfer performance of composite wicks over homogeneous wicks.

Another noteworthy conclusion was the evident performance superiority of the sintered nickel powder composite wicks over those of the copper powder. It seems probable that the filamentary morphology and fineness of the nickel powder observed in Section 5.2 greatly increased the thermal performance of these wicks. These results lend themselves well to the hypothesis of evaporation heat transfer enhancement, since other researchers have indicated a direct link between increased evaporative surface area and improved thermal performance.

6.2 Remarks on Manufacturing

Some shortcomings in manufacturing are also worth mentioning. Performance sometimes varied significantly between supposedly identical configurations. Also, some configurations displayed unpredictable results. These could have been caused by manufacturing uncertainties. Therefore, for manufacturing reproducibility, it is recommended to:

1. Accurately dispense the required amount of metal powder applied to the wick,
2. Automate the metal powder application phase,
3. Accurately verify wick porosity, and
4. Employ a controlled, vacuum evacuation process to minimize non-condensable gases.

6.3 Remarks on Testing

There are some important recommendations associated with the heat pipe test rig and the results obtained in Section 5.3 . Most importantly, a heat balance would provide more accurate effective thermal conductivity estimates. Although all heat pipe performances were essentially normalized through an identical test protocol, from an industrial application standpoint it would be necessary to verify these values in absolute terms. That is, these newly developed configurations would require a more rigorous validation program to ensure adequate performance. For this purpose it is recommended to:

1. Use more accurate T-type thermocouples for axial temperature measurements,
2. Measure the coolant flow rate with a traceable, calibrated flowmeter, and
3. Record the coolant temperature differential with high precision, high accuracy thermistors arranged in a Wheatstone bridge circuit.

The last point is probably the most important, since this arrangement is capable of accurately measuring the small temperature difference of the flowing coolant, a potentially large source of error in calorimetric experiments of this nature.

6.4 Concluding Words

In summary, the present research program concerning heat pipe performance enhancement through composite wick design was successful. Heat pipe design was based on standard procedures available in the literature. Manufacturing processes were created to fabricate novel, composite wick heat pipes aimed at increasing the effective thermal

conductivity and the maximum heat transfer rate of conventional heat pipes. These designs were based on biporous structures offering enhanced evaporation heat transfer and capillary limit optimization. A heat pipe test rig was conceptualized and built to assess thermal performance improvements. Substantial gains in heat transfer performance were achieved, with nickel powder/copper mesh composite wick heat pipes obtaining the highest level of thermal effectiveness.

While some questions were answered by this study, many more remain to be explored. These are associated with the precise mechanisms of heat transfer performance enhancement in porous media and a more detailed analysis of wick characteristics. If a more complete understanding of these phenomena are realized, even greater gains in thermal performance can be exploited in the future.

Appendix A Heat Pipe Design Calculations

a) Maximum allowable operating temperature: Calculate the maximum allowable operating temperature (the vapour temperature at the evaporator exit) based on the yield strength of the copper tube and end caps, whichever is lower. Use a safety factor of 3 on the tubing and an additional safety factor of 4 on the end caps.

Copper tubing container properties:

O.D: 0.375" (9.525 mm)
I.D.: 0.315" (8.001 mm)
Wall thickness: 0.03" (0.762 mm)
0.2% Yield Strength: ≈48MPa, fully annealed condition
Safety factor of 3 on the Yield Strength

Copper end cap properties:

Thickness: 0.06" (1.524 mm)
Diameter: 0.315" (8.001 mm)
0.2% Yield Strength: ≈48MPa, fully annealed condition
Additional safety factor of 4 on the above (due to uncertainty on the strength of the soldered end caps)

Solve for the maximum allowable internal pressure of the container using Equation (3-6) and rearranging for P:

$$P = \frac{2t_{wall}\sigma_{\max}}{d_o} = \frac{2 \times 7.62 \times 10^{-4} m \times 48MPa/3}{8.001 \times 10^{-3} m} = 3.05MPa$$

Now check the maximum allowable internal pressure that the end caps can sustain using Equation (3-8):

$$P = \frac{8t_{cap}^2 \sigma_{\max}}{d_{cap}^2} = \frac{8 \times \left(1.524 \times 10^{-3} m\right)^2 \times 16MPa/4}{\left(8.001 \times 10^{-3} m\right)^2} = 1.16MPa$$

This is lower than the maximum allowable internal pressure of the container. Therefore, the maximum operating temperature of the heat pipe will be based on this lower internal pressure. From Moran and Shapiro [32], the maximum operating temperature associated with this vapour pressure is:

$$T_{\max} \cong 186^{\circ}C @ 1.16MPa$$

b) Vapour core diameter: Calculate the minimum vapour core diameter to avoid compressibility effects.

Assume:

A heat input rate (Q_{in}) of 300 W
A vapour temperature (T_v) of 160°C

Properties of water at 160°C:

$h_{fg} = 2082.6 \times 10^3$ J/kg
$\rho_v = 3.256$ kg/m^3
$K' = 1.243$
$R_{vap} = 461.38$ J/kgK

From Equation (3-3):

$$d_v = \left(\frac{20Q}{\pi \rho_v h_{fg} \sqrt{K' R_{vap} T_v}} \right)^{\frac{1}{2}}$$

$$= \left(\frac{20 \times 300 W}{\pi \times 3.256 \, {}^{kg}/_{m^3} \times 2082.6 \times 10^3 \, {}^{J}/_{kg} \times \sqrt{1.243 \times 461.38 \, {}^{J}/_{kgK} \times 433.15 K}} \right)^{\frac{1}{2}}$$

$$= 7.52 \times 10^{-4} \, m = 0.752 \, mm$$

Therefore, if the vapour core diameter is larger than 0.752 mm, compressibility effects will be avoided. With a 4-layer wick of 100-mesh copper screen chosen for the heat pipe, the resultant vapour core is 6.18 mm, much larger than the required minimum.

c) Heat transfer rate and operating temperature: Calculate the approximate heat transfer rate of the heat pipe at an evaporator wall temperature of 160°C and a sink temperature of 24°C. Also, estimate the operating temperature (*vapour temperature*) at this heat transfer rate.

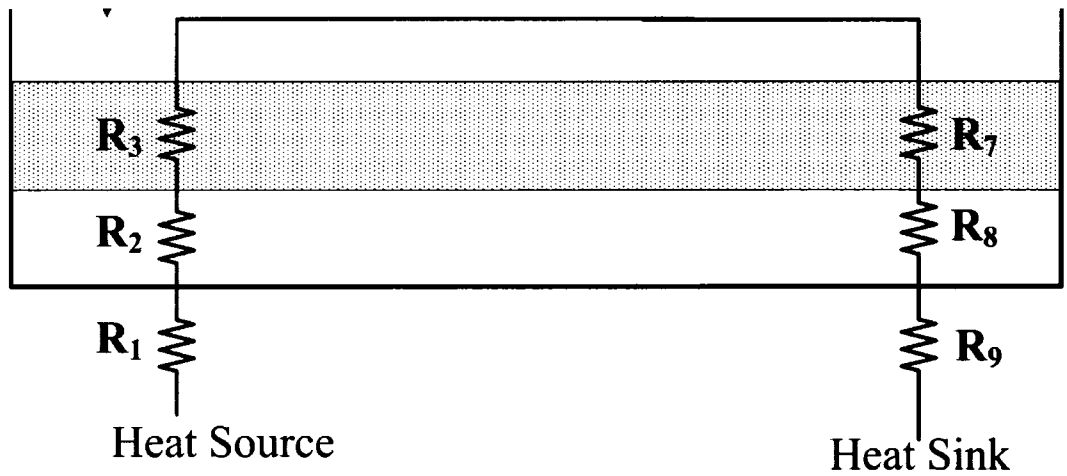

Assume:

The effective thermal conductivities of the wick at the evaporator and condenser ends are determined using working fluid and copper properties at 160°C.
The evaporator length (L_e) is 0.05715 m, while the condenser length (L_c) is 0.0666 m.
The wick thickness is 0.036" (0.9144 mm), such that the vapour core radius (r_v) is 0.1575" (4 mm)

Properties of copper:

k = 390.7 W/m°C @ 160°C
k = 400 W/m°C @ 24 °C

Properties of water:

k = 0.684 W/m°C @ 160°C (liquid)

Copper mesh properties:

Mesh Number: 100
Wire diameter, d_w: 0.0045" (0.1143 mm)

Since the wall temperature at the evaporator and condenser are assumed to be 160°C and 24°C respectively, there is no need to calculate the source and sink resistances, R_1 and R_9. Equations (2-25) to (2-28) are used to calculate the thermal resistances shown in the above network.

Estimating the resistance of the container wall at the evaporator (R_2) using:

$$R_2 = \frac{\ln\left(\frac{r_o}{r_i}\right)}{2\pi L_e k_{wall}} = \frac{\ln\left(\frac{0.1875''}{0.1575''}\right)}{2\pi \times 0.05715m \times 390.7 \, W/m^oC} = 1.243 \times 10^{-3} \; {}^oC/W$$

The liquid-saturated wick resistance at the evaporator (R_3) is given by:

$$R_3 = \frac{\ln\left(\frac{r_i}{r_v}\right)}{2\pi L_e k_{wick}}$$

First, calculate wick porosity, since it will be needed for k_{wick}:

$$\varepsilon = 1 - \frac{1.05\pi N d}{4} = 1 - \frac{1.05\pi \times 100 \frac{mesh}{in} \times 0.0045''}{4} = 0.629$$

Now calculate k_{wick}:

$$k_{wick} = \frac{k_l\left[k_l + k_s - (1-\varepsilon)(k_l - k_s)\right]}{(k_l + k_s) + (1-\varepsilon)(k_l - k_s)}$$

$$= \frac{0.684\left[0.684 + 390.7 - (1-0.629)(0.684 - 390.7)\right]}{(0.684 + 390.7) + (1-0.629)(0.684 - 390.7)} \frac{W}{m^oC}$$

$$= 1.486 \frac{W}{m^oC}$$

Therefore, R_3 is equivalent to:

$$R_3 = \frac{\ln\left(\frac{r_i}{r_v}\right)}{2\pi L_e k_{eff}} = \frac{\ln\left(\frac{0.1575''}{0.1215''}\right)}{2\pi \times 0.05715\,m \times 1.486\,{}^{W}\!/_{m^\circ C}} = 0.486\frac{^\circ C}{W}$$

The thermal resistance of the liquid-saturated wick at the condenser (R_7) is calculated with:

$$R_7 = \frac{\ln\left(\frac{r_i}{r_v}\right)}{2\pi L_c k_{wick}} = \frac{\ln\left(\frac{0.1575''}{0.1215''}\right)}{2\pi \times 0.0666\,m \times 1.486\,{}^{W}\!/_{m^\circ C}} = 0.417\frac{^\circ C}{W}$$

The thermal resistance of the container wall at the condenser (R_8) is given by:

$$R_8 = \frac{\ln\left(\frac{r_o}{r_i}\right)}{2\pi L_c k_{wall}} = \frac{\ln\left(\frac{0.1875''}{0.1575''}\right)}{2\pi \times 0.0666\,m \times 400\,{}^{W}\!/_{m^\circ C}} = 1.042 \times 10^{-3}\frac{^\circ C}{W}$$

Therefore, the overall heat transfer coefficient (U_{HP}) from Equation (2-30) is:

$$U_{HP}' = \frac{1}{(R_2 + R_3 + R_7 + R_8)\cdot A_{HP}}$$

$$= \frac{1}{\left(1.243\times10^{-3} + 0.486 + 0.417 + 1.042\times10^{-3}\right)\frac{^\circ C}{W} \times \left(\frac{\pi}{4}\times\left(9.525\times10^{-3}\,m\right)^2\right)}$$

$$= 15502.2\frac{W}{m^2\,^\circ C}$$

The heat transfer rate (Q), is calculated with Equation (2-31):

$$Q = U_{HP}' \cdot A_{HP} \cdot \Delta T_{HP}' = 15502.2 \frac{W}{m^2\,^\circ C} \times 7.1256 \times 10^{-5} m^2 \times (160 - 24)^\circ C$$
$$= 150.2 W$$

Now, calculate the overall heat transfer coefficient of R_2 and R_3, since these are the only thermal resistances from the heat input surface to the vapour core, as explained in Section 2.6.2. Use the surface area of the evaporator, A_{evap}:

$$U_{R_2+R_3} = \frac{1}{(R_2 + R_3)A_{evap}}$$

$$= \frac{1}{\left(1.243 \times 10^{-3} + 0.486\right) {}^\circ C/W \times \pi \times 9.525 \times 10^{-3} m \times 0.05715 m}$$

$$= 1200.2 \frac{W}{m^\circ C}$$

Finally, estimate the vapour temperature (T_v). This is the approximate operating temperature of the heat pipe:

$$\Delta T'_{HP} = T_{wall} - T_v = \frac{Q}{U_{R_2+R_3} A_{evap}}$$

$$= \frac{150\,W}{1200.2\,{}^{W}\!/_{m^2\,{}^{\circ}C} \times 1.71\times10^{-3}\,m^2}$$

$$\therefore T_v = 160^{\circ}C - \frac{150\,W}{1200.2\,{}^{W}\!/_{m^2\,{}^{\circ}C} \times 1.71\times10^{-3}\,m^2} = 87^{\circ}C \approx 90^{\circ}C$$

d) Capillary limit: Calculate the heat input to the evaporator (Q_e) at the capillary limit for an operating temperature of 90°C.

Assume:

The heat pipe operates in the horizontal orientation.

Properties of water at 90°C:

$h_{fg} = 2280.1\text{x}10^3$ J/kg
$\rho_l = 965.3$ kg/m^3
$\rho_v = 0.4453$ kg/m^3
$\mu_l = 3150\text{x}10^{-7}$ Ns/m^2
$\mu_v = 117\text{x}10^{-7}$ Ns/m^2
$\sigma = 60.8\text{x}10^{-3}$ N/m

First, find the effective pore radius of the wick (r_{eff}) from Equation (3-11):

$$r_{eff} = \frac{1}{2N} = \frac{1}{2\times100\frac{mesh}{in}} = 5\times10^{-3}\,in = 127\,\mu m$$

The porosity was calculated above and is equal to:

$$\varepsilon = 0.629$$

The wick permeability is calculated using Equation (3-12):

$$K = \frac{d_w{}^2 \varepsilon^3}{122(1-\varepsilon)^2} = \frac{(1.143\times10^{-4}\ m)^2 \times 0.629^3}{122(1-0.629)^2} = 1.93\times10^{-10}\ m^2$$

Now find the wick's cross-sectional area (A_w). From Figure 4-7, each mesh layer is twice the wire diameter, and there are 4 layers:

$$d_v = tube\ I.D. - 2\times t_w = 8.001\times10^{-3}\ m - 2\times(2\times1.143\times10^{-4} m \times 4\ layers)$$

$$d_v = 6.1722\times10^{-3} m$$

$$r_v = \frac{d_v}{2} = 3.0861\times10^{-3}\ m$$

$$A_w = \frac{\pi}{4}(tube\ I.D.^2 - d_v{}^2)$$

$$A_w = \frac{\pi}{4}\left((8.001\times10^{-3}\ m)^2 - (6.1722\times10^{-3}\ m)^2\right) = 2.036\times10^{-5}\ m^2$$

The effective length, l_{eff}, is calculated using Equation (2-8). The length of the heat pipe is 250.2 mm, while the lengths of the evaporator (l_e) and condenser (l_c) sections are 57.15 mm and 66.6 mm respectively:

$$l_{eff} = l_a + \frac{l_e + l_c}{2} = \left(heat\ pipe\ length - l_e - l_c\right) + \frac{l_e + l_c}{2}$$

$$= \left(250.2 - 57.15 - 66.6\right)mm + \left(\frac{57.15 + 66.6}{2}\right)mm$$

$$= 188.325\,mm = 0.188325\,m$$

From the capillary limit equation of Section 2.1.5:

$$\frac{2\sigma}{r_{eff}} \geq \frac{\mu_l Q_e l_{eff}}{\rho_l A_w h_{fg} K} + \frac{8\mu_v Q_e l_{eff}}{\pi \rho_v R_v^4 h_{fg}} + \rho_l g L_t \sin\phi$$

The equation will be solved for the heat input to the evaporator, *Qe*. Since the heat pipe is horizontal, the hydrostatic pressure term is zero. This gives:

$$Q_e = \frac{\dfrac{2\sigma}{r_{eff}}}{\dfrac{\mu_l l_{eff}}{\rho_l A_w h_{fg} K} + \dfrac{8\mu_v l_{eff}}{\pi \rho_v R_v^4 h_{fg}}}$$

Now, solving each term on the right hand side of the above equation:

$$\frac{2\sigma}{r_{eff}} = \frac{2 \times 60.8 \times 10^{-3}\ N/m}{1.27 \times 10^{-4}\ m} = 957.5\,Pa$$

$$\frac{\mu_l l_{eff}}{\rho_l A_w h_{fg} K} = \frac{3150 \times 10^{-7}\ Ns/m^2 \times 0.188325\,m}{965.3\ kg/m^3 \times 2.036 \times 10^{-5}\ m^2 \times 2280.1 \times 10^3\ J/kg \times 1.93 \times 10^{-10}\ m^2}$$

$$= 6.84\ \frac{s}{m^3}$$

$$\frac{8\mu_v l_{eff}}{\pi \rho_v R_v^4 h_{fg}} = \frac{8 \times 117 \times 10^{-7}\ Ns/m^2 \times 0.188325\,m}{\pi \times 0.4453\ kg/m^3 \times (3.0861 \times 10^{-3}\ m)^4 \times 2280.1 \times 10^3\ J/kg}$$

$$= 0.061\ \frac{s}{m^3}$$

Substituting the above values into the equation for *Qe*:

$$Q_e = \frac{957.5\,Pa}{6.84\ \frac{s}{m^3} + 0.061\ \frac{s}{m^3}} = 139\,W$$

<u>e) Boiling limit:</u> Calculate the boiling limit for an operating temperature of 90°C.

<u>Assume:</u>

The bubble radius (R_b)is 10^{-7} m
The meniscus radius (R_{men}) is equal to the effective pore radius of the wick = 127 μm
Use the properties for water at 90°C listed in Part (d)
The effective thermal conductivity of the wick (*keff*) is estimated to be 1.486 W/m°C
The inner container radius (R_i)= 4×10^{-3} m, the vapour space radius (R_v)=3.0861×10^{-3} m

Using Equation (2-17), the critical wall-to-vapour temperature is calculated first. Recall that the vapour temperature (T_v) must be converted to Kelvin:

$$\Delta T_{crit} = \frac{2\sigma T_v}{h_{fg}\rho_v}\left(\frac{1}{R_b} - \frac{1}{R_{men}}\right)$$

$$= \frac{2\times 60.8\times 10^{-3}\, {}^{N}\!/_{m} \times (273.15+90)K}{2280.1\times 10^{3}\, {}^{J}\!/_{kg} \times 0.4453\, {}^{kg}\!/_{m^3}}\left(\frac{1}{10^{-7}\, m} - \frac{1}{1.27\times 10^{-4}\, m}\right)$$

$$= 434.6\, K$$

Now calculate the boiling limit with Equation (2-19):

$$Q_b = \frac{2\pi L_e k_{wick}\Delta T_{crit}}{\ln\left(\frac{R_i}{R_v}\right)} = \frac{2\times\pi\times 0.05715\, m\times 1.486\, {}^{W}\!/_{mK}\times 434.6\, K}{\ln\left(\frac{4\times 10^{-3}\, m}{3.0861\times 10^{-3}\, m}\right)}$$

$$= 893.6\, W$$

Since the heat input due to the capillary limit (Q_e = *139 W*) is lower than that calculated due to the boiling limit (Q_b = *894 W*), the heat pipe will be capillary limited.

Appendix B Fluid Charging

Calculate the fluid charge necessary for heat pipe K1 (copper powder wick). Assume the density of copper is 8954 kg/m^3.

Measurements:

Post-sintered mass of heat pipe assembly: 0.09167 kg
Evaporator end cap clearance: 7.09 mm
Condenser end cap clearance: 7.06 mm
Tube length: 265.7 mm
Vapour core diameter: 4.7625 mm

a) Estimate porosity:

First, calculate the heat pipe length (L_t), equivalent to the wick length:

$$L_t = tube\,length - evaporator\ and\ condenser\ end\ cap\ clearances$$

$$= 265.7\,mm - 7.09\,mm - 7.06\,mm = 251.55\,mm$$

The vapour core area is:

$$A_v = \frac{\pi}{4} d_v^2 = \frac{\pi}{4}\left(4.7625 \times 10^{-3}\right)^2 = 1.7814 \times 10^{-5}\,m^2$$

Next, calculate the total wick volume (V_{wick}):

$$V_{wick} = container\ volume - vapour\ core\ volume$$

$$= \left(\frac{\pi}{4} \times \left(8.001 \times 10^{-3}\,m\right)^2 \times 0.25155\,m\right) - \left(1.7814 \times 10^{-5}\,m^2 \times 0.25155\,m\right)$$

$$= 8.166 \times 10^{-6}\,m^3$$

The wick mass is also required:

$$m_{wick} = heat\ pipe\ assembly\ mass - tube\ mass$$

$$= 0.09167\,kg - \frac{\pi}{4} \times \left[tube\ O.D.^2 - tube\ I.D.^2\right] \times L_t \times Density\ of\ copper$$

$$= 0.09167\,kg - \frac{\pi}{4}\left[\left(9.525 \times 10^{-3}\,m\right)^2 - \left(8.001 \times 10^{-3}\,m\right)^2\right] \times 0.2657\,m \times 8954\,{}^{kg}\!/_{m^3}$$

$$= 0.04176\,kg$$

With the wick mass known, we may calculate the volume of solid wick material (V_{solid}):

$$V_{solid} = \frac{m_{wick}}{Density\ of\ copper} = \frac{0.04176\,kg}{8954\,{}^{kg}\!/_{m^3}}$$

$$= 4.664 \times 10^{-6}\,m^3$$

The difference between the total volume of the wick and the solid volume is the pore volume. The pore volume divided by the total volume of the wick is the porosity:

$$\varepsilon = \frac{V_{wick} - V_{solid}}{V_{wick}} = \frac{\left(8.166 \times 10^{-6} - 4.664 \times 10^{-6}\right)m^3}{8.166 \times 10^{-6}\,m^3} = 0.43$$

<u>b) Calculate the fluid charge:</u>

First, the wick cross-sectional area is required:

$$A_w = \frac{\pi}{4} \times \left(tube\,I.D.^2 - d_v^{\,2}\right) = \frac{\pi}{4} \times \left(\left(8.001 \times 10^{-3}\ m\right)^2 - \left(4.7625 \times 10^{-3}\ m\right)^2\right)$$

$$= 3.25 \times 10^{-5}\ m^2$$

The fluid charge is calculated using Equation (4-1). A 10% overcharge is specified:

$$m = 1.1\left(A_v L_t \rho_v + A_w L_t \varepsilon \rho\right)_l$$

$$= 1.1\left(\begin{array}{l} 1.7814 \times 10^{-5}\ m^2 \times 0.25155\, m \times 0.5974\ {kg}/{m^3} \\ \qquad + 3.25 \times 10^{-5}\ m^2 \times 0.25155\, m \times 0.43 \times 958.77\ {kg}/{m^3} \end{array}\right)$$

$$= 3.71 \times 10^{-3}\ kg = 3.71\, g$$

Appendix C Cooling Jacket Drawings

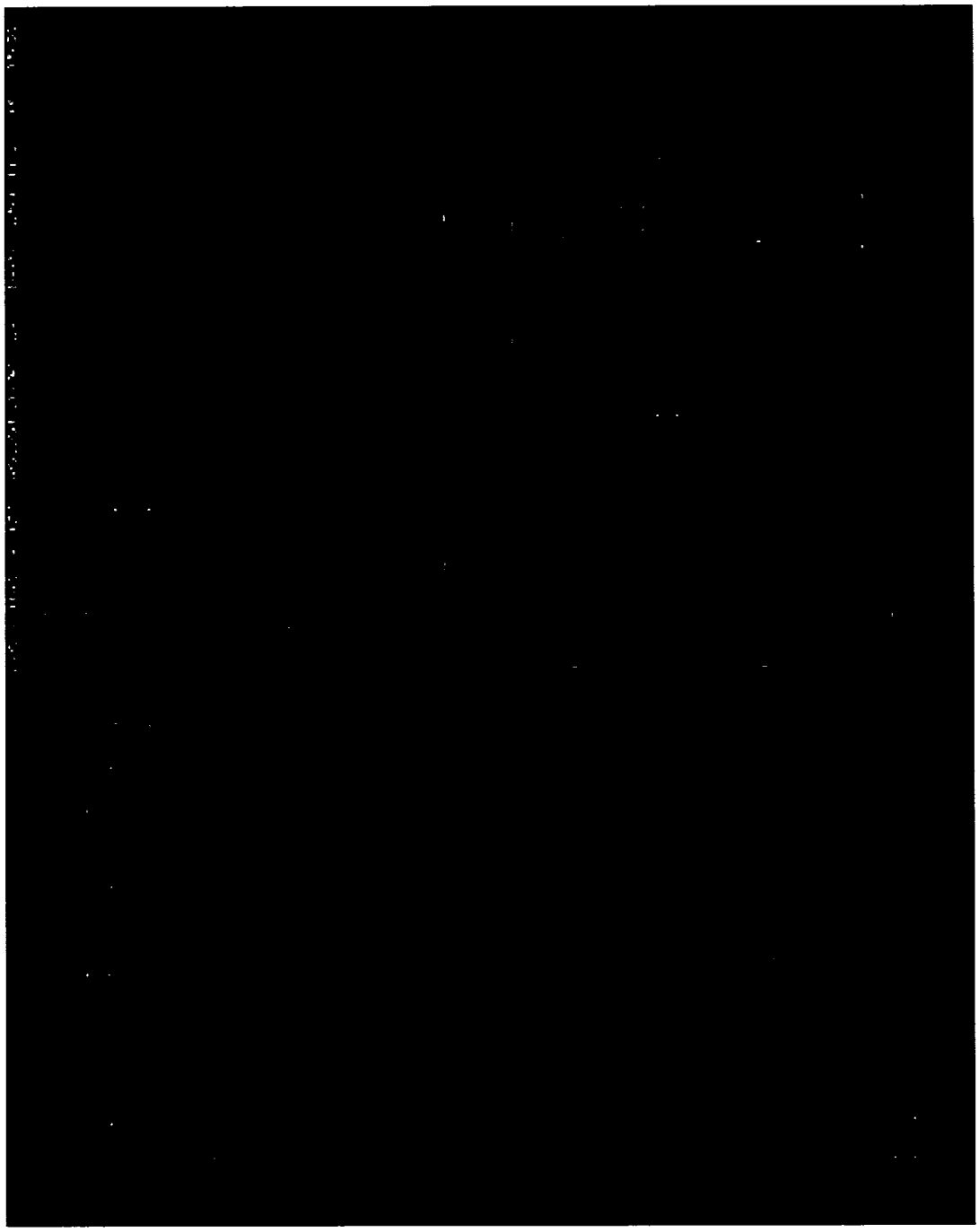

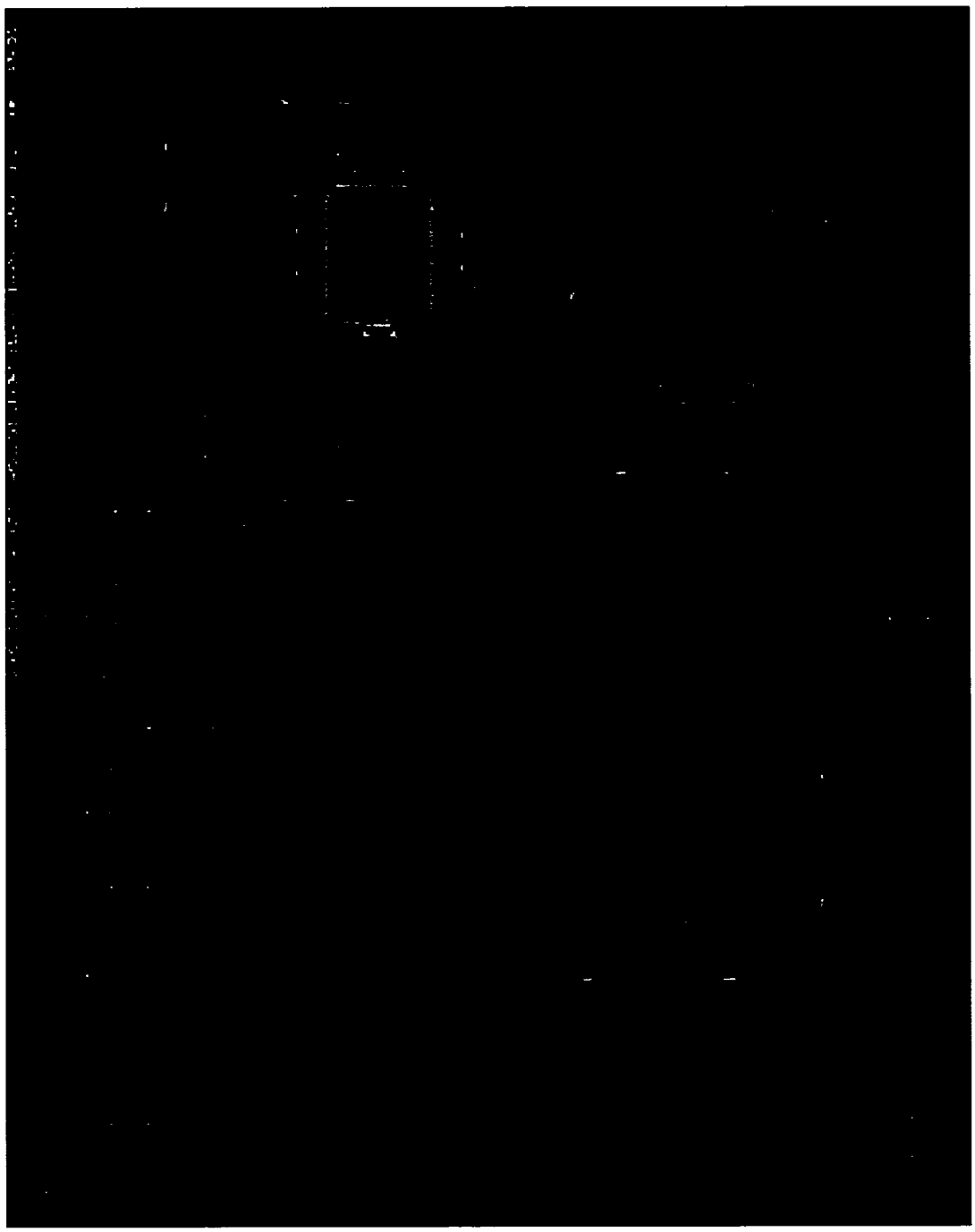

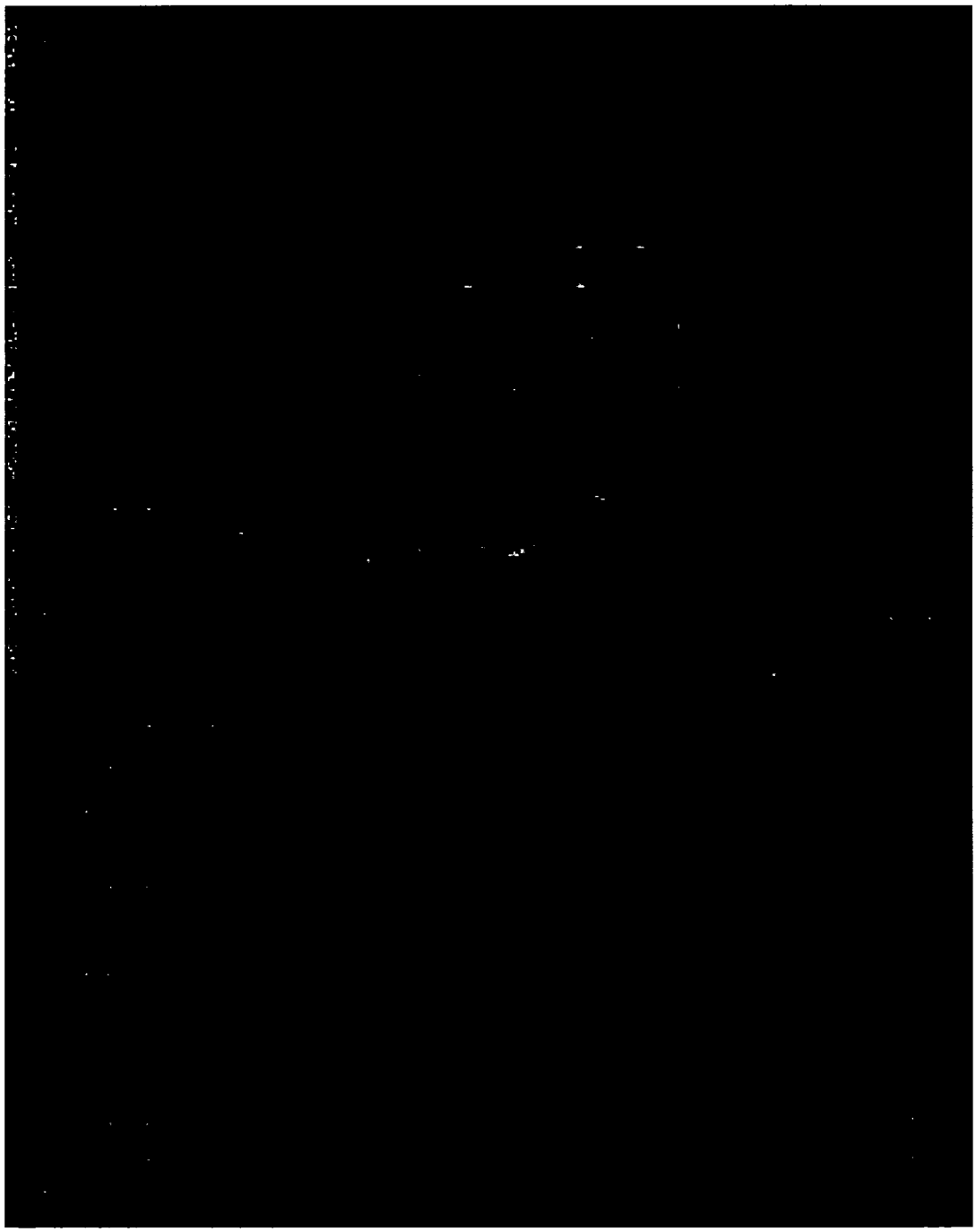

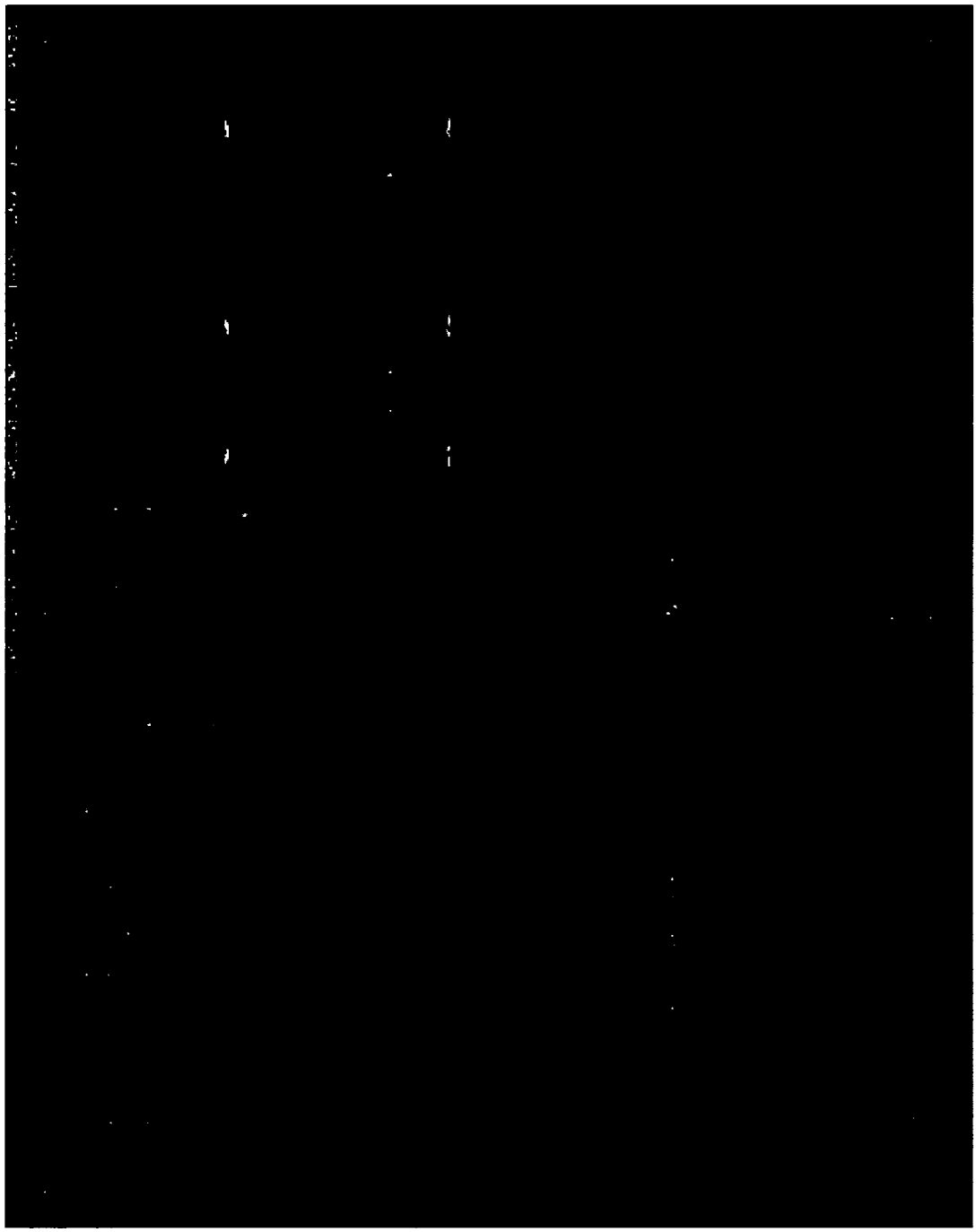

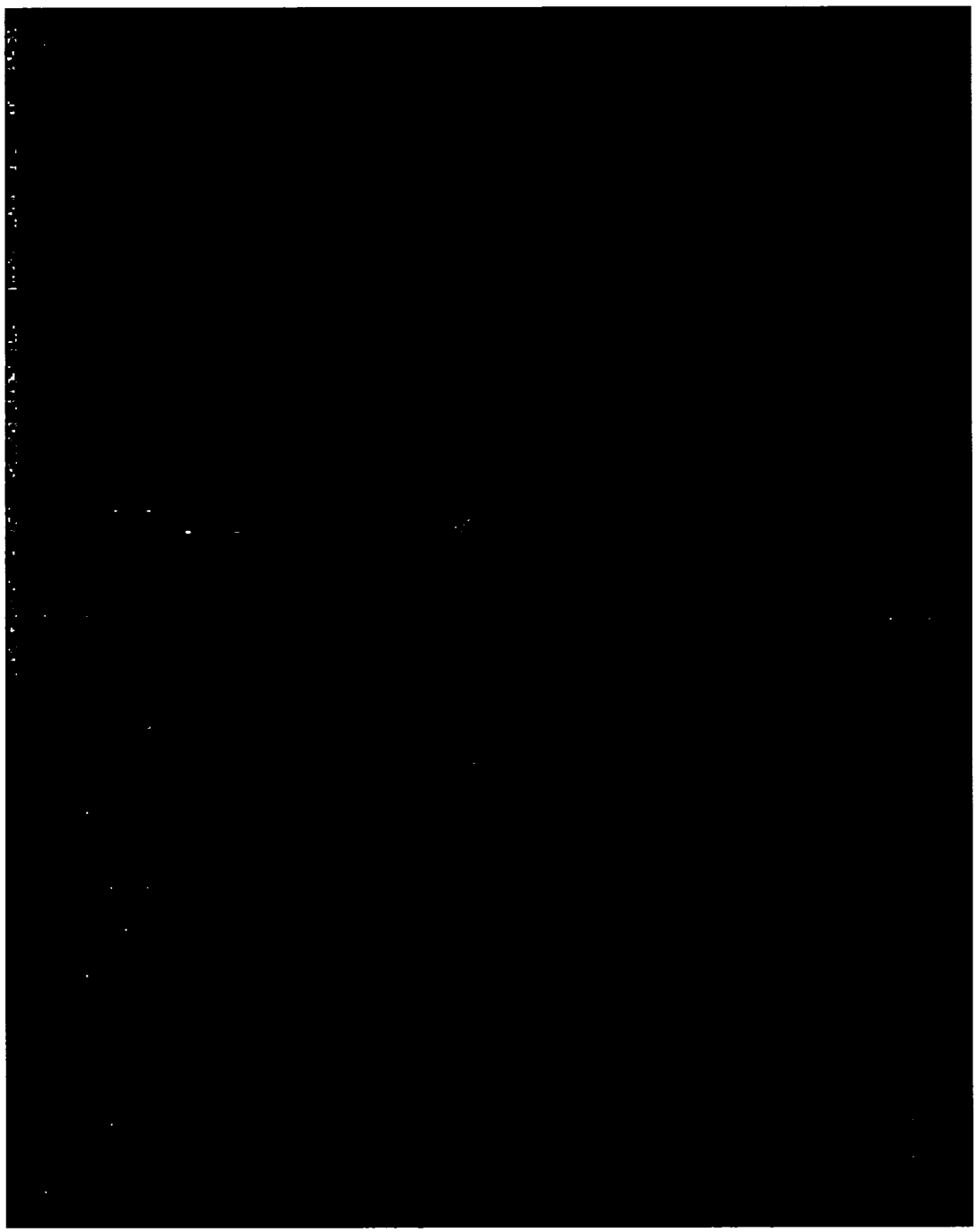

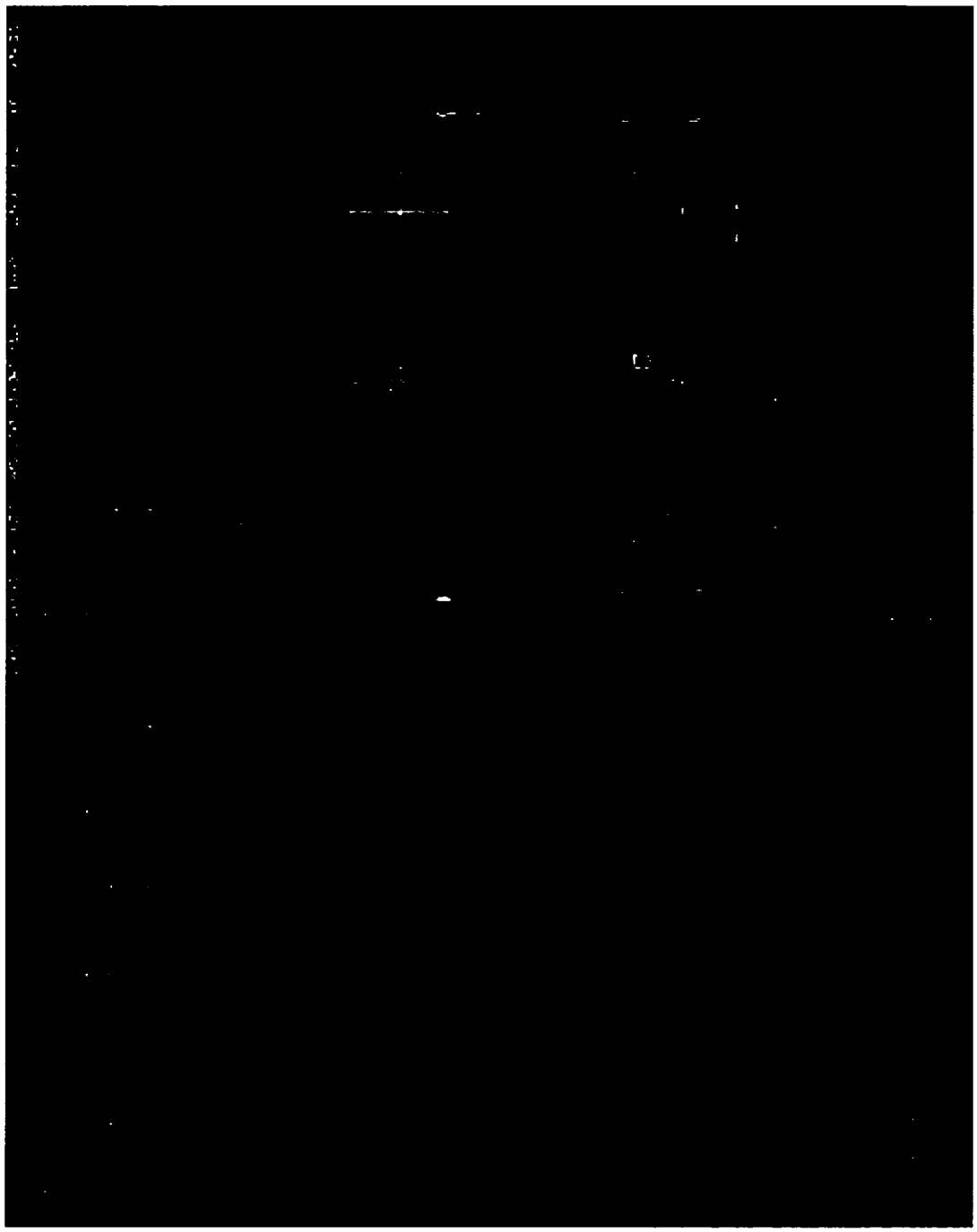

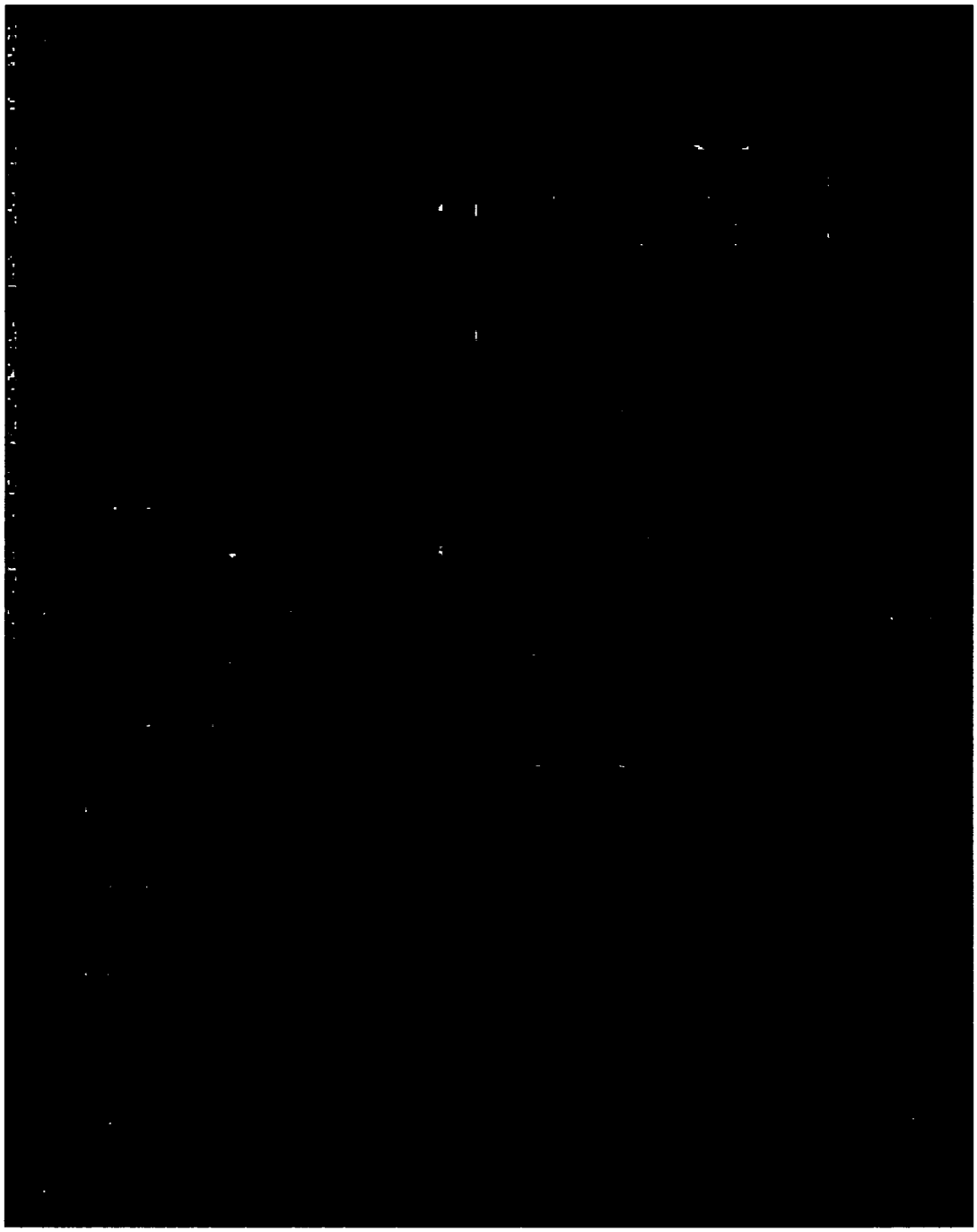

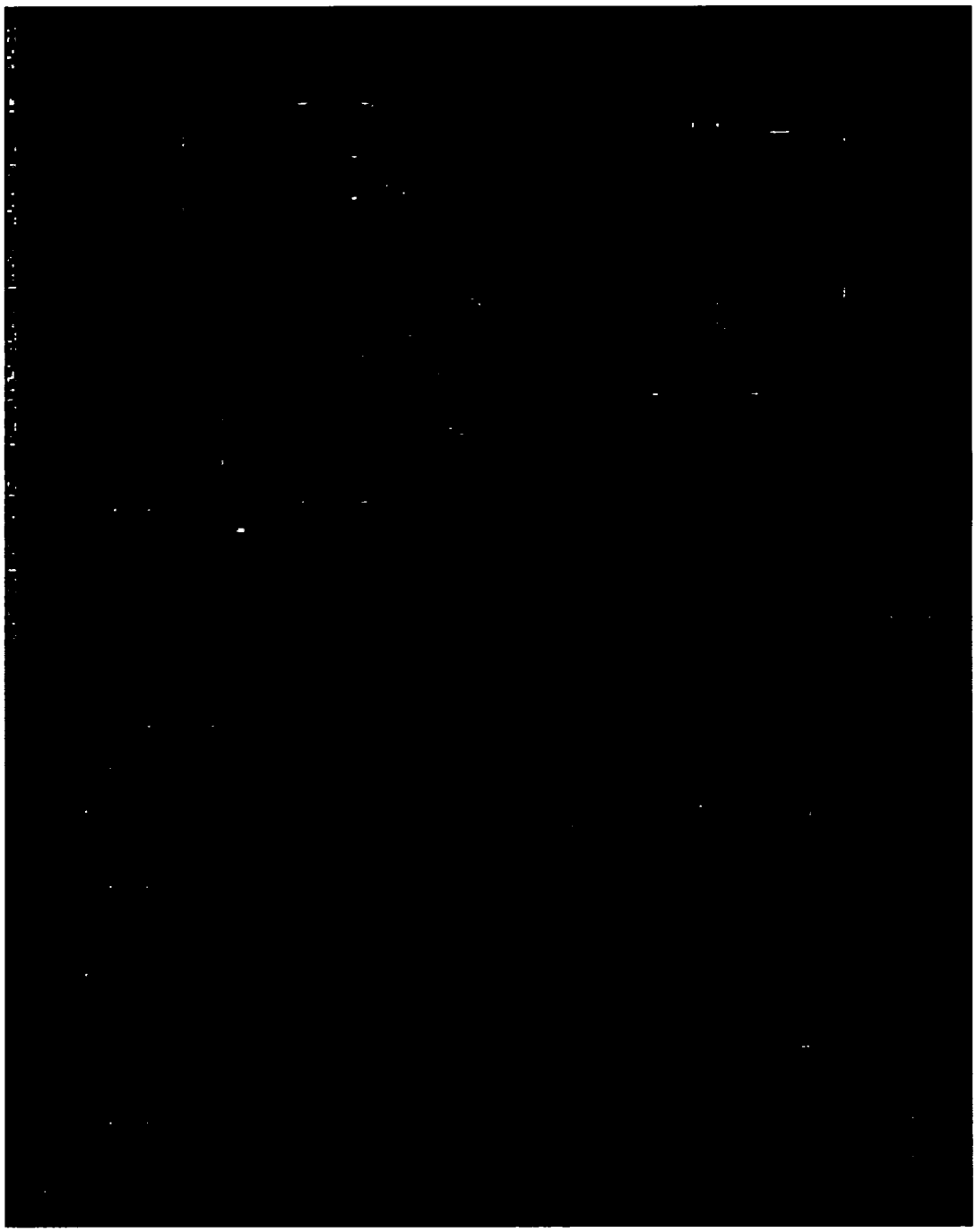

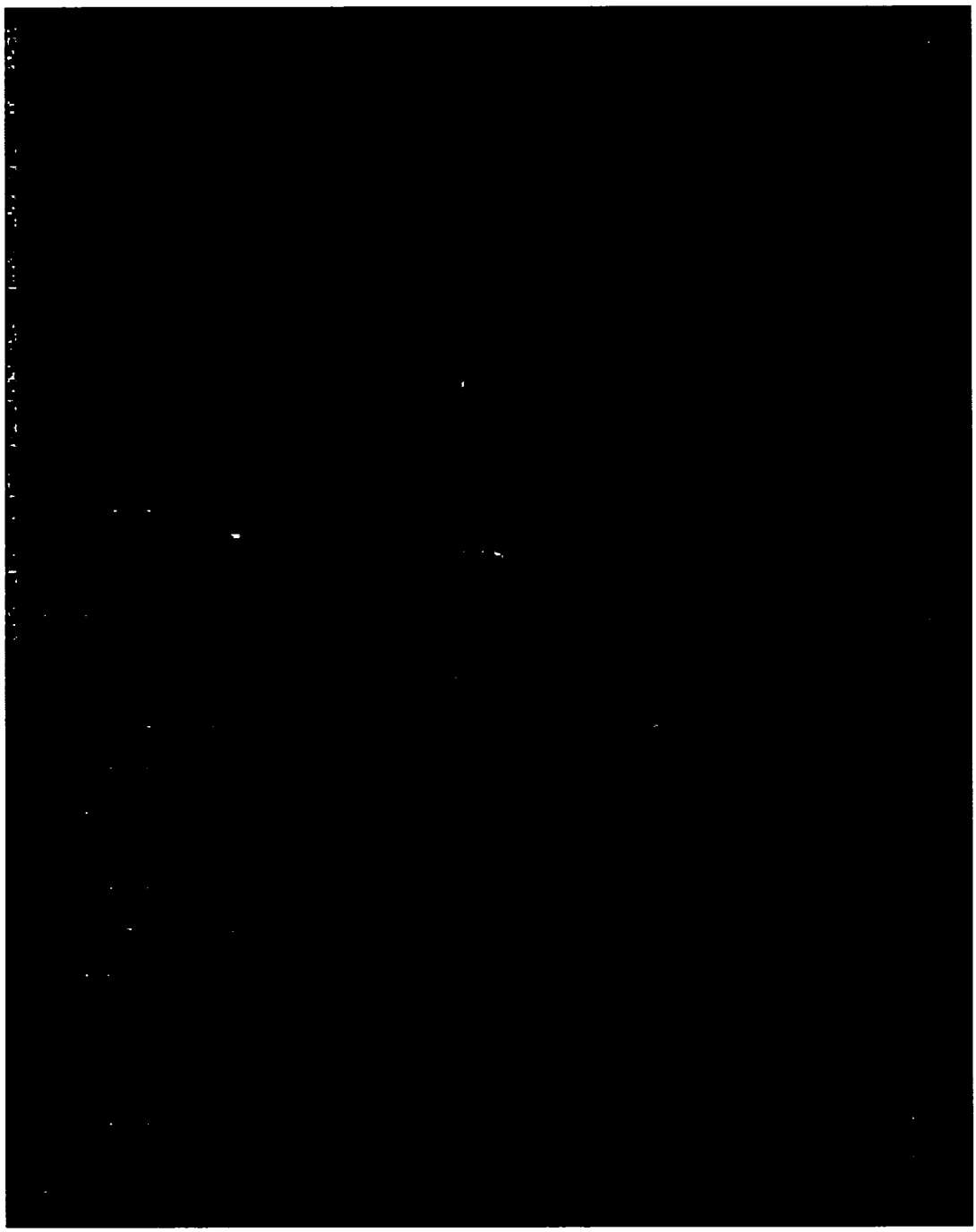

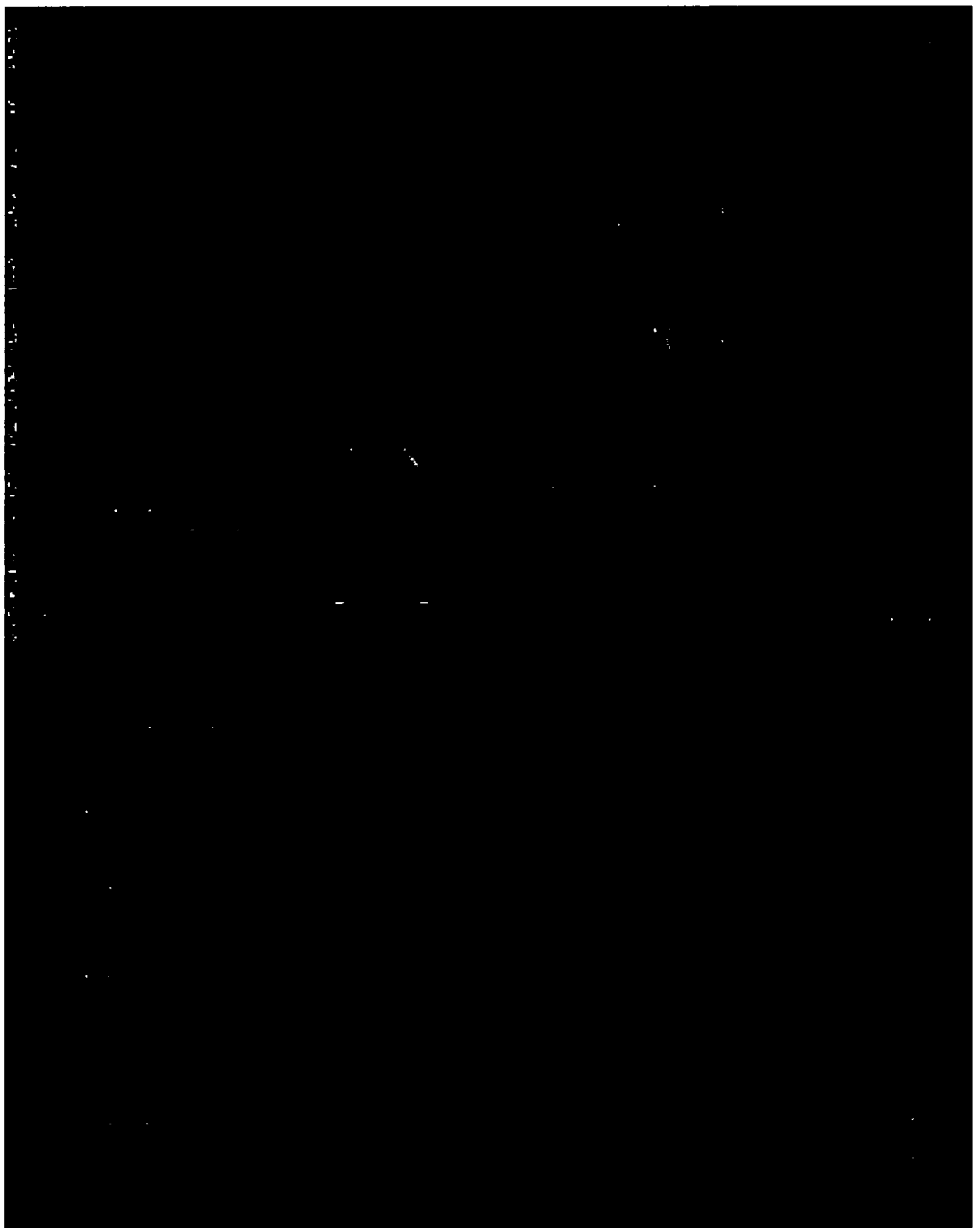

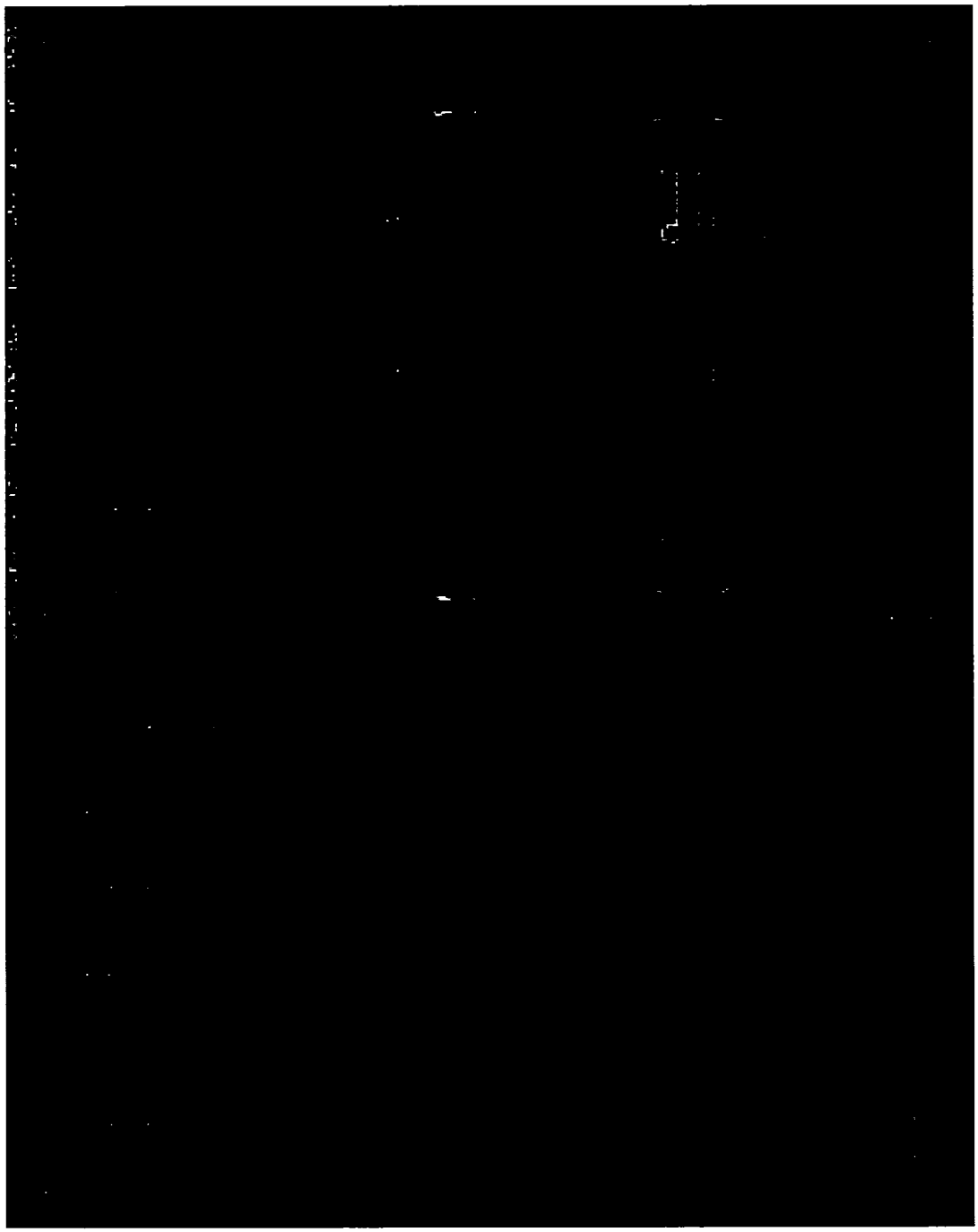

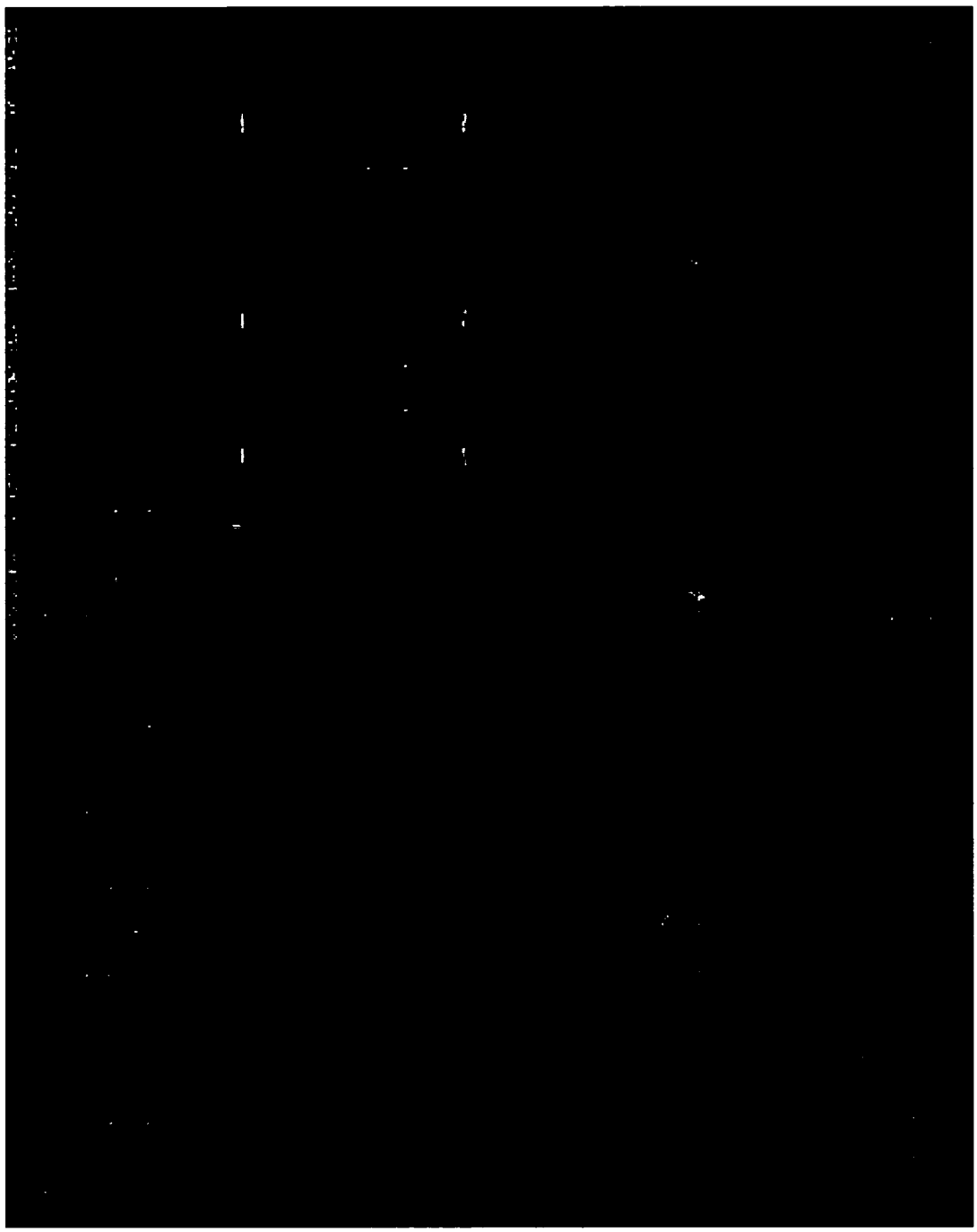

Appendix D Data Acquisition Program

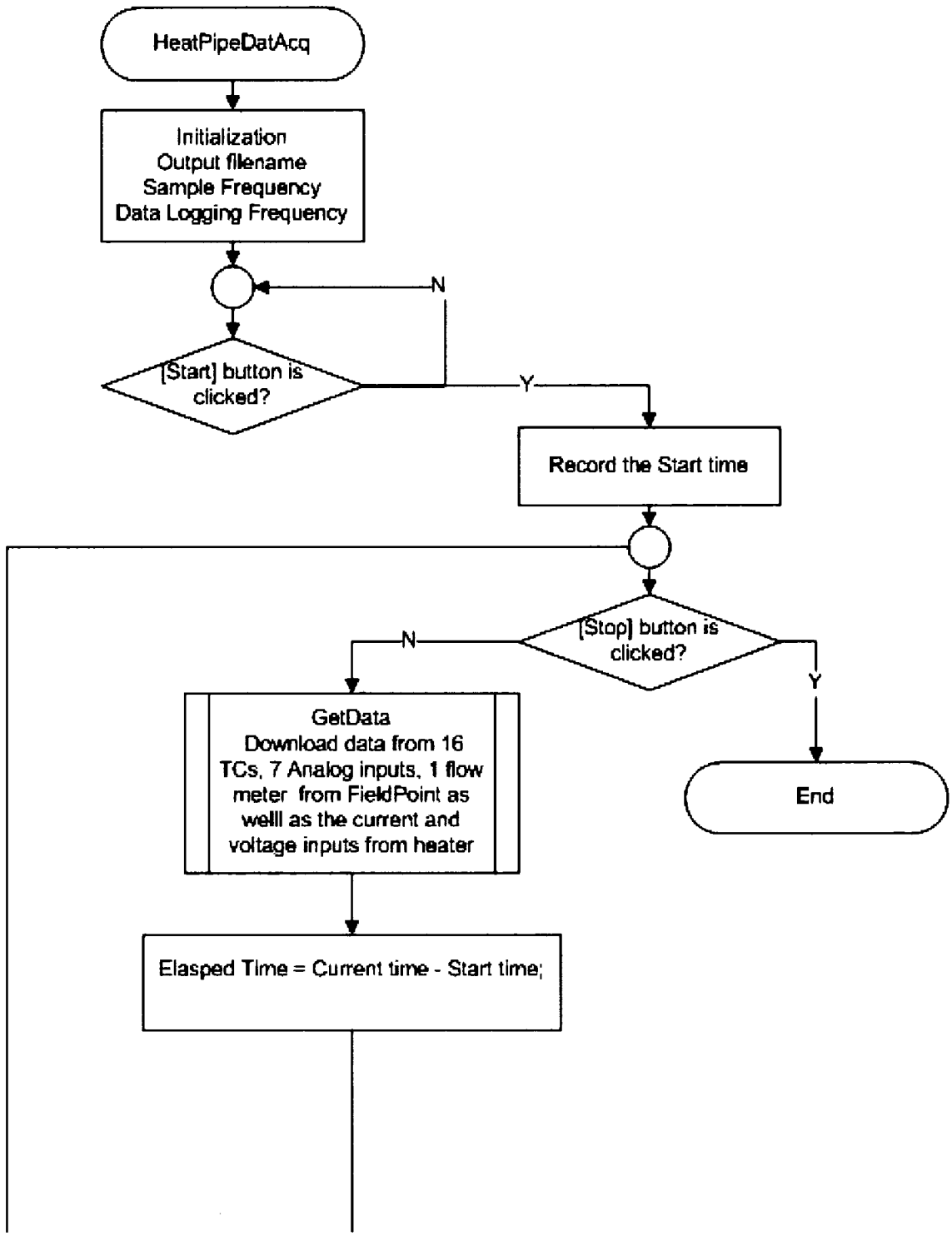

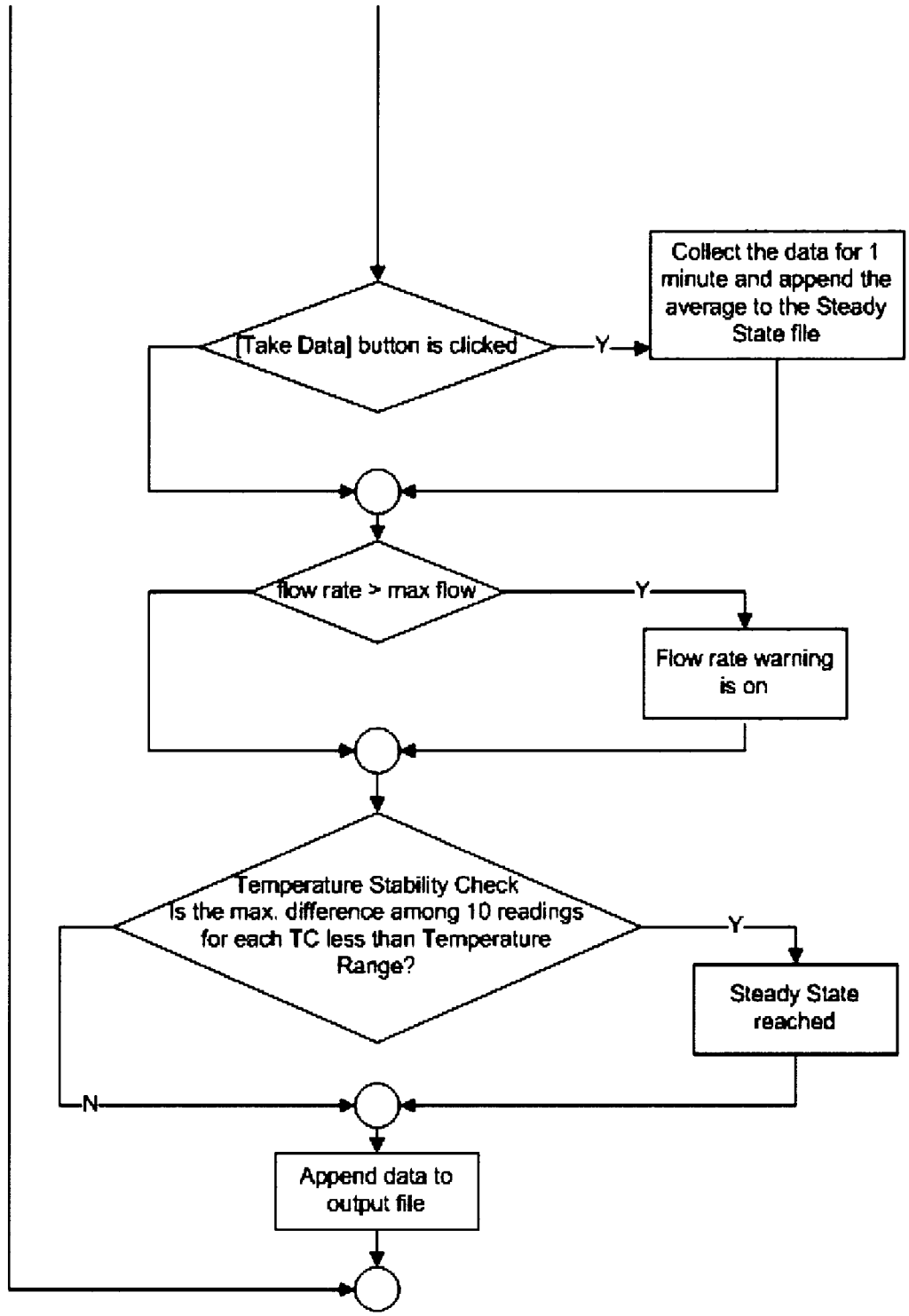

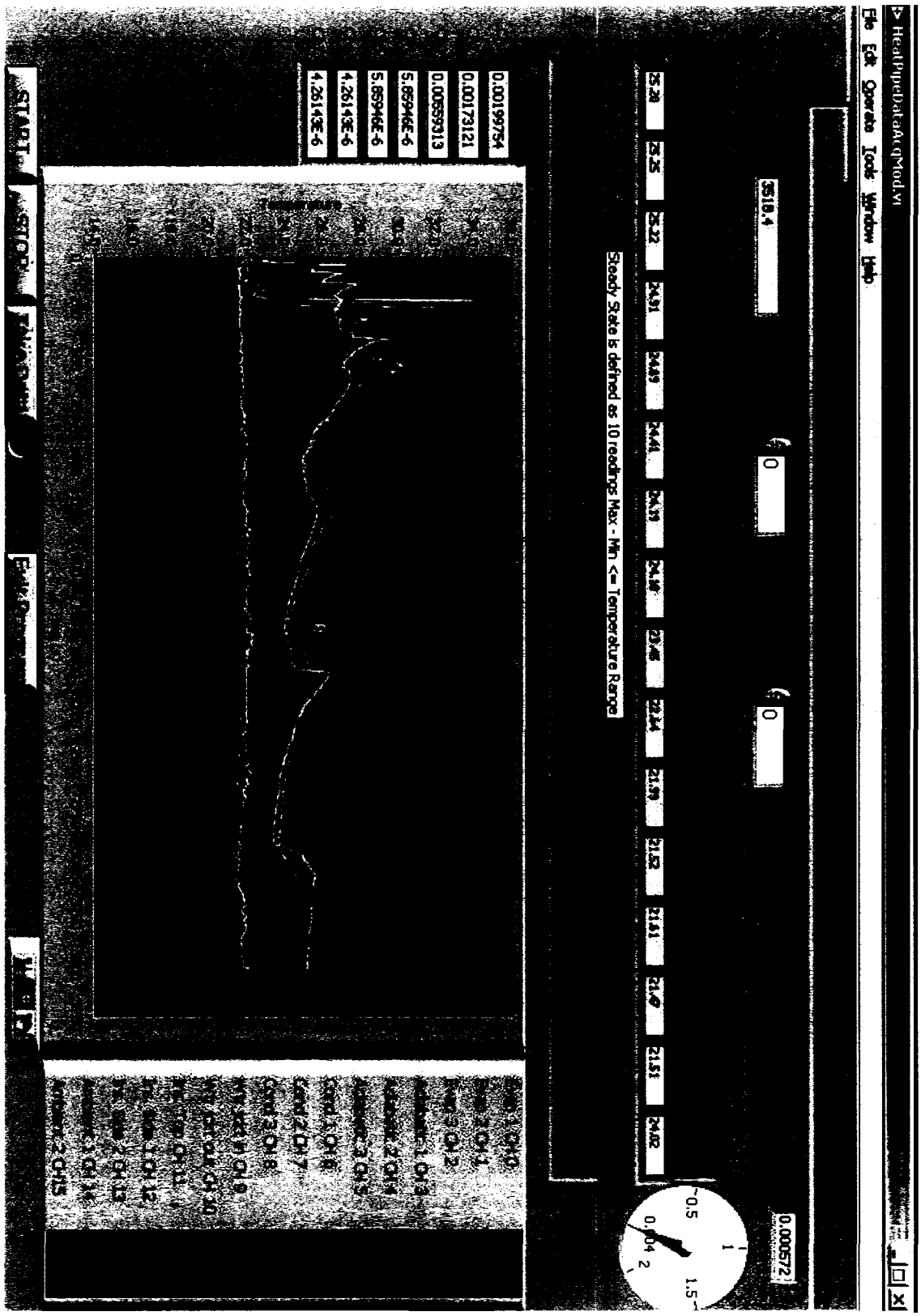

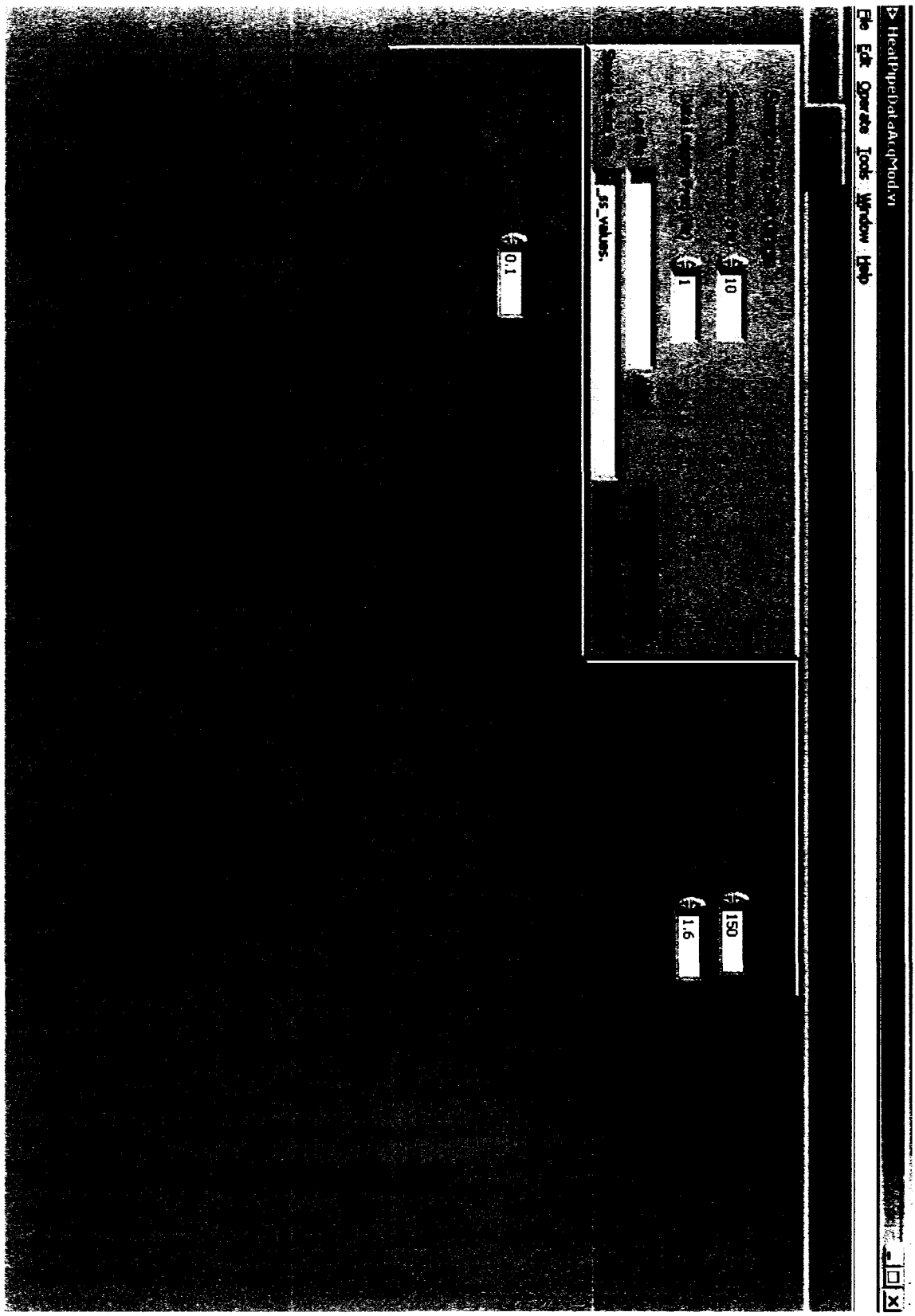

Appendix E "thermalPerformance" Program

```
function [data] = thermalPerformance(testRuns)

clear Flow; % Flow is also a Matlab variable. It must be explicitly cleared, otherwise it
              becomes confused with Flow from the .mat data files.

Answer = 'y';

count = 1;

lineMarkers = ['bo-'; 'gx-'; 'r*-'; 'cs-'; 'mv-'; 'yd-'; 'kp-']; % These are line markers used in
                                                                    plotting

legendTag = [];

while answer == 'y'

load (testRuns);  %testRuns is the name of the ".mat" file corresponding to the desired
                    heat pipe run

taredFlowRate = Flow - Flow(1); % Tares the flowrate by subtracting the zero flow
                                  reading from all values

end

if taredFlowRate > 1.606

   disp('Flowrate out of range');

end


heatPipeName = testRuns(3:4); % Assigns the appropriate name to the heat pipe based on
                                characters 3&4 in the file name

le = .05715; % Length of evaporator section in m

lc = .0666; % Length of condenser section in m. The condenser end plug extends into the
              water jacket ~3.2mm, but since there is no wick in this portion of the heat
              pipe, it is neglected in the calculations. The result is a shorter deltaX and a
              conservative estimate of effectiveK.
```

```
la = heatPipeLength - le - lc; % Length of adiabatic section (m)

deltaX = la + ((le + lc)/2); % Average effective length of heat pipe assuming evaporation
                               and condensation occur halfway through the evaporator and
                               condenser

heatIn = Voltage.*Current;


%%%%%%CALCULATE HEAT REMOVED%%%%%%

%This entire section describes the heat balance calculations. These results were not
    included in Section 5.3 , however they are listed here for documentation purposes.


%%%%%%CALCULATE WATER DELTA T%%%%%%

load thermistorCal2252; % Resistance vs temperature thermistor calibration data for 2252
                          ohm (25 C) thermistors

Vsup = 24; % Supply voltage = 24V. Voltage supplied to the voltage divider thermistor
             circuit.

resistor = 30050; % Resistance of the constant resistors in the voltage divider thermistor
                    circuits (ohms)

wtrInletR = AI1*resistor./(Vsup - AI1); % Resistance of the water inlet thermistor in the
                                          inlet voltage divider circuit (ohms)

wtrInletT = interp1(thermistorR, thermistorTemp, wtrInletR); %Water inlet temperature
                                                               (C)

wtrOutletR = AI2*resistor./(Vsup - AI2); % Resistance of the water outlet thermistor in
                                           the outlet voltage divider circuit (ohms)

wtrOutletT = interp1(thermistorR, thermistorTemp, wtrOutletR);

waterDeltaT = wtrOutletT - wtrInletT; % Temperature difference across the water jacket

%waterDeltaT = ch10 - ch9;

end
```

```
%%%%%CALCULATE COOLANT SPECIFIC HEAT & MASS FLOWRATE%%%%

% Coolant properties from Prestone Specific Heat graph and MSDS for Extended Life
    Coolant. Properties for water are from Holman (Heat Transfer, 9th ed.). A 50/50
    volume mixture of distilled water and coolant was used. Considering a 1 L mixture:

averageFluidTemp = (wtrInletT + wtrOutletT)/2;

load WaterData; % Properties of water

load specificHeatCoolant; % Contains data on the specific heat of aqueous Prestone
                                    coolant solutions

waterDensity = interp1(temp, density, averageFluidTemp);

% Assume a constant specific gravity for the coolant, from Prestone MSDS
     410. SG = (1.07 + 1.14)/2

coolantSG = (1.07 + 1.14)/2;


% Mass of coolant (kg) per litre = volume(L) x specific gravity of coolant x density of
    water at cooling fluid average temperature x 1 m^3 per 1000L:

massCoolant = 0.5*coolantSG*waterDensity/1000;

massWater = 0.5*1*waterDensity/1000; % For water, same calculation as above

massPercentCoolant = massCoolant./(massCoolant + massWater)*100;


% Interpolates to find the specific heat of the coolant/water solution at the average
    cooling fluid temperature:

specificHeat = interp2(xWeight, yTemp, zSpecificHeat, massPercentCoolant,
averageFluidTemp)*4186.8;

coolingSolutionDensity = (massCoolant + massWater)/1e-3; %in kg/m^3

massFlowrate = taredFlowRate / (60*1000) .* coolingSolutionDensity; %in kg/s


%%%%%%%%%%%%%%%%%%%%%%%%%%%%%%%%%%%%%%%%%%%%%%%%%

heatOut = massFlowrate.*specificHeat.*waterDeltaT; % Calculation of heat removed
```

```
%%%%%CALCULATE FREE CONVECTION LOSSES%%%%%

avHeaterInsTemp = (ch11 + ch12 + ch13)/3; % Average heater insulation temperature

avAmbientTemp = (ch14 + ch15)/2; % Average ambient temperature

Tf = (avHeaterInsTemp + avAmbientTemp)/2 + 273.15; %Absolute film temperature (K)

load airData; %Loads air tables

beta = Tf.^-1; % (K^-1)

heaterDia = 0.09; % Approximate diameter of heater wrapped with insulation (m)

heaterLength = 0.085; % Approximate heater length with insulation (m)


% Kinematic viscosity of air at the film temperature (m^2/s):

kinematicViscosity = interp1(airTemp, airKinematicVisc, Tf);

thermalCond = interp1(airTemp, airK, Tf); %Thermal conductivity of air at the film
                                                    temperature (W/m*C)

prandtlNo = interp1(airTemp, airPr, Tf); %Prandtl Number of air at the film temperature


if findstr(testRuns, 'horizontal') > 0 %Estimate the heat loss to the ambient along the
                                        horizontal heater. Assume isothermal surface, free
                                        convection

   orientation = ' Horizontal';

        % The Rayleigh Number:

   GrPr = (9.81.*beta.*abs(avHeaterInsTemp -
            avAmbientTemp)*heaterDia^3./kinematicViscosity.^2).*prandtlNo;

   denominator = (1 + (0.559./prandtlNo).^(9/16)).^(16/9);

        % For 10^-5 < Rayleigh No. < 10^12, Churchill and Chu (in Holman):

   Nusselt = (0.6 + 0.387*(GrPr./denominator).^(1/6)).^2;
```

```
    h = Nusselt.*(thermalCond/heaterDia); % The heat transfer coefficient in W/m^2*C

elseif (findstr(testRuns, 'assistG') > 0) % Estimate the heat loss to the ambient along the
                                            vertical heater. Assume isothermal surface, free
                                            convection

    orientation = ' Gravity Assisted';

        % The Rayleigh Number:

    GrPr = (9.81.*beta.*abs(avHeaterInsTemp -
            avAmbientTemp)*heaterLength^3./kinematicViscosity.^2).*prandtlNo;

    denominator = (1 + (0.492./prandtlNo).^(9/16)).^(8/27);

        % For 10^-1 < Rayleigh No. < 10^12:

    Nusselt = (0.825 + (0.387*GrPr.^(1/6)./denominator)).^2;

    h = Nusselt.*(thermalCond/heaterLength); % The heat transfer coefficient in
                                                W/m^2*C

elseif (findstr(testRuns, 'againstG') > 0) % Same equations as for 'assistG' above

    orientation = ' Against Gravity';

        % The Rayleigh Number:

    GrPr = (9.81.*beta.*abs(avHeaterInsTemp -
            avAmbientTemp)*heaterLength^3./kinematicViscosity.^2).*prandtlNo;

    denominator = (1 + (0.492./prandtlNo).^(9/16)).^(8/27);

        % For 10^-1 < Rayleigh No. < 10^12:

    Nusselt = (0.825 + (0.387*GrPr.^(1/6)./denominator)).^2;

    h = Nusselt.*(thermalCond/heaterLength); % The heat transfer coefficient in
W/m^2*C

else

    orientation = ' Gravity Assisted';
```

```
        %The Rayleigh Number:

    GrPr = (9.81.*beta.*abs(avHeaterInsTemp -
            avAmbientTemp)*heaterLength^3./kinematicViscosity.^2).*prandtlNo;

    denominator = (1 + (0.492./prandtlNo).^(9/16)).^(8/27);

    Nusselt = (0.825 + (0.387*GrPr.^(1/6)./denominator)).^2; % for 10^-1 < Rayleigh No.
< 10^12

    h = Nusselt.*(thermalCond/heaterLength); % The heat transfer coefficient in
                                                W/m^2*C

    disp('Wrong filename');

    %return;

end


heatLoss = h.*(pi*heaterDia*heaterLength).*(avHeaterInsTemp - avAmbientTemp);

%%%%%%%%%%%%%%%%%%%%%%%%%%%%%%%%%%%%%%%%%%%%%%%%%%%%


heatBalance = heatIn - heatOut - heatLoss;

heatPipeDeltaT = ch1 - ch7; % Heat pipe temperature difference between middle of
                                evaporator to middle of condenser

area = pi/4*9.525e-3^2; % The cross - sectional area of the heat pipe based on the outer
                            diameter

effectiveK = heatIn*deltaX./(area*heatPipeDeltaT); % The effective thermal conductivity
                                                        in W/mC

data = [heatIn, heatOut, heatLoss, heatBalance, heatPipeDeltaT, effectiveK];


%%%%SCREEN DATA DISPLAY%%%%

disp('Pwr Input(W)  Pwr Output(W)   Heat Loss(W)    Heat Bal.(W)   Delta T (C)  Keff
(W/m*C)');

format bank;
```

```
disp(data((2:end),:));

%%%%%%%%PLOTTING%%%%%%

lineMarker = lineMarkers(count,:);

count = count + 1;

xx = linspace(min(heatIn), max(heatIn));

yy = interp1(heatIn(2:end), effectiveK(2:end), xx, 'cubic');

%plot(heatIn, effectiveK, lineMarker, xx, yy);
plot(heatIn, effectiveK, lineMarker);

hold on;

title('Effective Thermal Conductivity vs Heat Input');

xlabel('Heat Input (W)');

ylabel('K_e_f_f (W/m*C)');

grid on;

legendTag = [legendTag;strcat(heatPipeName, orientation)];

legend(legendTag, 0);

answer = input('Plot another line?');

testRuns = input('Test run?');

end
```

Appendix F Additional Performance Results

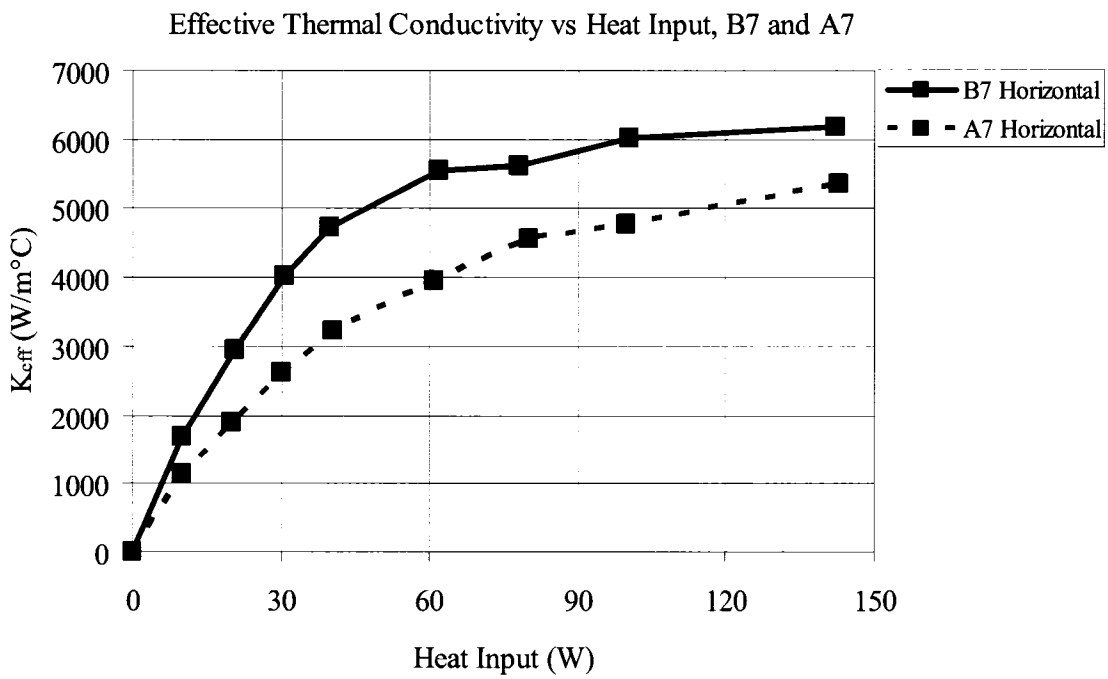

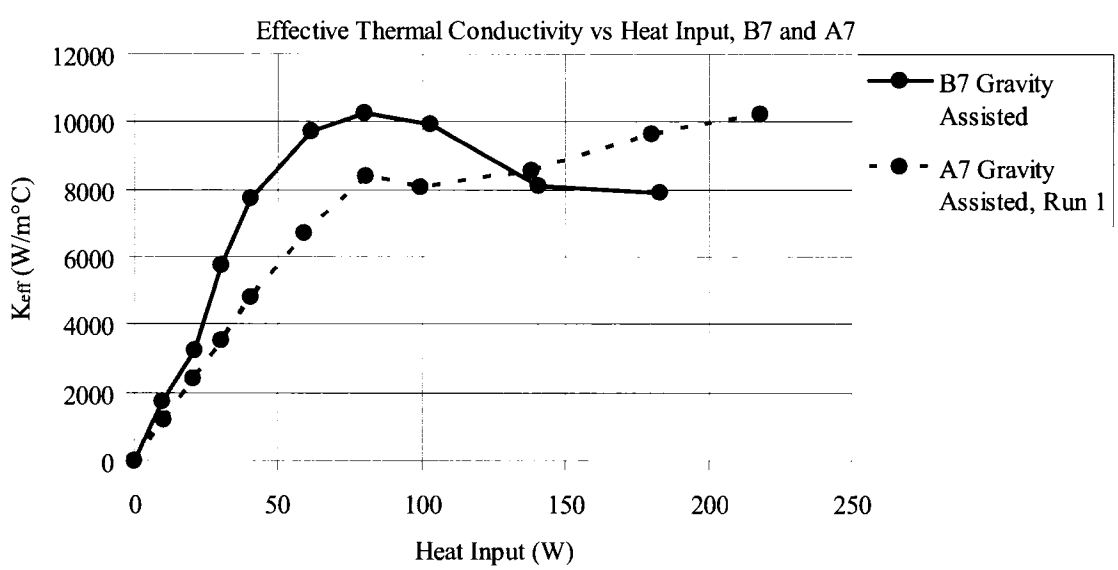

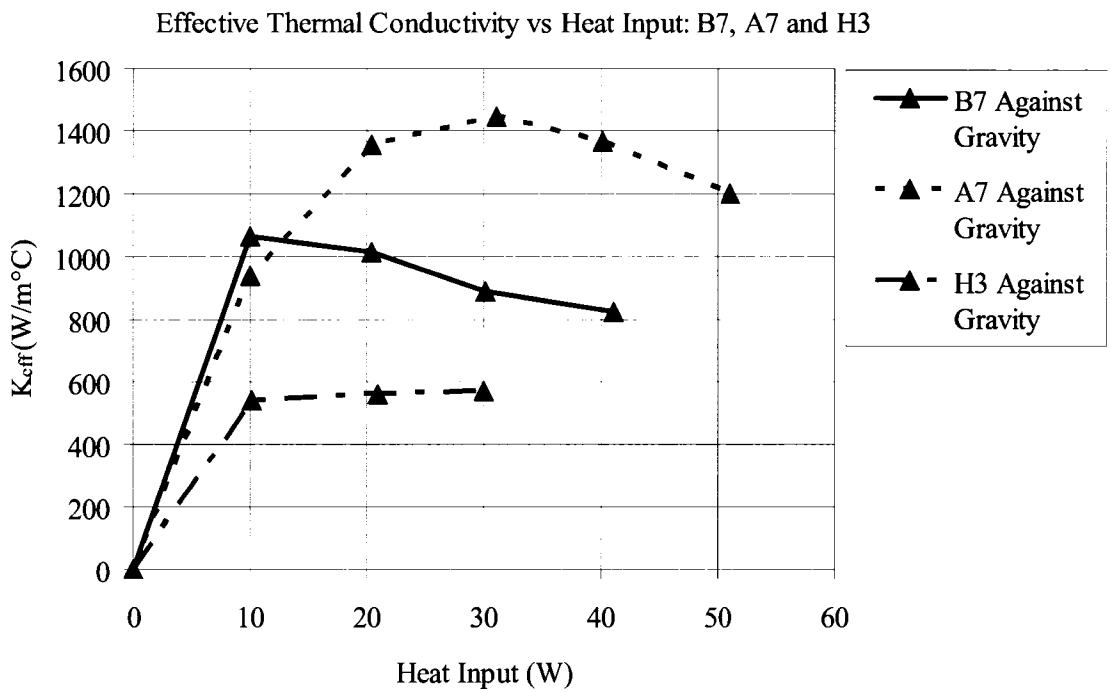

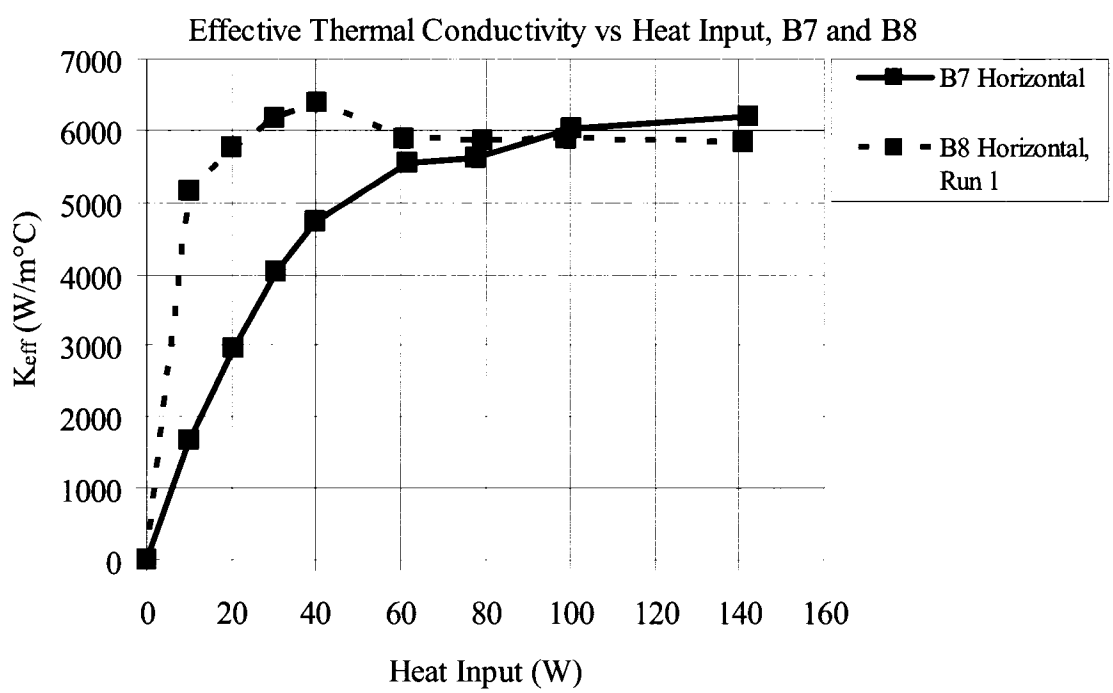

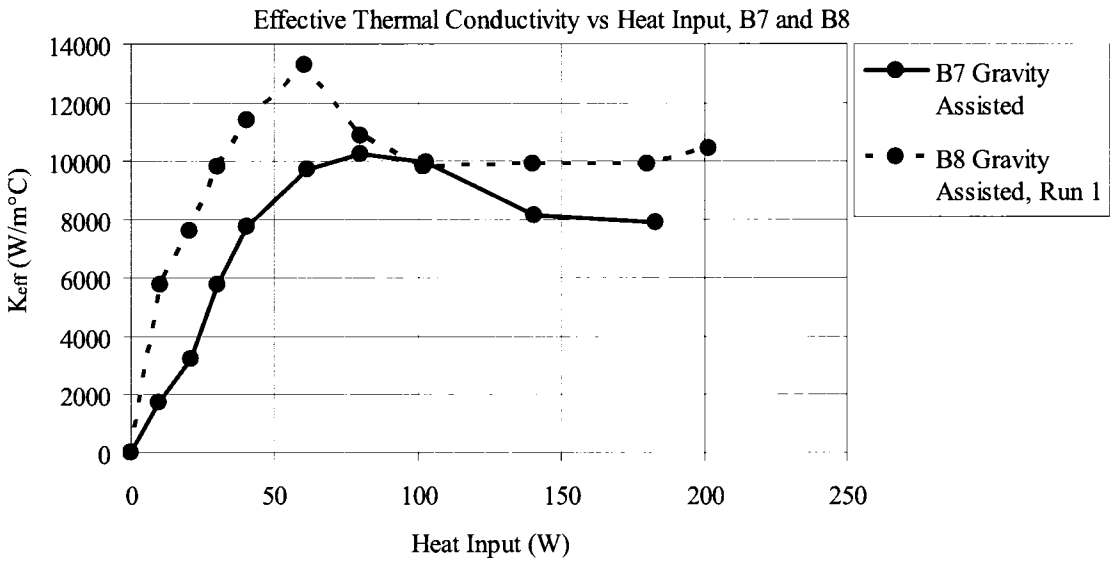

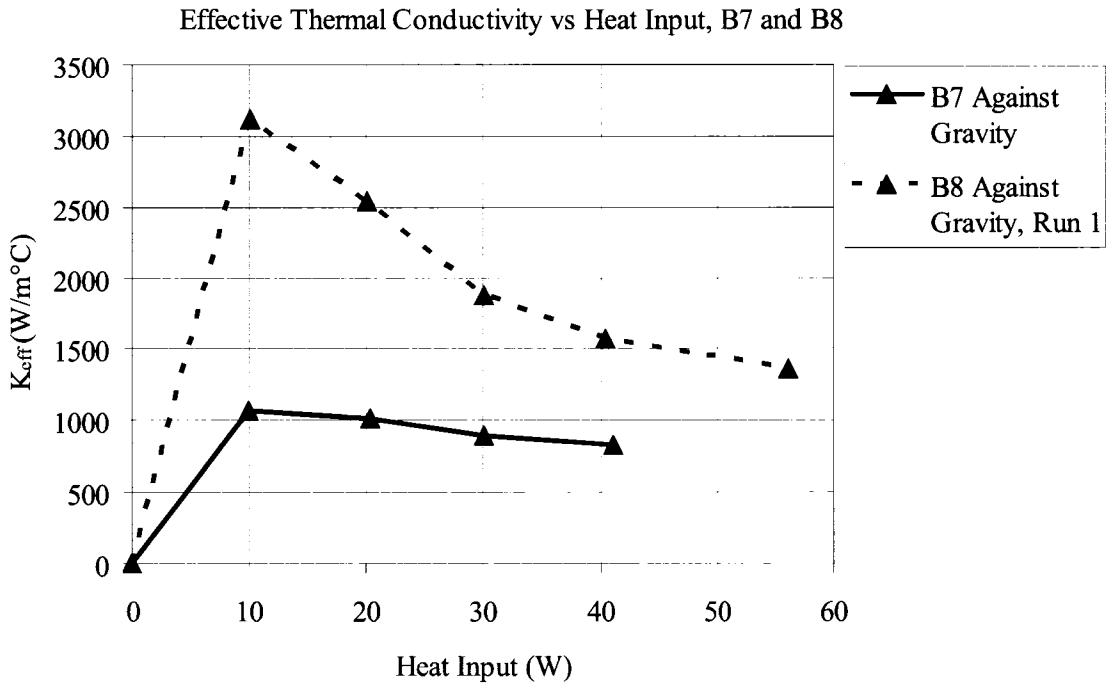

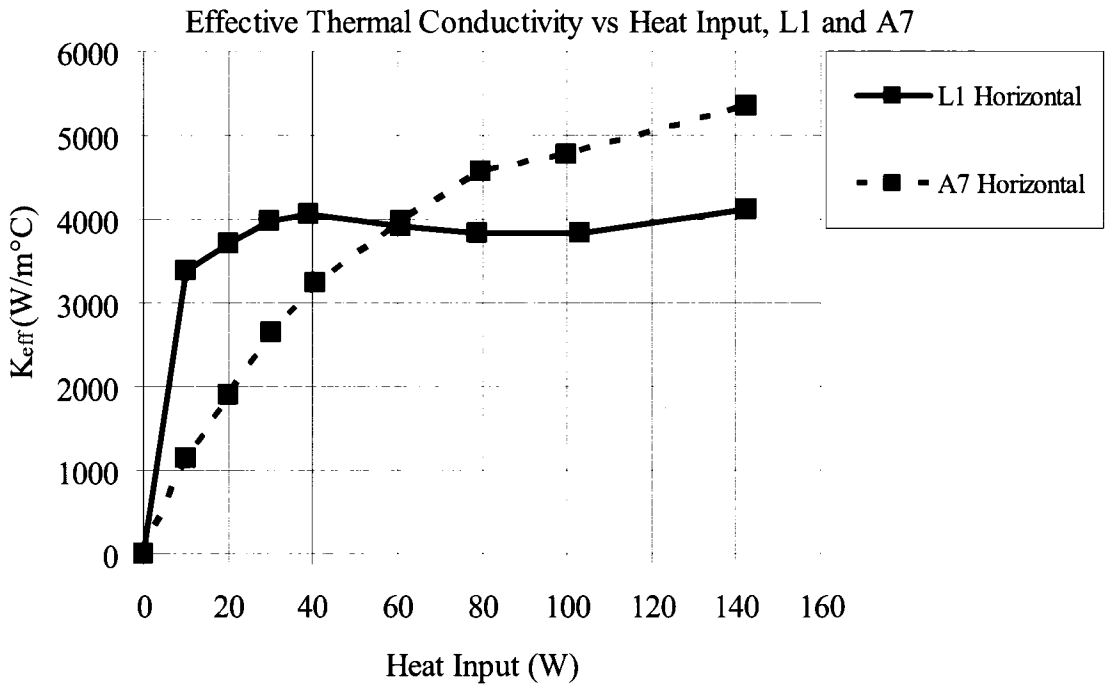

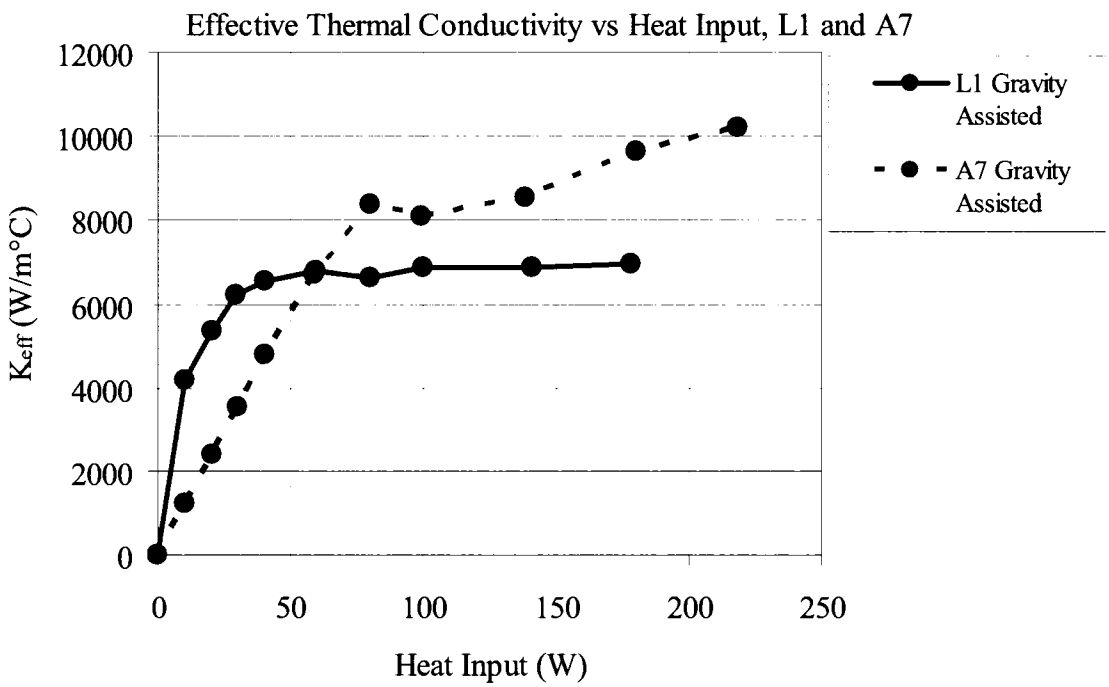

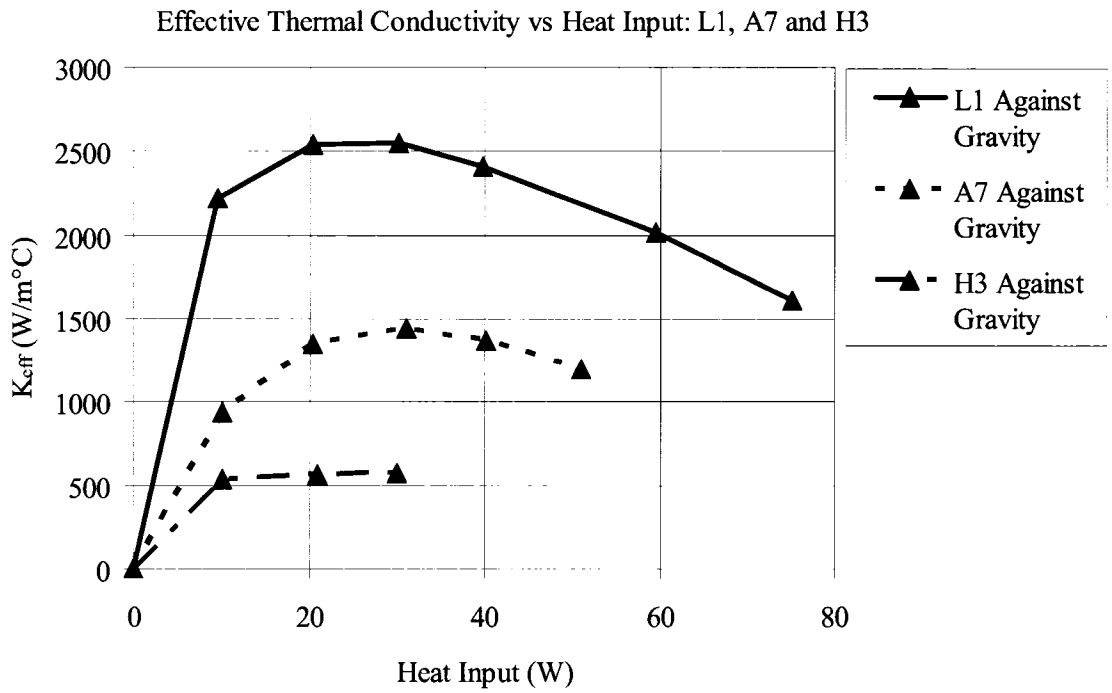

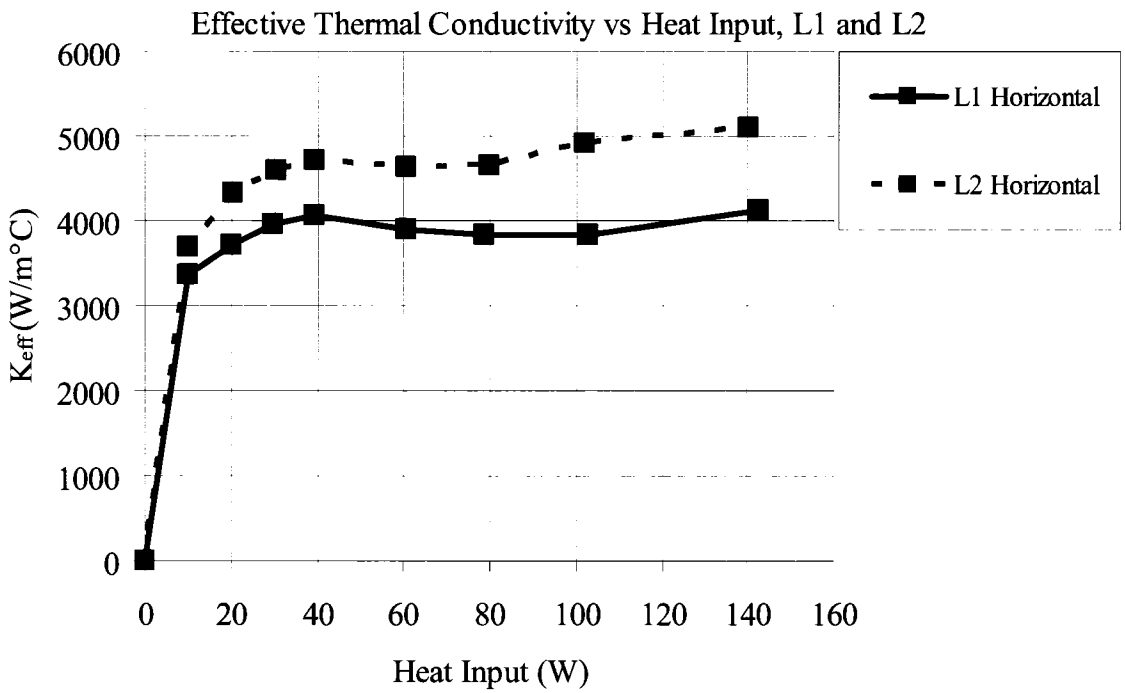

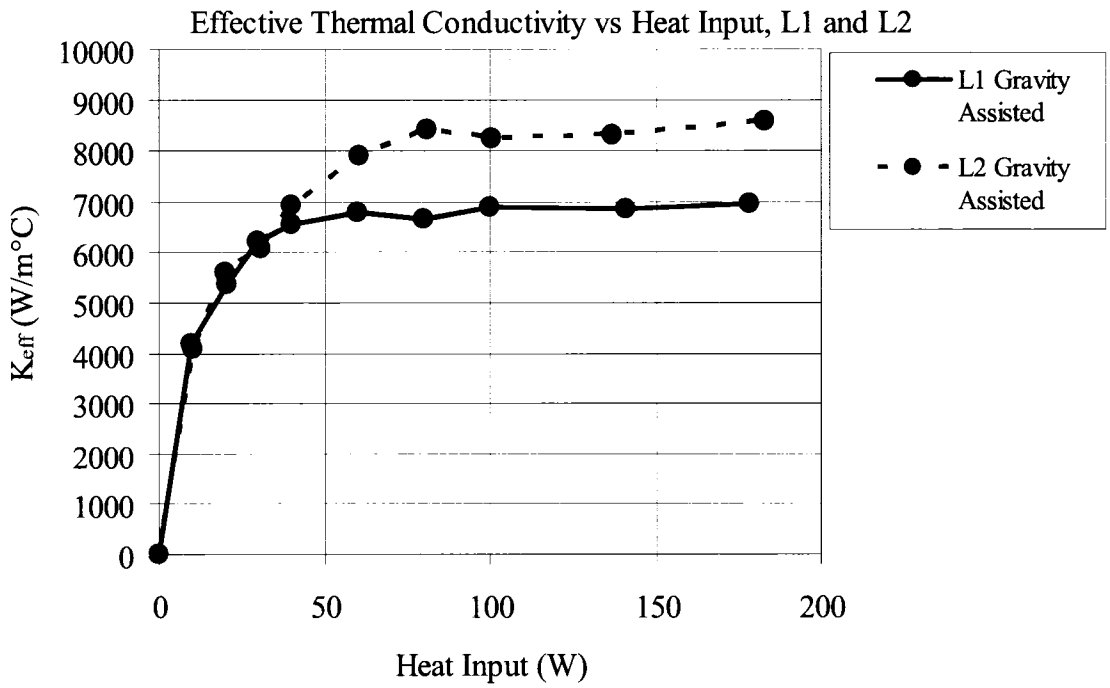

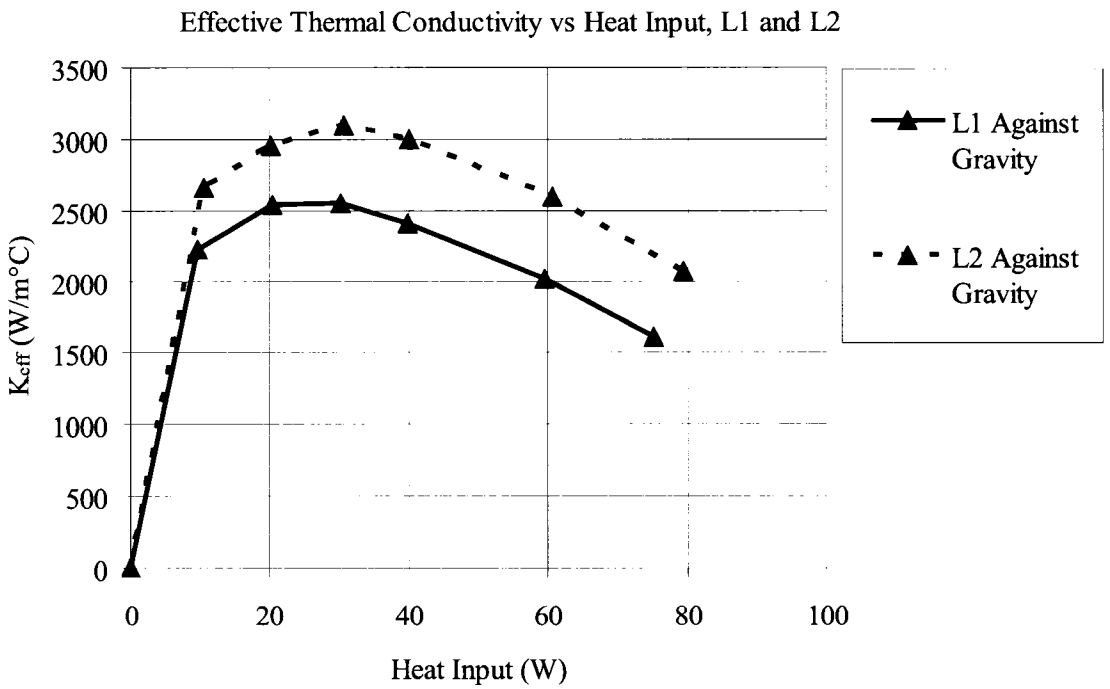

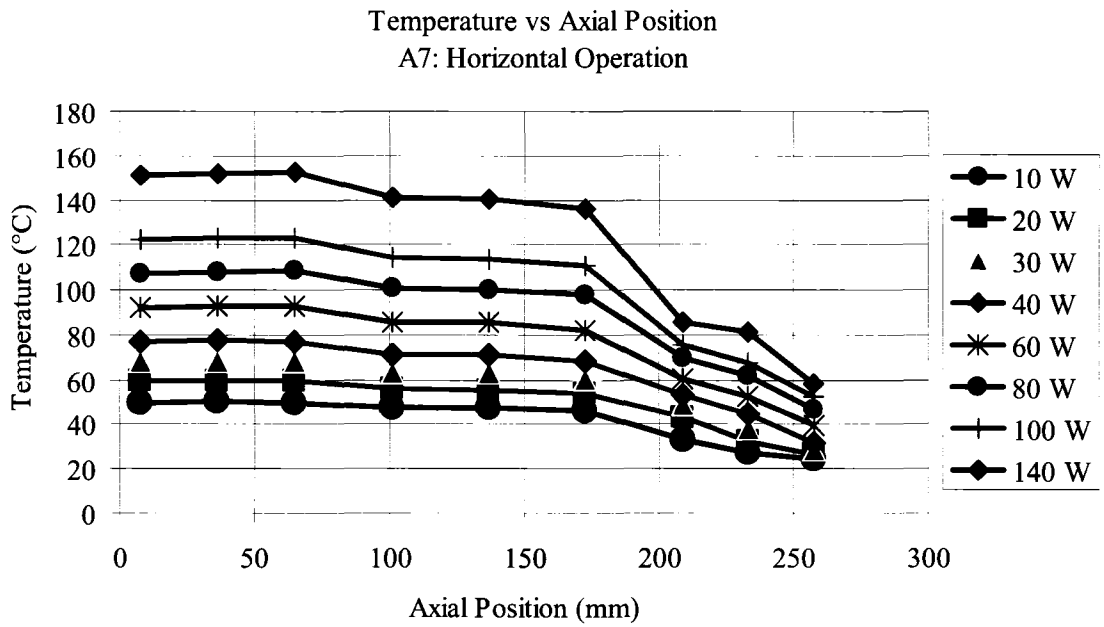

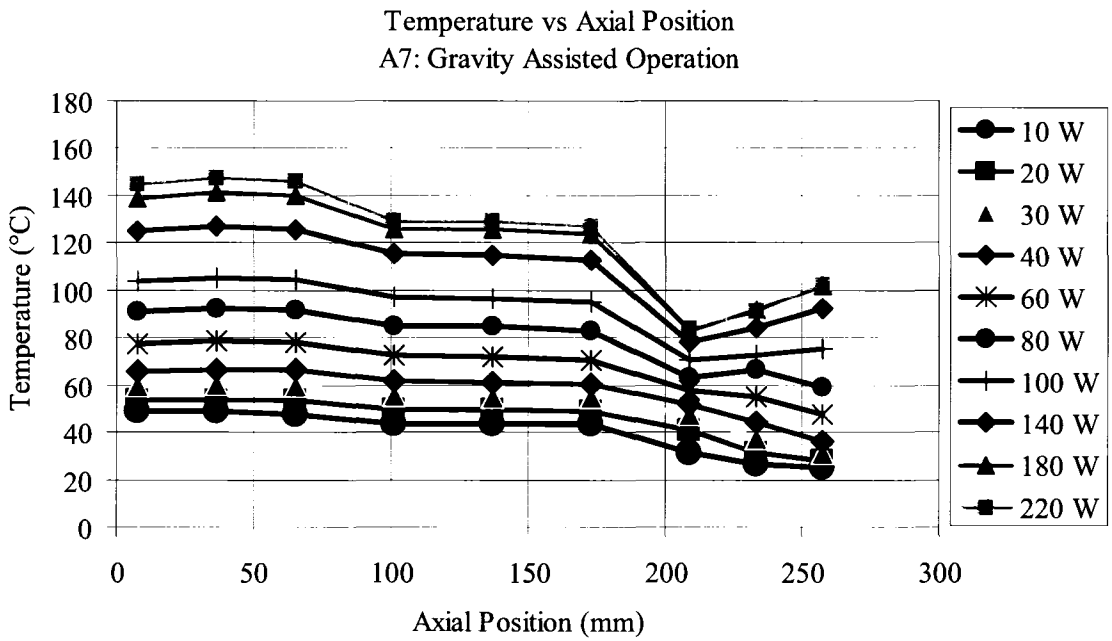

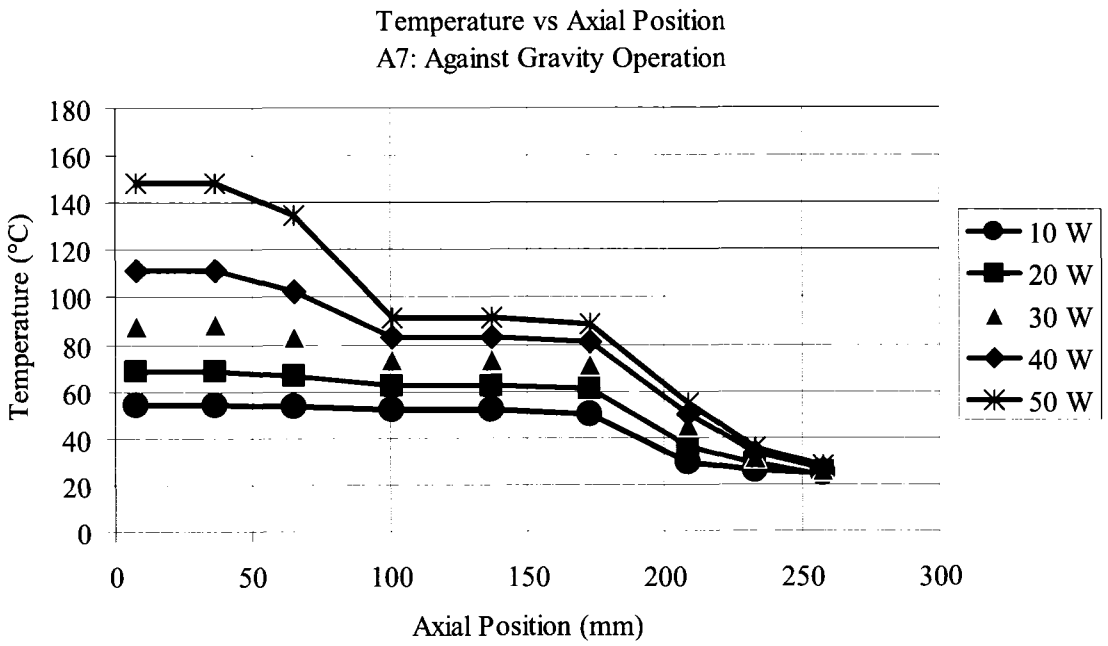

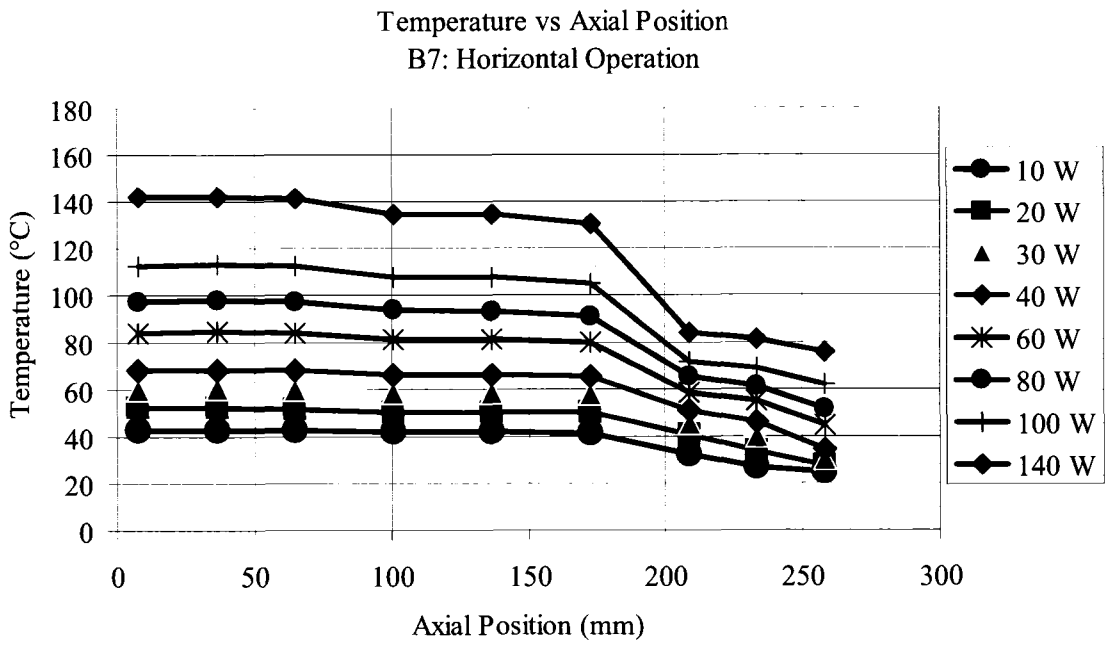

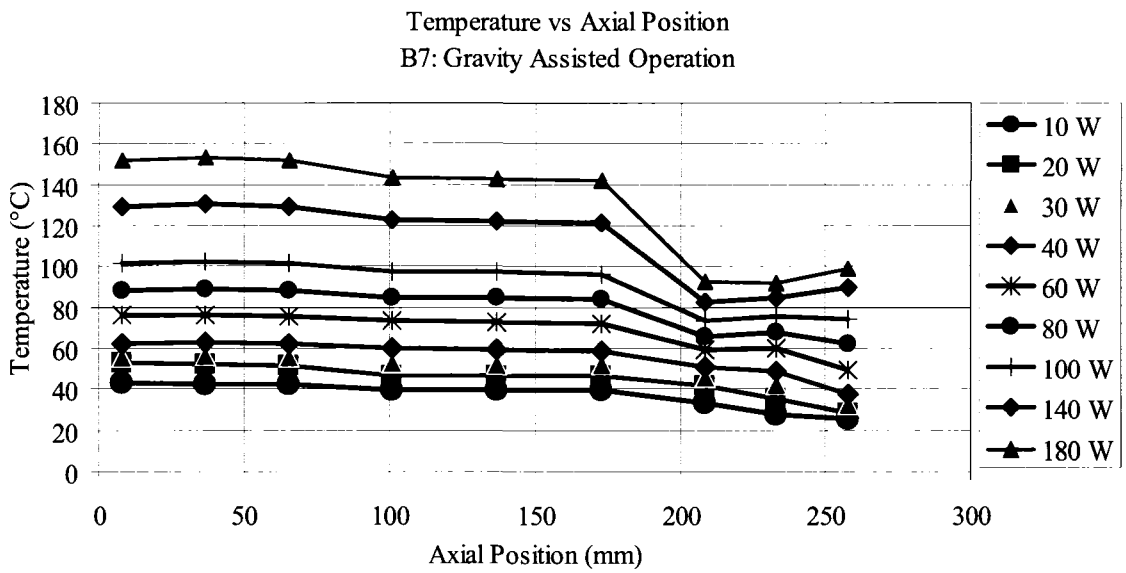

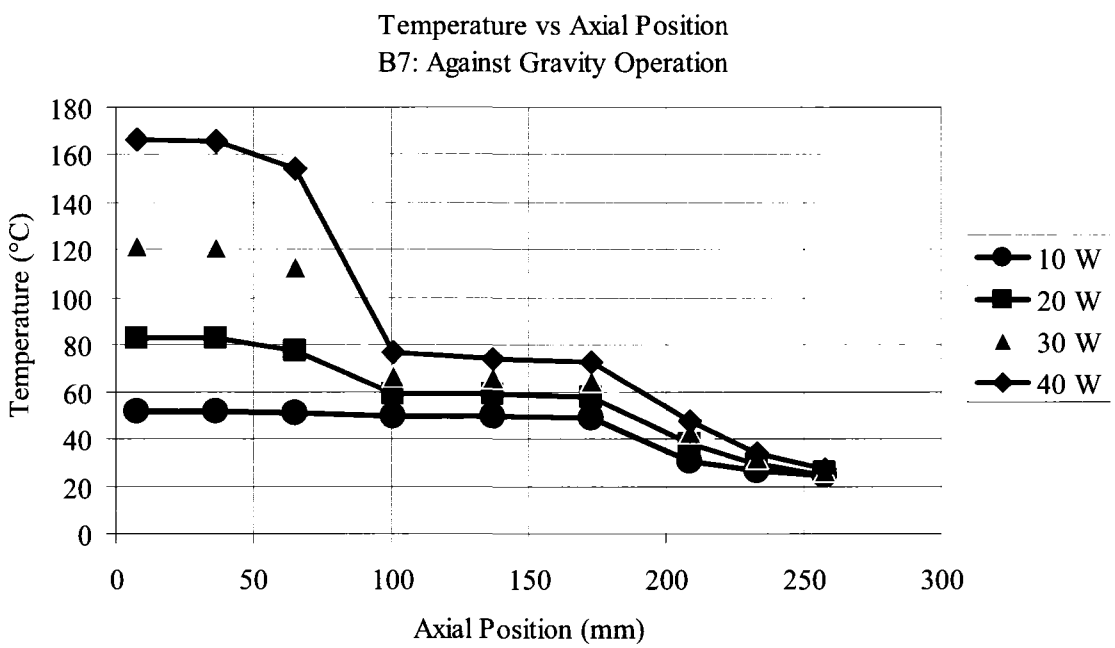

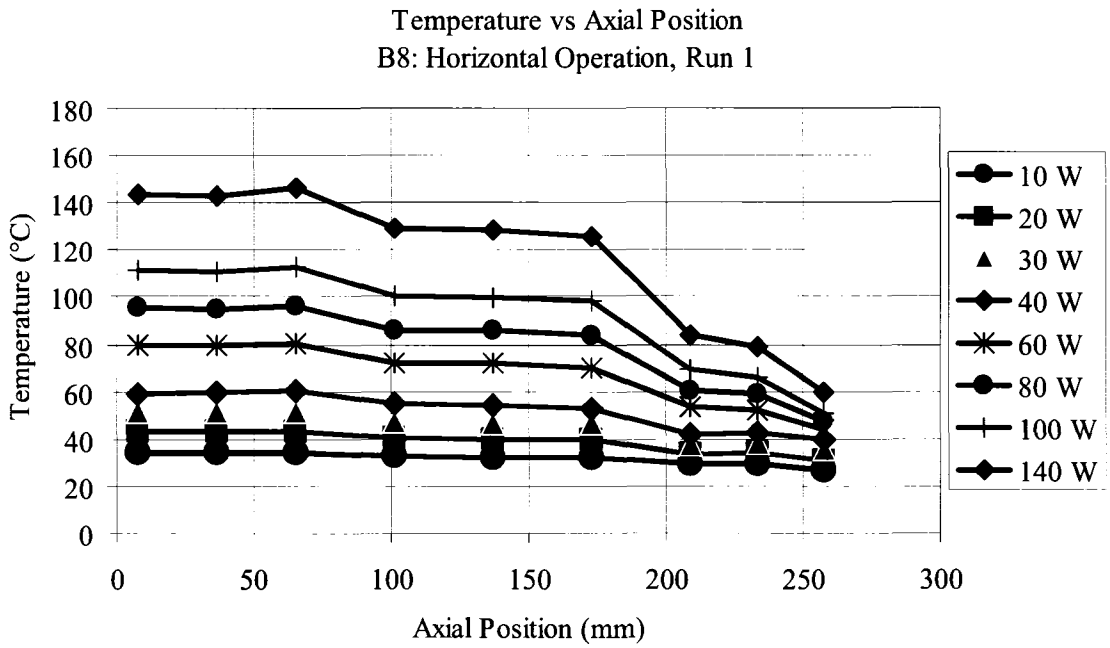

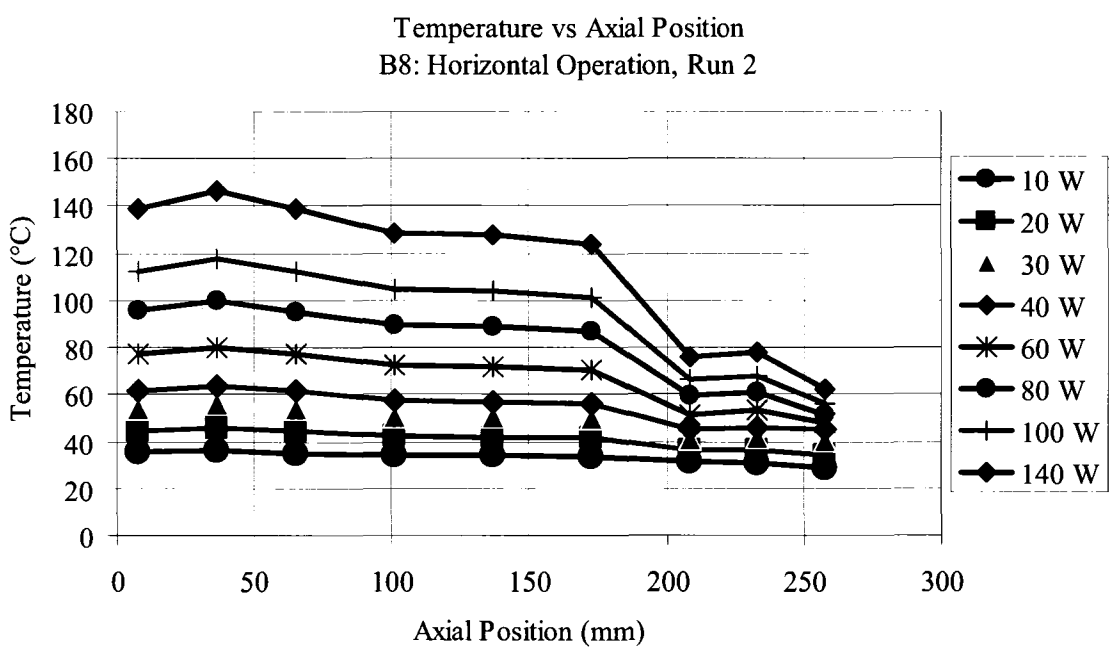

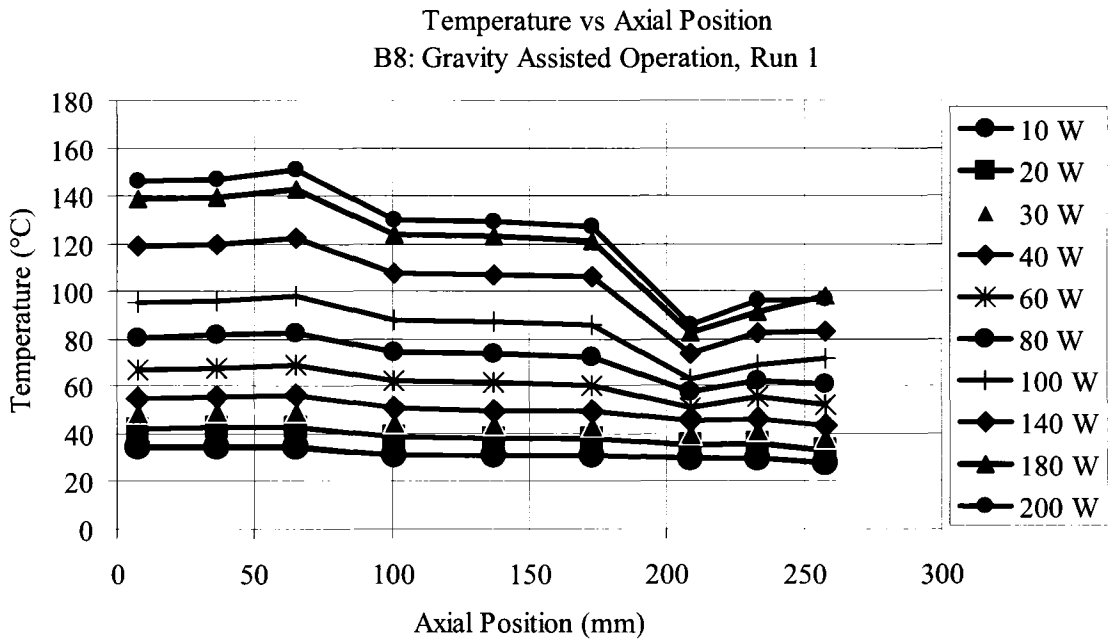

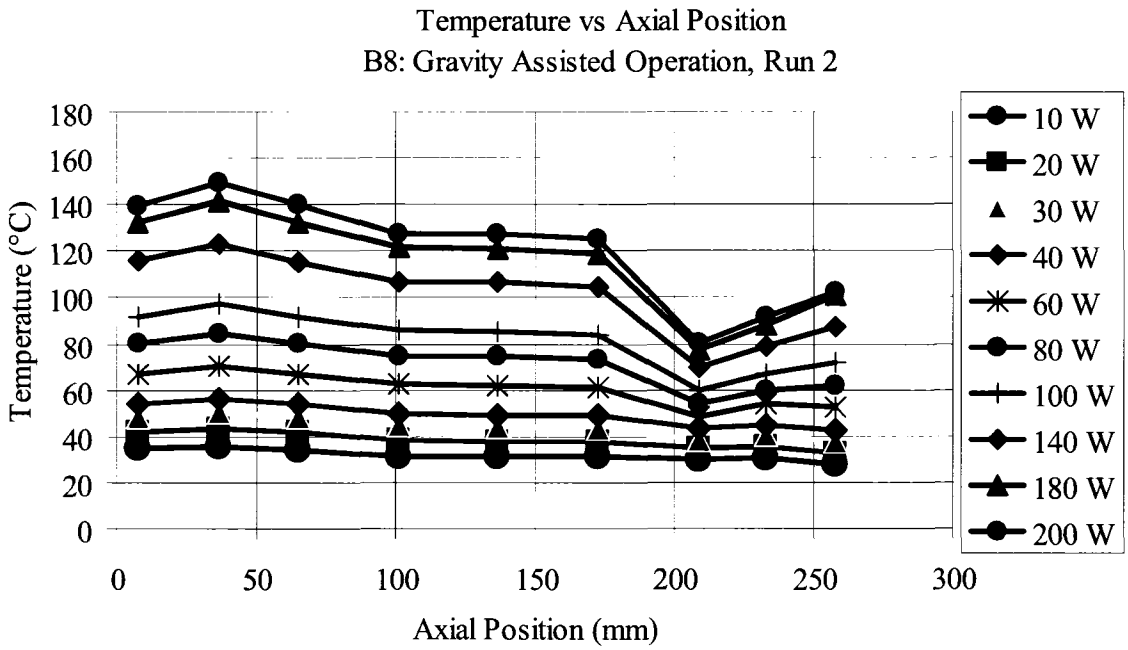

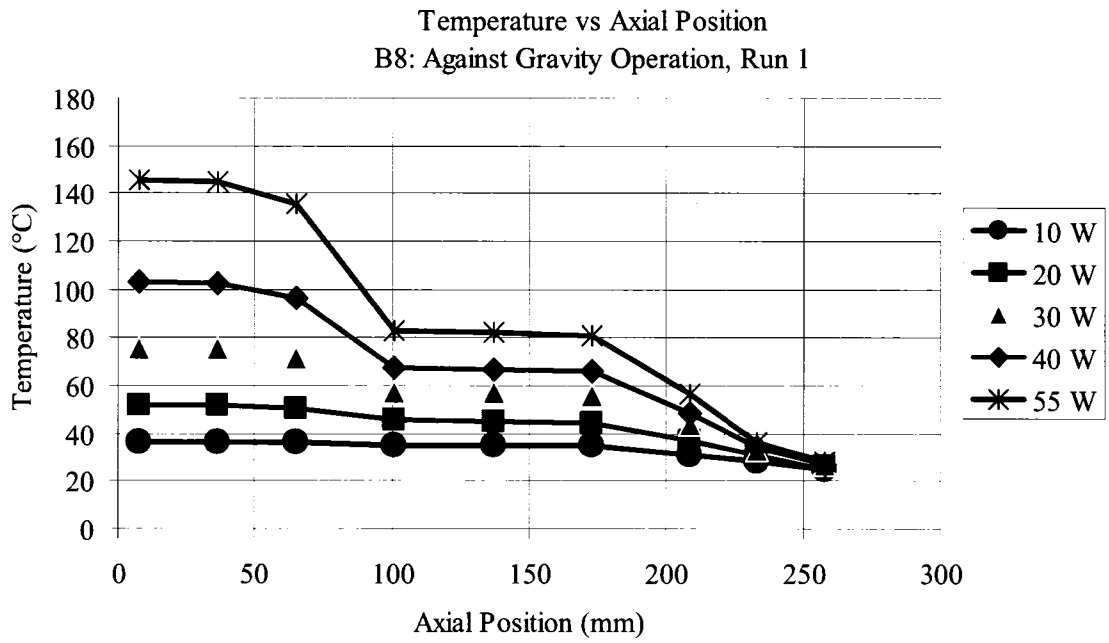

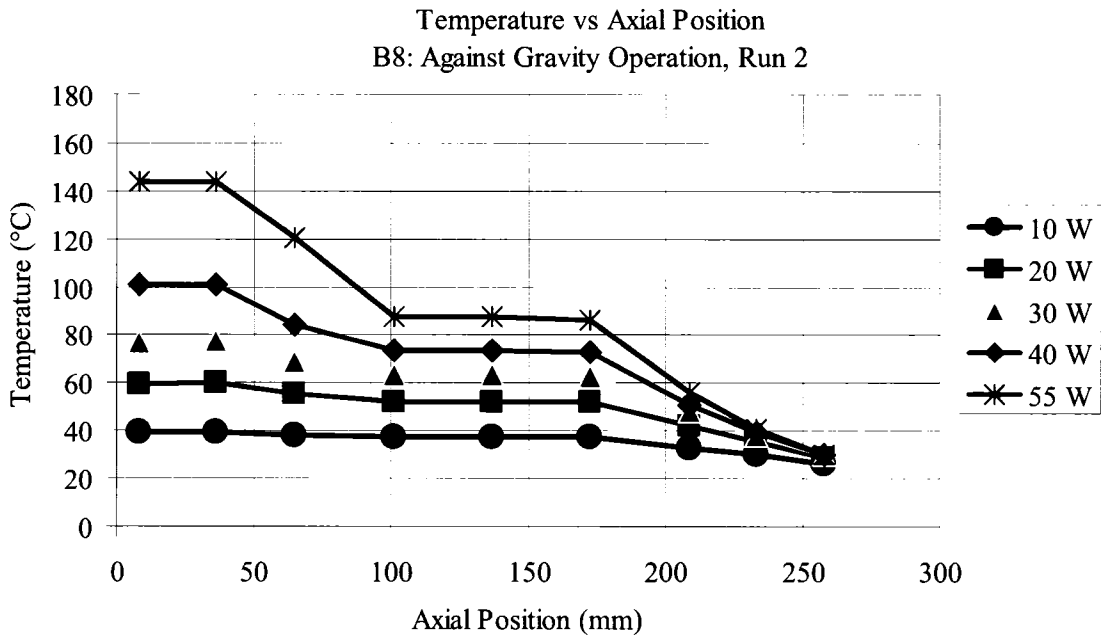

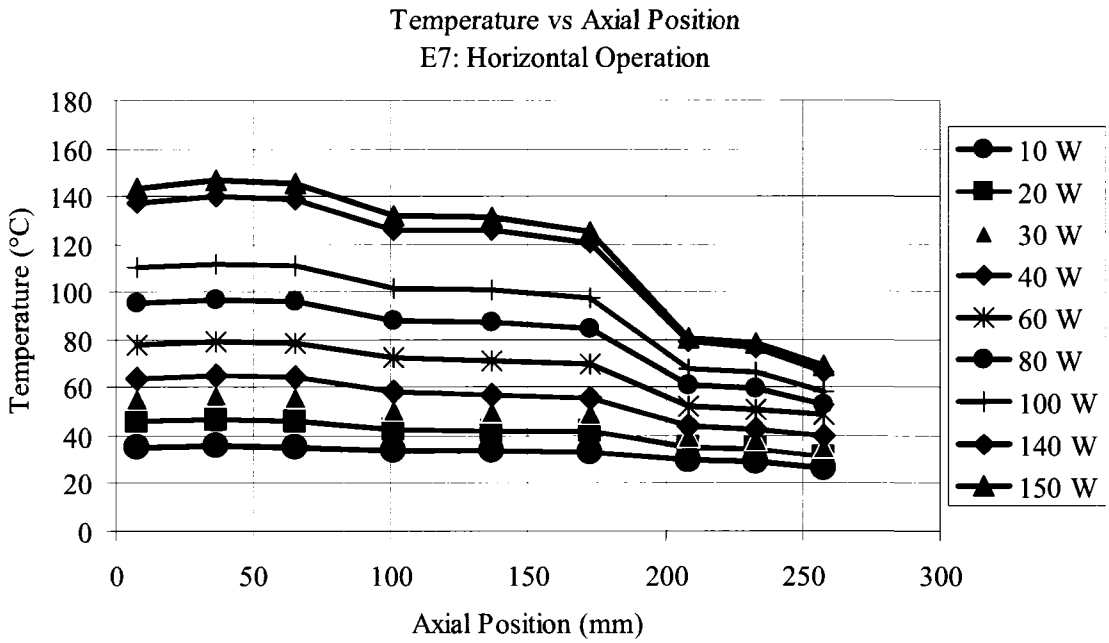

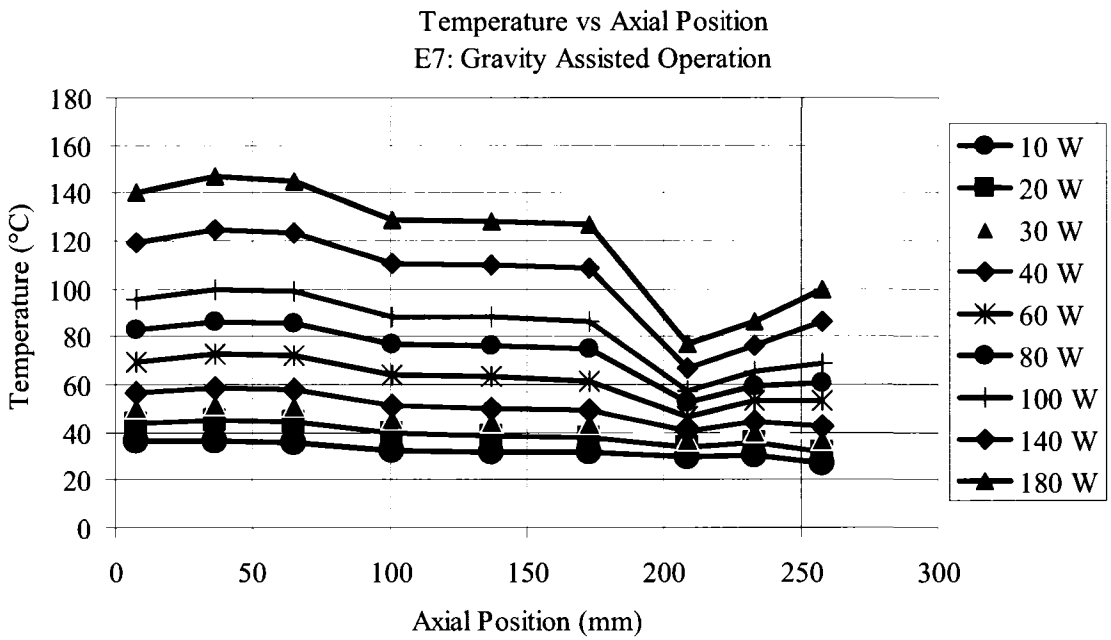

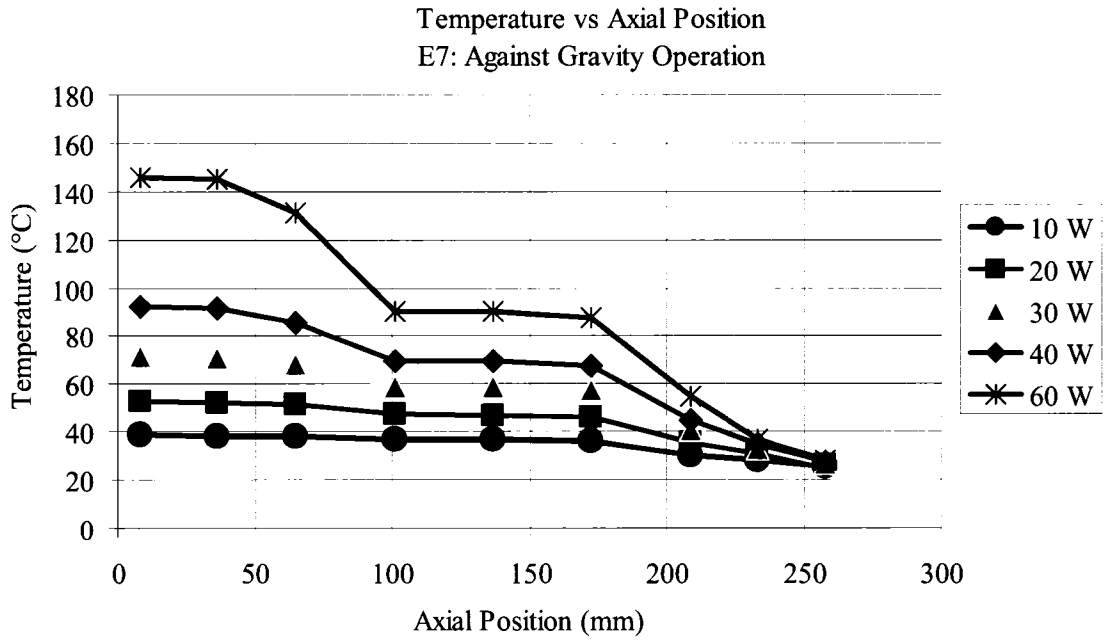

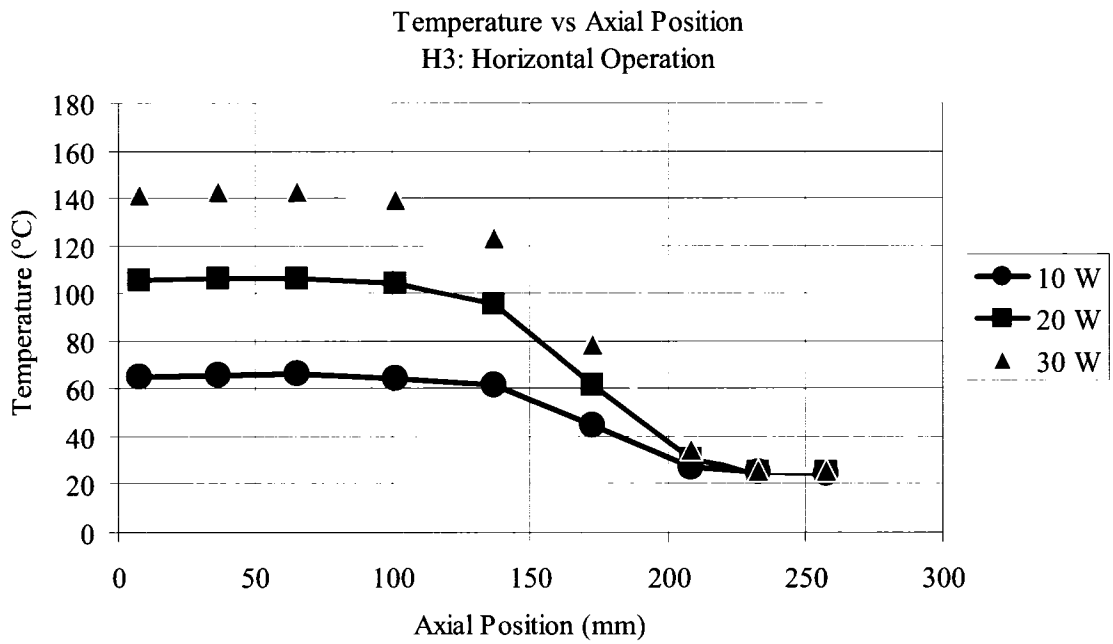

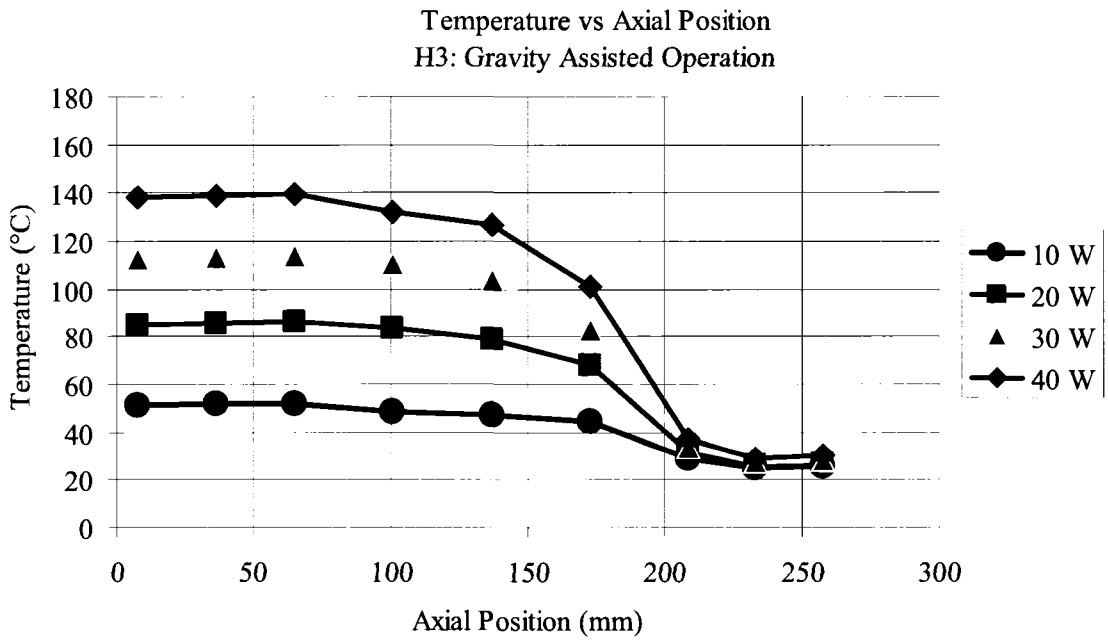

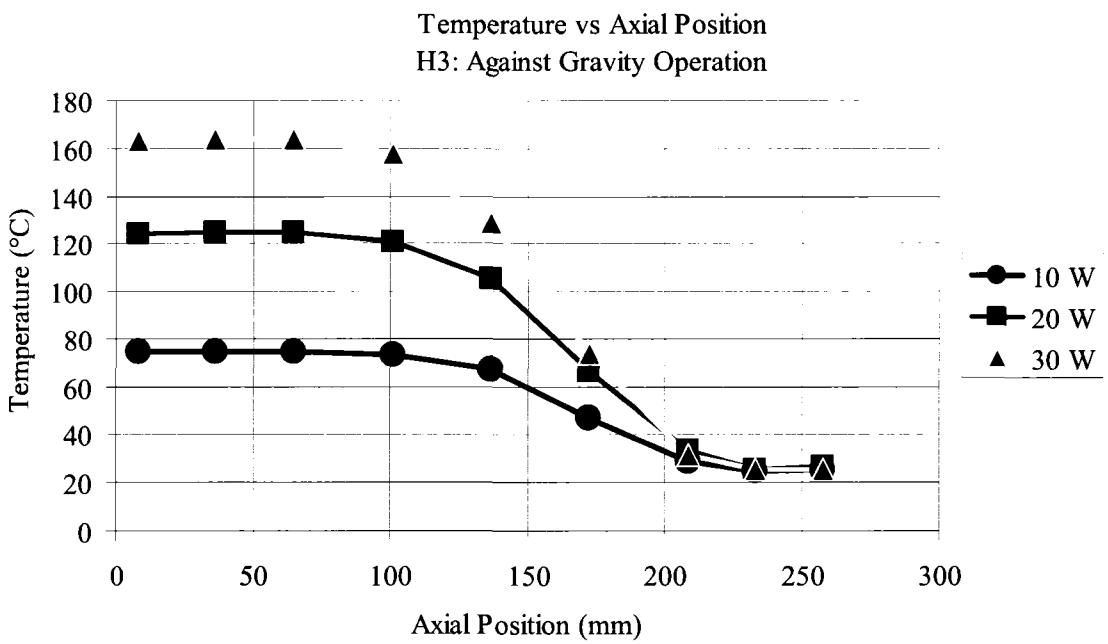

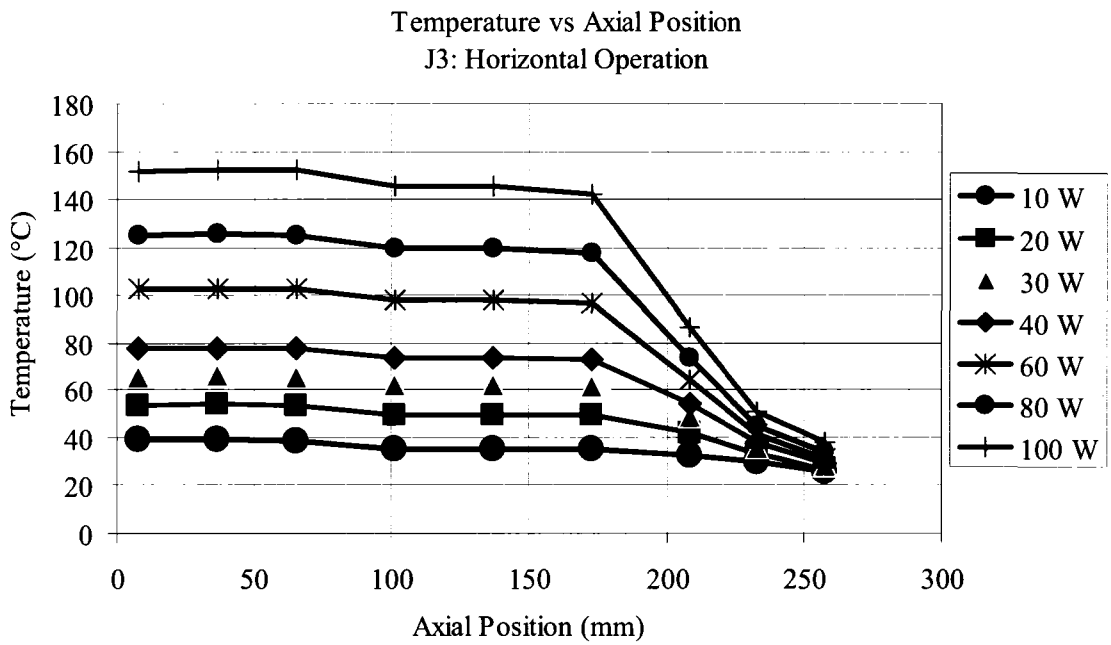

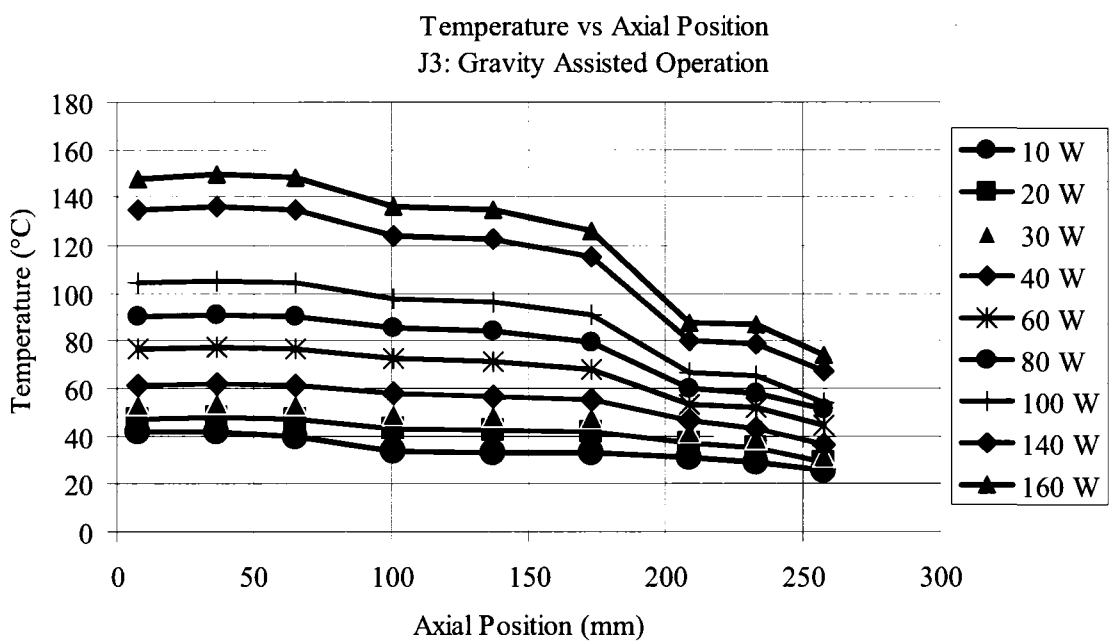

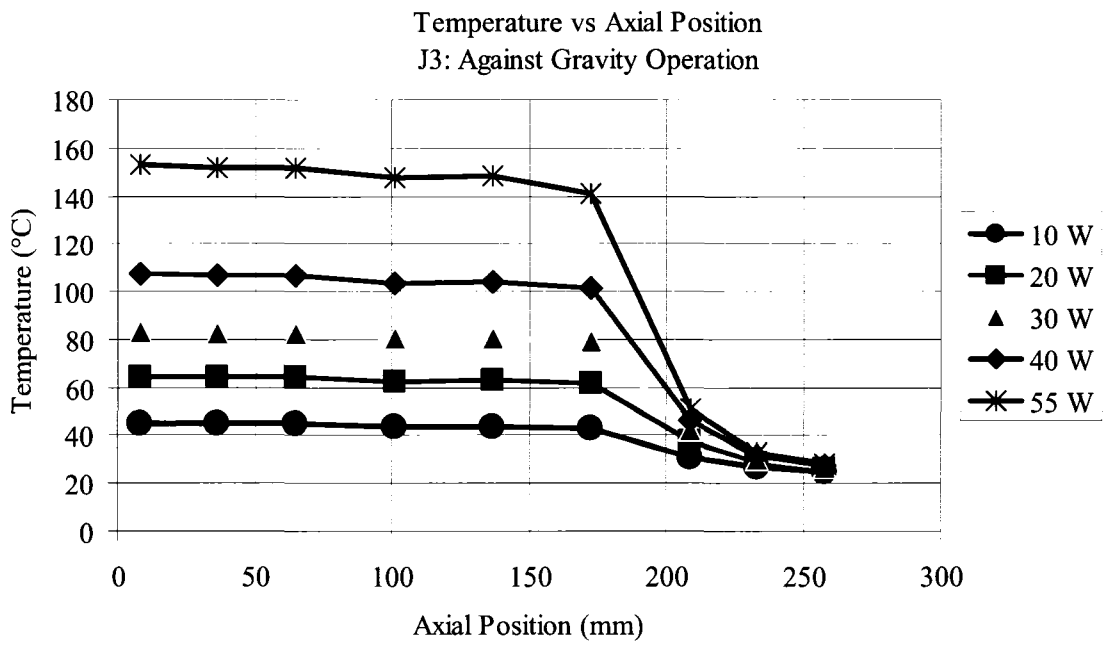

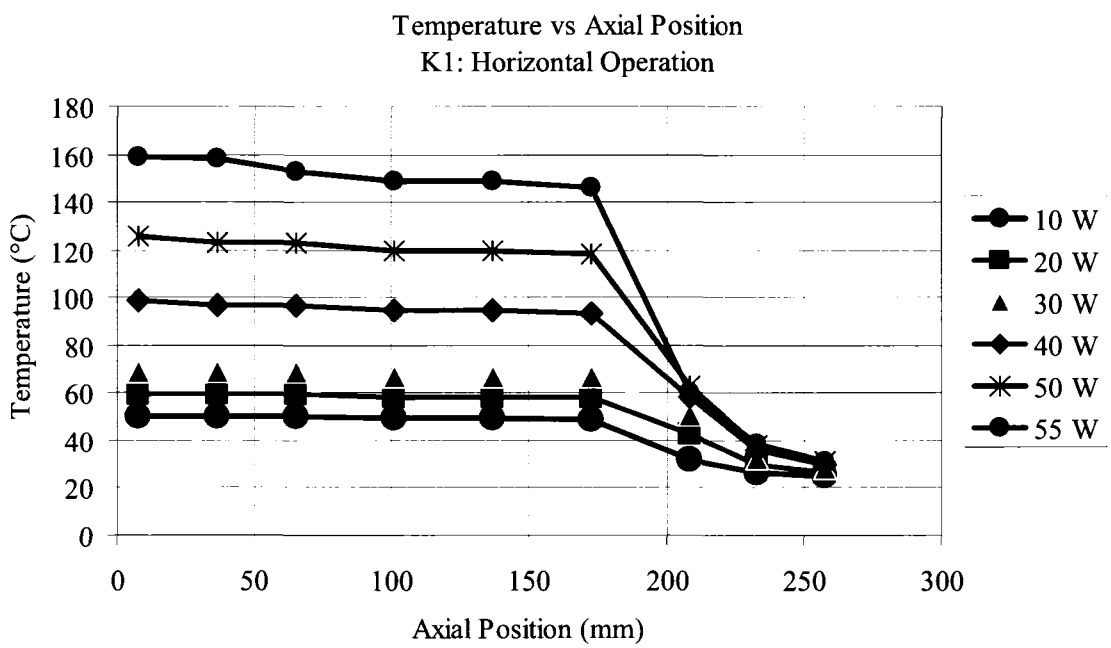

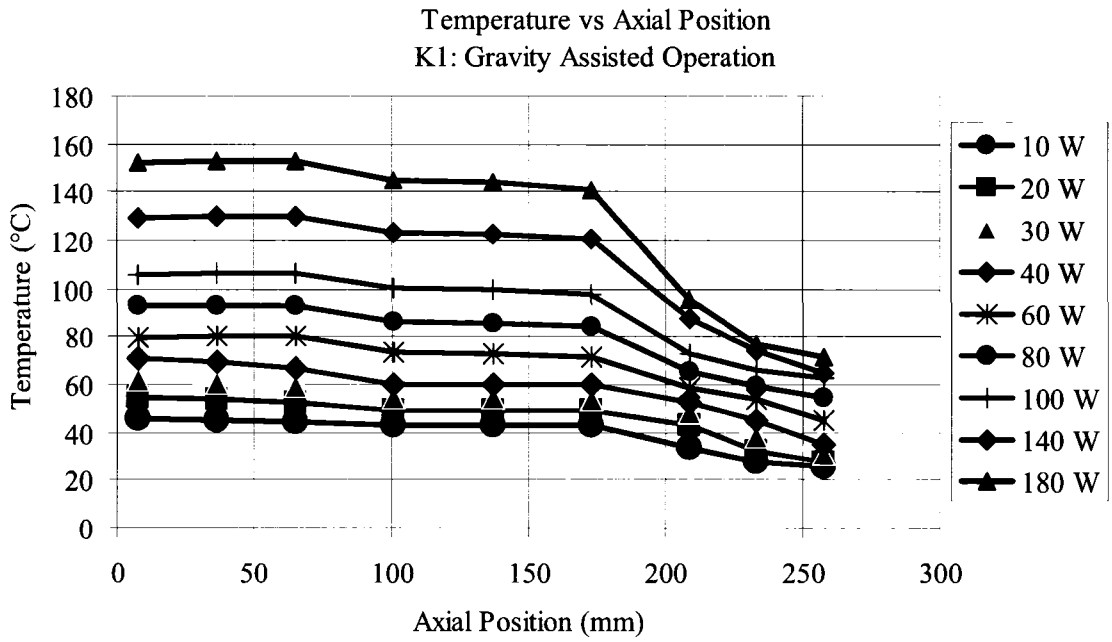

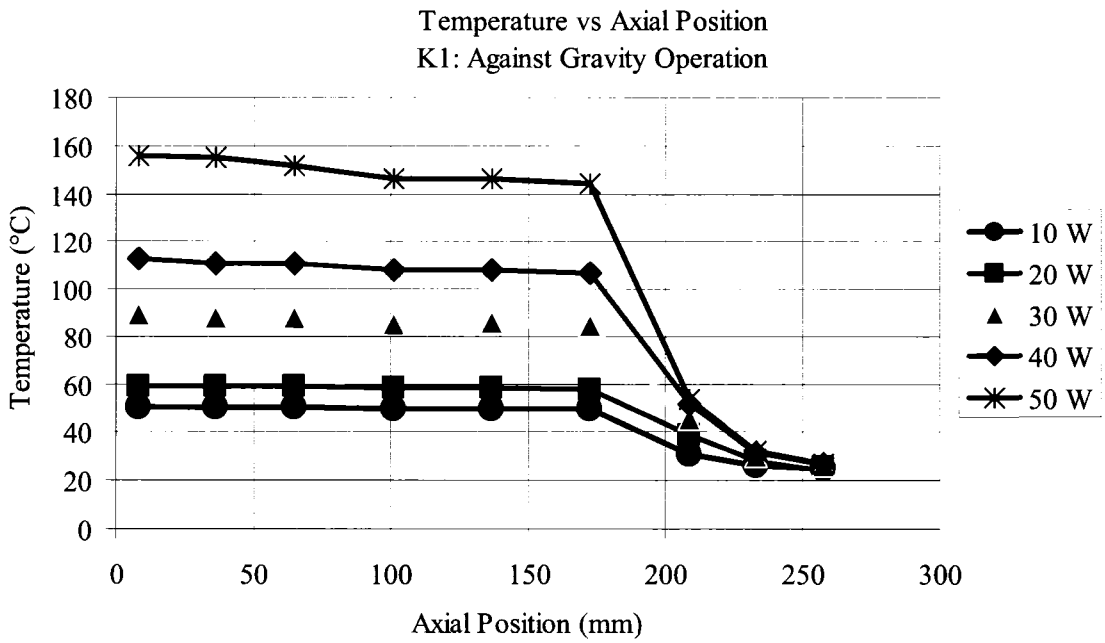

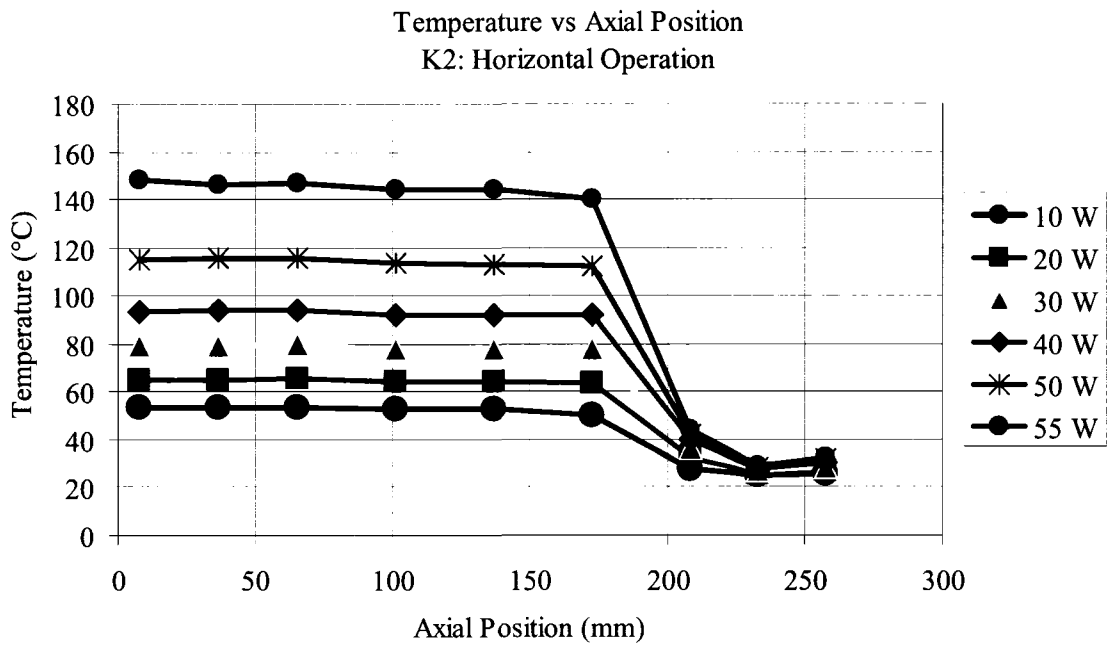

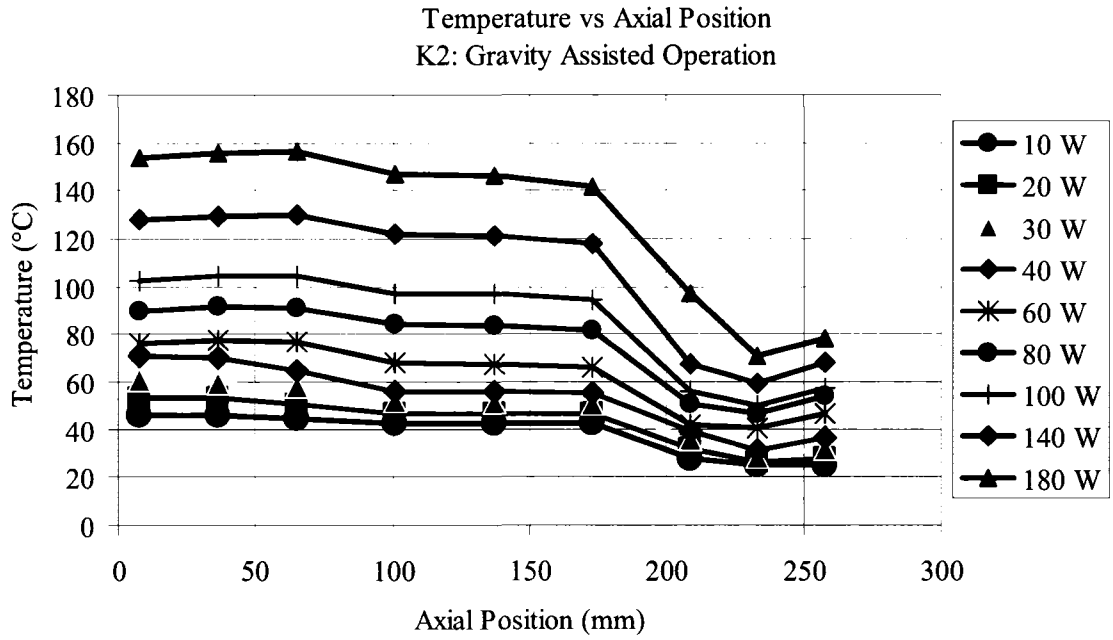

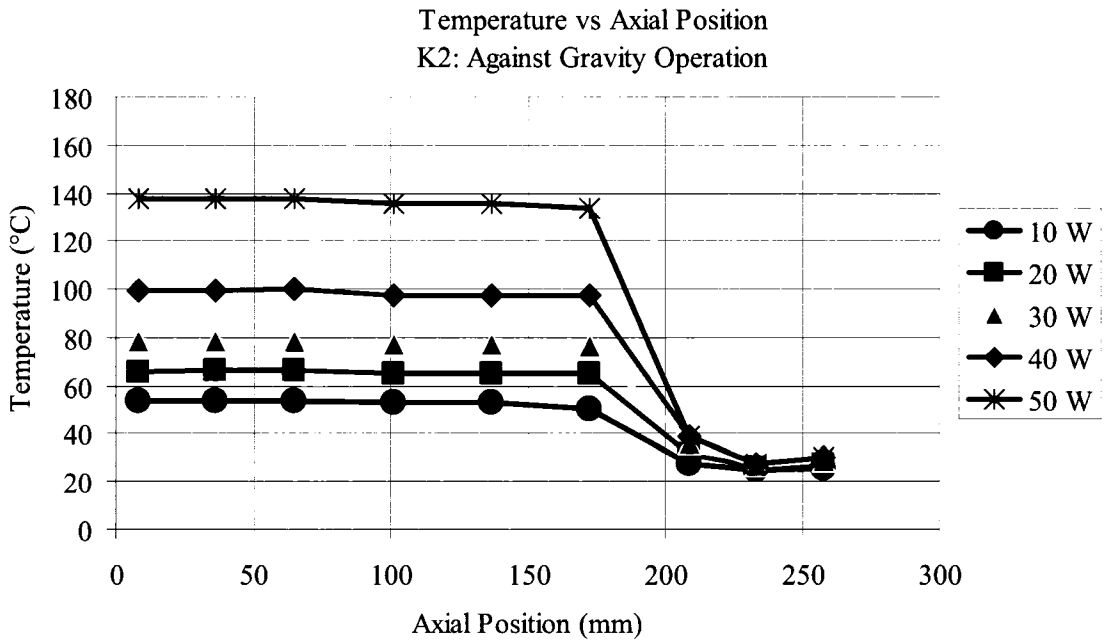

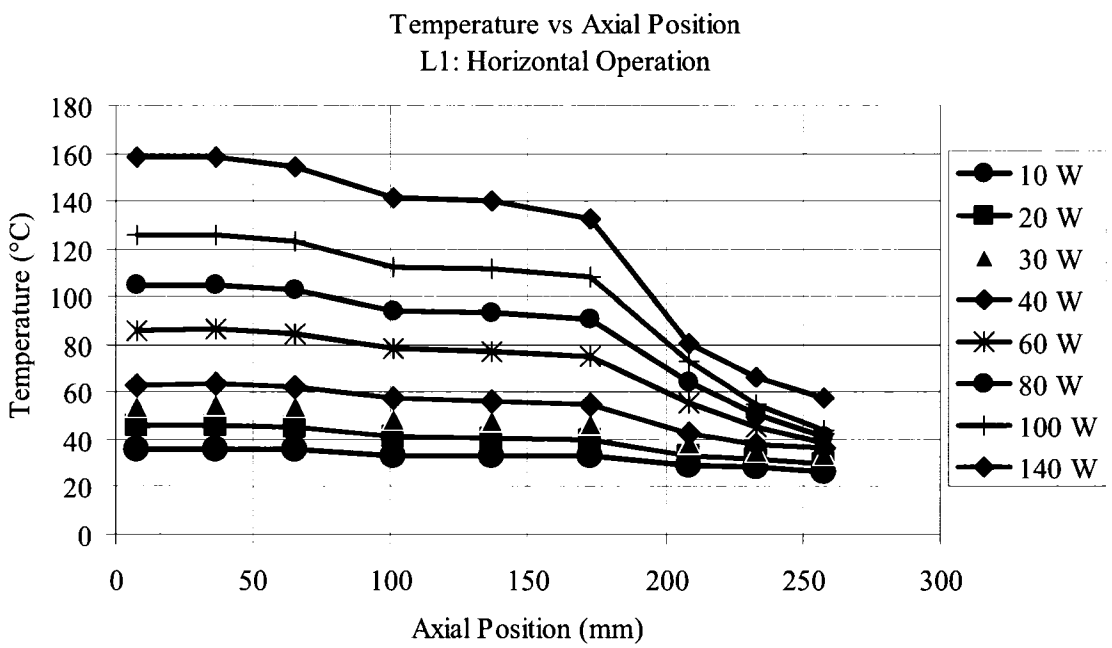

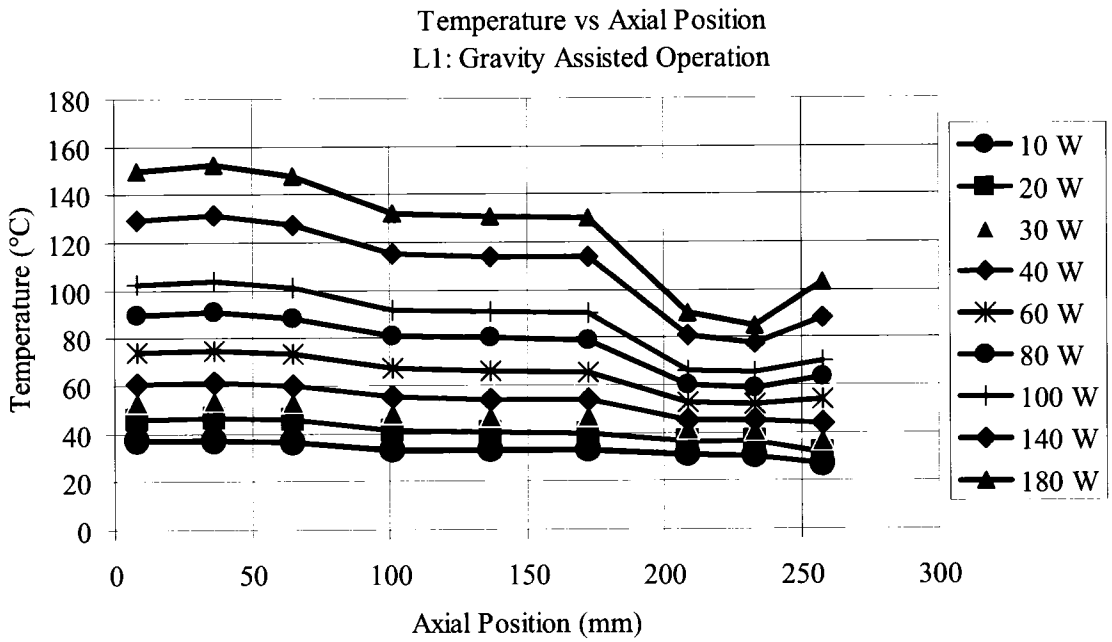

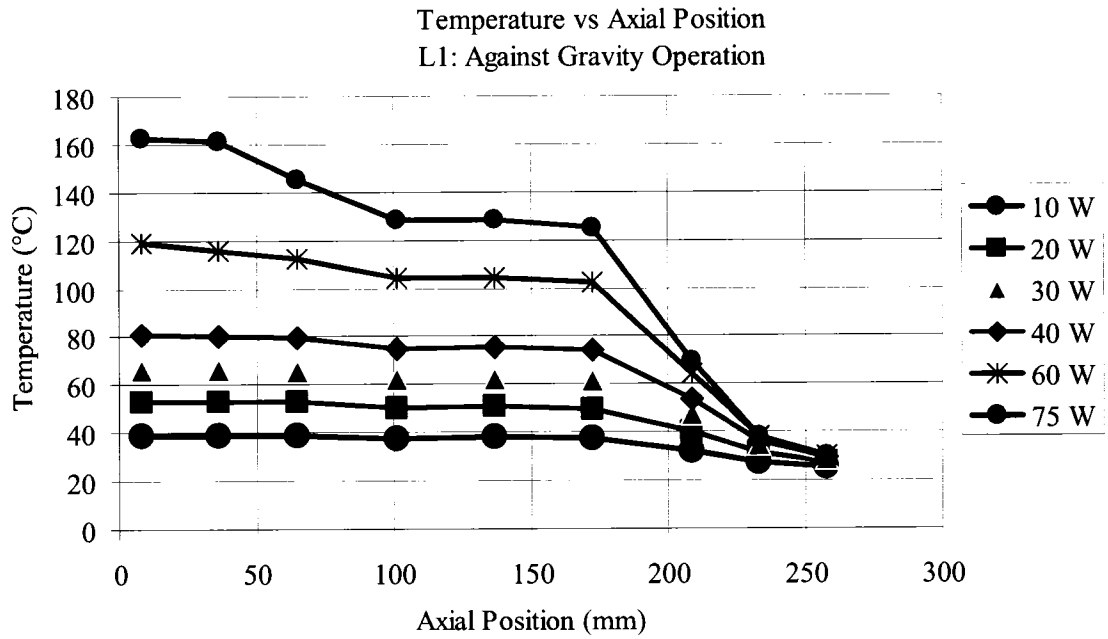

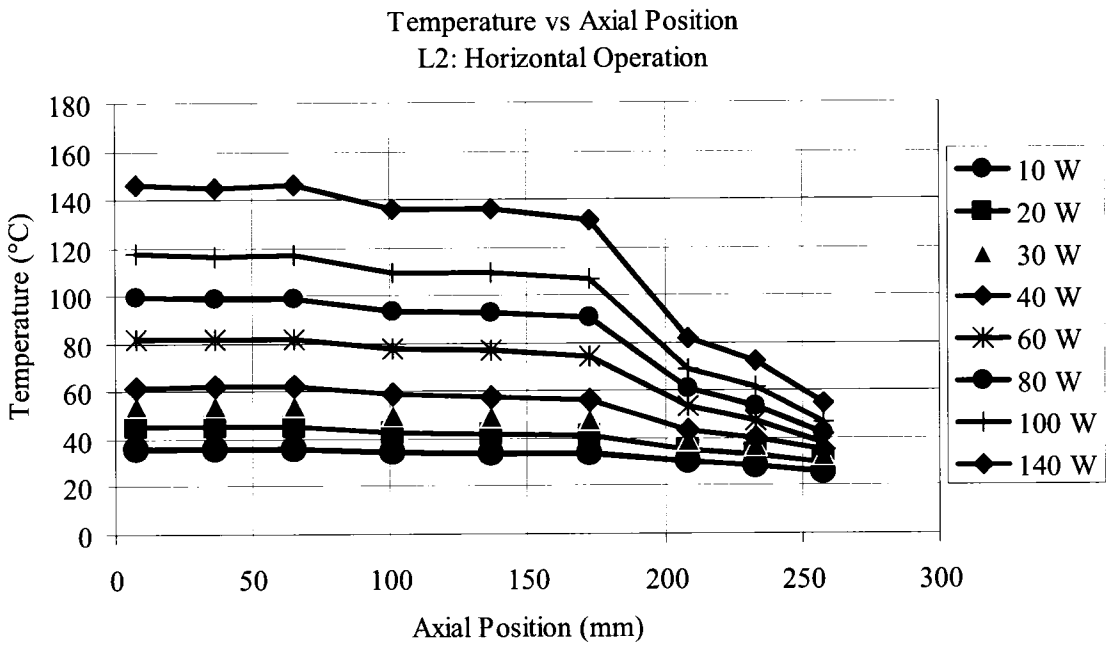

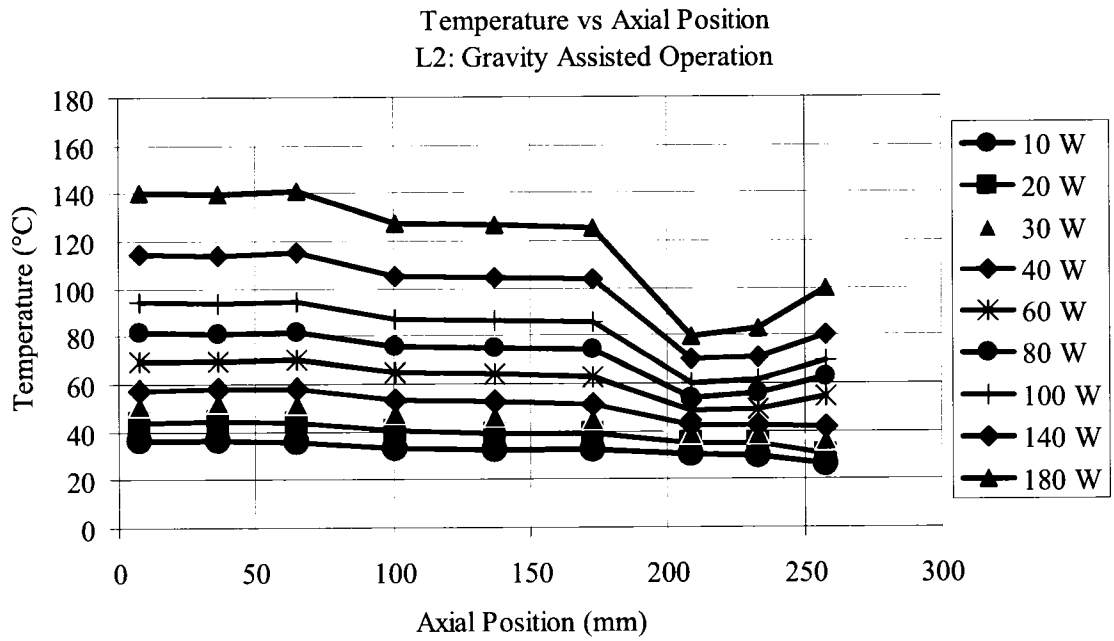

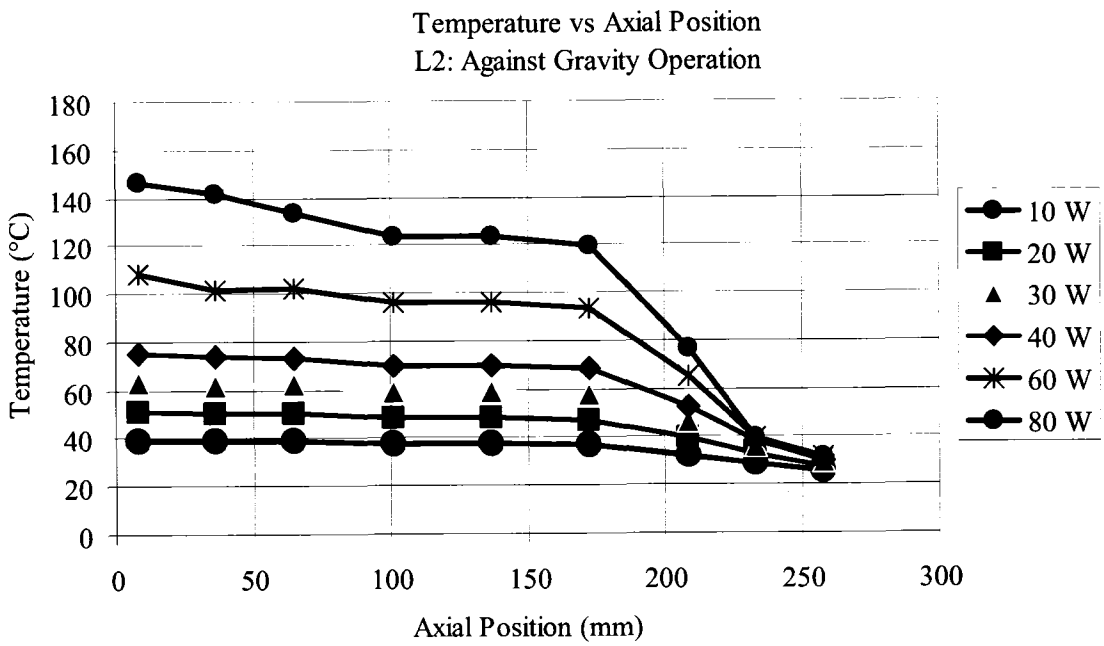

7 References

[1] Faghri, A., *Heat Pipe Science and Technology*, Taylor and Francis, Washington, USA, 1995.

[2] Grover G., Cotter, T., Erikson, G., *Structures of Very High Thermal Conductance*, Los Alamos Scientific Laboratory, Los Alamos, New Mexico, 1964.

[3] Cotter, T.P., *Theory of Heat Pipes: Los Alamos Scientific Laboratory Report No. LA-3246-MS,* Los Alamos Scientific Laboratory, Los Alamos, New Mexico, 1965.

[4] Anon, *Thermacore International, Inc. website,* www.thermacore.com, 2004

[5] Dunn, P., Reay, D.A., *Heat Pipes, Second Edition*, Pergamon Press, Oxford, England, 1978.

[6] Ali, A., DeHoff, R., Grubb, K., *Advanced Heat Pipe Thermal Solutions for Higher Power Notebook Computers,* Intel Corporation, Santa Clara, California, 1999.

[7] Anon, *Mobile Intel Pentium 4 Processor-M Datasheet*, Intel Corporation, Santa Clara, California, 2003.

[8] Lin, S., Sefiane, K., Christy J.R.E., *Prospects of Confined Flow Boiling in Thermal Management of Microsystems*, Applied Thermal Engineering, Vol. 22, pp. 825-837, 2002.

[9] Wang, J., Catton, I., *Vaporization Heat Transfer in Biporous Wicks of Heat Pipe Evaporators*, 13th International Heat Pipe Conference, Shanghai, China, pp. 1-11, 2004.

[10] Peterson, G.P., *An Introduction to Heat Pipes,* John Wiley and Sons, Inc., New York, N.Y., 1994.

[11] Baturkin, V., Zhuk, S., Vojta, J., Lura, F., Biering, B., Lotzke, H., *Elaboration of Thermal Control Systems on Heat Pipes for Microsatellites Magion 4, 5 and BIRD*, Applied Thermal Engineering, Vol. 23, No. 9, pp 1109-1117, 2003.

[12] Anon, *NASA Thermal Engineering Branch website*, http://mscweb.gsfc.nasa.gov/545web/groups/p2/projects/glas/glaslhp.html, 2004.

[13] Waters, E.D., *Heat Pipes for the Trans-Alaska Pipeline*, Second International Heat Pipe Conference, Bologna, Italy, 1976.

[14] Anon, *Alyeska Pipeline website*, http://www.alyeska-pipe.com, 2004.

[15] Jen, T.C., Gutierrez, G., Eapen, S., Barber, G., Zhao, H., Szuba, P.S., Labataille, J., Manjunathaiah, J., *Investigation of Heat Pipe Cooling in Drilling Applications. Part I: Preliminary Numerical Analysis and Verification*, International Journal of Machine Tools and Manufacture, Vol. 42, pp. 643-652, 2002.

[16] Chi, S. W., *Heat Pipe Theory and Practice: A Sourcebook*, McGraw-Hill Book Company, New York, N.Y., 1976.

[17] Franchi, G., *Convective Heat and Mass Transfer Term Project: The Effect of Wick Parameters on Heat Pipe Performance*, Carleton University, 2005.

[18] Léon y Léon, C.A., *New Perspectives in Mercury Porosimetry*, Advances in Colloid and Interface Science, Vol. 76-77, pp. 341-372, 1998.

[19] Maydanik, Y. F., Fershtater, Y.G., *Dimensions of Pores of Wicks of "Antigravity" Heat Pipes*, Heat Transfer-Soviet Research, Vol. 17, No. 4, pp. 119-126, 1985.

[20] Canti, G., Celata, G. P., Cumo, M., Furrer, M., *Thermal Hydraulic Characterization of Stainless Steel Wicks for Heat Pipe Applications*, Revue. Gen. Thermique., Vol. 37, pp. 5-16, 1998.

[21] Busse, C.A., *Pressure Drop in the Vapor Phase of Long Heat Pipes*, Proc. IEEE Conf. of Thermionic Conversion Specialists, Palo Alto, CA., pp. 1279-1287, 1967.

[22] Levy, E.K., *Theoretical Investigation of Heat Pipes Operating at Low Vapour Pressures*, Trans. Am. Soc. Mech. Engrs., Vol. 90B, p. 547, 1968.

[23] Mughal, M.P., Plumb, O.A., *An Experimental Study of Boiling on a Wicked Surface*, International Journal of Heat and Mass Transfer, Vol. 39, No. 4, pp. 771-777, 1996.

[24] Shaubach, R.M.., Dussinger, P.M., Bogart, J.E, *Boiling in Heat Pipe Evaporator Wick Structures*, Proceedings of the 7th International Heat Pipe Conference, Minsk, Belarus, 1990.

[25] Gu, J., *Convective Heat and Mass Transfer Course Notes: Boiling*, Carleton University, Ottawa, 2005.

[26] Holman, J.P., *Heat Transfer, Ninth Edition*, McGraw-Hill, New York, NY, 2002.

[27] Bergles, A.E., Rohsenow, W.M., *ASME Journal of Heat Transfer*, Vol. 86, p. 365-371, 1964.

[28] Brautsch, A., Kew, P., *Examination and Visualization of Heat Transfer Processes During Evaporation in Capillary Porous Structures*, Applied Thermal Engineering, Vol. 22, pp. 815-824, 2002.

[29] Cotter, T.P., *Heat Pipe Startup Dynamics*, Proceedings of the 1967 Thermionic Conversion Specialist Conference, pp. 344-348, Palo Alto, California, 1967.

[30] Zuo, Z.J., Faghri, A., *A Network Thermodynamic Analysis of the Heat Pipe*, International Journal of Heat and Mass Transfer, Vol. 41, No. 11, pp. 1473-1484, 1998.

[31] Abo El-Naser, A., El-Haggar, S.M., *Effective Thermal Conductivity of Heat Pipes*, Heat and Mass Transfer, Vol. 32, pp. 97-101, 1996.

[32] Moran, M.J., Shapiro, H.N., *Fundamentals of Engineering Thermodynamics, 4th Edition*, John Wiley and Sons, New York, N.Y., 2000.

[33] Anon, *The Chemical Institute of Canada, Hamilton Section website,* http://home.nas.net/~dbc/cic_hamilton/dictionary/c.html, 2004.

[34] Tien, Chen, *Non-Condensable Gases in Heat Pipes*, 5th International Heat Pipe Conference, Tsukuba, Japan, 1984.

[35] Kreeb, H., Groll, M., Zimmerman, P., *Life Test Investigations with Low Temperature Heat Pipes*, 1st International Heat Pipe Conference, Stuttgart, 1973.

[36] Yamamoto, Tanaka, *Long-Term Test of Sodium Heat Pipe*, 5th International Heat Pipe Conference, Tsukuba, Japan, 1984.

[37] Busse, C.A., Campanile, A, Loens, J., , *Hydrogen Generation in Water Heat Pipes at 250°C*, 1st International Heat Pipe Conference, Stuttgart, 1973.

[38] Dunn, P., Reay, D.A., *Heat Pipes, Third Edition*, Pergamon Press, New York, 1982.

[39] Williams, R., Harris, D., *Cross-Plane and In-Plane Porous Properties Measurements of Thin Metal Felts: Applications in Heat Pipes*, Experimental Thermal and Fluid Science, Vol. 27, pp 227-235, 2003.

[40] Anon, *Cleveland Wire Cloth company website,* www.wirecloth.com/rawmaterials.html, 2004.

[41] Anon, *International Wire Weavers Association website,* www.wire-cloth.com/reference/glossary.htm, 2004.

[42] Gupta, A., Upadhya, G., *Optimization of Heat Pipe Wick Structures for Low Wattage Electronics Cooling Applications*, Advances in Electronics Packaging, Vol. 2, pp. 2129-2137, 1999.

[43] Imura, H., Kozai, H., Ikeda, Y., *Effective Pore Radius of Screen Wicks*, Heat Transfer Engineering, Vol. 15, No. 4, pp. 24-32, 1994.

[44] Marcus, B. D., *Theory and Design of Variable Conductance Heat Pipe*, Report No. CR-2018, NASA, Washington, D.C., 1972.

[45] Hoa, C., Demolder, B., Alexandre, A., *Roadmap for Developing Heat Pipes for ALCATEL SPACE's Satellites*, Applied Thermal Engineering, Vol. 23, pp. 1099-1108, 2003.

[46] Wang, J., Catton, I., *Enhanced Evaporation Heat Transfer in Triangular Grooves Covered with a Thin Fine Porous Layer*, Applied Thermal Engineering, Vol. 21, pp. 1721-1737, 2001.

[47] Groll, M., Schneider, M., Sartre, V., Zaghdoudi, M.C., Lallemand, M., *Thermal Control of Electronic Equipment by Heat Pipes*, Revue Gen. Thermique, Vol. 37, pp 323-352, 1998.

[48] Beddoes, J., Bibby, M.J., *Principles of Metal Manufacturing Processes*, John Wiley & Sons, Inc., New York, N.Y., 1999.

[49] Peterson, G.P., *Modeling, Fabrication and Testing of Micro Heat Pipe Arrays: An Update*, Applied Mechanics Review, Vol. 49, No. 10, Part 2, pp. S175-S183, 1996.

[50] Groover, M. P., *Fundamentals of Modern Manufacturing, Second Edition*, John Wiley and Sons, Inc., New York, N.Y., 2002.

[51] Leong, K.C., Liu, C.Y., *Characterization of Sintered Copper Wicks Used in Heat Pipes*, Journal of Porous Materials, Vol. 4, pp. 303-308, 1997.

[52] Reimbrecht, E.G., Wendhausen, P., Fredel, M.C., Bazzo, E., *Manufacturing of Flat Porous Structures for Capillary Pump Applications*, Key Engineering Materials, Vols. 189-191, pp. 455-460, 2001.

[53] Dowson, G., *Powder Metallurgy: The Process and its Products*, IOP Publishing Ltd, Bristol, England, 1990.

[54] Callister, W., *Materials Science and Engineering: An Introduction*, John Wiley and Sons, Inc., N.J., 2003.

[55] Banhart, J., *Manufacture, Characterization and Application of Cellular Metals and Metal Foams*, Progress in Materials Science, Vol. 46, pp. 559-632, 2001.

[56] German, R. M., *Powder Metallurgy Science, 2nd Edition*, Metal Powder Industries Federation, Princeton N.J., 1994.

[57] Beddoes, J., *MAAE 4102 Course Notes, Chapter 7: Creep,* Carleton University, Ottawa, 2003.

[58] Tracey, V.A., *Sintering of Porous Nickel-Theoretical and Practical Considerations*, Modern Developments in Powder Metalllurgy, Vol. 12, pp. 423-438, 1981.

[59] Kajikawa, T., Takazawa, H., *Heat Transfer Performance of Metal Fiber Sintered Surfaces*, Heat Transfer Engineering, Vol. 4, No.1, pp. 57-66, 1983.

[60] North, M., Rosenfeld, R., *Liquid Film Evaporation from Bidisperse Capillary Wicks in Heat Pipe Evaporators*, 9th International Heat Pipe Conference, Albuquerque, NM, pp. 143-147, 1995.

[61] Hanlon, M., Ma, H., *Evaporation Heat Transfer in Sintered Porous Media*, Transactions of the ASME, Vol. 125, pp. 644-652, 2003.

[62] Wang, J., Merilo, E., Catton, I., *Investigation of Evaporation Heat Transfer in Porous Wicks for High Heat Flux Applications*, Proceedings of ASME NHTC'01 35th National Heat Transfer Conference, pp. 1063-1070, Anaheim, California, 2001.

[63] Konev, S.K., Polasek, F., Horvat, L., *Investigation of Boiling in Capillary Structures*, Heat Transfer-Soviet Research, Vol. 19, No. 1, pp. 14-17, 1987.

[64] Wang, J., Catton, W., *Biporous Heat Pipes for High Power Electronic Device Cooling*, 17th IEEE SEMI-THERM Symposium, pp. 211-218, 2001.

[65] North, M., Sarraf, D., Rosenfeld, J., *High Heat Flux Loop Heat Pipes*, Proceedings of the 6th European Space Symposium, Noordwijk, The Netherlands, pp. 371-376, 1997.

[66] Semenic, T., Lin, Y., Catton, I., *Use of Liquid Film Evaporation in Biporous Media to Achieve High Heat Flux over Large Areas*, Proceedings of 2005 ASME Summer Heat Transfer Conference, San Francisco, CA, pp. 63-68, 2005.

[67] Cao, X.L., Cheng, P., Zhao, T.S., *Experimental Study of Evaporative Heat Transfer in Sintered Copper Bidispersed Wick Structures*, Journal Of Thermophysics and Heat Transfer, Vol. 16, No. 4, 2002.

[68] Anon, *McMaster-Carr website*, www.mcmaster.com, 2006.

[69] Smithells, C.J., Brandes, E.A., Brook, G.B., *Smithells Metals Reference Book, 7th Edition*, Butterworth-Heinemann, Oxford, Boston, 1998.

[70] Anon, *Copper Development Association Website*, www.copper.org/resources/properties, 2006.

[71] Anon, *Sulzer Metco Website*, www.sulzermetco.com, 2006.

[72] Huang, X., Franchi, G., *Hybrid Wicking Material for Use in High Performance Heat Pipes*, US patent, 11/185,013 filed July 20, 2005 and PCT/CA 2005/00001141 filed July 20, 2005.

[73] Anon, *INCO Type 255 Filamentary Nickel Powder Product Data Sheet,* www.incosp.com/pdf/sp_nickelType255_en.pdf, 2006.

[74] Anon, *Cole-Parmer Refrigerated Recirculation Chiller Operator's Manual*, Cole-Parmer Instrument Company, Vernon Hills, IL, 1999.

[75] Anon, *The Temperature Handbook*, Omega Engineering, Inc., Stamford, CT., 2003.

[76] Anon, *Fluke 45 Dual Display Multimeter User's Manual*, Fluke Corporation, Everett, WA, 1999.

[77] Anon, *Low Volume Rotating Vane Flowmeter Model DPM*, Kobold Messring GmbH, Hofheim/Taunus, Germany, 2005.

[78] Anon, *FieldPoint Operating Instructions: FP-TC-120 and cFP-TC-120 8-Channel Thermocouple Input Modules*, National Instruments Corporation, Austin, TX, 2005.

[79] Anon, *FieldPoint Operating Instructions: FP-AI-100 and cFP-AI-100 Eight-Channel, 12-Bit Analog Input Modules*, National Instruments Corporation, Austin, TX, 2005.

[80] Anon, *FieldPoint FP-1000/FP-1001 User Manual*, National Instruments Corporation, Austin, TX, 2003.

[81] Anon, *OMEGATHERM® Thermally Conductive Silicone Paste Instruction Sheet*, Omega Engineering, Inc., Stamford, CT., 2005.

[82] Kempers, R., Robinson, A., Ching, C., Ewing, D., *Effect of Fluid Loading on the Performance of Wicked Heat Pipes*, Proceedings of the 2004 ASME Heat Transfer/Fluids Engineering Division Summer Meeting, North Carolina, U.S.A., 2004.

[83] Wadden, J., *Introductory Physics of Electromagnetism with Engineering Applications: 75.104 Lab Manual*, Carleton University, Ottawa, 1999.

[84] Wheeler, A.J., Ganji, A.R., *Introduction to Engineering Experimentation*, Prentice-Hall, Inc., New Jersey, 1996.